universität wien

DISSERTATION

Titel der Dissertation

High Resolution Mobility Spectrometry Of Molecular Ions And Their Effect On The Charging Probabilities Of Airborne Particles Under Bipolar Diffusion Charging Conditions

angestrebter akademischer Grad

Doktor der Naturwissenschaften (Dr. rer. nat.)

Verfasserin / Verfasser:	Mag. Gerhard Steiner
Matrikel-Nummer:	A9847981
Dissertationsgebiet (lt. Studienblatt):	091 411 Physik
Betreuerin / Betreuer:	Ao. Univ. Prof. Dr. Georg P. Reischl

Wien, im April 2011

Acknowledgements

In the course of the years of my doctoral studies, many people have significantly contributed to the creation of this thesis.
First of all, I have to thank Prof. Georg Reischl for supervising my thesis and encouraging me to try new and unusual approaches to solve – not only - scientific problems. I also have to thank the Austrian Science Funds FWF for providing the necessary finical support under grant P20837-N20.

I also want to express my gratitude to all the members and former members of the Viennese aerosol group who always had time for fruitful discussions and debates. Here, my special thanks go to Prof. Regina Hitzenberger who not only proof read this thesis but also supported me in many ways over the past years. I want to thank Prof. Paul Wagner for providing deeper insights in fundamental physics during our jointly held introduction to physics lecture, and Dr. Paul Winkler for motivating me to participate to conferences and workshops and thereby broadening my scientific mind.
As modern scientific work goes hand in hand with international cooperation, my special thanks go to Prof. Markku Kulmala from the University of Helsinki, who started supporting me since the end of my diploma thesis. I am very grateful for the often repeated visits to Helsinki and the warm welcome in Prof. Kulmalas' working group. I also want to thank Prof. Michel Attoui from the University Paris XII for introducing me into using the electrospray method and numerous conversations on science and life.
I want to thank my family who made it possible for me to start my University studies and who will always play an important part in my life.

Last but not least I have to thank my wife Claudia and my son Maximilian, who both were unbelievably patient especially close to the completion of this thesis. Only due to their help and support it was possible to finish this thesis.

Abstract

The aim of this thesis is to gain more insights in the properties of molecular ions that are of special importance for the understanding of new particle formation in the atmosphere. The knowledge of the properties of molecular ion clusters is of crucial importance also for the application of the most widely used nanoparticle sizing-technique, the Electrical Mobility Spectrometry (EMS), since they are required to establish a defined charging state on aerosol particles. As most of the available EMS-instrumentation is not suitable for the detection of < 3nm particles or clusters, a new high resolution Differential Mobility Analyzer, called UDMA, was designed and tested in the framework of this thesis. This new instrument allows high resolution mobility measurements of airborne particles and molecular clusters. The critical properties of the charging ions are determined over a large variety of different operating conditions and varying degrees of carrier gas purity. The experiments showed that depending on the operating conditions, very different ion clusters are produced and the mean ion mobility (mean ion mobility equivalent diameter) and consequently also the overall mean ion mass is alternating between higher or lower values. These properties are the input parameters for the most commonly accepted charging theory of airborne nanoparticles in a bipolar ionic atmosphere (Fuchs, 1963). The dependency of the calculated charging probabilities on the properties of the charging ions is evaluated and discussed in detail.

Kurzfassung

Das Ziel dieser Arbeit ist es, einen tieferen Einblick in die Eigenschaften molekularer Ionen zu gewinnen, die von besonderer Wichtigkeit für das Verständnis der Partikelneubildung in der Atmosphäre sind. Aber auch für die Anwendung der am weitesten verbreiteten Methode zur Größenbestimmung von Nanopartikeln, der Elektrostatischen Mobilitäts Spektrometrie (EMS), ist die Kenntnis der Eigenschaften von molekularen geladenen Clustern von essentieller Bedeutung, da diese für die Herstellung eines definierten Ladungszustandes auf Aerosolpartikeln benötigt werden. Da die meisten kommerziell erhältlichen EMS-Geräte für die Detektierung von Partikeln < 3nm nicht geeignet sind, wurde im Rahmen dieser Arbeit ein neuer hoch auflösender Differentieller Mobilitäts Analysator, genannt UDMA, konzipiert und getestet. Dieses neue Gerät erlaubt hoch auflösende Mobilitätsmessungen von Gas getragenen Partikeln und molekularen Clustern. Damit wurden die wesentlichen Eigenschaften der aufladenden Ionen für eine Vielzahl verschiedener Arbeitsbedingungen und Reinheitsgraden des Trägergases bestimmt. Die Experimente zeigen, dass - abhängig von den jeweiligen Arbeitsbedingungen - sehr verschiedene Ionen-Cluster produziert werden und damit die mittlere Ionenmobilität (mittlerer Ionenmobilitätsequivalentdurchmesser) und auch die mittlere Ionenmasse großen Schwankungen unterworfen sind. Diese Eigenschaften sind die Eingangsparameter für die am weitesten akzeptierte Ladungstheorie von Gas getragenen Nanopartikeln in einer bipolaren Ionenatmosphäre (Fuchs, 1963). Die Abhängigkeit der berechneten Ladungswahrscheinlichkeiten von den Eigenschaften der aufladenden Ionen wird in dieser Arbeit detailliert besprochen und evaluiert.

Contents

1. Introduction

Aerosol particles affect human life in multiple ways: health issues and respiratory problems are linked to air pollution, smoke, fog and smog strongly decrease visibility and also the occurrence of beautiful coloured sunsets also indicates the presence of aerosols. They influence our life also through almost endless industrial and medical applications and advances in nanotechnology allow the synthesis of materials with so far unmatched physical and chemical properties. But maybe most important, aerosols are thought to strongly contribute to Earth's radiative balance and play a role in climate change (IPCC, 2007): as a direct effect, aerosols scatter sunlight directly back into space and as an indirect effect, aerosols in the lower atmosphere can influence the microphysical properties of clouds' both short- and longwave radiative fluxes. As the magnitude of the impact of both effects on Earth's climate is still highly uncertain, there is for sure an essential need for more in depth investigations.
Especially the particle size range below 3nm has become of high scientific interest in the past years, as it covers the initial steps of new particle formation in the atmosphere (Kulmala et al. 2007) from charged and uncharged molecular clusters to larger agglomerates and further to aerosol particles which can act as cloud condensation nuclei (CCN).

Therefore, this doctoral thesis is a continuation of the work started with my master's thesis (Steiner, 2006) to characterize aerosols and clusters in the very small particle size range below 3nm. The aim of this work is to gain deeper insights in the properties of molecular ions and their interaction with airborne particles and clusters.

The most adequate measurement technique for particles and clusters below 3nm at ambient pressure is the Electrical Mobility Spectrometry (EMS) which allows the classification of charged airborne particles witch respect to their electrical

mobility. However, most of the available EMS-instrumentation is limited to a particle size-analysis down to approximately 3nm as the strong Brownian motion of the small particles obscures high resolution measurements. The accurate and high resolution analysis and classification of molecular ions is of special importance for laboratory experiments that are aiming to simulate the nucleation processes which lead to new particle formation in the atmosphere.

Also for the application of the EMS method itself, the properties of molecular ions are of essential importance, since their knowledge forms the fundamental basis for the conversion from a measured mobility distribution into a corresponding number size distribution. This inversion requires the knowledge of the correct charging state of the particles. If it is not known a priori, a rather well defined charging state can be achieved by mixing the particles with a large number of positive and negative ions (bipolar charging). Further, with the knowledge of the properties of the charging ions, the charging probabilities of the particles carrying i elementary charges can be calculated.

To identify the controlling parameters that have to be optimized for the development of high resolution instrumentation that is able to access the very low particle – or actually molecular cluster – size range, in chapter 2 the theory behind the EMS method and the most commonly accepted theory of the charging process of aerosol particles in a bipolar ionic atmosphere is thoroughly summarized and reviewed.

Subsequently, in chapter 3, the design and development criteria for a new high resolution Differential Mobility Analyzer (DMA), called the UDMA, as well as calibration techniques and performance tests are presented.

The objective of chapter 4 is to describe the main experimental work performed in this thesis: the precise determination of the electrical mobilities of the ions that are involved in the charging / neutralization process of aerosol particles. As the most widely used aerosol chargers are based on ionizing radiation originating from radioactive decay of instable isotopes, in this study (almost exclusively) a charger based on ^{241}Am is used.

The electrical mobilities and therefore also the size distributions of the charging ions are determined during a large variety of different operating conditions:

different carrier gases and carrier gas purities, alternative ionizing processes and different relative humidity.

The assumption of most likely formed ion cluster species by the ionizing radiation in a charger - also supported by mass spectrometric measurements described in the literature - leads to an attempt to identify the specific cluster species produced in the charger.

The additional use of an empirical mass-mobility relationship also allows at least a rough estimation of the masses of the investigated molecular ions. This way, the mean mobilities and mean masses of the charging ions – the only necessary input parameters for the calculation of the charging probabilities of aerosol particles - are experimentally determined.

Finally, this information is used to calculate the aerosol charging probabilities depending on the properties of the ions that are generated in the charger at different operating conditions.

2. Electrical Mobility Spectrometry

Electrical Mobility Spectrometry (EMS) is a measurement technique, where particles are classified according to their electrical mobility. The idea of the mobility classification goes back to John Zeleny and his work at the Cavendish laboratories in England around 1898 as thoroughly summarized by Flagan in his overview of the history of electrical aerosol measurements (Flagan, 1998). Pioneering work was done by Knutson and Whitby (1975a, 1975b) making the EMS method a standard technique in the field of aerosol science by improving the theory as well as the classifying instrumentation.

The big advantage of this method is on the one hand the applicability over several orders of magnitude regarding both particle size and concentration at the same relative resolution and on the other hand the lack of influences and disturbances on the aerosol by the measuring procedure itself.

The electrical mobility spectrometry classifies particles according to their electrical mobility. Consequently, the aerosol of interest has to be charged. Many particle formation processes go hand in hand with the generation of electrically charged particles. Nevertheless, a stable and well defined saturation charging state cannot be assumed a priori for mostly all generation processes. Therefore, particle charging is of great interest and importance for numerous scientific fields.

In the atmosphere, airborne particles always interact with ionic molecules, primarily caused by cosmic radiation. At a mean natural ion-concentration of about 10^3 ion pairs per cm^3 (positively and negatively charged), initially neutral particles will acquire charges from these ions by collision due to their random Brownian motion. Aerosols that are initially charged will lose their charges as they attract oppositely charged ions. These competing processes lead to a stable stationary charging state, called Boltzmann equilibrium.

For atmospheric conditions, a stable charging state will be achieved after some hours of residence time. However, for the experimental determination of particle number size distributions a stable stationary charging state on the aerosol particles

will be most likely achieved by exposing them to a sufficiently high concentration of ions of both polarities.

Therefore, charging or neutralizing devices are used to produce a large amount of ions which can interact with the aerosol to bring it into a defined charging state, no matter what its charging state was before the charging process. Furthermore one can speak of a uniquely defined charging probability; a probability for the amount of elementary charges on the particles.

2.1. Charging Mechanisms

In principle, a difference can be made between three main charging mechanisms, discussed in the upcoming sections and following the description and classification given by Hinds (1999).

Static Electrification

For this charging mechanism, particles become charged by the separation from the bulk material or its surfaces. Important examples for this mechanism are spray charging and contact charging.

Spray charging or spray electrification results from the disruption of charged liquid surfaces or electrolyte surfaces by bubbling or atomization, leading to charged droplets. Contact charging results from the separation of particles from surfaces. As the particles contact the surface, the charge is transferred to equalize the Fermi levels of both materials. When the particles are again separated from the surface, they have an excess or deficiency of electrons.

As one can see, this charging mechanism typically occurs during the formation or re-suspension process of aerosol particles and is not a reliable charging mechanism. Nevertheless it has to be kept in mind and must be accounted for the further treatment of the particles.

Field Charging

Here, charging takes place by unipolar ions in the presence of a strong electric field. For example, this mechanism occurs during a corona discharge.

Because of the rapid motion of the ions in the electric field there are frequent collisions between ions and particles. When an initially uncharged particle (of a substance with finite conductivity) is placed in a uniform electric field, it distorts the field as shown in Fig. 2.1 to Fig. 2.3, adapted from Hinds (1999).

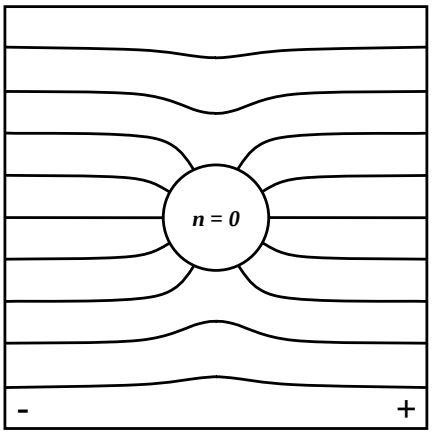

Fig. 2.1 An uncharged particle is placed in a uniform electric field

The lines in the graphs represent the electric field lines and therefore also the trajectories of the ions, travelling along the field lines. The extent of distortion is dependent on the dielectric constant ε of the particle but also on the number of charges on the particle.

As the ions travel along a field line intersecting with the particle, they will collide and transfer their charge to the particle. As the particle becomes charged, it tends to repel further incoming ions as they have the same polarity. This way, the electric field is altered and the field strength and therefore the number of field lines converging on the particle are reduced. This situation is shown in Fig. 2.2 for negative ions colliding with the particle.

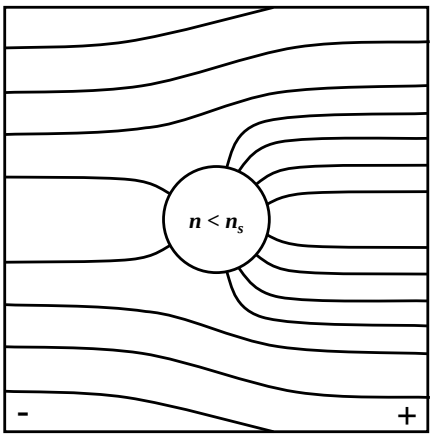

Fig. 2.2 The particle acquires negative charges and alters the electric field.

The field strength on the left in direction of the negative electrode is reduced by the presence of negative charges on the particle. The same way, the field strength on the right in direction to the positive electrode increases with increasing number of negative charges on the particle.

Finally, the charge on the particle reaches a point where no more negative ions can reach the particle and no field lines converge onto the particle any more (Fig. 2.3). This maximum charging condition is called saturation charging state.

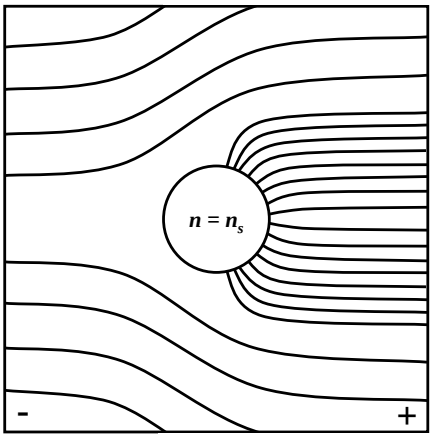

Fig. 2.3 The particle reaches the saturation charging state

For conditions where diffusion charging can be neglected the number of charges acquired through field charging can be calculated according to equation [2.1].

$$n(t) = n_s \cdot \left(\frac{\pi \cdot e_0 \cdot Z_i \cdot N_i \cdot t}{1 + \pi \cdot e_0 \cdot Z_i \cdot N_i \cdot t} \right) \quad [2.1]$$

where

$$n_s = \left(\frac{3\varepsilon}{\varepsilon + 2} \right) \cdot \left(\frac{E \cdot D_p^2}{4 \cdot e_0} \right) \quad [2.2]$$

represents the saturation charging state, ε the particle's dielectric constant, E the strength of the electric field the particle is placed in, e_0 the elementary charge, Z_i the mean electrical mobility of the ions, $N_i \cdot t$ the product between the number concentration of ions and the duration t of the charging process and D_p the particles diameter.

Diffusion Charging

If particles are mixed with unipolar ions, they are charged by random collisions between ions and particles due to their Brownian motion. This mechanism does not require an electric field nor is it dependent on the material. As the charge on the particle accumulates, it generates a field that tends to repel additional ions, therefore reducing the rate at which the ions arrive.

Because of the frequent collisions between the small ions and particles, the ions are in thermal equilibrium with the gas molecules and have a Maxwell-Boltzmann distribution of their velocity. As the charge on the particles increases, fewer ions have sufficient energy to overcome the barrier of the repulsive potential caused by the equally charged particle. This way, the charging rate slowly approaches zero.

An approximate expression for the number of charges n acquired by a particle of diameter D_p by diffusion charging during a time t is given in equation [2.3]

$$n = \frac{D_p \cdot kT}{2{e_0}^2} \ln\left(1 + \frac{\pi \cdot D_p \cdot \bar{c}_i \cdot {e_0}^2 \cdot N_i \cdot t}{2 \cdot kT} \right) \quad [2.3]$$

With $\bar{c}_i$ the ions mean thermal speed, k the Boltzmann constant, e_0 the elementary charge, N_i the concentration of ions and T the thermodynamic temperature.

According to Hinds (1999), this expression is valid within a factor of 2 for 0.1-2µm for a $N_i \cdot t$ product larger than 10^7.

As the number of charges acquired through field charging (see [2.2]) is proportional to D_p^2 for field charging and proportional to D_p for diffusion charging (see [2.3]), field charging is the dominant mechanism for large particles (approx. > 1µm), whereas diffusion charging dominates the size range below 0.1µm (100nm) even in the presence of an electric field. Fig. 2.4 illustrates the dominating size ranges of field charging and diffusion charging by plotting the particle diameter versus the mean electrical mobility of the particles carrying i elementary charges. In between the dominating regions, there is a more complicated situation where both mechanisms operate simultaneously.

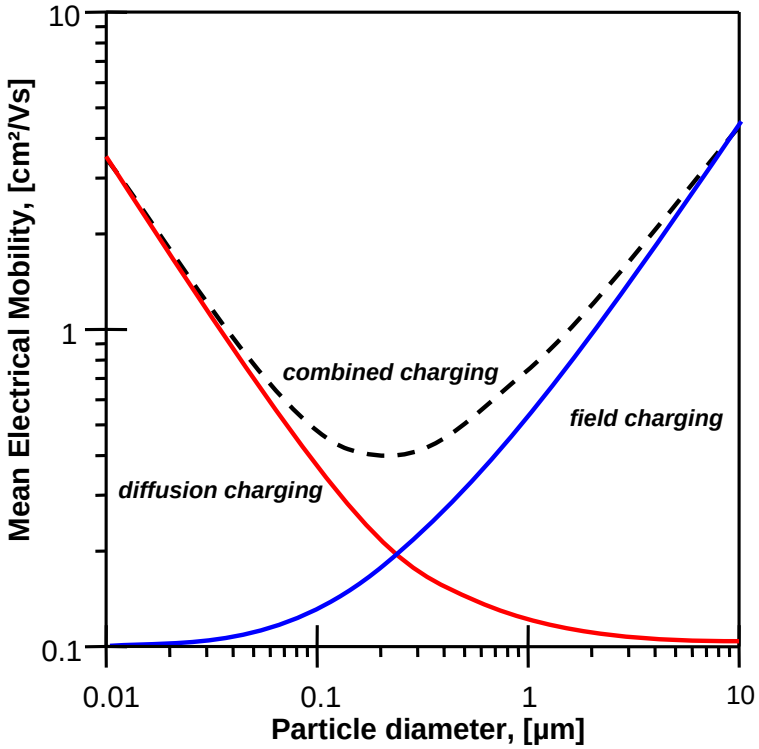

Fig. 2.4 The dominating size ranges of field charging and diffusion charging.

The situation is different when ions of both polarities (positive and negative) are present. This case is called bipolar diffusion charging, or more precisely, "neutralization". If approximately the same number of positive and negative ions is present, some particles that are initially neutral will acquire charges from these ions by collisions due to their random Brownian motion. Aerosols that are initially charged will loose their charge or their charging state will be reduced as their charge attracts ions of the opposite polarity. These competing processes lead to a stationary charging state of the particles called Boltzmann equilibrium.

2.2. The Boltzmann Charge Distribution

As already mentioned in the previous section, in the simplest situation, the same number of positive and negative ions is present in the carrier gas. Due to their random Brownian motion, particles and ions will collide and initially neutral particles will be charged and initially charged particles will be neutralized.

The bipolar charge distribution on aerosols was already treated extensively in theory as early as 1937 (see Fuchs, 1963) and by many other authors (e.g. Bricard 1949, Gunn 1954).

Most of the "early" charging theories were based on the assumption that after some relaxation time a steady state equilibrium will be achieved where in time average $(i\text{-}1)$ and $(i+1)$ fold charged particles will become i-fold charged to the same extent as i-fold charged particles will be lost due to the neutralization by the colliding ions. Because of the frequent collision between ions and particles, both will be in a thermal as well as charge equilibrium. Therefore also the electric energy of the particles should follow a Boltzmann statistic.

Accordingly, the number of particles per unit volume $N(E)$ with the electric energy E is given by:

$$N(E) = A \cdot g(E) \cdot \exp\left(-\frac{E}{k \cdot T}\right) \qquad [2.4]$$

Where A is a normalizing constant, $g(E)$ the statistical weight of the particle's energy state , k Boltzmanns' constant and T the absolute temperature.

For a particle with diameter D_p carrying i elementary charges, the electric energy results to:

$$E=E_0+\frac{i^2 \cdot e_0^2}{D_p} \qquad [2.5]$$

As the electric energy of a particle is independent of the polarity of the charge, the statistical weight $g(E)$ for every charging state i will be $g(E)=2$.

Consequently, the number of particles per unity volume carrying i elementary charges of both polarities equals to

$$N_i^{\pm}=2 \cdot N_0 \cdot \exp\left(-\frac{i^2 \cdot e_0^2}{D_p \cdot k \cdot T}\right) \qquad [2.6]$$

and the total number N of particles (neutral and charged) per unit volume to:

$$N=N_0+\sum_{i=1}^{\infty} N_i^{+}+\sum_{i=1}^{\infty} N_i^{-}=N_0+2 \cdot \sum_{i=1}^{\infty} N_i \qquad [2.7]$$

Finally, the probability $\alpha(D_p,i)$ for a particle with diameter D_p carrying i elementary charges can be calculated from the ratio of the concentration of the i-fold charged particles N_i to the total concentration N:

$$\alpha\left(D_p,i\right)=\frac{N_i}{N}=\frac{\exp\left(-\frac{i^2 \cdot e_0^2}{D_p \cdot k \cdot T}\right)}{1+2 \cdot \sum_{j=1}^{\infty}\exp\left(-\frac{j^2 \cdot e_0^2}{D_p \cdot k \cdot T}\right)} \qquad [2.8]$$

To illustrate the situation, the charging probabilities $\alpha(D_p,i)$ for particles in the size range from 1 to 1000 nm carrying up to 5 elementary charges are computed and plotted in Fig. 2.5.

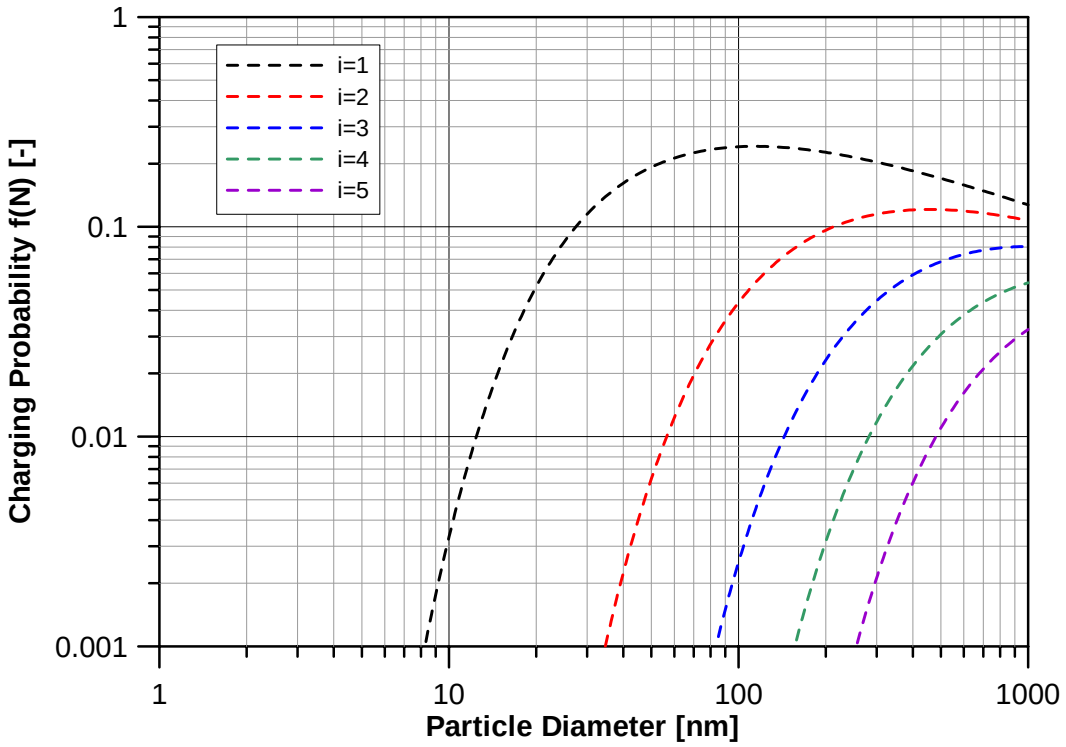

Fig. 2.5 Charging probabilities for up to 5-fold charged particles in the size range from 1 to 1000 nm calculated according the Boltzmann law.

The first experimental results approaching the ultrafine particle size range by Liu and Pui (1974) showed good agreement with the Boltzmann charge distribution for particles down to 20nm for sodium chloride particles.

The Boltzmann law describes the charge distribution on the particles by an equilibrium between ions and particles and assumes a continuous distribution of the energy states on the particle. According to Fuchs (1963), in reality the situation is much better described by a steady state equilibrium as the charging ions leave their charge on the particle and are “torn of as neutral molecules rather than ions”. Also the continuous energy distribution only applies for rather large particles where the charging probabilities for different charging states are almost equal. Therefore, according to Fuchs (1963) a “detailed equilibrium” is not observed here and the correct calculation of the steady state charge distribution on aerosol particles (especially for ultrafine particles < 100nm) requires a kinetic method to calculate the rate of diffusion of the ions towards the particle.

Further more, the experimental data presented by some other authors (e.g. Reischl et al 1983, Hussin et al. 1983, Wiedensohler and Fissan 1991) show that the

Boltzmann charge distribution clearly underestimates the number of charged particles below 30nm diameter, indicating that the theory by Fuchs is the best to describe the diffusion charging process.

2.3. The Fuchs Charging Theory

This section will give a short but complete overview of the charging theory according to Fuchs (1963) using the well known method of flux matching at the limiting sphere. The following description will keep very closely to the one given by Reischl et al. (1996) as they have summarized Fuchs' theory in such a clear and unambiguous manner that it is hard to find another way of describing it without adding vague and inexplicit statements.
As stated by Reischl et al. (1996), the "beauty" of Fuchs' theory is that only two ion parameters have to be known: their electrical mobility and their mass. All other ion input parameters can be derived from the latter two properties. Originally, Fuchs described the charging process as symmetrical where positively and negatively charged ions have the same properties (i.e. same mobility and same mass). However, already the investigations by Hussin et al. (1983) and Adachi et al. (1985) have shown that the bipolar charge distribution in atmospheric air is asymmetrical, meaning that the mean mobilities and masses of positive and negative ions are different.

Therefore, in this work, Fuchs' charging theory is presented in such a way, that the parameters that are influenced by the ions' polarities are always superscripted with $(\pm)$ to account for the different ion properties. Furthermore, the main part of the experimental work of this thesis focuses on the investigation of the different properties of the charging ions.

Different from rather "classical" charging theories that try to extend the equilibrium gas kinetic theory to the interaction of gaseous ions with aerosol

particles and postulating that these processes are still following a Boltzmann statistic, the Fuchs charging theory is based on a steady state ion flux towards a sphere that is related to the ion-particle combination coefficient.

The charge transfer by gaseous ions interacting with the aerosol particles is characterized by the ionic Knudsen number Kn_{ion}; the ratio of the ionic mean free path λ_{ion} to the particle radius a.

$$Kn_{ion}=\frac{\lambda_{ion}}{a} \qquad [2.9]$$

In the continuum regime ($Kn_{ion}\rightarrow 0$), the diffusion of the ions to aerosol particles is determined by the solution of the continuous diffusion equation for ions in the electric field of a charged particle. To apply the theory for the transition regime ($0.1 < Kn_{ion} < 10$) and for the free molecule regime ($Kn_{ion}\rightarrow \infty$), where the particle diameter is in the same size range as the mean free path of the carrier gas molecules, gas kinetic arguments including details of the ion trajectories in the vicinity of the particle have to be taken into account.

Fuchs (1963) used the method of the limiting sphere that was first applied to the charging problem by Arendt and Kallmann (1926): The limiting sphere's radius δ is in the order of one ionic mean free path larger than the particle radius and divides the space around a spherical particle into two regions.

$$\delta = a + \lambda_{ion} \qquad [2.10]$$

Outside the limiting sphere, the ions move according to the continuous diffusion equation. Ions entering the spheres' radius and moving inside are assumed to travel without collisions with gas molecules as in a vacuum.

In the continuum regime (large particles) and without the presence of electric fields, the flux of ions to a spherical particle is given by the flux caused by diffusion processes (statistical) and a term caused by the electric field of the charged particle (aligned):

$$\vec{j}=\vec{j}_D+\vec{j}_E \qquad [2.11]$$

The term caused by diffusion $\vec{j}_D$ can be expressed by Fick's law

$$\vec{j}_D=-D\cdot grad\,(n) \qquad [2.12]$$

where D is the ions' diffusion coefficient an n their concentration. The motion of the ions in the electric field of the particle is given by equation [2.13]:

$$\vec{j}_E=\vec{v}\cdot n=B\cdot\vec{F}\cdot n \qquad [2.13]$$

with $\vec{v}$ the ions' drift velocity, B the ions' mechanical mobility and $\vec{F}$ the Coulomb and image force acting on the ions.

By using the equation of continuity

$$\frac{\partial n}{\partial t}+div\left(\vec{j}\right)=0 \qquad [2.14]$$

and assuming that the ions' diffusion coefficient D as well as their mechanical mobility B will be constant in time, we get

$$\frac{\partial n}{\partial t}=D\cdot\nabla^2(n)-B\cdot div\left(\vec{F}\cdot n\right) \qquad [2.15]$$

Assuming further that the ions diffusion process to the particle will be a quasi-stationary event, the number of ions approaching the particle will not change in time ($\partial n/\partial t=0$) and equation [2.15] changes to:

$$D\cdot\nabla^2(n)=B\cdot div\left(\vec{F}\cdot n\right). \qquad [2.16]$$

As the problem has a spherical symmetry, equation [2.16] can be transformed into polar coordinates:

$$D\cdot\frac{1}{r^2}\cdot\frac{d}{dr}\left(r^2\cdot\frac{dn}{dr}\right)=B\cdot\frac{1}{r^2}\cdot\frac{d}{dr}\left(r^2\cdot\vec{F}\cdot n\right) \qquad [2.17]$$

or

$$\frac{d}{dr}\left(D\cdot\frac{dn}{dr}-B\cdot F\cdot n\right)=0\,. \qquad [2.18]$$

Consequently, the constant net steady-state flux I_c of ions through a sphere of radius *r,* concentric with the aerosol particle, can be equated to

$$I_c = 4 \cdot \pi \cdot r^2 \cdot \left(D \cdot \frac{dn(r)}{dr} - B \cdot F(r) \cdot n(r) \right) \qquad [2.19]$$

The solution of $n(r)$ of equation [2.19] that satisfies the boundary condition that the ions' number density far from the particle must be equal to the macroscopic density $n_0 = n(r \to \infty)$ is given by

$$n(r) = \exp\left[-\frac{\Phi(r)}{k \cdot T} \right] \left\{ n_0 + \frac{I_c}{4 \cdot \pi \cdot D} \cdot \int_{\infty}^{r} \frac{1}{\rho^2} \cdot \exp\left[\frac{\Phi(r)}{k \cdot T} \right] \cdot dr \right\} \qquad [2.20]$$

where the Einstein relation $D = B \cdot k \cdot T$ (Einstein, 1905) has been used.

$\Phi(r)$ is the electrostatic potential energy of an ion in the field of a charged particle:

$$\Phi(r) = -\int_{\infty}^{r} F(r) \cdot dr \qquad [2.21]$$

The force $F(r)$ acting on the ion can be expressed by a term accounting for the (attractive or repulsive) Coulomb interaction between ion and particle $F_C(r)$ and by a term $F_I(r)$ accounting for the attractive image force due to the polarization interaction of a sphere with a point charge:

$$F(r) = F_C(r) + F_I(r) \qquad [2.22]$$

with

$$F_C(r) = \frac{e_0^2}{4 \cdot \pi \cdot \varepsilon_0} \cdot \frac{i}{r^2} \qquad [2.23]$$

where both particle and ion are treated as point charges and i is considered positive if the charges of the ion and the particle are of the same polarity. In the second term

$$F_I(r) = -\frac{e_0^2}{4 \cdot \pi \cdot \varepsilon_0} \cdot \left\{ K \cdot \frac{a^3}{2 \cdot r^2 \cdot (r^2 - a^2)} \right\} \qquad [2.24]$$

a stands for the particle's radius and $K=1$ for a perfectly conducting particle; for non-conducting particles with a relative dielectric permittivity ε_r, K becomes

$$K \cong \frac{\varepsilon_r - 1}{\varepsilon_r + 1} \qquad [2.25]$$

This way, equation [2.21] can be transformed to

$$\Phi(r) = \frac{e_0^2}{4 \cdot \pi \cdot \varepsilon_0} \cdot \left\{ \frac{i}{r} - K \cdot \frac{a^3}{2 \cdot r^2 \cdot (r^2 - a^2)} \right\} \qquad [2.26]$$

and by using equations [2.20] and [2.26], the quasi-stationary ion flux I_c to the particle in the continuum limit can be written as:

$$I_{ci}^{\pm} = \frac{4 \cdot \pi \cdot D^{\pm} \left\{ n_0^{\pm} - n^{\pm}(r) \cdot \exp\left[\frac{\Phi_i(r)}{k \cdot T} \right] \right\}}{\int_r^{\infty} \frac{1}{\rho^2} \cdot \exp\left[\frac{\Phi_i(r)}{k \cdot T} \right] d\rho} \qquad [2.27]$$

The superscript ($\pm$) accounts for the different properties of positive and negative ions; the subscript i accounts for the number and polarity of charges on the particle. Again, i is considered positive if the charges of the ions and of the particles are of the same polarity.

To eliminate the unknown quantity $n(r)$, a second (inner) boundary condition is needed. This inner boundary condition has to ensure, that the flux through a limiting sphere is equal to the diffusion-mobility flux I_c outside the limiting sphere of radius δ and also equal to the microscopic ion flux I_k inside the limiting sphere. This method is called “flux matching”.

Generally, the flux I_k is proportional to the ion concentration n at the radius δ of the limiting sphere.

$$I_k(\delta) = \beta \cdot n(\delta) \qquad [2.28]$$

Applying the method of flux matching, the fluxes can be written as

$$I_k(\delta) = I_c(\delta) = I \qquad [2.29]$$

yielding an expression for the total ion flux I to the particle:

$$I_i^{\pm} = \frac{n_0^{\pm} \cdot \beta_i^{\pm} \cdot \exp\left[-\frac{\Phi_i\left(\delta^{\pm}\right)}{k \cdot T}\right]}{1+\exp\left[-\frac{\Phi_i\left(\delta^{\pm}\right)}{k \cdot T}\right] \cdot \frac{\beta_i^{\pm}}{4 \cdot \pi \cdot D^{\pm}} \cdot \int_{\delta^{\pm}}^{\infty} \frac{1}{\rho^2} \cdot \exp\left[\frac{\Phi_i(\rho)}{k \cdot T}\right] d\rho} \quad [2.30]$$

Still, $\beta_i^{\pm}$ is an unknown quantity that has to be determined from the theory of the kinetic flux inside the limiting sphere.

The microphysics inside the limiting sphere

According to geometric and statistical considerations, Fuchs (1963) gives the following expression for the radius $\delta^{\pm}$ of the limiting sphere:

$$\delta^{\pm} = \frac{a^3}{\lambda^{\pm 2}}\left[\frac{1}{5}\left(1+\frac{\lambda^{\pm}}{a}\right)^5 - \frac{1}{3}\left(1+\frac{\lambda^{\pm 2}}{a^2}\right)\left(1+\frac{\lambda^{\pm}}{a}\right)^3 + \frac{2}{15}\left(1+\frac{\lambda^{\pm 2}}{a^2}\right)^{5/2}\right] \quad [2.31]$$

where $\lambda^{\pm}$ is the mean free path of the positive (+) and negative (-) ions, and a the aerosol particle's radius. Following the arguments of Huang and Seinfeld (1988), the ionic mean free path $\lambda^{\pm}$ can be expressed as

$$\lambda^{\pm} = \frac{16\sqrt{2}}{3\pi} \cdot \frac{D^{\pm}}{\bar{c}^{\pm}} \cdot \left(\frac{M}{M+\bar{m}^{\pm}}\right)^{1/2} \quad [2.32]$$

Where $D^{\pm}$ is the ions' diffusion coefficient, $\bar{c}^{\pm}$ their mean thermal velocity, $\bar{m}^{\pm}$ their mean mass and M the carrier gas molecules' masses.

The free molecular flux of ions crossing the limiting sphere and reaching the particle can be written as

$$I_k = \left(4 \cdot \pi \cdot \delta^2\right) \cdot \left[\frac{n(\delta) \cdot \bar{c}^{\pm}}{4}\right] \cdot \alpha \quad [2.33]$$

Where $[n(\delta) \cdot \bar{c}]/4 = j_0$ is the ionic flux through a surface element of unit area of the limiting sphere toward one side as given by the kinetic theory of gases with

$\bar{c}^{\pm}$ the mean thermal velocity of the ions that can be calculated according to equation [2.34].

$$\bar{c}^{\pm} = \sqrt{\frac{8 \cdot k \cdot T}{\pi \cdot \bar{m}^{\pm}}} \qquad [2.34]$$

$\bar{m}^{\pm}$ denotes the mean ions mass.

In equation [2.33], α stands for the collision parameter that represents the fraction of ions emerging from the limiting sphere that actually reach the particle.

By combining equations [2.28] to [2.30] with the expression for the molecular flux I_k of ions inside the limiting sphere in equation [2.33], the unknown quantity $\beta_i^{\pm}$ from equation [2.30] becomes

$$\beta_i^{\pm} = \pi \cdot \delta^{\pm 2} \cdot \bar{c}^{\pm} \cdot \alpha_i^{\pm} \qquad [2.35]$$

In the absence of electrostatic forces, α is given as the ratio of the geometric cross sections of the particle and the limiting sphere:

$$\alpha = \left(\frac{a}{\delta}\right)^2 \qquad [2.36]$$

In this case, the ions will have linear trajectories as shown in Fig. 2.6 and the collision probability α is given by the purely geometric capture cross section.

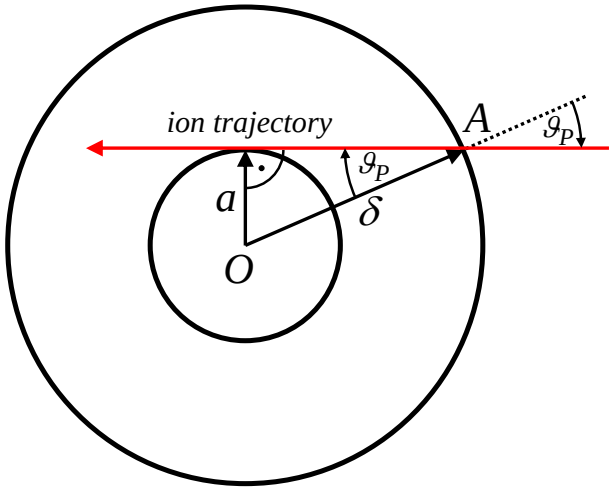

Fig. 2.6 Ion trajectory inside the limiting sphere without an electric field.

In the presence of an electric field, the ion trajectories become distorted and will be dependent on the forces acting on the ions. For attractive forces, α will be increased, and decreased for repulsive forces respectively.

$$\alpha_{attractive} > \left(\frac{a}{\delta}\right)^2 \qquad [2.37]$$

$$\alpha_{repulsive} < \left(\frac{a}{\delta}\right)^2 \qquad [2.38]$$

For an attractive ion – particle potential, the situation is also shown in Fig. 2.7.

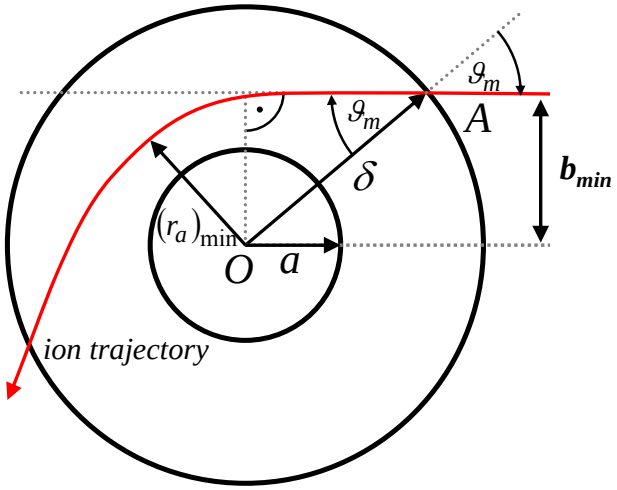

Fig. 2.7 Ion trajectory inside the limiting sphere for an attractive force acting on the ions.

For the calculation of α, the minimal distance $(r_a)_{min}$ has to be found between the particle center 0 and the trajectory of the ion emerging from the point A on the limiting sphere and moving inside with the mean thermal energy $3kT/2$.

This critical orbit with its corresponding impact parameter b_{min} represents the closest passing trajectory which just avoids capture. Consequently, ions with an impact parameter $b < b_{min}$ are captured by the particle. Once b_{min} is determined, the collision probability α in the presence of an electric field can be calculated:

$$\alpha = \left(\frac{b_{\min}}{\delta} \right)^2 \qquad [2.39]$$

As the motion of the ion in the vicinity of the particle is described by the two-body theory of classical mechanics, the impact parameter b_{min} corresponding to the minimum distance $(r_a)_{min}$ is found by applying the conservation laws of energy and angular momentum to the motion of the ions in the central force field of the particle and is obtained as:

$$b^2 = r_a^2 \cdot \left\{ 1 + \frac{2}{3 \cdot k \cdot T} \cdot \left[\Phi(\delta) - \Phi(r_a) \right] \right\} \qquad [2.40]$$

The ion-particle combination coefficiants

The so called combination coefficients or attachment coefficients η represent the combination rate of ions and particles:

$$\eta = \frac{I}{n_0} \qquad [2.41]$$

Here, I stands for the flux of ions reaching the particle and n_0 is the macroscopic (undisturbed) number concentration of the ions.

By using the expression for the total ion flux on the particle in equation [2.30]:

$$I_i^{\pm} = \frac{n_0^{\pm} \cdot \beta_i^{\pm} \cdot \exp\left[-\frac{\Phi_i(\delta^{\pm})}{k \cdot T} \right]}{1 + \exp\left[-\frac{\Phi_i(\delta^{\pm})}{k \cdot T} \right] \cdot \frac{\beta_i^{\pm}}{4 \cdot \pi \cdot D^{\pm}} \cdot \int_{\delta^{\pm}}^{\infty} \frac{1}{\rho^2} \cdot \exp\left[\frac{\Phi_i(\rho)}{k \cdot T} \right] d\rho}$$

and the quantity $\beta_i^{\pm}$ from equation [2.35]

$$\beta_i^{\pm} = \pi \cdot \delta^{\pm 2} \cdot \bar{c}^{\pm} \cdot \alpha_i^{\pm}$$

The attachment coefficient for ions of both polarities can be written as

$$\eta_i^{\pm}=\frac{\pi\cdot\delta^{\pm 2}\cdot\bar{c}^{\pm}\cdot\alpha_i^{\pm}\cdot\exp\left[-\frac{\Phi_i\left(\delta^{\pm}\right)}{k\cdot T}\right]}{1+\exp\left[-\frac{\Phi_i\left(\delta^{\pm}\right)}{k\cdot T}\right]\cdot\frac{\delta^{\pm 2}\cdot\bar{c}^{\pm}\cdot\alpha_i^{\pm}}{4\cdot D^{\pm}}\cdot\int_{\delta^{\pm}}^{\infty}\frac{1}{\rho^2}\cdot\exp\left[\frac{\Phi_i(\rho)}{k\cdot T}\right]d\rho} \quad [2.42]$$

and by substituting $x=a/\rho$, where a is the particle's radius, as:

$$\eta_i^{\pm}=\frac{\pi\cdot\delta^{\pm 2}\cdot\bar{c}^{\pm}\cdot\alpha_i^{\pm}\cdot\exp\left[-\frac{\Phi_i\left(\delta^{\pm}\right)}{k\cdot T}\right]}{1+\exp\left[-\frac{\Phi_i\left(\delta^{\pm}\right)}{k\cdot T}\right]\cdot\frac{\delta^{\pm 2}\cdot\bar{c}^{\pm}\cdot\alpha_i^{\pm}}{4\cdot D^{\pm}\cdot a}\cdot\int_{0}^{1}\exp\left[\frac{\Phi_i\left(a/x\right)}{k\cdot T}\right]dx} \quad [2.43]$$

to convert the integrals' boundaries in the denominator.

The charging probabilities

The discussion in the preceding section concerning the microscopic processes in the vicinity of a charged particle resulted in the calculation of the ion-particle attachment coefficients. However, the macroscopic charge state of an aerosol has to be determined by the kinetics of the charging process itself.

According to the review by Reischl et al. (1996), for a monodisperse aerosol with a particle number concentration that is low compared to the ion concentration and low enough to neglect coagulation and particle electrostatic dispersion and further any wall effects or other spatial gradients, a charge acquisition balance equation can be described:

$$\frac{dN_p^{\pm}}{dt}=\eta 2_{p-1}^{\pm}\cdot n^{\pm}\cdot N_{p-1}^{\pm}+\eta 1_{p+1}^{\mp}\cdot n^{\mp}\cdot N_{p+1}^{\pm}-\eta 2_p^{\pm}\cdot n^{\pm}\cdot N_p^{\pm}-\eta 1_p^{\mp}\cdot n^{\mp}\cdot N_p^{\pm} \quad [2.44]$$

$N_p^{\pm}$ stands for the number concentration of positively and negatively charged particles carrying p elementary charges and $n^{\pm}$ denotes the number concentration of positive and negative ions. $\eta 2_p^{\pm}$ corresponds to the attachment coefficient of

ions on particles carrying p charges of the opposite sign. $\eta 1_p^{\pm}$ corresponds to the attachment coefficient of ions on particles carrying p charges of the same sign.

For a steady state (quasi stationary) equilibrium, where

$$\frac{dN_p^{\pm}}{dt} = 0, \qquad [2.45]$$

the aerosol balance equation from [2.44] decouples from the corresponding ion balance equations (Hoppel and Frick, 1986) and a combination of subsequent expressions give:

$$\frac{N_p^{\pm}}{N_{p-1}^{\pm}} = \frac{n^{\pm}}{n^{\mp}} \cdot \frac{\eta 2_{p-1}^{\pm}}{\eta 1_p^{\mp} + \frac{n^{\pm}}{n^{\mp}} \cdot \eta 2_p^{\pm} - \eta 1_{p+1}^{\mp} \cdot \frac{N_{p+1}^{\pm}}{N_p^{\pm}}} \qquad [2.46]$$

Different from Fuchs' original derivation, where both ion polarities where assumed to have the same number concentration ($n^+ = n^-$) and the same properties taken into account by means of the attachment coefficients ($\eta 1_p^+ = \eta 1_p^-$ and $\eta 2_p^+ = \eta 2_p^-$) equation [2.46] allows not only for different steady-state concentration of positive and negative ions but also for different physical properties such as ion mobilities and ion masses.

Equation [2.46] directly leads to:

$$\frac{N_p^{\pm}}{N_0} = \frac{N_1^{\pm}}{N_0} \cdot \frac{N_2^{\pm}}{N_1^{\pm}} \cdot \frac{N_3^{\pm}}{N_2^{\pm}} \cdots \frac{N_p^{\pm}}{N_{p-1}^{\pm}} = \prod_{j=1}^{p} A_j^{\pm} \qquad [2.47]$$

with

$$A_j^{\pm} = \frac{N_j^{\pm}}{N_{j-1}^{\pm}} = \frac{n^{\pm}}{n^{\mp}} \cdot \frac{\eta 2_{j-1}^{\pm}}{\eta 1_j^{\mp} + \frac{n^{\pm}}{n^{\mp}} \cdot \eta 2_j^{\pm} - \eta 1_{j+1}^{\mp} \cdot \frac{N_{j+1}^{\pm}}{N_j^{\pm}}} \qquad [2.48]$$

Resulting in a recursion formula for $A_j^{\pm}$:

$$A_j^{\pm} = \frac{N_j^{\pm}}{N_{j-1}^{\pm}} = \frac{n^{\pm}}{n^{\mp}} \cdot \frac{\eta 2_{j-1}^{\pm}}{\eta 1_j^{\mp} + \frac{n^{\pm}}{n^{\mp}} \cdot \eta 2_j^{\pm} - \eta 1_{j+1}^{\mp} \cdot A_{j+1}^{\pm}} \qquad [2.49]$$

From equation [2.47], the number concentration of p-fold positively or negatively charged particles is given as

$$N_p^{\pm} = N_0 \cdot \prod_{j=1}^{p} A_j^{\pm} \qquad [2.50]$$

Hence, the total number concentration N of all particles can be written as

$$N = N_0 + \sum_{k=1}^{m} \left(N_k^- + N_k^+ \right) \qquad [2.51]$$

The combination of equations [2.50] and [2.51] leads to the ratio of the number concentration of p-fold charged particles of both polarities to the total number of particles for a given size. This ratio $f_p^{\pm}$ is also called „charging probability“.

$$f_p^{\pm} = \frac{N_p^{\pm}}{N} = \frac{\prod_{j=1}^{p} A_j^{\pm}}{1 + \sum_{k=1}^{m} \left\{ \prod_{j=1}^{k} A_j^- + \prod_{j=1}^{k} A_j^+ \right\}} \qquad [2.52]$$

And the fraction of uncharged particles is given by.

$$f_0 = \frac{N_0}{N} = \frac{1}{1 + \sum_{k=1}^{m} \left\{ \prod_{j=1}^{k} A_j^- + \prod_{j=1}^{k} A_j^+ \right\}} \qquad [2.53]$$

To illustrate the charging probabilities according to Fuchs's theory, Fig. 2.8 shows the charging probabilities $\alpha(D_p, i)^-$ for negatively charged aerosol particles, carrying up to five elementary charges, in a bipolar ionic atmosphere at steady-state charge equilibrium.

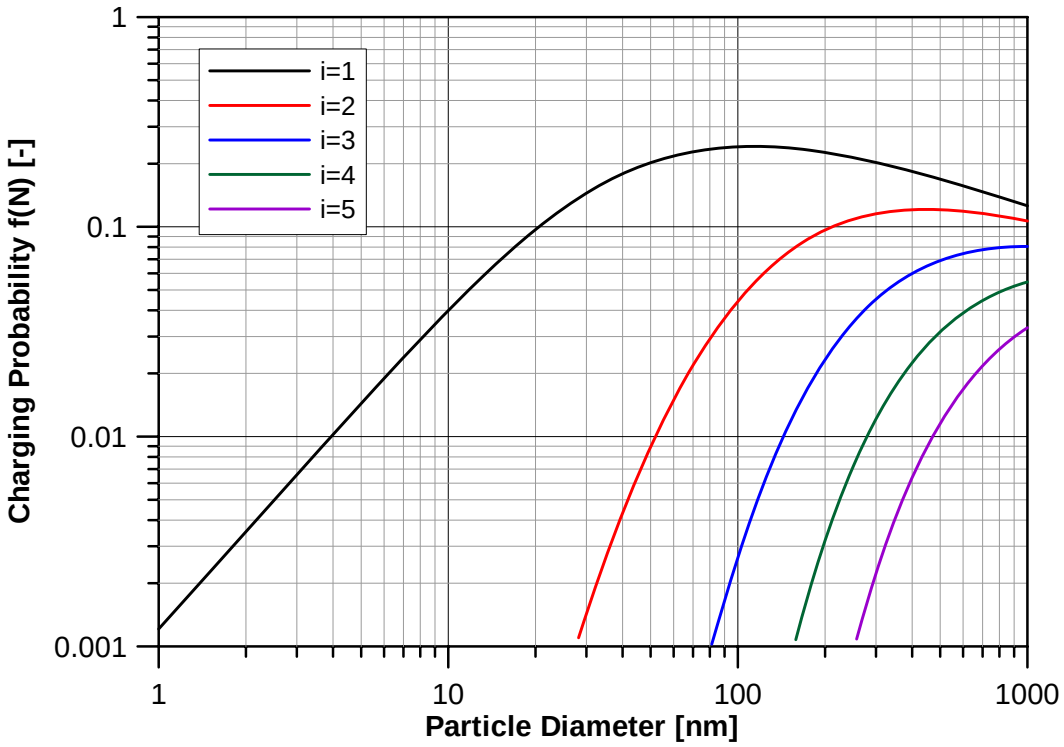

Fig. 2.8 Charging probabilities for negatively charged aerosol particles in a bipolar ionic atmosphere with charging states i up to five

Fig. 2.9 compares Fuchs' charge distribution to the Boltzmann charge distribution again for negative polarity and for particles carrying up to two elementary charges. As already mentioned earlier, the Boltzmann distribution almost neglects the charging probability for singly charged particles below 10nm whereas Fuchs' theory still predicts a significant fraction of singly charged particles in the size range below 10nm.

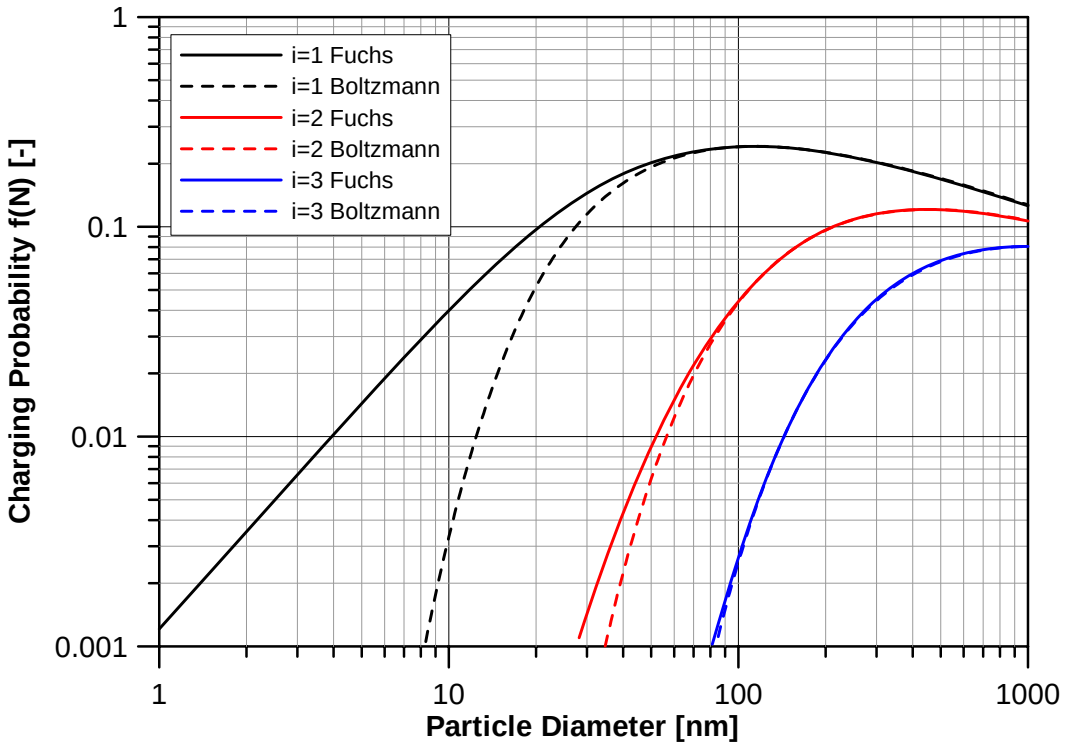

Fig. 2.9 Comparison between the Boltzmann and Fuchs charge distribution on aerosols

As can be seen clearly from equation [2.52], the calculation of the charging probabilities according to Fuchs' theory requires a quite laborious numerical calculation.

For a more convenient calculation, Wiedensohler (1988) derived an approximation formula for the bipolar charge distribution on aerosols that can be solved analytically:

$$f(N) = 10^{\left[\sum_{j=0}^{5} a_j(i)\cdot(\log D_p)^j\right]} \qquad [2.54]$$

It is important to note that the particle diameter D_p in equation [2.54] has to be entered in [nm]. According to Wiedensohler (1988), this approximation equation is valid for the size range from 1nm to 1000nm for uncharged (i = 0), singly charged (i = -1, 1) and for doubly charged particles (i = -2, 2) in the size range from 20nm to 1000nm.

The approximation coefficients $a_j(i)$ were determined by Wiedensohler (1988) by a least-square regression analysis and are given in Tab. 2.1

$a_j(i)$	$i = -2$	$i = -1$	$i = 0$	$i = 1$	$i = 2$
a_0	-26.3328	-2.3197	-0.0003	-2.3484	-44.4756
a_1	35.9044	0.6175	-0.1014	0.6044	79.3772
a_2	-21.4608	0.6201	-0.3073	0.4800	-62.8900
a_3	7.0867	-0.1105	-0.3372	0.0013	26.4492
a_4	-1.3088	-0.1260	0.1023	-0.1544	-5.7480
a_5	0.1051	0.0297	-0.0105	0.0320	0.5059

Tab. 2.1 Approximation coefficients $a_j(i)$ of Wiedensohler's formula

Fig. 2.10 displays Wiedensohler's approximated charging probabilities for singly and doubly charged positive and negative ions, as well as for particles carrying no charge at all.

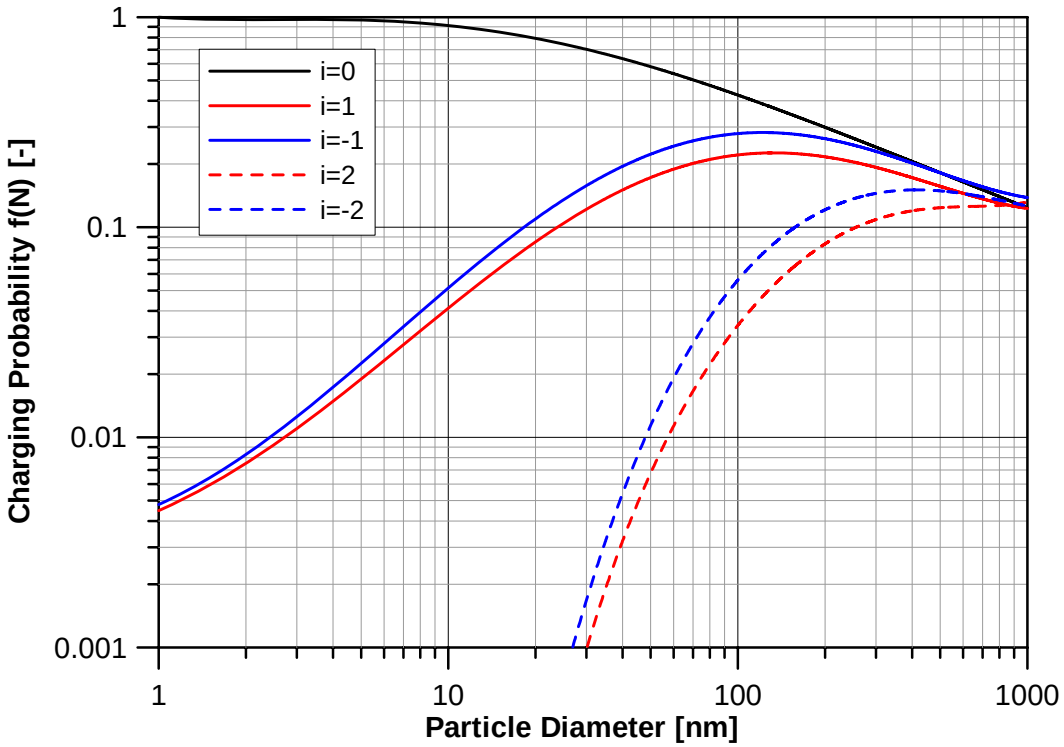

Fig. 2.10 Wiedensohler's approximated charging probabilities

One remarkable difference between the graphs calculated with Wiedensohler's approximation and the graphs using Fuchs' syntax is the significantly higher charging probability for singly charged particles below about 3nm in Wiedensohler's approximation. Here, different assumptions for the α-parameter are made. In Wiedensohler's model, α becomes 1 for very small particles and attractive forces whereas throughout this work, an adopted version of Fuchs' original syntax, as presented in Reischl et al. (1996) following the considerations by Hoppel and Frick (1986), is used. According to that, ions that enter the limiting sphere with sufficiently high energy will pass the particle without being captured, even if the potential is attractive. This also allows for α values smaller than unity for very small particles and attractive forces and therefore the charging probabilities will generally be lower than compared to Wiedensohler's approximation formula.

2.4. The Vienna Type DMA

The core component for electrostatic mobility measurements is the so called Differential Mobility Analyzer (DMA). Most commonly, DMAs are designed as cylindrical capacitors. Nevertheless, there exist designs with a rectangular flow channel in a planar plate design (Fernández de la Mora 1999) and radial designs (Zhang et al. 1995) which are also very successful for rather specific applications.
One remarkable feature of the DMA is the possibility to use it as an analyzing device as well as a classifying device. That said, together with an appropriate aerosol generator, it can be used to classify one specific mobility band out of a broad particle distribution to serve as a source of monodispersed particles.

For the cylindrical design, the best known designs are the Vienna type (Reischl, 1991; Winklmayr et al., 1991) and TSI type (Knutson and Whitby, 1975a), based on Hewitt´s design (Hewitt, 1957). Radial designs are known as the "French radial type" called "SMEC" (Mesbah et al., 1993; Ooghe et al., 1994) and the

"American radial type" also known as the "Caltech RDMA" (Zhang et al., 1995; Zhang et al., 1996).
Good overviews on the development of Differential Mobility Analyzer (DMA) designs can be found in the reviews by Knutson and Whitby (1975a, 1975b), Winklmayr et al. (1991), Rosell-Llompart et al. (1996), Reischl et al. (1997) and also in the brilliant overview of DMA development in the last century by Flagan (1998).

The DMA development in Vienna was initiated by Benjamin Liu in the late 1970's. He suggested applying the technologies developed in Vienna for building high precision aerosol centrifuges and cascade impactors (Berner 1976) to DMAs. The first Vienna type DMAs were designed and used for ambient aerosol particle measurements and were optimized for a large size range from 3nm to 1000nm. The major difference to the Minneapolis design (Hewitt´s design) was a bullet shaped inner electrode providing a steadily accelerating sheath air flow in the region where the aerosol is introduced to the sheath air flow and an improved aerosol inlet system. As Hewitt's design used a radial inlet of the aerosol flow, the Vienna type introduced a tangential inlet of the aerosol flow into the DMA. Also the excess air outlet was redesigned to avoid distortions of the flow pattern in the classifying channel. Although the Vienna DMA was designed for a large size range, shortened versions of the initial design were found to be able to extend the lower particle size limit to 1nm. That way it was possible to determine the mobility distribution of ionic molecular clusters originating from bipolar diffusion chargers (Winklmayr et al., 1991) with, to be honest, rather poor resolution. High resolution mobility measurements of the latter ions were first, to the author's knowledge, presented in the work by De Juan and Fernández de la Mora (1998) and will be discussed in more detail later in this work.

In general, two groups of parameters determine the performance of the DMA: the geometry parameters (R_1-outer radius of the inner electrode, R_2-inner radius of the outer electrode, L - effective axial distance between aerosol inlet and aerosol outlet) and the operating conditions (Q_{sh} - sheath air flow rate, Q_a - aerosol flow

rate, Q_s - sample air flow rate, Q_{ex} – excess air flow rate). A schematic cross-section of the Vienna type DMA is shown in Fig. 2.11.

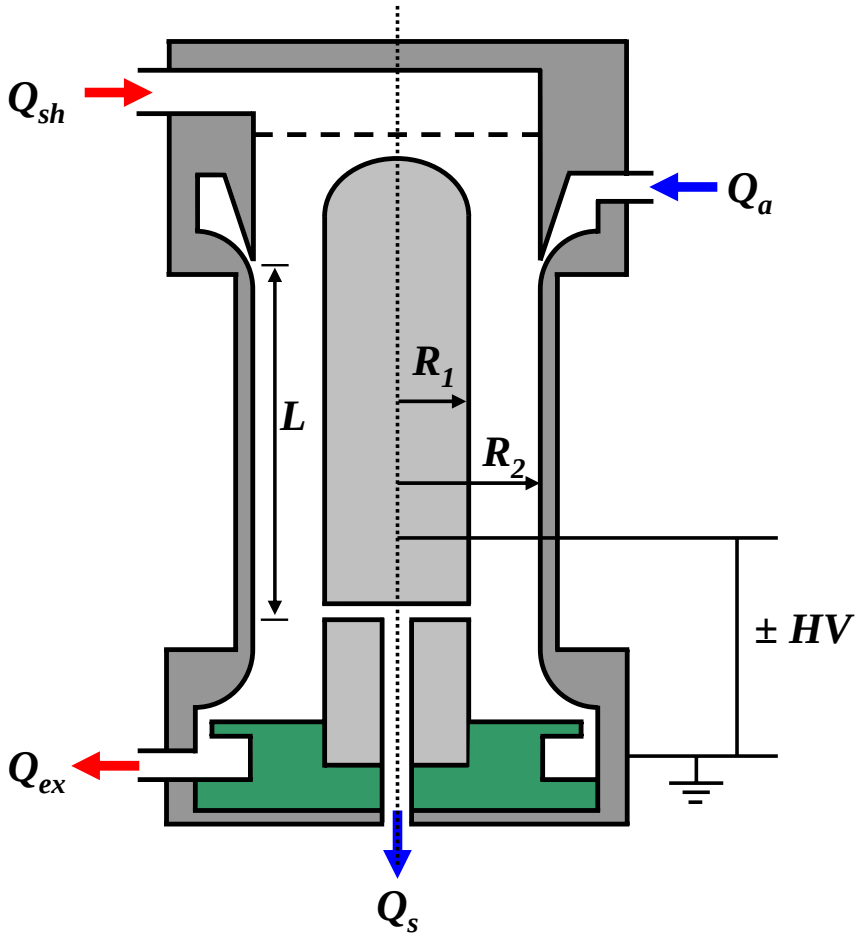

Fig. 2.11 Schematic cross-section of a Vienna type DMA

For the typical Vienna type design the purified sheath air Q_{sh} is introduced tangentially on top of the DMA. A nylon laminarization screen (mesh size approximately 50µm) shortly after the air inlet ensures an effective laminiarization of the sheath air flow which is one of the crucial prerequisites for operating a DMA properly. The aerosol inlet volume flow Q_a is fed tangentially through an inlet port in the outer electrode into an annular cavity. A blade like shape of the inner walls and a curvature at the inner side of the outer electrode provide a smooth transition of the aerosol flow into the sheath air flow. Therefore, both airflows can be merged very smoothly which is a main criterion for the classification characteristics. The particles drift according to their electrical mobility in the direction of the electric field $\vec{E}$ radially as well as axially through

the sheath air flow towards an annular exit slit in the inner electrode as shown schematically in Fig. 2.12.

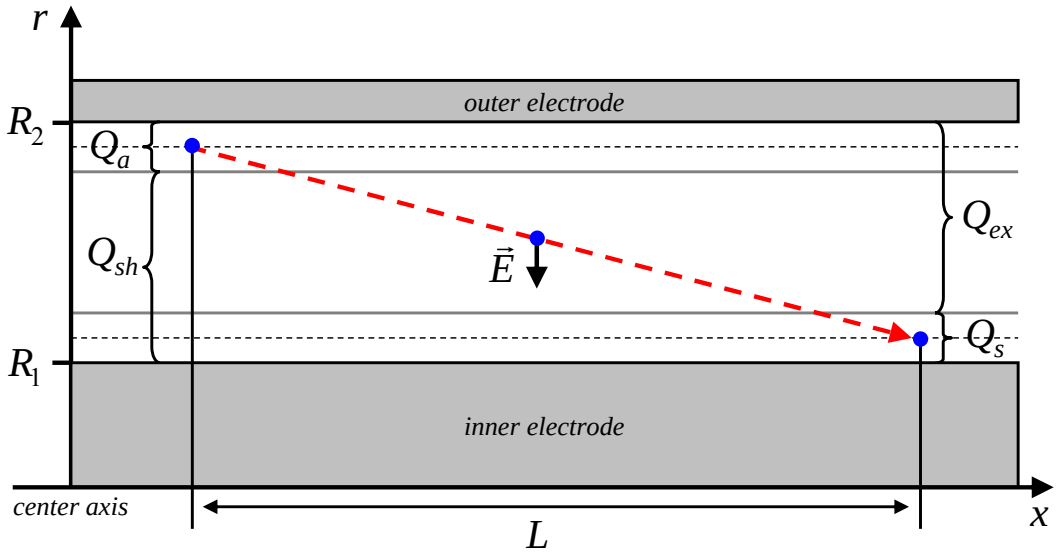

Fig. 2.12 Path of the particles through the electric field.

At fixed geometry parameters (R_2, R_1, L) and operating conditions (Q_{sh}, Q_a, Q_s, Q_{ex}), a unique correlation exists between the adjusted voltage on the inner electrode and the electrical mobility of the particles which enter the slit with the sample air flow Q_s from the aerosol air flow Q_a. The classified clusters exit the classification channel as sample air flow Q_s by a narrow annular exit slit in the inner electrode. At the bottom of the DMA, the residual air flow exits the DMA as excess air Q_{ex}.

To provide the electric field between the DMA's electrodes, a high voltage potential (max. 10 kV; positive and negative polarity are possible) is applied to the inner electrode. In the usual Vienna type DMA design the high voltage connection for the inner electrode is installed in the bottom insulator. In a more sophisticated and improved Vienna DMA design, the so called UDMA, discussed later, the high voltage connection is mounted at the top of the UDMA to reduce diffusion losses in the exit section by shortening the pathway of the classified particles into the directly flanged sensor .

2.5. The Electrical Mobility

The following sections on the basic principles governing the operation of a DMA are mainly based on the fundamental reviews by Knutson and Whitby (1975a, 1975b), Reischl (1991) and Flagan (1998).

The mechanical mobility B of a particle is defined as the ratio between the particles drift velocity $\vec{v}$ and the force $\vec{F}$ acting on the particle:

$$B = \frac{\vec{v}}{\vec{F}} \qquad [2.55]$$

Accounting for electrostatic forces, equation [2.55] $B = \frac{\vec{v}}{\vec{F}}$ changes to

$$B = \frac{\vec{v}}{i \cdot e_0 \cdot \vec{E}} \qquad [2.56]$$

where i is the number of elementary charges on the particle and e_0 the elementary charge.

Following these conversions, the electrical mobility Z of a particle is defined as

$$Z = i \cdot e_o \cdot B \qquad [2.57]$$

and describes the proportionality factor between electric field strength $\vec{E}$ and the resulting drift velocity $\vec{v}$ of the (charged) particle in the direction of the field.

$$\vec{v} = \vec{E} \cdot Z \qquad [2.58]$$

At constant geometric and operational parameters, the particle's electrical mobility is only a function of the applied voltage to the inner electrode of the DMA:

$$Z = Z(V) \qquad [2.59]$$

with (R_2, R_1, L) and (Q_{sh}, Q_a, Q_{ex}, Q_s) = *const.*

To derive the relation between electrical mobility and voltage applied to the inner electrode, the easiest way is to choose a coordinate system with the x-axis in direction of the cylinder axis. Due to the prerequisite of the cylindrical geometry, also the flow pattern $dx/dt = v(x,r) = v(r)$ will be of cylindrical symmetry and

the drift velocity of the particle will only depend on the radial distance from the cylinder axis:

$$\frac{dr}{dt} = Z \cdot \left|\vec{E}(r)\right| \qquad [2.60]$$

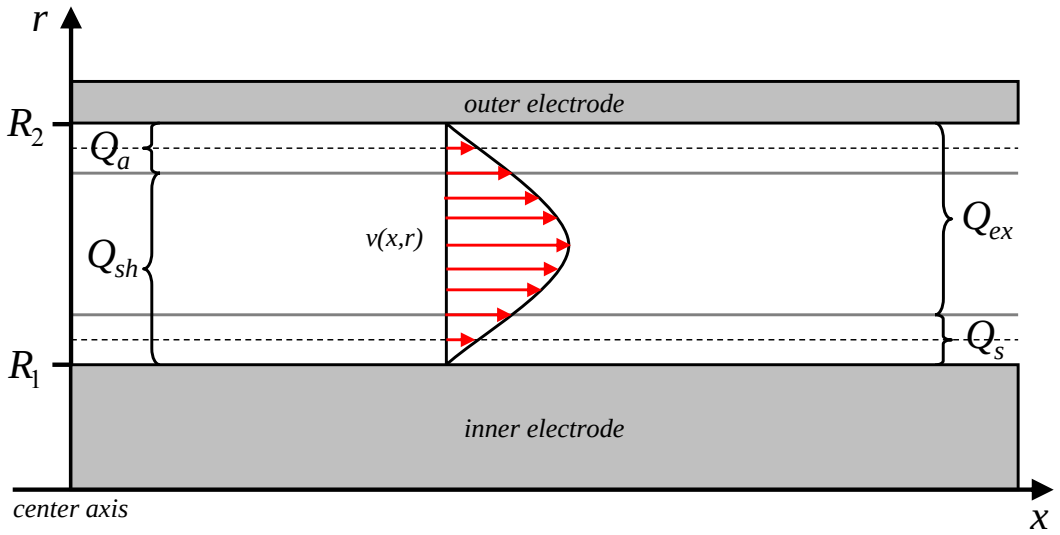

Fig. 2.13 Flow pattern through the DMA' classification channel.

In a cylindrical capacitor, the electric field strength $\left|\vec{E}(r)\right|$ is given as:

$$\left|\vec{E}(r)\right| = \frac{V}{r \cdot \ln\left(R_2 / R_1\right)} \qquad [2.61]$$

Where V is the voltage applied to the inner electrode, r the radial distance from the center axis of the capacitor, R_1 the outer radius of the inner electrode and R_2 the inner radius of the outer electrode. Therefore, the equation for the path of the aerosol particle through the DMA's channel is given by:

$$\frac{dx}{dr} = \frac{dx}{dt} \cdot \frac{1}{\frac{dr}{dt}} = \frac{\ln\left(R_2/R_1\right)}{Z \cdot V} \cdot r \cdot v(r) \qquad [2.62]$$

This equation is readily integrated into

$$\int_{x_1}^{x_2} dx = \frac{\ln\left(R_2/R_1\right)}{Z \cdot V} \cdot \int_{r_1}^{r_2} r \cdot v(r) \cdot dr \qquad [2.63]$$

For a channel length L it can be can be further transformed to

$$L = \frac{\ln(R_2/R_1)}{2 \cdot \pi \cdot Z \cdot V} \cdot \int_{r_1}^{r_2} 2 \cdot \pi \cdot r \cdot v(r) \cdot dr \qquad [2.64]$$

and results in an expression for the electrical mobility:

$$Z = \frac{1}{V} \cdot \left(\frac{\ln(R_2/R_1)}{2 \cdot \pi \cdot L} \right) \cdot \int_{r_1}^{r_2} 2 \cdot \pi \cdot r \cdot v(r) \cdot dr \qquad [2.65]$$

For a further simplification, the integral $\int_{r_1}^{r_2} 2 \cdot \pi \cdot r \cdot v(r) \cdot dr$ has to be transformed.

$2 \cdot \pi \cdot r \cdot dr$ is the area of a circular ring with radius *r* and width *dr*. Therefore, $2 \cdot \pi \cdot r \cdot v(r) \cdot dr$ corresponds to the flow through this area and the integral $\int_{r_1}^{r_2} 2 \cdot \pi \cdot r \cdot v(r) \cdot dr$ defines the volume flow Q_{r_1,r_2} through the hollow cylinder with radii r_1 and r_2.

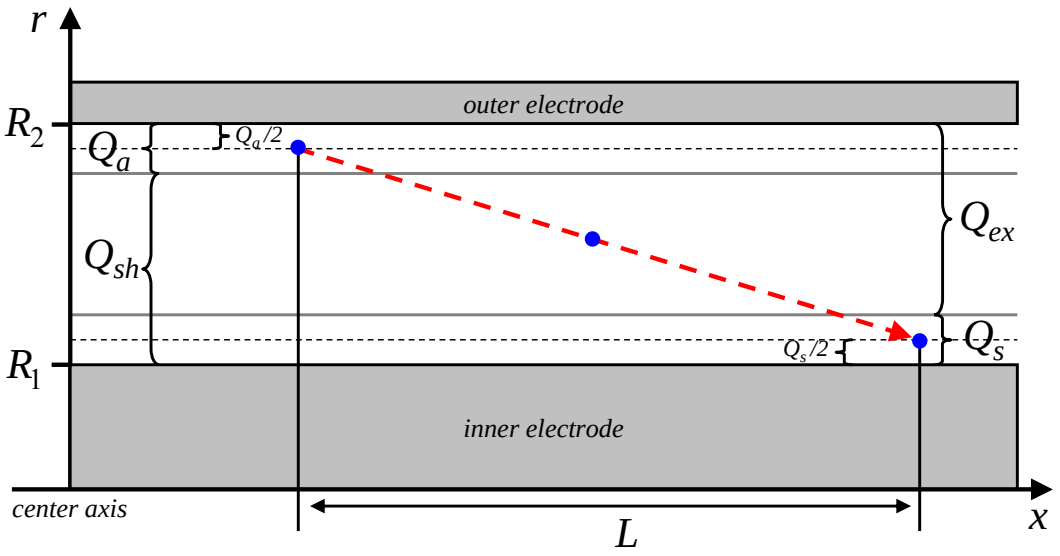

Fig. 2.14 Path of a particle through the DMA's channel

If we define, according to Fig. 2.14, a mean electrical mobility Z from the center of the aerosol flow Q_a with the coordinates ($r = r_2$, $x = 0$) to the center of the sample air flow Q_s with coordinates ($r = r_1$, $x = L$), the integral can be split into:

$$\int_{r_1}^{r_2} 2\pi \cdot r \cdot v(r) \cdot dr = \int_{R_1}^{R_2} 2\pi \cdot r \cdot v(r) \cdot dr - \int_{R_1}^{r_1} 2\pi \cdot r \cdot v(r) \cdot dr - \int_{r_2}^{R_2} 2\pi \cdot r \cdot v(r) \cdot dr$$

$$\int_{r_1}^{r_2} 2\pi \cdot r \cdot v(r) \cdot dr = \left(Q_{sh} + Q_a\right) - \frac{1}{2} \cdot Q_s - \frac{1}{2} \cdot Q_a$$

or

$$\int_{r_1}^{r_2} 2\pi \cdot r \cdot v(r) \cdot dr = \left(Q_{ex} + Q_s\right) - \frac{1}{2} \cdot Q_s - \frac{1}{2} \cdot Q_a \qquad [2.66]$$

Consequently, the integral $\int_{r_1}^{r_2} 2 \cdot \pi \cdot r \cdot v(r) \cdot dr$ can be expressed just by the volumetric flowrates as

$$\begin{aligned} \int_{r_1}^{r_2} 2\pi \cdot r \cdot v(r) \cdot dr &= Q_{sh} + \frac{\left(Q_a - Q_s\right)}{2} \\ &= Q_{ex} + \frac{\left(Q_s - Q_a\right)}{2} \\ &= \frac{\left(Q_{sh} + Q_{ex}\right)}{2} \end{aligned} \qquad [2.67]$$

This way, the mean electrical mobility Z of the particles leaving the DMA at the annular exit slit with the voltage V applied to the inner electrode of the DMA is defined as:

$$Z = \frac{1}{V} \cdot \frac{\ln(R_2 / R_1)}{2 \cdot \pi \cdot L} \cdot \frac{(Q_{sh} + Q_{ex})}{2} \qquad [2.68]$$

It is important to note that this relation is independent of the actual trajectory of the particles through the DMA's channel. Therefore, this definition of the particle's electrical mobility is independent of the flow profile and also independent of changes in the flow profile in axial direction of the DMA.

2.6. From Mobility to Diameter

Inside the DMA's channel, the particles experience a drag force in the continuous viscous sheath air flow Q_{sh}. For spherical particles, the resulting force can be expressed by the Stokes' law:

$$\vec{F} = \frac{3\pi \cdot \eta \cdot D_p \cdot \vec{v}}{C(D_p)} \qquad [2.69]$$

where η is the dynamic viscosity of the carrier gas, D_p the particle's diameter, $\vec{v}$ the drift velocity of the particle and $C(D_p)$ the Cunningham slip correction factor that accounts for the case when the particle's size approaches the size range of the mean free path of the carrier gas molecules. For larger particles, $C(D_p)$ converges to 1 (see Fig. 2.15).

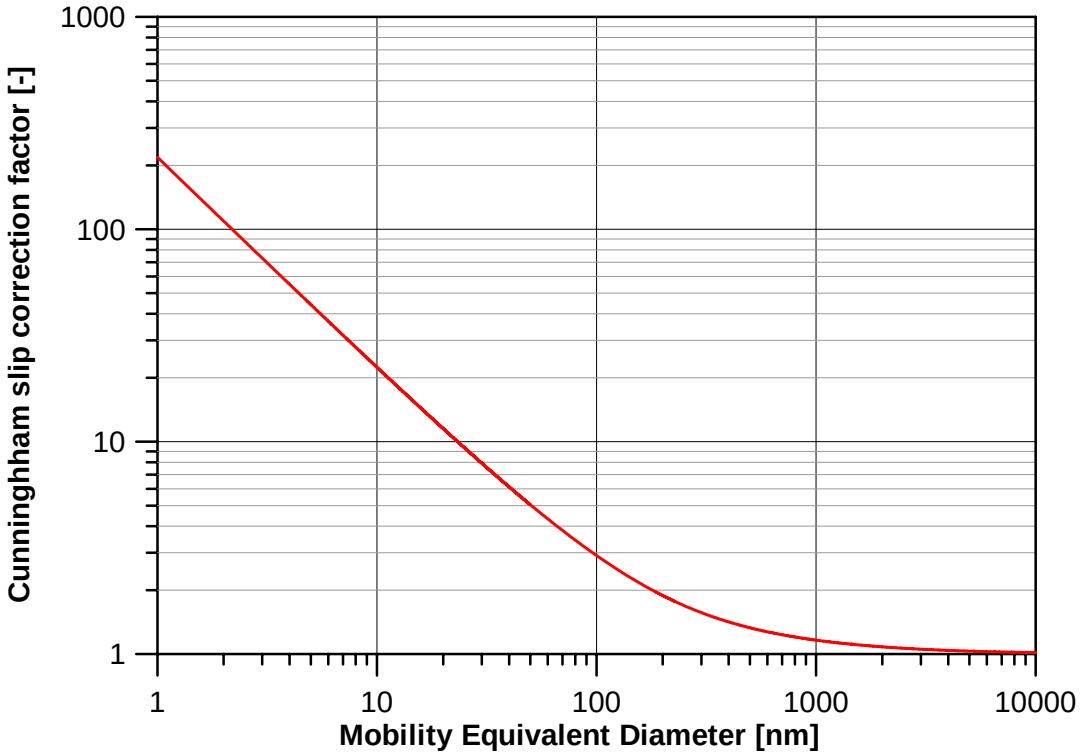

Fig. 2.15 The Cunningham slip correction factor $C(D_p)$ versus particle size.

$$C(D_p) = 1.0 + A \cdot \left(\frac{\lambda}{D_p} \right) + B \cdot \left(\frac{\lambda}{D_p} \right) \cdot \exp\left(-C \cdot \left(\frac{D_p}{\lambda} \right) \right) \qquad [2.70]$$

with the coefficients

$$\begin{aligned} A &= 2.492 \\ B &= 0.84 \\ C &= 0.43 \end{aligned} \qquad [2.71]$$

given by Fuchs (1964) and λ the mean free path of the carrier gas molecules. For standard conditions (p=1013 mbar, T=25°C), λ = 65.3nm. Many authors have reported slightly different values for the slip correction coefficients A, B and C (e.g. Friedlander, 2000). However, in this work only the values given by Fuchs (1964) are in use.

The mechanical mobility B of a particle as defined in equation [2.55]

$$B = \frac{\vec{v}}{\vec{F}}$$

can be transformed by using Stokes' law in equation [2.69] to

$$B = \frac{C(D_p)}{3\pi \cdot \eta \cdot D_p} \qquad [2.72]$$

Accounting for electrostatic forces, equation [2.56] defines the electrical mobility Z as

$$Z = i \cdot e_o \cdot B$$

where i is the number of elementary charges on the particle and e_0 the elementary charge.

Using equations [2.57] and [2.72], the electrical mobility of a spherical particle carrying i elementary charges can be expressed by:

$$Z = \frac{i \cdot e_0}{3 \cdot \pi \cdot \eta} \cdot \frac{C\left(D_p\right)}{D_p} \qquad [2.73]$$

Here, D_p stands for the "mobility equivalent diameter", which is equal to the diameter of a spherical particle having the same electrical mobility as a particle of

unknown shape. This expression for the electrical mobility can be compared with the one in equation [2.68] that has been derived by solving the integral for the equation of the path of the particles through the cylindrical canal of the DMA and the electric field, and using air flow coordinates. As a reminder, equation [2.68] states:

$$Z = \frac{1}{V} \cdot \frac{\ln(R_2 / R_1)}{2 \cdot \pi \cdot L} \cdot \frac{(Q_{sh} + Q_{ex})}{2}$$

For the ideal case of symmetric operating conditions ($Q_a = Q_s$, $Q_{sh} = Q_{ex}$), [2.68] changes to

$$Z = \frac{1}{V} \cdot \frac{\ln(R_2 / R_1)}{2 \cdot \pi \cdot L} \cdot Q_{sh} \qquad [2.74]$$

Equating [2.73] and [2.74] for the electrical mobility Z leads to

$$\frac{i \cdot e_0}{3 \cdot \pi \cdot \eta} \cdot \frac{C(D_p)}{D_p} = \frac{1}{V} \cdot \frac{\ln(R_2 / R_1)}{2 \cdot \pi \cdot L} \cdot Q_{sh} \qquad [2.75]$$

resulting in the basic relation between the particle diameter and the DMA's geometrical and operational parameters, where typically the adjustable voltage on the inner electrode is the only variable parameter.

For practical use, equation [2.73] or [2.75] is sometimes laboriously to use as the calculation of a diameter D_p from a given (measured) mobility Z can only be derived through an iteration process as also the Cunningham slip correction factor $C(D_p)$ is dependent on particle size.

A much more convenient calculation of the particle's diameter from a given mobility can be derived by a linearization of the function $C(D_p)/D_p$. For very small particle sizes, $C(D_p)/D_p$ (see also [2.70]) becomes proportional to $(A\lambda + B\lambda)/D_p^2$ (with A and B as slip correction coefficients from [2.71]). Therefore, equation [2.73] turns to:

$$Z = \frac{i \cdot e_0}{3 \cdot \pi \cdot \eta} \cdot \frac{(A\lambda + B\lambda)}{{D_p}^2} \qquad [2.76]$$

Accordingly, the particle's electrical mobility can be expressed as

$$Z = const. \cdot \frac{1}{D_p{}^2} \qquad [2.77]$$

Where the constant factor

$$const. = \frac{i \cdot e_0}{3 \cdot \pi \cdot \eta} \cdot (A\lambda + B\lambda) \qquad [2.78]$$

is depended on the elementary charge e_0, the viscosity of the carrier gas η, the mean free path of the carrier gas molecules λ and the slip correction factors A and B.

An analogous approximation, only valid for very small singly charged particles (0.5nm < D_p < 5nm), was described by Mäkelä at al. (1996) with

$$Z = 2.2458 \times 10^{-22} \cdot D_p^{-1.9956} \qquad [2.79]$$

where the mobility is given in [m^2/Vs] and the diameter in [m].

2.7. The Number Size Distribution

Since the EMS classifies the particles according to their electrical mobility, the direct result of the measurement is a mobility distribution containing the charging state of the particles as an additional parameter. Under certain conditions, this mobility distribution can be converted into the much more practical number size distribution – plotting the concentration of the aerosol vs. the particle size. These conditions are:

- an upper limit of the aerosol size distribution in the measurement range
- temporal stability of the aerosol
- the knowledge of the charge distribution on the aerosol

The first requirement can be even more easily taken care of by technical means; e.g. by the application of a pre cut-off device (pre-impactor, electrostatic precipitator,…), if necessary.

The second requirement can be only satisfied by a measurement cycle that runs as fast as possible, which is mainly limited by the response time of the used sensor, e.g. a Faraday Cup Electrometer (FCE) or a Condensation Particle Counter (CPC).

The third requirement can only be satisfied by applying an appropriate charging on the particles and calculating the corresponding charging probabilities, as not all particles (particle sizes) will be charged to the same extent.
For the particle size range below 10nm, only singly charged particles need to be considered as the charging probability for higher charging states is negligible, but for larger particle sizes, also multiply charged particles have to be taken into account (see also section 2.3.). As already discussed in detail in sections 2.2. and 2.3., the corresponding charging probabilities can be derived by numerical calculations.

Let us first of all consider a mobility interval $[Z, Z+\delta Z]$. In this interval we find all particle sizes D_p where the $D_{p,i}$ satisfy equation [2.73]:

$$Z = \frac{i \cdot e_0}{3 \cdot \pi \cdot \eta} \cdot \frac{C(D_{p,i})}{D_{p,i}}$$

where the index i defines the charging state or the particle. Consequently, a certain mobility interval contains a discrete spectrum of different particle sizes $D_{p,i}$, starting with the smallest diameter $D_{p,1}$ of particles carrying only one elementary charge. Accordingly, the number size distribution $\frac{dN}{dD_p}$, or the more commonly used $\frac{dN}{d\ln D_p}$, where N denotes the concentration of the particles, can be expressed by:

$$\frac{dN_i}{d\ln(Z)} = \sum_{i=1}^{i=\infty} \frac{dN_i}{d\ln(D_p)} \cdot \psi(D_p)\,|_{D_p = D_{p,i}} \qquad [2.80]$$

with

$$\psi(D_p) = \frac{1}{D_p} \cdot \frac{C(D_p)}{D_p} \cdot \left(\frac{\partial}{\partial D_p} \left(\frac{C(D_p)}{D_p} \right) \right)^{-1} \qquad [2.81]$$

The dimensionless function $\psi(D_p)$ only depends on the particle diameter. Its value approaches 0.5 for small particles (diameter *<10 nm*) and 1.0 for large particles (diameter > *1 µm*). (see Fig. 2.16)

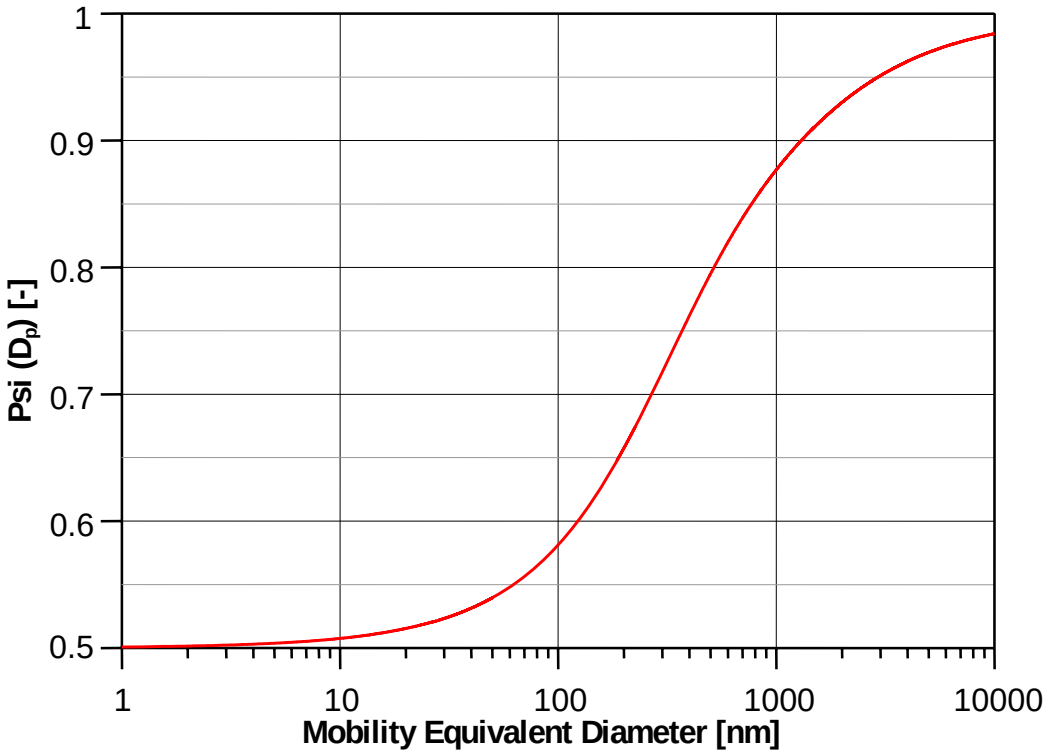

Fig. 2.16 The dimensionless function $\psi(D_p)$.

If a Condensation Particle Counter is used as a sensor, the output signal already corresponds to particle counts per unit time and only has to be integrated over the duration of the measurement of the mobility / size interval.

If a Faraday Cup electrometer is used as a sensor, the output signal corresponds to the current of ions entering the faraday cage. For a given volume flow Q_{fce} through the FCE, the particle concentration N can be calculated with equation [2.82]:

$$N = \frac{I}{i \cdot e_0 \cdot Q_{fce}} \qquad [2.82]$$

With I the ion current, i the charging state on the particles, e_0 the elementary charge and Q_{fce} the volume flow through the FCE. For typical everyday-lab conditions, and therefore typically used units, equation [2.82] changes to:

$$N = \frac{I}{i \cdot e_0 \cdot Q_{fce}} \cdot \frac{10^{-15} \cdot 1000}{60} \qquad [2.83]$$

where the concentration N is given in [cm^{-3}], the current I in [fA] and Q_{fce} in [L/min]

Since the relative resolution of the DMA with respect to electrical mobility is an instrument specific constant, $\psi(D_p)$ also describes the resolution with respect to particle size. For small particles, the relative resolution with respect to particle size is therefore twice the resolution for large particles – a unique feature of this method compared to other aerosol sizing instruments. More on the resolution power and performance of DMAs can be found in section 2.9. “DMA Performance and Resolution Power”.

Each point of a mobility distribution contains information on the upper part of the size distribution starting from a smallest particle diameter $D_{p,1}$. Caused by this fact a mobility distribution cannot generally converted point by point into a number size distribution. To evaluate a single point of the number size distribution one has to use the whole part of the mobility distribution for values of Z smaller than Z_p (according to $D_{p,1}$).

As can be seen from equation [2.80], the number size distribution splits up into fractions of different charging states of the particles. Most of the information is already included in the mobility distribution of the singly charged particles. For small particles < 50nm the influence of the multiply charged particles is only a second order effect because of the rapidly decreasing charging probabilities in this size range. (see section 2.3.).

In a first order approximation, the influence of the multiply charged particles may be neglected and the number size distribution can be calculated point by point, using the appropriate charging probabilities. However, it has to be pointed out that this approximation cannot be applied in general, especially if an aerosol with a noticeable fraction of particles larger than 50 nm diameter is investigated. The number size distribution of the charged particles is therefore the product of the initial number size distribution and the charging probability function $\alpha(D_p, i)$:

$$\frac{dN_i}{d\ln(D_p)} = \frac{dN}{d\ln(D_p)} \cdot \alpha(D_p, i) \qquad [2.84]$$

Consequently, the total number size distribution is specified by

$$\frac{dN}{d\ln(D_p)} = \sum_{i=-\infty}^{i=\infty} \frac{dN_i}{d\ln(D_p)} \cdot \alpha(D_p, i), \qquad [2.85]$$

the sum of uncharged and charged particles.

2.8. The Transfer Function of DMAs

In general, a transfer function describes the relation between inlet and outlet signals, depending on one or more parameters. For a DMA, the transfer function describes the relation between the concentrations of the inlet aerosol and the classified particles, depending on particle mobility and the voltage applied to the inner electrode. Therefore, it describes the proportion of the aerosol entering the DMA at Q_a that reaches the sample outlet Q_s at a given voltage (having a defined mobility). Furthermore, the full width at half maximum (FWHM) of the transfer

function $Tr(Z)$ and the extent of diffusion losses specify the performance and resolution power of a DMA. Diffusion effects will be considered in the next section 2.9., as here only the ideal behaviour will be discussed.

As given in formula [2.68] in the previous section, the mean electrical mobility of particles being classified at a voltage V is defined as:

$$Z = \frac{1}{V} \cdot \frac{\ln(R_2 / R_1)}{2 \cdot \pi \cdot L} \cdot \frac{(Q_{sh} + Q_{ex})}{2}$$

For a fixed voltage (and of course constant geometric parameters), the electrical mobility can also be expressed just by the volume flow rates in so called flow coordinates.

$$Z = \underbrace{\frac{1}{V} \cdot \frac{\ln(R_2 / R_1)}{2 \cdot \pi \cdot L}}_{const.} \cdot \underbrace{\frac{(Q_{sh} + Q_{ex})}{2}}_{Z'} \qquad [2.86]$$

and

$$Z' = Z \cdot V \cdot \underbrace{\frac{2 \cdot \pi \cdot L}{\ln(R_2 / R_1)}}_{const'.} \qquad [2.87]$$

with

$$Z' = \frac{(Q_{sh} + Q_{ex})}{2}. \qquad [2.88]$$

With this simple transformation, the transfer function can be easily determined by using Fig. 2.17: The aerosol particles with the highest mobilities that have a chance to be transferred from the aerosol inlet flow Q_a to the sample outlet Q_s move along the trajectory from point *A* to point *B* (steepest trajectories) which enter the DMA at Q_a and exit it with the sample air flow Q_s. The aerosol particles with the lowest mobilities are those with the trajectory from *C* to *D*.

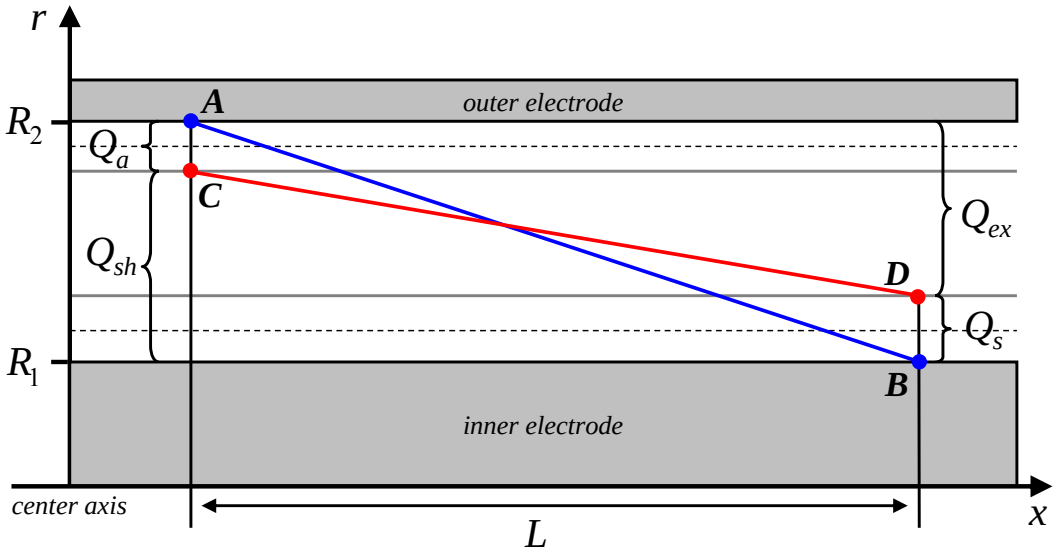

Fig. 2.17 Highest and lowest mobility trajectories through the DMA.

Accordingly, the maximum mobility equals to

$$Z'_{\max} = \int_{B}^{A} 2\pi \cdot r \cdot v(r) \cdot dr = Q_{sh} + Q_a = Q_{ex} + Q_s \qquad [2.89]$$

This also means, that the transfer function $Tr(Z' \geq Z'_{\max}) \equiv 0$ as all particles with mobility $Z' \geq Z'_{\max}$ have a steeper trajectory than the ones from *A* to *B* and will be deposited on the inner electrode before they reach the sample air outlet at point *B*.

Similarly, the minimum mobility equals to :

$$Z'_{\min} = \int_{D}^{C} 2 \cdot \pi \cdot r \cdot v(r) \cdot dr = Q_{sh} - Q_s = Q_{ex} - Q_a \qquad [2.90]$$

and the transfer function $Tr(Z' \leq Z'_{\min}) \equiv 0$ as all particles with an electrical mobility $Z' \leq Z'_{\min}$ have a flatter trajectory than the ones with the trajectory from *C* to *D* and will leave the DMA with the excess air flow rate Q_{ex} and therefore do not reach the sample air outlet Q_s.

According to these considerations, the possible mobility range is limited to:

$$(Q_{sh} - Q_s) \leq Z' \leq (Q_{sh} + Q_a) \qquad [2.91]$$

Consequently, the maximum of the transfer function $Tr_{\max}(Z')$ is given by the relation $Tr_{\max}(Z') = \min\left(1, \frac{Q_a}{Q_s}\right)$, since in the case of $Q_s > Q_a$ (illustrated in Fig. 2.18) the difference flow $(Q_s - Q_a) > 0$ (clean gas) contains no more particles and the particle concentration is diluted according to the ratio of Q_a / Q_s . In the case of $Q_s < Q_a$ (illustrated in Fig. 2.19), the concentration of the particles cannot become larger than in Q_a and the excess aerosol flow of Q_a is removed by the excess gas flow Q_{ex}.

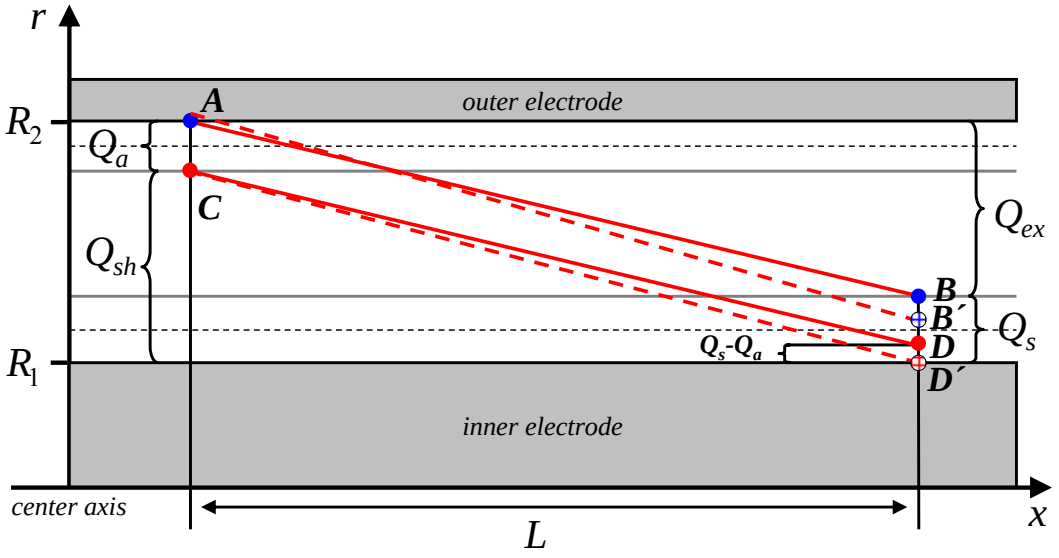

Fig. 2.18 Transfer function in the case $Q_s > Q_a$.

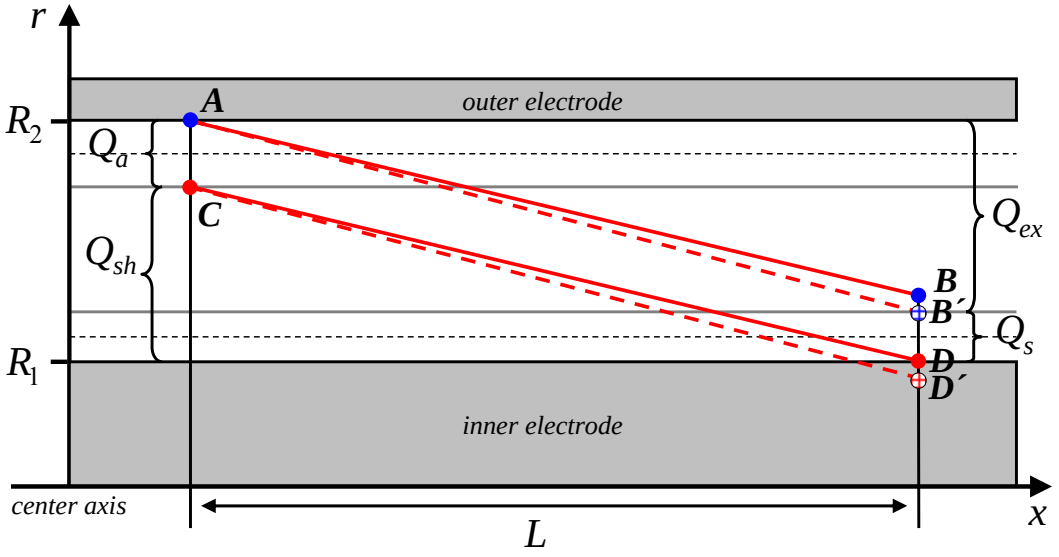

Fig. 2.19 Transfer function in the case $Q_s < Q_a$.

To calculate the transfer function in the range between $Tr(Z')=0$ and the maximum value of $Tr_{\max}(Z')=\min\left(1,\frac{Q_a}{Q_s}\right)$, as a start only mobilities smaller than the mobility at the maximum value of the transfer function $Z'_{\max}=Q_{sh}+Q_a=Q_{ex}+Q_s$ are considered. In this case the trajectory starting from point *A* will end somewhere between the points *B* and *D* at a value Q_x and the transfer function is equal to the ratio of the volumetric flow rates Q_x/Q_s. Therefore, for $\max(Q_{sh},Q_{ex})\le Z'\le(Q_{sh}+Q_a)$ and $Z'=(Q_{sh}+Q_a)-Q_x$ one obtains for the transfer function a linear dependency, rising with decreasing mobilities *Z'*:

$$Tr(Z')=\min\left(1,\frac{Q_a}{Q_s},\frac{Q_x}{Q_s}\right)=\min\left(1,\frac{Q_a}{Q_s},\frac{(Q_{sh}+Q_a)-Z'}{Q_s}\right) \quad [2.92]$$

Considering mobilities somewhat larger than the minimum mobilities $Z'_{\min}=Q_{sh}-Q_s=Q_{ex}-Q_a$, the trajectory starting from point *C* ends somewhere between the two points B and D at a value of Q_x and the transfer function is again equal to the ratio of the volumetric flow rates Q_x/Q_s.

For the mobility range: $(Q_{sh}-Q_s)\le Z'\le\min(Q_{sh},Q_{ex})$ and $Z'=(Q_{sh}-Q_s)+Q_x$, one obtains again a linear transfer function, rising for increasing mobilities.

$$Tr(Z')=\min\left(1,\frac{Q_a}{Q_s},\frac{Q_x}{Q_s}\right)=\min\left(1,\frac{Q_a}{Q_s},\frac{Z'-(Q_{sh}-Q_s)}{Q_s}\right) \quad [2.93]$$

Finally, the transfer function for the entire mobility range $0<Z'<\infty$ can be expressed by:

$$Tr(Z')=\min\left(1,\frac{Q_a}{Q_s},\frac{(Q_{sh}+Q_a)-Z'}{Q_s},\frac{Z'-(Q_{sh}-Q_s)}{Q_s}\right) \quad [2.94]$$

For the ideal case of symmetric operating conditions ($Q_a = Q_s$; $Q_{sh} = Q_{ex}$), the transfer function $Tr(Z')$ has the form of an isosceles triangle with its maximum at 1 (Fig. 2.20).

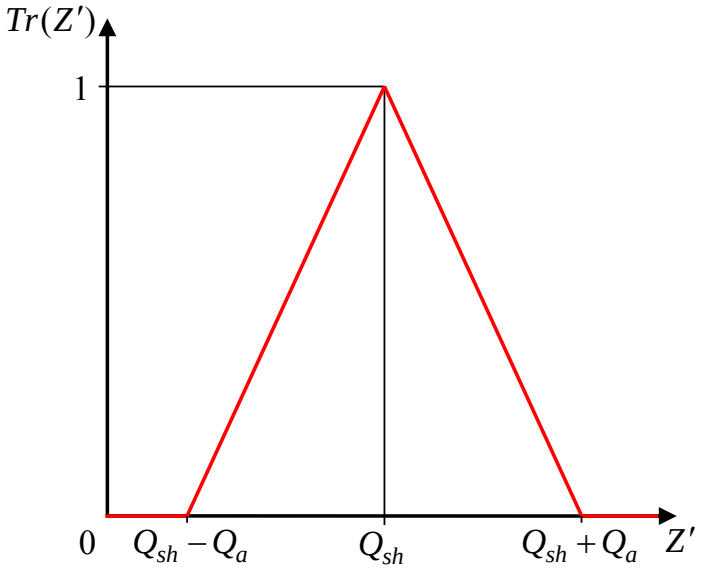

Fig. 2.20 Transfer function of the DMA $Tr(Z')$ for Q_a=Q_s and Q_{sh}=Q_{ex}.

The situation for unsymmetrical flow conditions, where $Q_a \geq Q_s$ and $Q_a \leq Q_s$ is shown in Fig. 2.21 and Fig. 2.22.

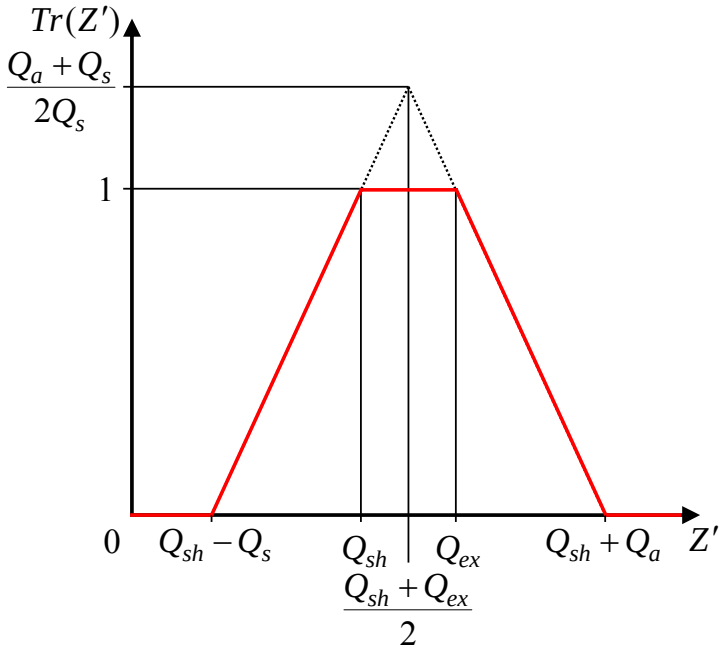

Fig. 2.21 Transfer function of the DMA *Tr(Z')* in the case of Q_a>Q_s.

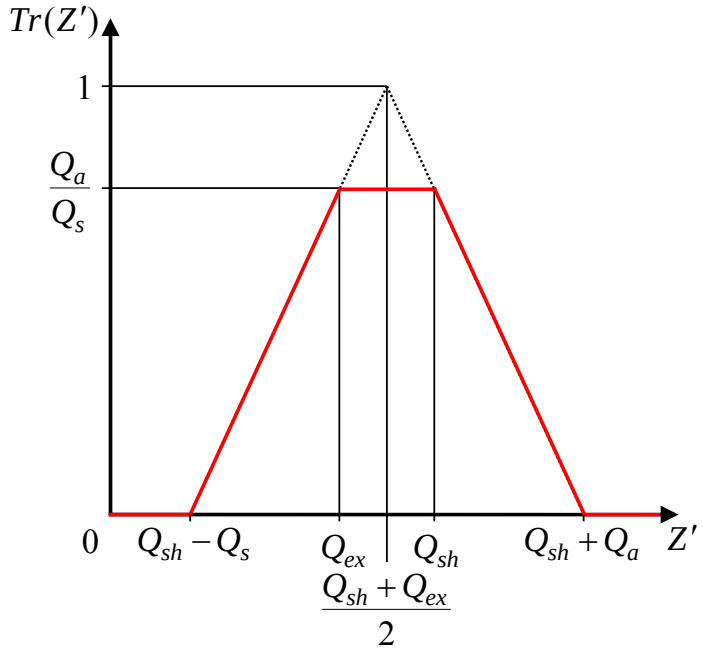

Fig. 2.22 Transfer function of the DMA *Tr(Z′)* in the case of $Q_a < Q_s$.

2.9. DMA Performance and Resolution Power

As already mentioned at the beginning of section 2.8., the FWHM of the DMA's transfer function is a measure for the resolution power of the DMA. Only at symmetric operating conditions ($Q_{sh} = Q_{ex}$, $Q_a = Q_s$) the transfer function for non diffusing particles has the form of an isosceles triangle (Fig. 2.20), resulting in a minimum of the half width. In this case, the ratio between the half width ($\Delta Z'$) to Z' is equal to the ratio between Q_a and Q_{sh},

$$\frac{\Delta Z'}{Z'} = \frac{Q_a}{Q_{sh}} \qquad [2.95]$$

or in terms of mobility equivalent diameters:

$$\frac{\Delta D_p}{D_p} = \psi(D_p) \cdot \frac{\Delta Z'}{Z'} = \psi(D_p) \cdot \frac{Q_a}{Q_{sh}} \qquad [2.96]$$

where $\psi(D_p)$ (see Fig. 2.16) is a dimensionless function dependent on the particle diameter and the Cunningham slip correction factor (equation [2.70]).

For very small particles, electrical mobility spectrometry has to deal with a broadening of the DMA's transfer function especially caused by diffusion processes. This broadening is typically altering the triangular shape into a somewhat flattened Gaussian curve (Fig. 2.23) and can be calculated with numerical methods (Tammet, 1970, Stolzenburg, 1988, Fernández de la Mora, 2002). In principle, the broadening depends on the geometry of the DMA as well as on the operating conditions such as volume flow rates, carrier gas composition, air pressure and the carrier gas temperature.

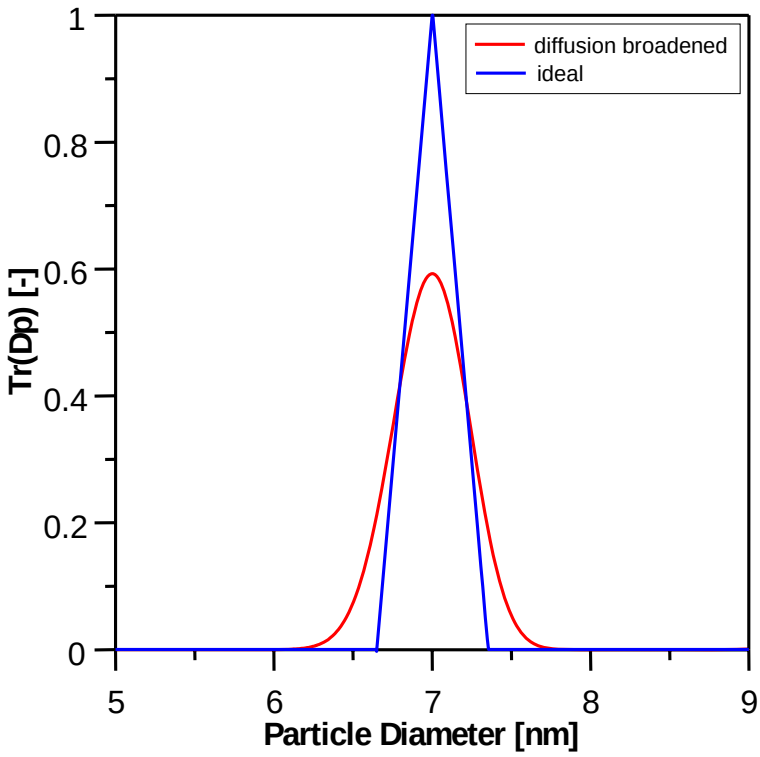

Fig. 2.23 Shape of ideal and diffusion broadened transfer function at 7nm for a standard Vienna type DMA (R_1=25mm, R_2=33mm, L=110mm) at typical operating conditions ($Q_{sh} = Q_{ex} = 20$ L/min; $Q_a = Q_s = 2$ L/min).

For completeness, a brief summary of the basic formulae for the calculation of the broadening of the transfer function according to the most widely used algorithm given by Stolzenburg (1988) as similarly presented by Reischl et al. (1997) is given:

To simplify the further derivation, the mean electrical mobility Z can be converted into a dimensionless function mobility Z_m [-].

$$Z_m = Z \cdot \underbrace{\left[V \cdot \frac{2 \cdot \pi \cdot L}{\ln\left(R_2 / R_1\right)} \cdot \frac{2}{Q_{sh} + Q_{ex}} \right]}_{const.}, \quad [-] \qquad [2.97]$$

Then, the diffusion corrected transfer function is given by:

$$Tr(Z_m) = \frac{\sigma}{\sqrt{2}\cdot\beta\cdot(1-\delta)}\cdot\left\{\Omega\left[\frac{Z_m-(1+\beta)}{\sqrt{2\cdot\sigma}}\right]+\Omega\left[\frac{Z_m-(1-\beta)}{\sqrt{2\cdot\sigma}}\right]\right.$$
$$\left.-\Omega\left[\frac{Z_m-(1+\beta\cdot\delta)}{\sqrt{2\cdot\sigma}}\right]-\Omega\left[\frac{Z_m-(1-\beta\cdot\delta)}{\sqrt{2\cdot\sigma}}\right]\right\} \quad [2.98]$$

The parameters β and δ are only dependent on the flowrates:

$$\beta = \frac{Q_a + Q_s}{Q_{sh} + Q_{ex}} \quad [2.99]$$

$$\delta = \frac{Q_s - Q_a}{Q_a + Q_s} \quad [2.100]$$

On the way through the DMA's channel, the particles undergo a dimensionless root-mean-square diffusional displacement $\sigma = \sigma^* \cdot \sqrt{Z_m}$ due to Brownian motion:

$$\left(\sigma^*\right)^2 = G\cdot\ln\left(\frac{R_2}{R_1}\right)\cdot\frac{k\cdot T}{i\cdot e_0\cdot V} \quad [2.101]$$

Where i is the number of elementary charges on the particle, e_0 the elementary charge, k Boltzmann's constant, T the temperature of the carrier gas and G an auxiliary function

$$G = 4\cdot\frac{(1+\beta)^2}{1-\gamma}\cdot\left[I(\gamma)+\left(2\cdot\kappa\cdot(1+\beta)\right)^{-2}\right] \quad [2.102]$$

The parameters γ, κ and the function $I(\gamma)$ are only dependent on the DMA's geometry:

$$\gamma = \left(\frac{R_1}{R_2}\right)^2, \quad 0<\gamma<1 \quad [2.103]$$

$$\kappa = \frac{L\cdot R_2}{(R_2^2 - R_1^2)}, \quad \kappa > 0 \quad [2.104]$$

$$I(\gamma)=\frac{\frac{1}{4}\cdot\left(1-\gamma^2\right)\cdot(1-\gamma)^2+\frac{5}{18}\cdot\left(1-\gamma^3\right)\cdot(1-\gamma)\cdot\ln(\gamma)+\frac{1}{12}\cdot\left(1-\gamma^4\right)\cdot(\ln(\gamma))^2}{(1-\gamma)\cdot\left[-\frac{1}{2}\cdot(1+\gamma)\cdot\ln(\gamma)-(1-\gamma)\right]^2} \quad [2.105]$$

Finally, the function $\Omega(x)$ is given by

$$\Omega(x)=x\cdot erf(x)+\frac{1}{\sqrt{\pi}}\cdot\exp\left(-x^2\right) \quad [2.106]$$

where $erf(x)$ is the Gaussian error function:

$$erf(x)=\frac{2}{\sqrt{\pi}}\int_0^x\exp\left(-u^2\right)\cdot du \quad [2.107]$$

The error function can not be evaluated in a closed form but can be developed into a Taylor series:

$$erf(x)=\frac{2}{\sqrt{\pi}}\sum_{n=0}^{\infty}\frac{(-1)^n x^{2n+1}}{n!(2n+1)}=\frac{2}{\sqrt{\pi}}\left(x-\frac{x^3}{3}+\frac{x^5}{10}-\frac{x^7}{42}+\frac{x^9}{216}-\ldots\right) \quad 8]$$

In the case of symmetric flow conditions ($Q_{sh} = Q_{ex}$, $Q_a = Q_s$), relations [2.99] and [2.100] become

$$\beta=\frac{Q_a+Q_s}{Q_{sh}+Q_{ex}}=\frac{Q_a}{Q_{sh}} \quad [2.109]$$

$$\delta=\frac{Q_s-Q_a}{Q_a+Q_s}=0 \quad [2.110]$$

and the diffusion corrected transfer function equals to

$$Tr(Z_m)=\frac{\sigma}{\sqrt{2}\cdot\beta}\cdot\left\{\Omega\left[\frac{Z_m-(1+\beta)}{\sqrt{2}\cdot\sigma}\right]+\Omega\left[\frac{Z_m-(1-\beta)}{\sqrt{2}\cdot\sigma}\right]-2\cdot\Omega\left[\frac{Z_m-1}{\sqrt{2}\cdot\sigma}\right]\right\} \quad [2.111]$$

To illustrate this diffusion broadening, Fig. 2.24 shows the calculated broadening of the transfer function of a standard Vienna type DMA (R_1=25mm, R_2=33mm, L=110mm) at typical operating conditions (Q_{sh} = Q_{ex} = 20 L/min; Q_a = Q_s = 2 L/min) for several particle diameters.

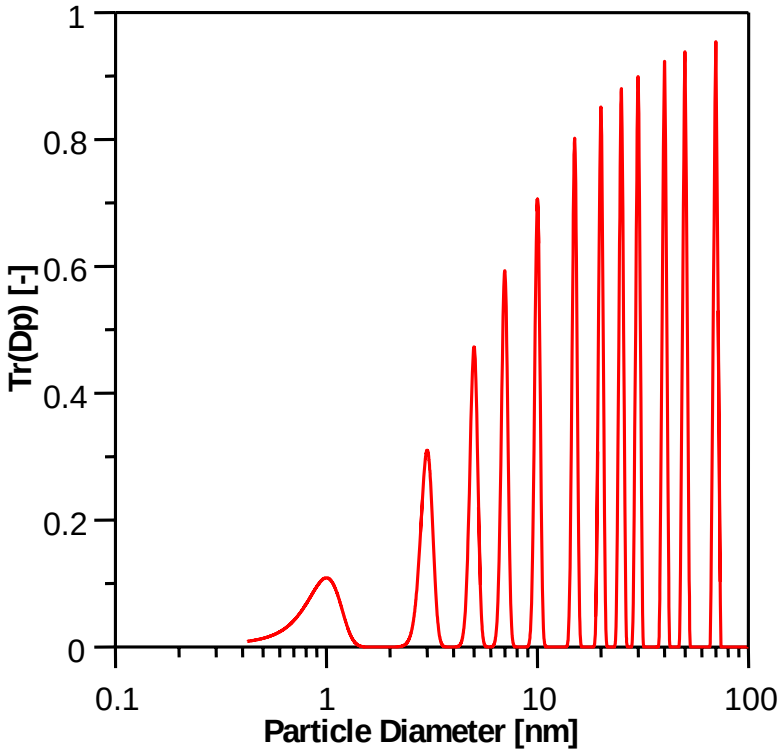

Fig. 2.24 Diffusion broadening of the transfer function of a Vienna – type DMA (R_1=25mm, R_2=33mm, L=110mm) for several particle sizes at typical operating conditions ($Q_{sh} = Q_{ex} = 20$ L/min; $Q_a = Q_s = 2$ L/min)

When approaching smaller particle sizes, the transfer function looses its ideal triangular shape and the broadening increases more and more, resulting in a deterioration of the DMA's resolution power. The same effect can be seen in Fig. 2.25 where the relative full width at half maximum (FWHM) of the DMA transfer function is plotted versus particle diameter. For a standard Vienna type DMA at typical operating conditions, the FWHM increases from its ideal value of approx. 5% (flow rate ratio 1:10 and $\psi(D_p) \approx 0.5$ in the observed size range (see Fig. 2.16)) with decreasing particle size to about 15% at a particle size of 1nm.

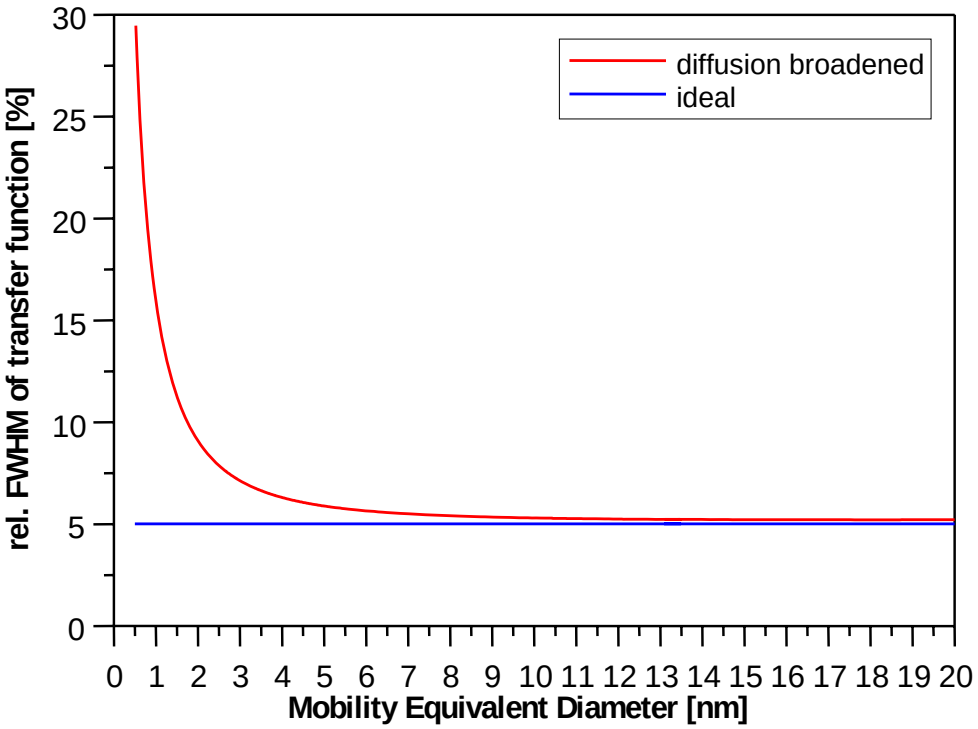

Fig. 2.25 Effect of diffusion broadening on the transfer function of a DMA for R_1=25mm, R_2=33mm, L=110mm, Q_{sh}=20 L/min and Q_s=2 L/min.

Evidently, this performance is inappropriate for the measurement of sub-3nm particles and clusters. As one main objective of this work was to improve the available instrumentation that is able to access this size range, chapter 3 will describe the design criteria and specifications of the so called “UDMA”, a new Vienna type high resolution DMA developed in the framework of this thesis.

3. High Resolution Electrical Mobility Spectrometry

As the behavior of nanometer sized particles down to molecular clusters has become of special interest in the last years (Kulmala et al. 2007; Winkler et al. 2008), several authors have reported improved DMA designs not only capable of accessing the size range below 3 nm but also optimized to measure the mobility distribution of molecular clusters (Rossell-Llompart et al. 1996; Eichler 1997; De Juan and Fernández de la Mora 1998; Hermann 2000; Rosser and Fernández de la Mora 2005; Martínez-Lozano and Fernández de la Mora 2006; Brunelli et al. 2009).These developments also include design modifications, carried out to obtain a better resolution regarding ion mobility and ion mobility equivalent diameter respectively.

Parts of the following chapter were already published in the article "A Medium Flow, High-Resolution Vienna DMA Running in Recirculating Mode" (Steiner et al. 2010). The complete article can be found in Appendix A**.**

The crucial parameters for high resolution measurements of molecular clusters are the channel length L, the aspect ratio $L/(R_2 - R_1)$ of the classifying region, where R_1 is the outer diameter of the inner electrode and R_2 the inner diameter of the outer electrode, and the sheath air flow Q_{sh}. Following the basic ideas of improving the DMA resolution from 1996 (Rossell-Llompart et al. 1996), a redesign of the Vienna type DMA with a short channel length L of 15.5 mm and an aspect ratio $L/(R_2-R_1)$ of about 2 (Vienna type NDMA) was investigated for flow rates up to 43 L/min (Steiner 2006). The NDMA was designed for an improved performance in the size range below 10 nm compared to the performance of the original Vienna DMA (L = 110 mm, aspect ratio: 13.75). The NDMA was mainly used for the generation of monodisperse aerosol particles between 2 nm and 10 nm with a resolution power ranging from a relative FWHM of the transfer function of 9% to 15% in mobility size. However the NDMA could

not reach the theoretically obtainable resolution, mainly because of an inadequate sheath air laminarization in the inlet system. The high-flow, high-resolution DMAs developed in the last few years by other groups mainly obtain the necessary resolution power by an increased sheath air flow rate up to several cubic meters per minute. Due to the lack of suitable leak free high flow pumps, the high flow, high resolution DMAs are mostly operated as open systems. The enormous sheath air flow is typically maintained by modified vacuum cleaner pumps (Fernández de la Mora and Attoui 2007), where the sheath air is drawn from the ambient laboratory air into the DMA. Unfortunately, in this operation mode, the option of a well defined and controlled composition of the gas flow through the DMA, which is a crucial feature for operating a DMA inline with carrier gas sensible instrumentation, is lost. However, in recent studies, where high flow DMAs have been used as mobility classifiers in front of highly sensitive condensation nuclei counters (Gamero-Castano and Fernández de la Mora 2000a,b) and a mass spectrometer (Fernández de la Mora et al. 2005; Hogan and Fernández de la Mora 2009), low leakage vacuum cleaner pumps have been successfully used for operating the high flow DMAs in a closed loop arrangement, where the excess air flow Q_{ex} is established by an aspirated gas flow and recirculated to the DMA as sheath air flow Q_{sh} (Jokinen and Mäkelä 1997). Nevertheless, most standard DMAs operating in a closed loop arrangement do not provide the required resolution power in this size range. Typically, they are operated at relatively low sheath air flow rates compared to their channel length and therefore show a large diffusion broadening of their transfer functions.

For the purpose of satisfying the above mentioned experimental needs, the design of the Vienna type NDMA was modified in this work to obtain the desired resolution without abandoning the option to operate the DMA in a closed loop arrangement.

In principle, two major changes were carried out: the aspect ratio of the classifying region was reduced from about 2 to 1 and the inlet and outlet section of the sheath air flow was completely redesigned to reduce the pressure drop within the DMA to easier allow high volume flow rates. The result of these and some minor other improvements is the so called Vienna type UDMA.

3.1. The Vienna Type UDMA High Resolution DMA

The UDMA is a refinement of the well known Vienna type DMA design, and therefore has the form of a vertical cylindrical capacitor. To reduce weight, most parts of the UDMA are manufactured of aluminum. Special attention was paid to the quality of the polishing of the interior surfaces, as only well polished optically reflective surfaces provide a well defined homogeneous electric field between the electrodes. The tube joints for the inlet and outlet flow ports are made of stainless steel; bottom and top insulators are made of PEEK (polyetheretherketone).
A cross-section of the UDMA is shown in Fig. 3.1.

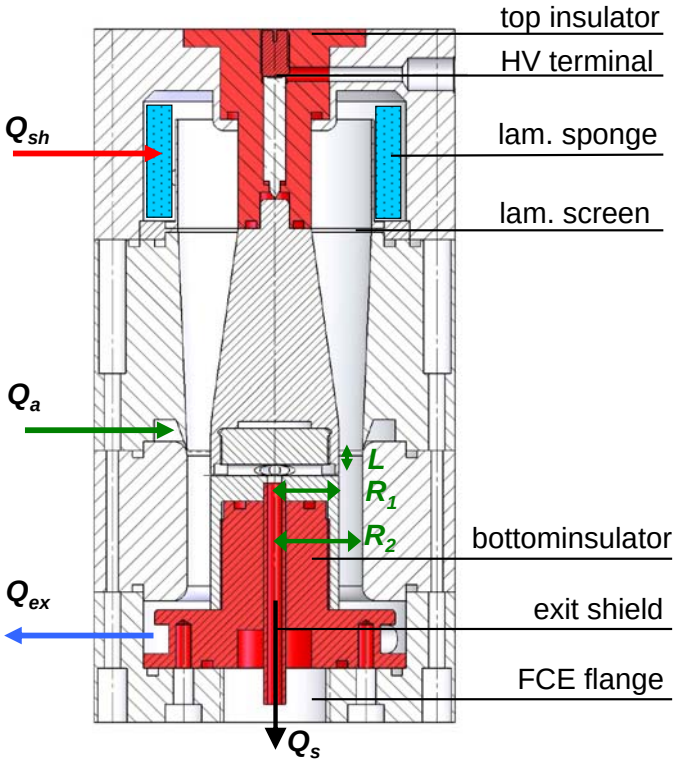

Fig. 3.1 Schematics of the Vienna-type UDMA;
R_1=17.5mm, R_2=24mm, L=6.5mm

The purified sheath air Q_{sh} is introduced by four tangential stainless steel connection tubes at the top of the UDMA. The interior upper part mainly consists of a cup-shaped bracket for a woven nylon laminarization screen of 0.2mm thickness and a mesh size of 50µm. The cavity between the sheath air inlet ports and the outer wall of the cup-shaped bracket is filled with a stainless steel laminarization sponge to eliminate the tangential component of Q_{sh} in order to provide a uniform laminar flow through the UDMA. For the laminarization sponge, an ordinary stainless steel scrub pad, mainly utilized for dish washing, was used. The upper part of the channel between the electrodes is converging to accelerate the sheath air flow.

The aerosol inlet volume flow Q_a is fed tangentially through an inlet port in the outer electrode into an annular cavity. A blade like shape of the inner walls and a curvature at the inner side of the outer electrode provide a smooth transition of the aerosol flow into the sheath air flow. Therefore, both airflows can be merged very smoothly which is a main criterion for the classification characteristics.

The classified clusters exit the classification channel as sample air flow Q_s by a narrow annular exit slit in the inner electrode and subsequently enter a directly flanged custom-built Faraday Cup Electrometer (FCE) for detection (see Fig. 3.2). The FCE used in this work is a slightly modified and updated version of the one described by Winklmayr et al. (1991). At the bottom of the UDMA, the residual air flow Q_{ex} exits the UDMA by four tangential connection tubes mounted antipodal to the sheath air inlet ports.

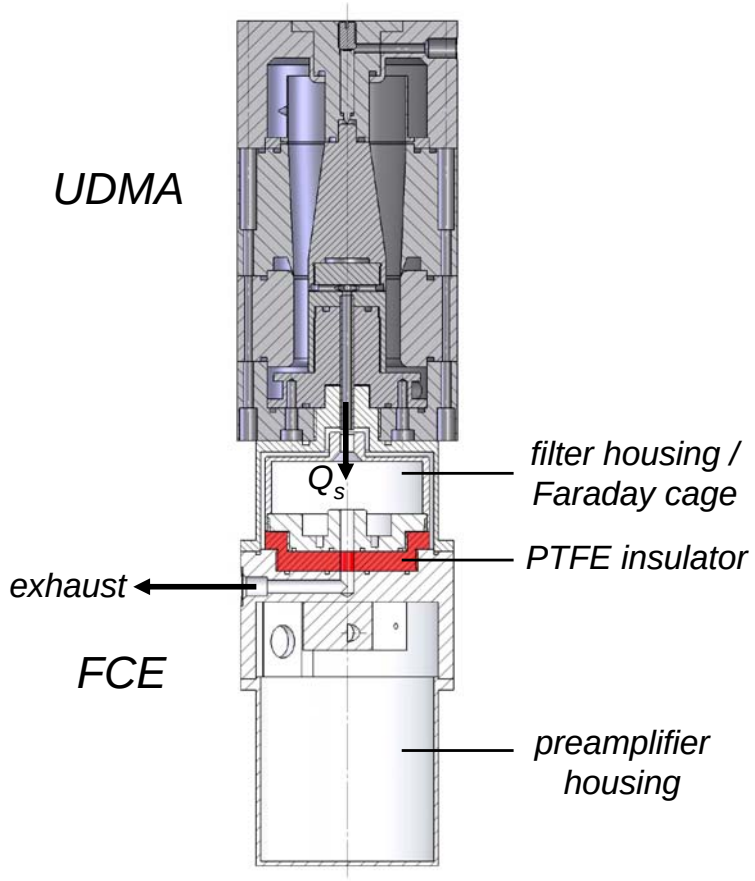

Fig. 3.2 Vienna-type UDMA with directly flanged Faraday Cup Electrometer

To provide the electrical field between the UDMA's electrodes, a high voltage potential (max. 10 kV; positive and negative polarity are possible) is applied to the inner electrode. Here, one major redesign was applied to the terminal port of the high voltage power supply. In the usual Vienna-type DMA design the high voltage connection for the inner electrode is installed in the bottom insulator. To reduce diffusion losses in the exit section, one design goal was to keep the axial distance between the annular exit slit in the inner electrode and the inlet port of the FCE as short as possible. Therefore, in the new UDMA, the high voltage joint is mounted at the top of the UDMA. The high voltage power cord is fixed to a cylindrical brass pin, localized in the center axis of the top insulator. The high voltage pin is shaped on one end to a sharply tipped cone to safely connect the high voltage power supply to the inner electrode.

Another improvement in the exit section is a polyurethane exit shield tube which was found to minimize surface charge effects acting on the particles on their way

through the bottom insulator to the outlet port and therefore reducing diffusion losses of the classified particles.

As Brownian motion is one of the limiting factors for mobility measurements in the size range below 3 nm, one of the main goals was to minimize the residence time of the particles and clusters within the UDMA. For fixed electrode radii R_1 (=17.5mm) and R_2 (=24mm), the controlling parameters for the residence time are the sheath air flow rate Q_{sh} and the channel length L (=6.5mm). In this design an equal channel length and width of 6.5 mm (aspect ratio of 1) was chosen as Rossell-Llompart et al. (1996) suggested a channel length to width ratio near unity (based on a detailed analysis of the Peclet number) to minimize diffusive broadening.

One of the major tasks of this work was to set up clean and purified sheath air flows (Q_{sh}) in a closed loop arrangement. The design of the flow control system was carried out in two steps. In a first instance, a flow control unit consisting of four high performance membrane pumps (HYCO, type ABF71/4C-7R) was designed. Four silica gel diffusion dryers (each with a volume of approximately 1 litre), four active carbon filters and four HEPA filters provide an efficient purification of the sheath air flow. A plenum chamber with a volume of 31 litres was installed to absorb and reduce pressure shocks on the vacuum side of the membrane pumps. By merging the four membrane pumps, a flow rate up to 300 L/min of clean and purified air is achieved. Fig. 3.3 shows two pictures of the first flow control unit.

Fig. 3.3 Pictures of the first flow control unit allowing for flow rates up to 300 L/min

As the UDMA is designed to operate at much higher flow rates, in a second step, a heavy duty 8-head membrane pump (HYCO type ML-130.85-ZV-D14/1.3 kW) capable of providing the UDMA with 540 L/min sheath air flow was used. Due to the gas compression at the outlet of the pump, a high flow heat exchanger unit had to be installed to cool the air flow and to stabilize its temperature to prevent temperature effects on the mobility measurements. Another approach to cool the high air flow is to use stainless steel tubing for the duct of the sheath air flow and to immerse it into a tank of chilled water (Fernández de la Mora and Attoui, 2007). However, without the cooling, the temperature of the sheath air flow increases by 30° Celsius in a few minutes, severely compromising the mobility measurement.

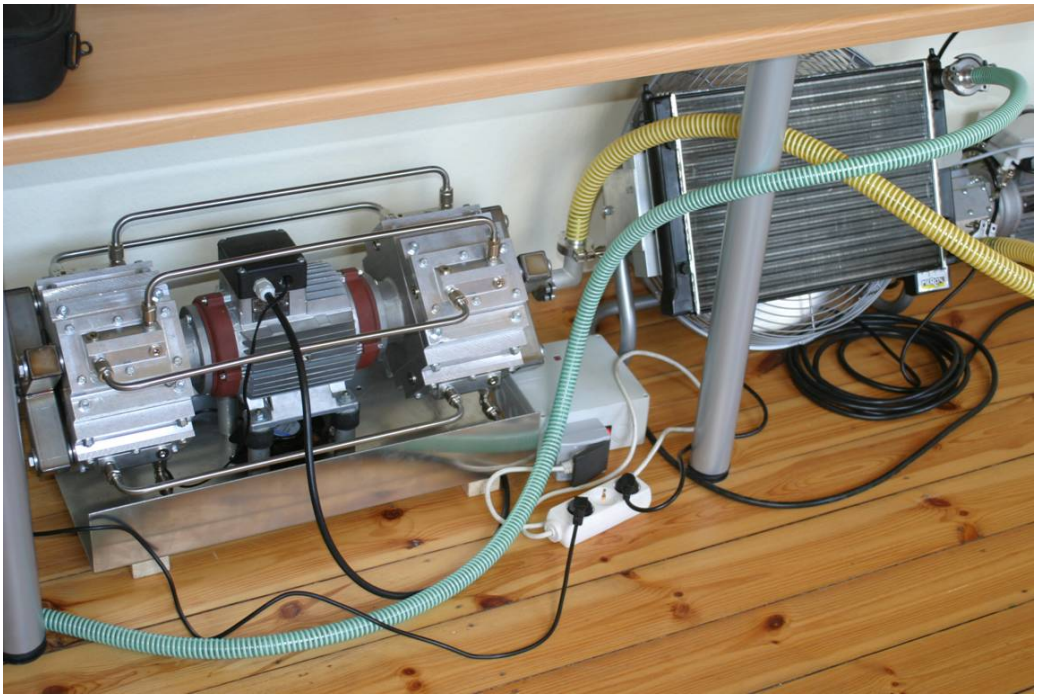

Fig. 3.4 8-head membrane pump with the high flow heat exchanger unit

By combining both available flow systems, a stable sheath air flow of approximately 700 L/min was achieved for operating the UDMA in closed loop. It should be mentioned, that at this flow rate the UDMA is operating with high resolution power at a rather high Reynolds number of approximately 6300. Also, the exact knowledge of the sheath air flow rate is not necessary as long as the airflow stays stable. More details on this are given in section 3.2.

A third flow system, involving a modified vacuum clean blower, was used only briefly for some test purposes, described in section 3.3. All other experiments performed in this thesis used the combination of the first two flow control units with a careful purification of the sheath air flow.

The sample air flow Q_s is maintained by drawing an air flow of typically 6.5 L/min, fixed by a critical orifice, through the FCE. As the UDMA is operated under symmetric flow conditions ($Q_{sh} = Q_{ex}$ and therefore $Q_s = Q_a$), this way an equally sized inlet aerosol volume flow Q_a is provided.

3.2. Calibration of High Resolution DMAs

Well defined and well known operating conditions are a crucial prerequisite for high resolution mobility measurements. Unfortunately, the precise determination of volumetric flow rates up to several m^3/min is a very difficult and time consuming task and small deviations of the effective channel length from the nominal value have a large impact on the DMA's classification characteristics. As it is difficult to determine actual/effective channel length and actual sheath air flow rate, high flow and high resolution DMAs have to be calibrated with an adequate mobility standard. Assuming a constant but unknown sheath air flow rate Q_{sh} and channel length L, the DMA equation (compare equation [2.74])

$$Z = \frac{1}{V} \cdot \frac{\ln(R_2 / R_1)}{2 \cdot \pi \cdot L} \cdot Q_{sh}$$

where Z is the aerosol particle's electrical mobility, V the voltage applied to the inner electrode, R_1 the outer diameter of the inner electrode and R_2 the inner diameter of the outer electrode, can be transformed to

$$Z = K \cdot \frac{1}{V} \qquad [3.1]$$

where

$$K = \frac{\ln(R_2 / R_1)}{2 \cdot \pi \cdot L} \cdot Q_{sh} \qquad [3.2]$$

is the DMA's operational characterization factor.

This characterization factor can be determined experimentally by feeding aerosol particles with a well known electrical mobility to the DMA and recording the voltage where most of the particles are transferred from Q_a to Q_s (the voltage at the peak signal of the mobility spectrum). Applying this method, the calibrated DMA can be operated without knowing exactly the geometric parameters and the sheath air flow rate (Rosell-Llompart et al., 1996; De Juan and Fernández de la

Mora, 1998). The generation of monodisperse particles for DMA calibration in the size range above 4nm is discussed by Chen et al. (1995) and for sizes down to about 2.6nm by Imanaka et al. (2006) using an electrospray generator. Primary electrical mobility standards, also generated with an electrospray source, were reviewed by Ude and Fernández de la Mora (2005) using Tetraalkylammonium halide clusters and by Ku and Fernández de la Mora (2009) using clusters of a larger diversity of substances.

Since the discovery of the electrospray by John Fenn and coworkers in 1989 (Fenn et al., 1989), the electrospray method is widely used for the generation of well-defined nanometer sized particles and molecular clusters for various scientific fields. Its applications are ranging from the use as ionization source for mass spectrometric investigations to the production of ion beams in a vacuum for electrical propulsion in space (e.g. Romero-Sanz et al., 2005).
Basically, a liquid sample – that is meant to be atomized – is raised to a high voltage potential and exposed to a strong electric field. The electric field induces a surface charge on the liquid that forces the surface of the liquid into a conical shape (due to the balance between surface tension and electrical forces), called Taylor cone (Taylor, 1964). The electrical forces further cause a jet of droplets emanating from the tip of the Taylor cone and dispersing into a fine spray of highly charged droplets (see Fig. 3.5).

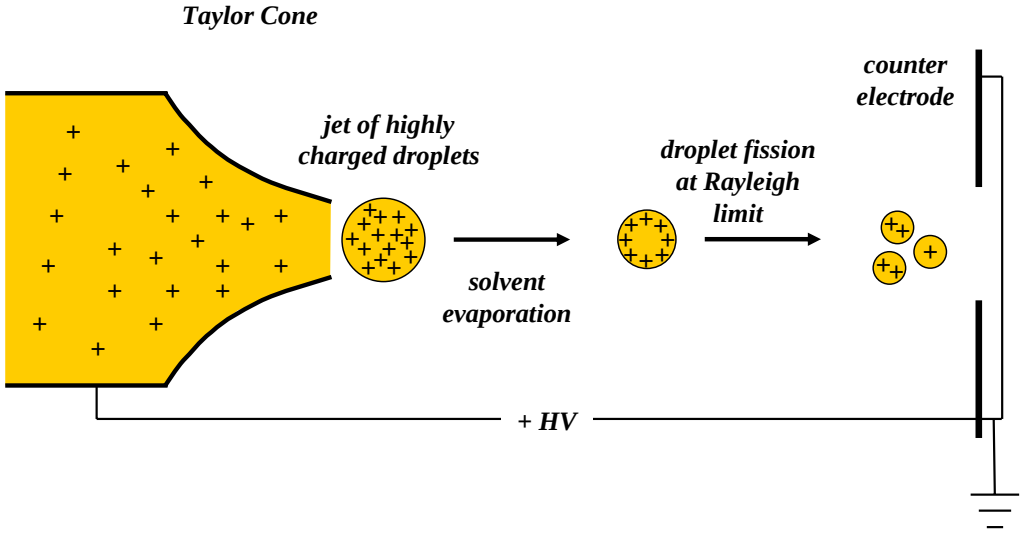

Fig. 3.5 Operating principle of an electrospray generator in positive ion mode.

Subsequently, the solvent liquid evaporates resulting in a coulombic fission of the droplets when Rayleigh's charge limit is exceeded (e.g. Hinds, 1999). This process finally leads to (in the ideal case) singly charged ultrafine particles or clusters.

The electrospray generator used in this work for the generation of the calibration standards for the high resolution UDMA is a slightly modified version of the design presented by Rosell-Llompart and Fernández de la Mora (1994). The redesign used in this work, already discussed in detail in the diploma thesis by Wimmer (2009), features an improved observation of the interior of the electrospray chamber. For this purpose an LED light source and an optical system with a high resolution microscope camera (3 mega pixel) are attached to the generator.

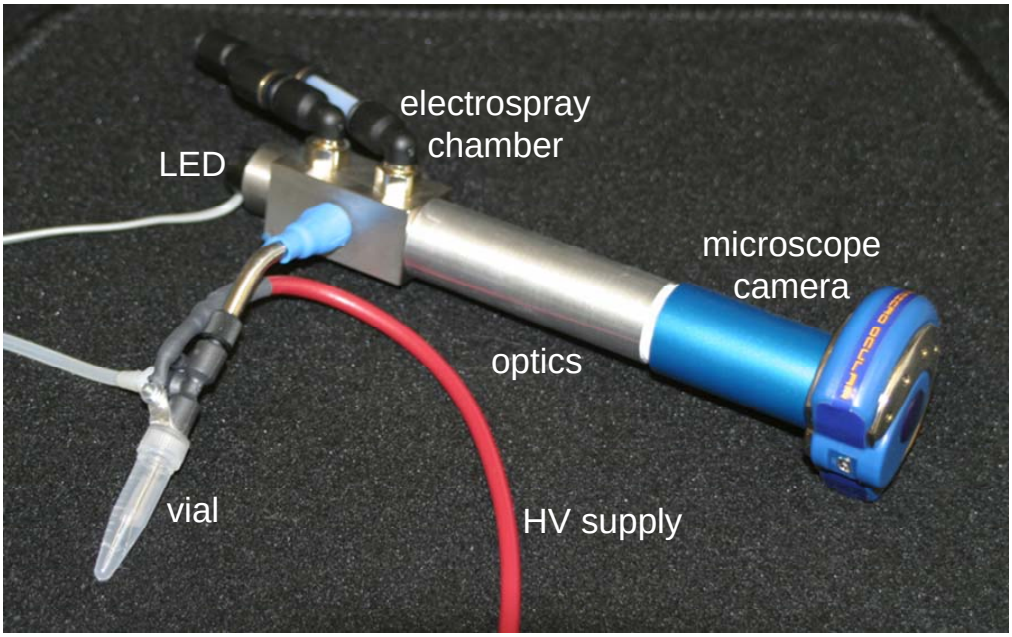

Fig. 3.6 Electrospray generator with integrated optical system

Furthermore, all metallic parts are manufactured of stainless steel to avoid chemical reactions. A silica capillary of 39 µm inner diameter and 360 µm outer diameter and a length of 20 cm is shaped on one end to a conical tip to support the formation of the Taylor Cone. It is housed in a 6 mm tubing connected on one side to the grounded electrospray chamber. On the other side it ends in a T-piece connector attached to the liquid sample reservoir and a pressure supply. An

overpressure of approximately 100 mbar is adjusted to provide the liquid flow rate through the capillary. Commercially available top threaded 1.5 cm^3 vials are used as reservoir for the liquid sample. To supply the suspended sample with a high voltage potential a platinum wire is immersed into the liquid. An adjustable computer controlled high voltage power supply provides up to +/- 5 kV. The outlet port connector screwed into the main body serves as counter electrode. A cross section of the electrospray generator is shown in Fig. 3.7.

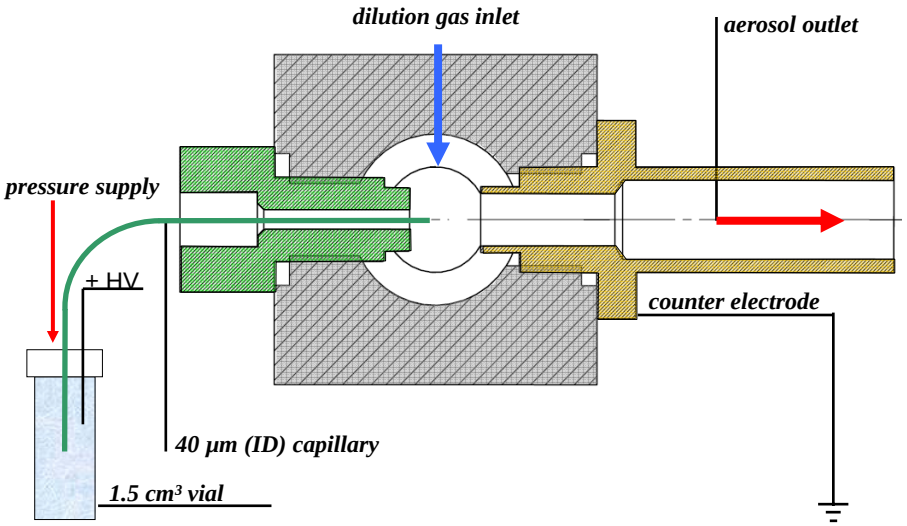

Fig. 3.7 Schematics of the redesigned electrospray generator.

On the top of the electrospray chamber, two dilution air inlets are located in the vicinity of the tip of the capillary. As they are positioned eccentrically to the capillary's axis, an additional aerodynamic focusing of the dilution air flow to the generator outlet port is obtained. The improved optical system consists of an inbuilt LED light source with a diffuser plate and an achromatic convex lens with a focal length of 20mm. A length variable tube of approximately 20cm is mounted between the magnification lens and the microscope camera to adjust the focal point. This way, a detailed observation of the shape and therefore also the stability of the Taylor cone is possible (Fig. 3.8).

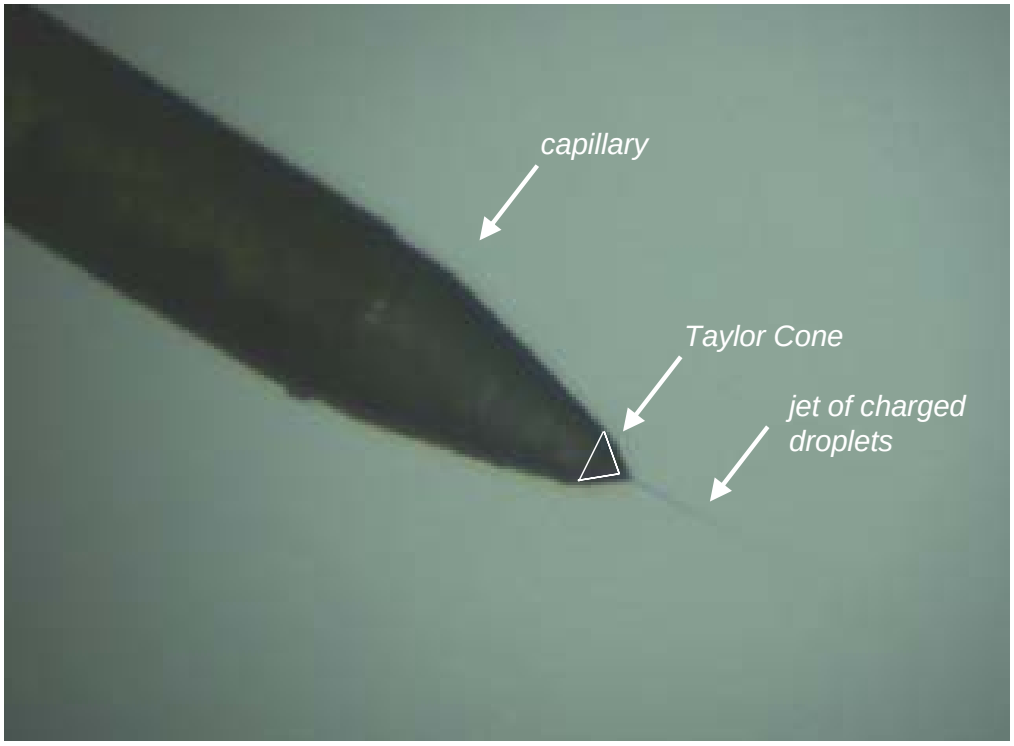

Fig. 3.8 Close-up picture of the conically shaped capillary with Taylor cone and jet of highly charged droplets.

Tetraalkylammonium halide salts, dissolved in high grade methanol where used to generate mobility standards for DMA calibration and performance tests. Their mobility distribution yields a unique pattern of peaks, associated with stable cluster species of the form $A^+(AB)_n$ where "A" denotes the Tetraalkylammonium ion (monomer) and "AB" the neutral Tetraalkylammonium halide molecule. In this work, four different salts were used:

TBAI	Tetrabutylammonium iodide	used in this work
TPAI	Tetrapentylammonium iodide	
THABr	Tetraheptylammonium bromide	
TDDABr	Tetradodecylammonium bromide	
TMAI	Tetramethylammonium iodide	
TPrAI	Tetrapropylammonium iodide	
TDABr	Tetradecylammonium bromide	

Tab. 3.1 Various Tetraalkylammonium halide salts

The properties of Tetraalkylammonium halide salt ion clusters reviewed by Ude and Fernández de la Mora (2005) and used in this work are listed in Tab. 3.2: m stands for the ions' molecular mass, Z for their electrical mobility, D_p for the corresponding mobility equivalent diameter as defined by equation [2.73] and D_p^{Ude} for the diameter values given by Ude and Fernández de la Mora (2005). Slight deviations of the diameter values are caused by the use of different coefficients for the slip correction.

ion	config.	formula	m [amu]	Z [cm^2/Vs]	D_p [nm]	D_p^{Ude} [nm]
TMAI	$(A+)(AB)_0$	$C_4H_{12}N^+$	74.15	2.1786	-	1.05
	$(A+)(AB)_1$	$C_8H_{24}N_2I^+$	275.20	1.4771	-	1.20
	$(A+)(AB)_2$	$C_{24}H_{36}N_3I^+$	476.25	1.0893	-	1.39
TPrAI	$(A+)(AB)_0$	$C_{12}H_{28}N^+$	186.36	1.6155	-	1.16
	$(A+)(AB)_1$	$C_{24}H_{56}N_2I^+$	499.63	0.9940	-	1.45
	$(A+)(AB)_2$	$C_{36}H_{84}N_3I^+$	812.89	0.7474	-	1.66
TBAI	$(A+)(AB)_0$	$C_{16}H_{36}N^+$	242.47	1.3928	1.21	1.24
	$(A+)(AB)_1$	$C_{32}H_{72}N_2I^+$	611.84	0.8673	1.53	1.55
	$(A+)(AB)_2$	$C_{48}H_{108}N_3I_2^+$	981.21	0.6897	1.73	1.73
TPAI	$(A+)(AB)_0$	$C_{20}H_{44}N^+$	298.58	1.2191	1.29	-
	$(A+)(AB)_1$	$C_{40}H_{88}N_2I^+$	724.06	0.7643	1.63	-
	$(A+)(AB)_2$	$C_{60}H_{132}N_3I_2^+$	1149.54	0.6134	1.82	-
THABr	$(A+)(AB)_0$	$C_{28}H_{60}N^+$	410.95	0.9709	1.44	1.47
	$(A+)(AB)_1$	$C_{56}H_{120}N_2Br^+$	901.64	0.6540	1.76	1.78
	$(A+)(AB)_2$	$C_{84}H_{180}N_3Br_2^+$	1392.34	0.5283	1.97	1.97
TDAB	$(A+)(AB)_0$	$C_{40}H_{84}N^+$	579.27	0.7782	-	1.64
	$(A+)(AB)_1$	$C_{80}H_{168}N_2Br^+$	1238.29	0.5417	-	1.95
	$(A+)(AB)_2$	$C_{120}H_{252}N_3Br_2^+$	1897.30	0.4257	-	2.19
TDDABr	$(A+)(AB)_0$	$C_{48}H_{100}N^+$	691.48	0.7138	1.69	1.70
	$(A+)(AB)_1$	$C_{96}H_{200}N_2Br^+$	1462.72	0.4926	2.04	2.04

Tab. 3.2 Properties of Tetraalkylammonium halide clusters

Fig. 3.9 to Fig. 3.16 show the monomer $(A^+)_1(AB)_0$ and dimer $(A^+)_1(AB)_1$ structures of the used clusters, simulated for this thesis with the programme "ChemBioOffice Ultra 2010 12.0" from "CambridgeSoft®".

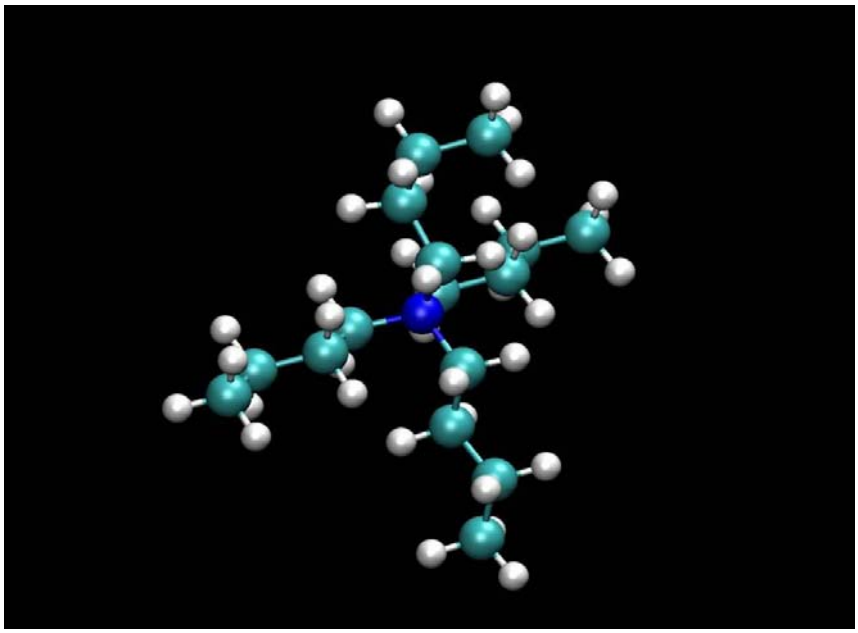

Fig. 3.9 Molecular structure of the Tetrabutylammonium iodide (TBAI) monomer $(A^+)(AB)_0$

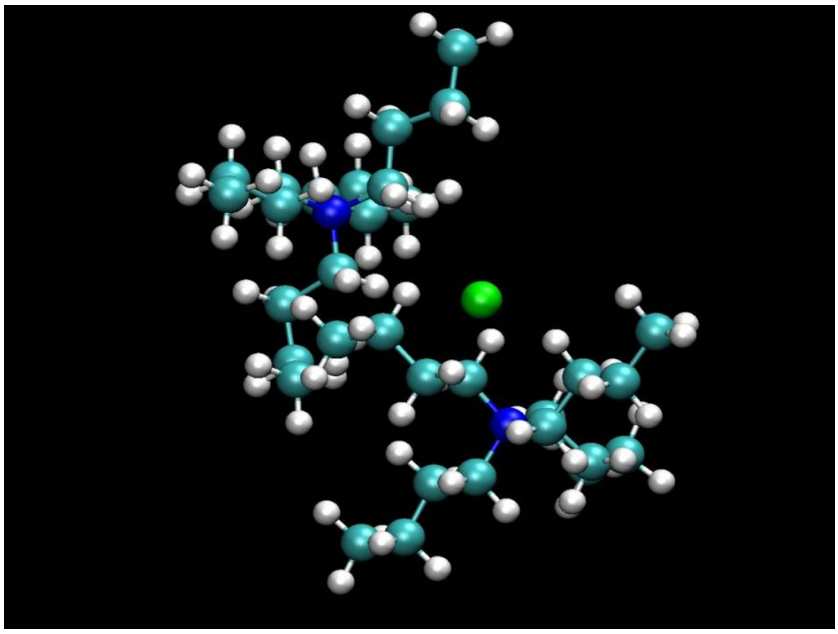

Fig. 3.10 Molecular structure of the Tetrabutylammonium iodide (TBAI) dimer $(A^+)_1(AB)_1$

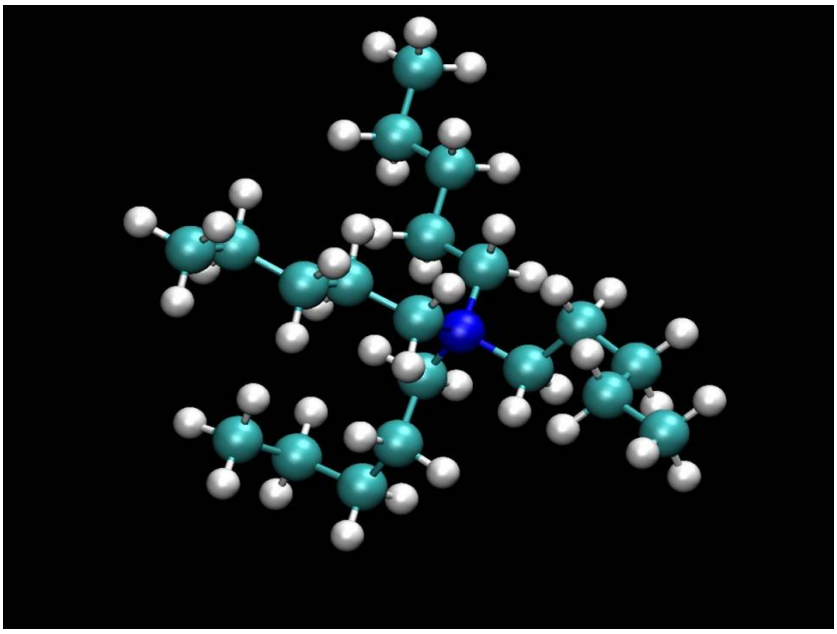

Fig. 3.11 Molecular structure of the Tetrapentylammonium iodide (TPAI) monomer $(A^+)(AB)_0$

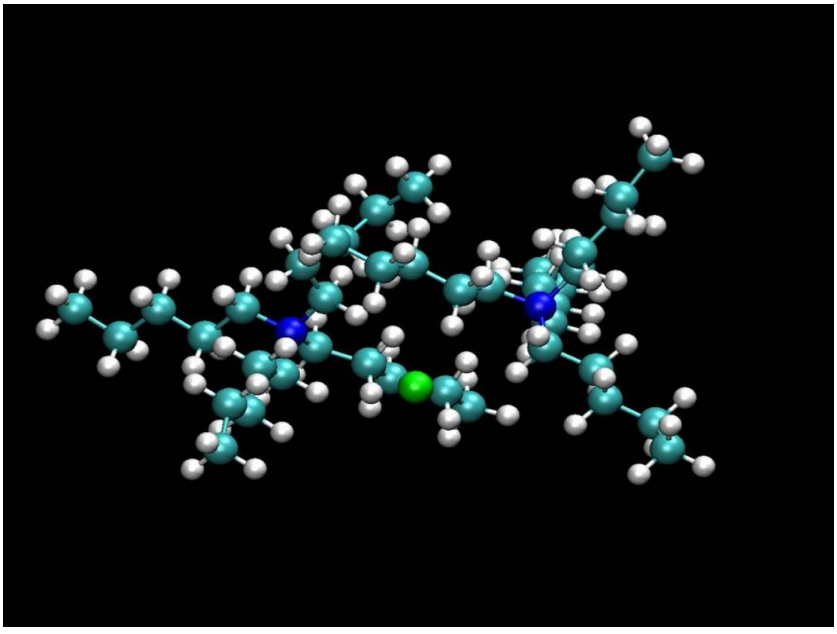

Fig. 3.12 Molecular structure of the Tetrapentylammonium iodide (TPAI) dimer $(A^+)_1(AB)_1$

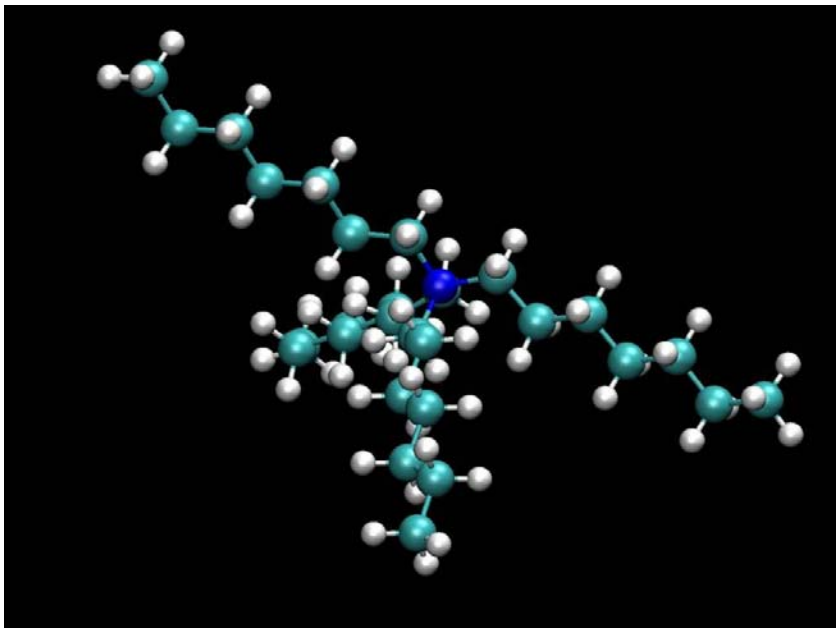

Fig. 3.13 Molecular structure of the Tetraheptylammonium bromide (THABr) monomer $(A^+)(AB)_0$

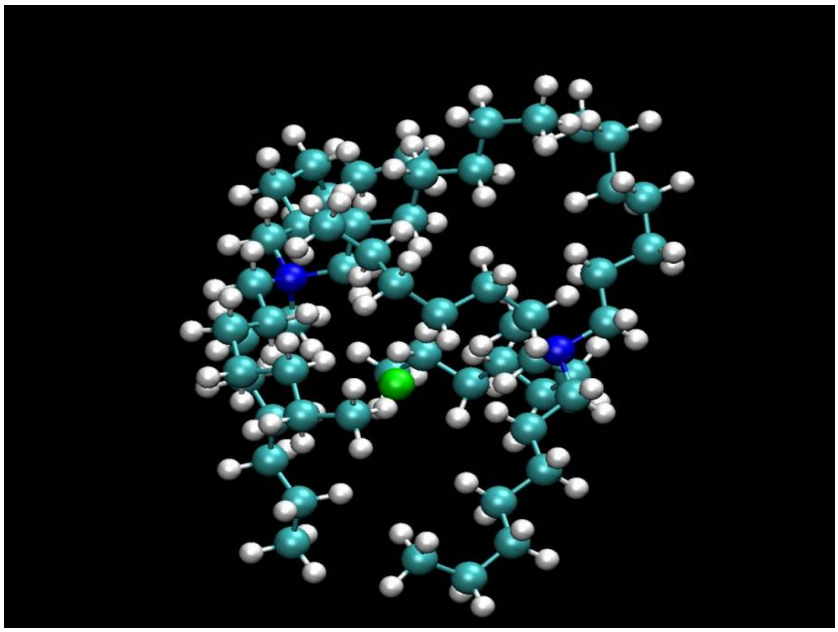

Fig. 3.14 Molecular structure of the Tetraheptylammonium bromide (THABr) dimer $(A^+)_1(AB)_1$

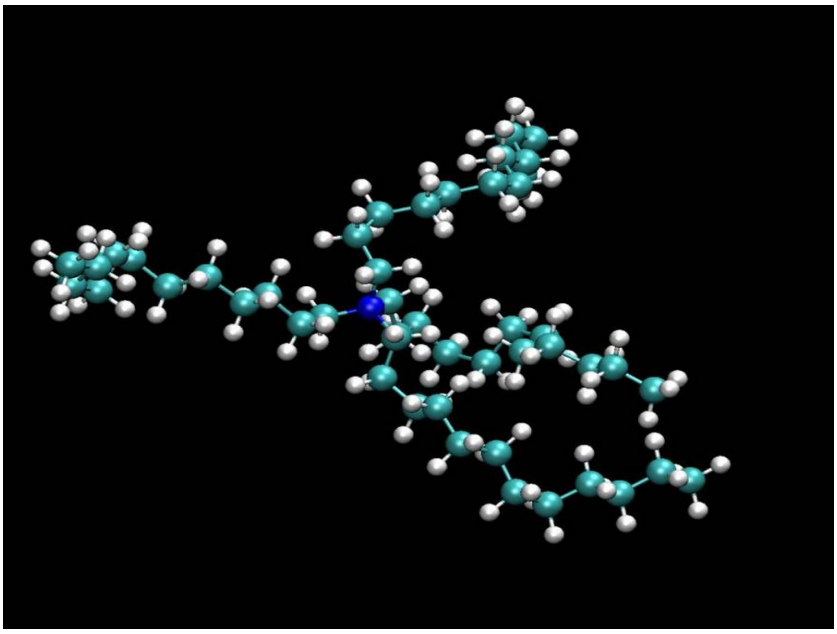

Fig. 3.15 Molecular structure of the Tetradodecylammonium bromide (TDDABr) monomer $(A^+)(AB)_0$

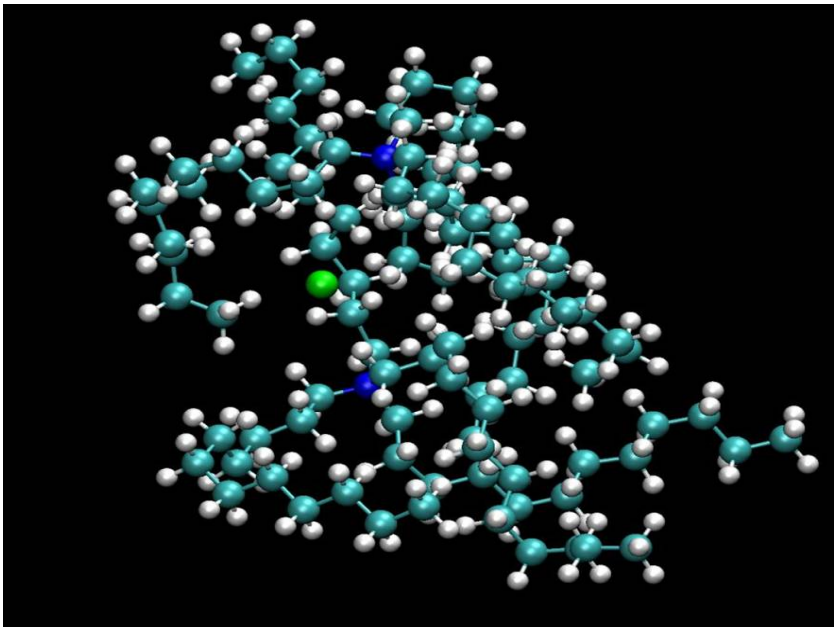

Fig. 3.16 Molecular structure of the Tetradodecylammonium bromide (TDDABr) dimer $(A^+)_1(AB)_1$

In the previous pictures, the dark blue spheres indicate the nitrogen atom in the middle of the molecule. It is surrounded by four, tetrahedral orientated C-H groups, where the cyan coloured spheres indicate the carbon and the white ones the hydrogen atoms.
For the dimer clusters, the bright green sphere indicates the loosely bonded halide atom; here iodide and bromide.

As already mentioned in the beginning of this chapter, a DMA can be calibrated by feeding aerosol particles with a well known electrical mobility and recording the peak voltage signal of the measured distribution. An example of such a voltage scan is given in Fig. 3.17 for THABr.

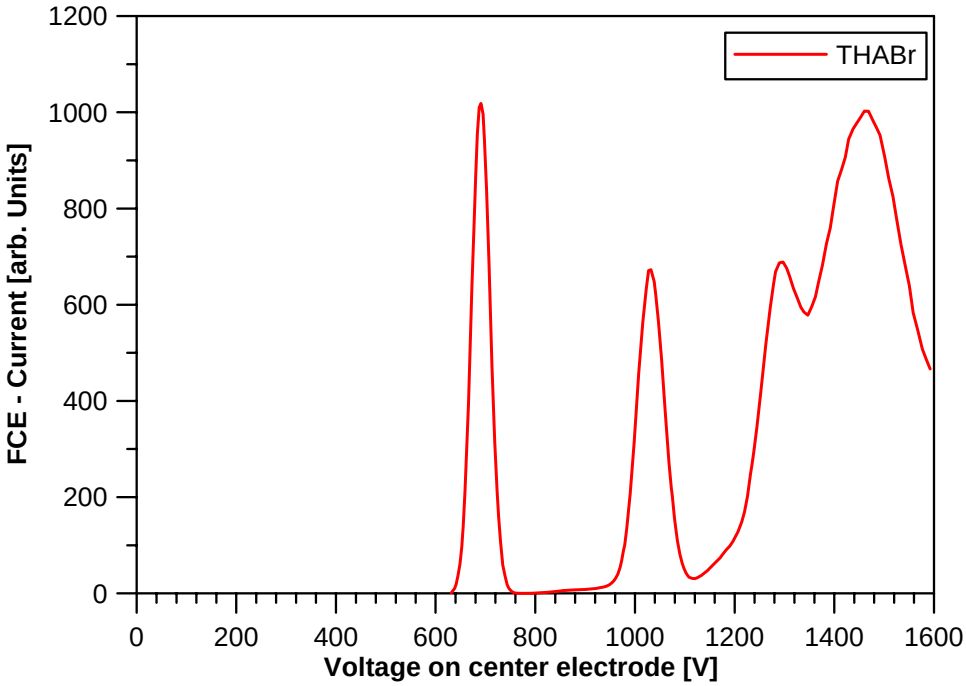

Fig. 3.17 Peak voltage identification for THABr

The single cluster configurations can be identified by their constant mobility or voltage ratio. For the given voltage distribution with well distinguishable peaks at U_1=690V and U_2=1030V and a voltage ratio of $U_2/U_1 \cong 1.49$, the first peak at 690V is associated to the monomer cluster and the second peak to the dimer cluster. With the well known electrical mobilities of those clusters (Ude and

Fernández de la Mora, 2005), every point of the voltage scale can be converted into a corresponding electrical mobility (see also equation [2.74]):

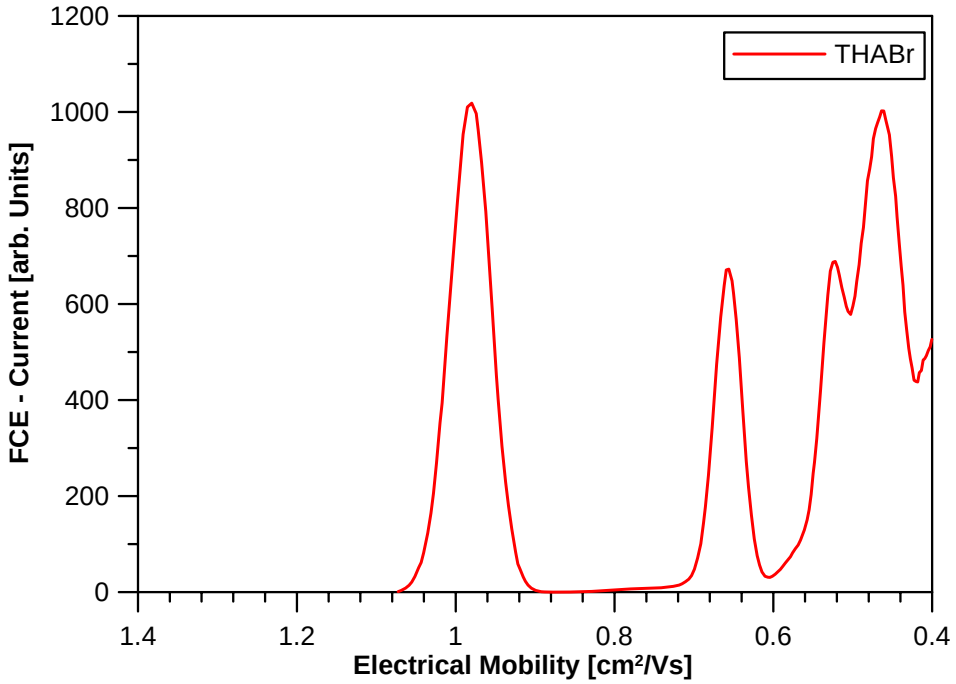

Fig. 3.18 Calibrated mobility distribution of THABr

With the knowledge of the correlation between electrical mobility and particle diameter (equation [2.73]), the mobility distribution can be converted into a size distribution:

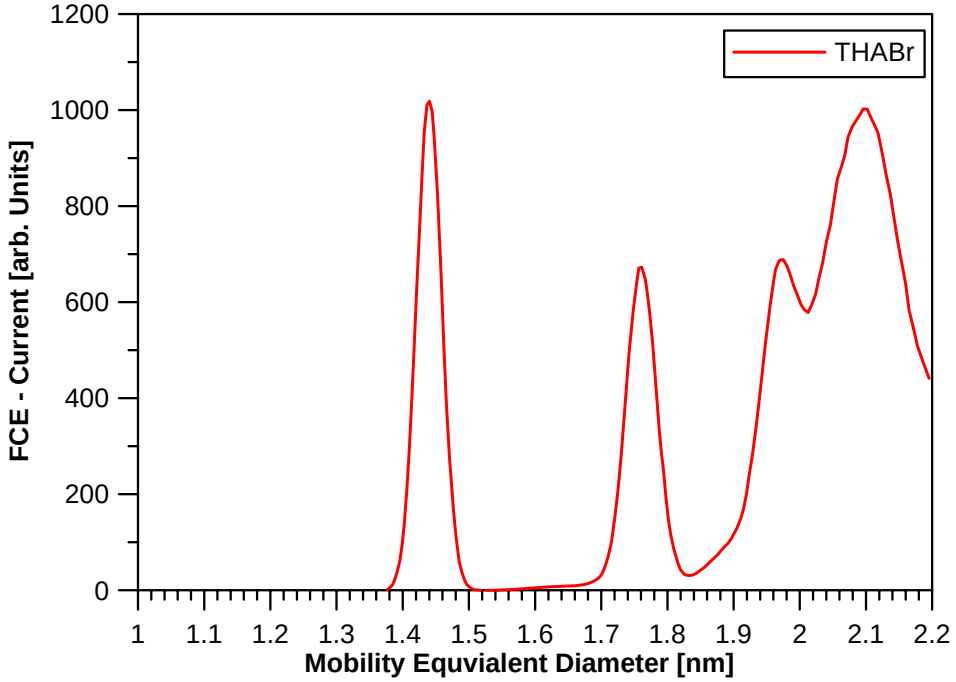

Fig. 3.19 Size distribution of THABr

For constant geometric parameters and also a constant but unknown sheath air flow rate Q_{sh}, the DMA's operational characterization factor K (equation [3.1]) can be determined and the DMA can also be used for the measurement of particles of unknown electrical mobility. This calibration procedure can be performed with any particle species with well known electrical mobility. For the other Tetraalkylammonium halide salts used in this work, the calibration leeds to the size distributions shown in Fig. 3.20 to Fig. 3.22.

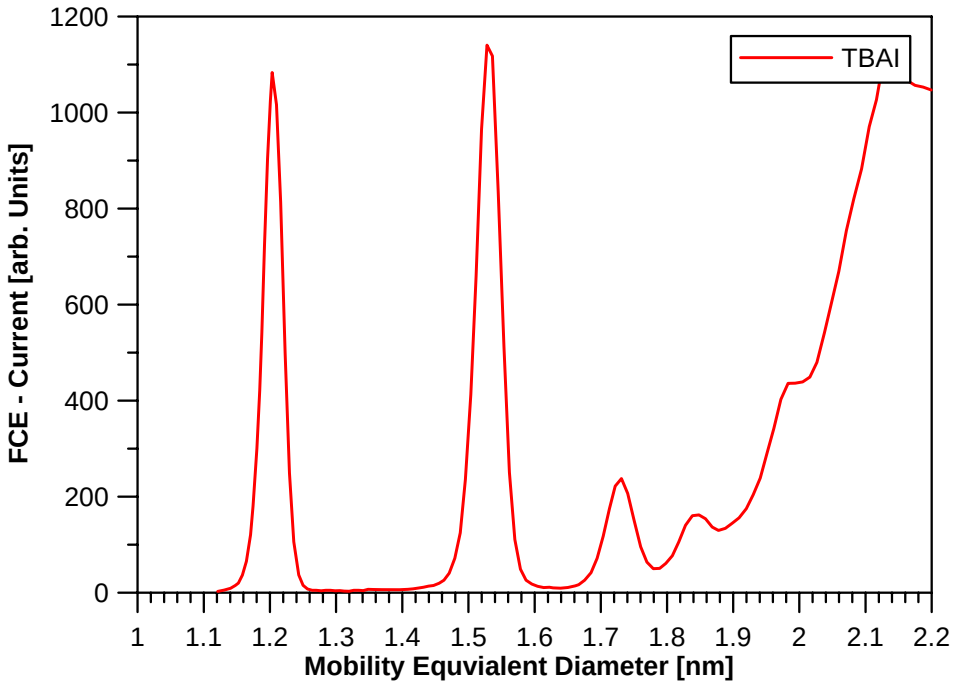

Fig. 3.20 Size distribution of TBAI

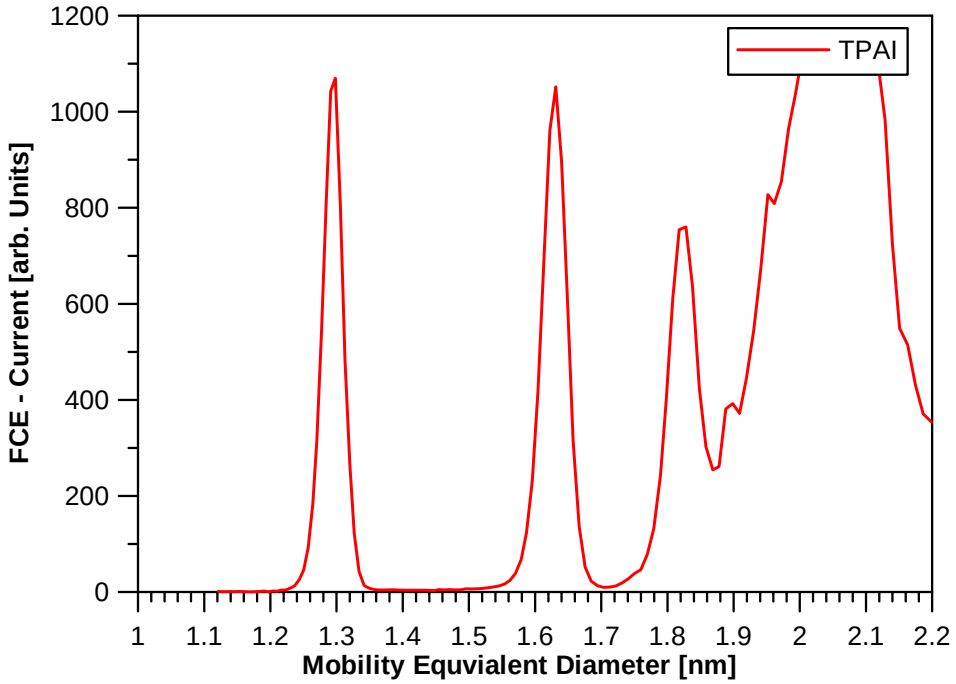

Fig. 3.21 Size distribution of TPAI

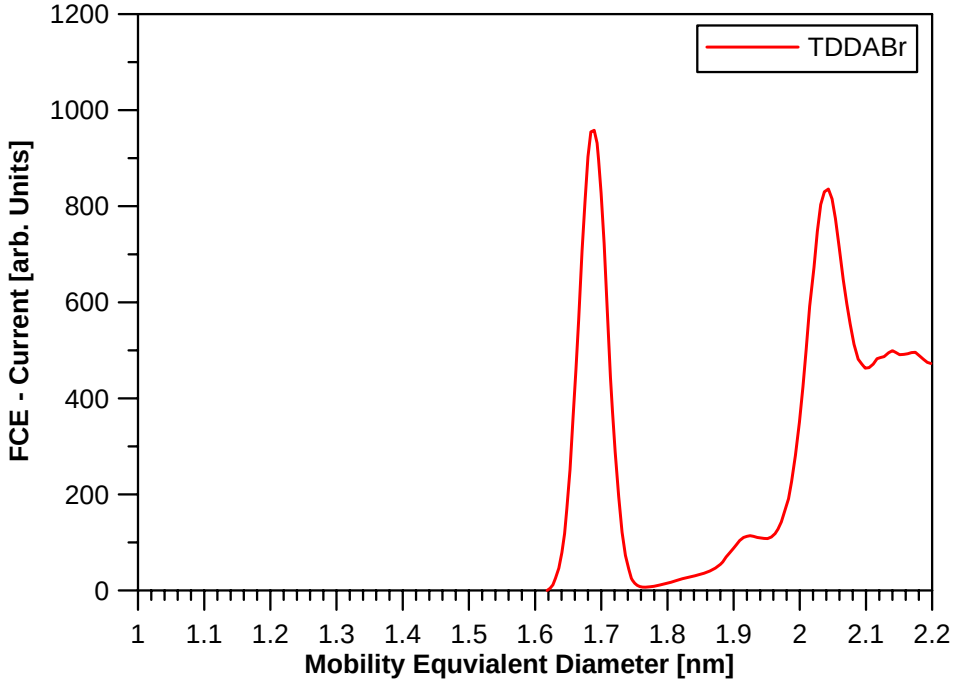

Fig. 3.22 Size distribution of TDDABr

3.3. Performance of the High Resolution UDMA

The first performance test of the new high resolution UDMA was carried out in the "classical" "tandem DMA" setup (Rader and McMurry, 1986) (Fig. 3.23) together with one of the state of the art high resolution DMAs developed by Juan Fernández de la Mora and Michel B. Attoui (R_2 = 33.95 mm; R_1 = 24.95 mm at the aerosol outlet slit, L = 110 mm), which is typically referred as "Attoui DMA". An overview of the "Attoui" DMA can also be found in the work by Heim et al. (2010).

For the evaluation of a DMA's performance or transfer function respectively, a "tandem setup" usually consists of two identical DMAs lined up in series as classifier DMA and analyzer DMA. The classifying DMA extracts one mobility band out of a rather broad size distribution of a test aerosol. By analyzing the monodisperse mobility fraction with the second DMA, the FWHM of the mean mobility can be determined. As the DMAs are supposed to be identical in their geometry and are operated at the same flow conditions, the measured FWHM corresponds to the FWHM of the transfer function about twice as large as for one of the DMAs. The general equations governing a configuration of two DMAs in series were recently summarized by Stolzenburg and McMurry (2008) including different geometric dimensions and operating conditions of the two DMAs as well as the broadening of the transfer function due to particle diffusion.

In the case of using molecular clusters with a well known electrical mobility and a negligible standard deviation as test aerosol (mobility standards), the classifier and analyzer DMA do not need to be identical in their geometric dimensions, nor be operated at the same gas flow conditions, as the aerosols selected by the classifier DMA still can be considered as monomobile. In this setup Fig. 2.23), the classifier DMA ("Attoui DMA") was run at a sheath air flow rate of approximately 1400 L/min provided by a modified vacuum cleaner blower. At that time, the analyzing UDMA wasn't yet equipped with the stainless steel laminarization sponge in the inlet region of the sheath air flow and was operated

at a comparably low sheath air flow of approximately 280 L/min, only using the flow control unit consisting of four high performance membrane pumps.

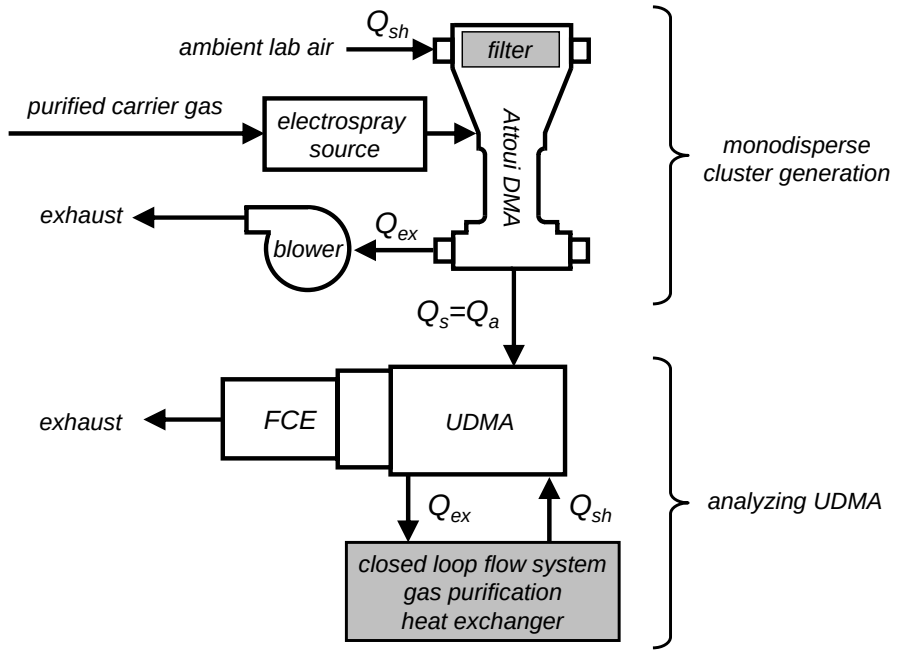

Fig. 3.23 Tandem DMA setup.

The result of this first performance test is given in Fig. 3.24, showing the THABr (see Tab. 3.1) scan of the "Attoui DMA" as a gray line with a relative FWHM of the THABr monomer peak at 1.44nm of 5.7% in mobility-size. For the calibration, the "Attoui DMA" was set to a fixed voltage corresponding to the $A^+(AB)_0$ monomer peak, only allowing these clusters to pass the classifier DMA. Surprisingly, at these inappropriate flow conditions the monodisperse monomer peak analyzed by the UDMA (red line) shows only a slightly broader FWHH of the $A^+(AB)_0$ peak (6.6%), but also a notably asymmetric shape of the analyzed peak.

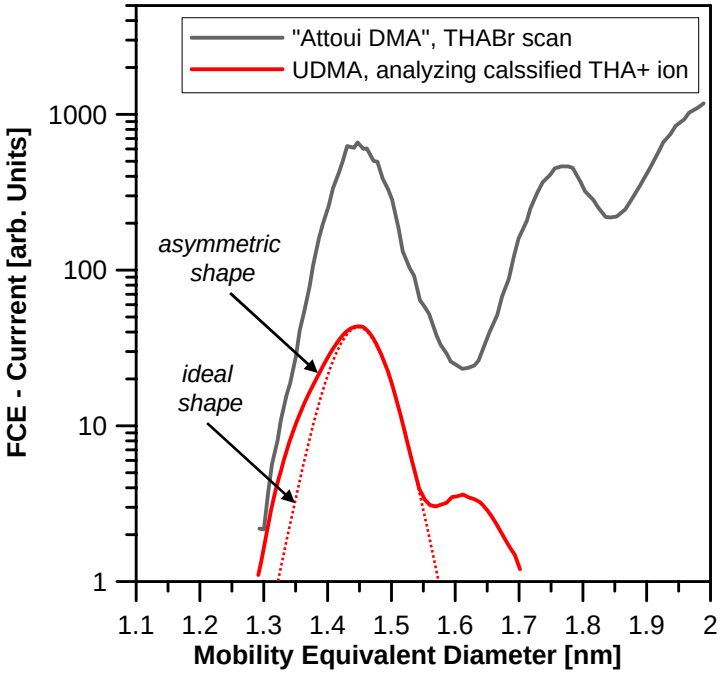

Fig. 3.24 THABr in ADMA – UDMA tandem measurement setup.

This asymmetry indicates poor flow conditions within the UDMA which were found to be caused by turbulences in the sheath air flow, distorting the UDMA's transfer function. Most likely, this swirl is caused by the tangential inlet system of the sheath air flow. As a result, a stainless steel laminarization sponge was installed to minimize the tangential component of the air flow to provide a uniform non turbulent flow of the sheath air, which is in general the most crucial condition for high resolution mobility measurements (e.g. Winklmayr et. al. 1991)

A second, a bit more unconventional, performance test was carried out following the approach of Rosell-Llompart et al. (1996): here, electrospray generated molecular clusters of very well defined mobility and negligible width of their size distribution are fed directly to the UDMA which is analyzing the mobility spectrum (Fig. 3.25).

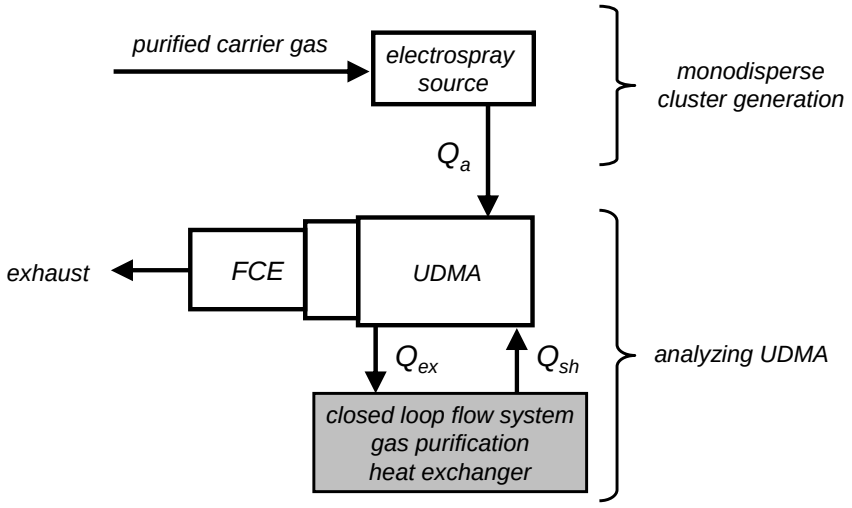

Fig. 3.25 Performance test using monomobile molecular clusters.

Applying this approach one still has to be aware of a potential polydispersity of the molecular clusters. For the clusters used in this work (tetralkylammonium halides), data sets from other DMA performance tests in the literature (Martinez-Lozano and Fernández de la Mora, 2005) indicate a FWHM of considerably less than 1% of the THA^+ monomer cluster. Therfore, the THA^+ cluster can be considered as strictly monomobile and monodisperse. To evaluate the DMA's transfer function, one simply has to determine the width of the peak in the mobility spectrum that corresponds to the THA^+ ion cluster which, because of the high monodispersity of the cluster, is only broadened by the width of the DMA's transfer function.

Fig. 3.26 gives an overview of experimentally determined FWHM's of the UDMA at different flowrate ratios Q_a/Q_{sh} for the tetraheptylammonium bromide monomer (THA^+) and dimer cluster. For these datasets, the sheath air flow rate Q_{sh} varied between 450 L/min and 988 L/min (using the modified vacuum blower as sheath air supply mentioned at the end of section 3.1.). The red dots correspond to the experimentally determined FWHM's of the UDMA transfer function for the THA^+ cluster and the red line to the theoretically predicted diffusion broadened DMA transfer function for the corresponding size of the THA^+ cluster according

to Stolzenburg (1988). The data presented in blue correspond to the dimer cluster $A^+(AB)_1$ of tetraheptylammonium bromide with a size of 1.76nm.

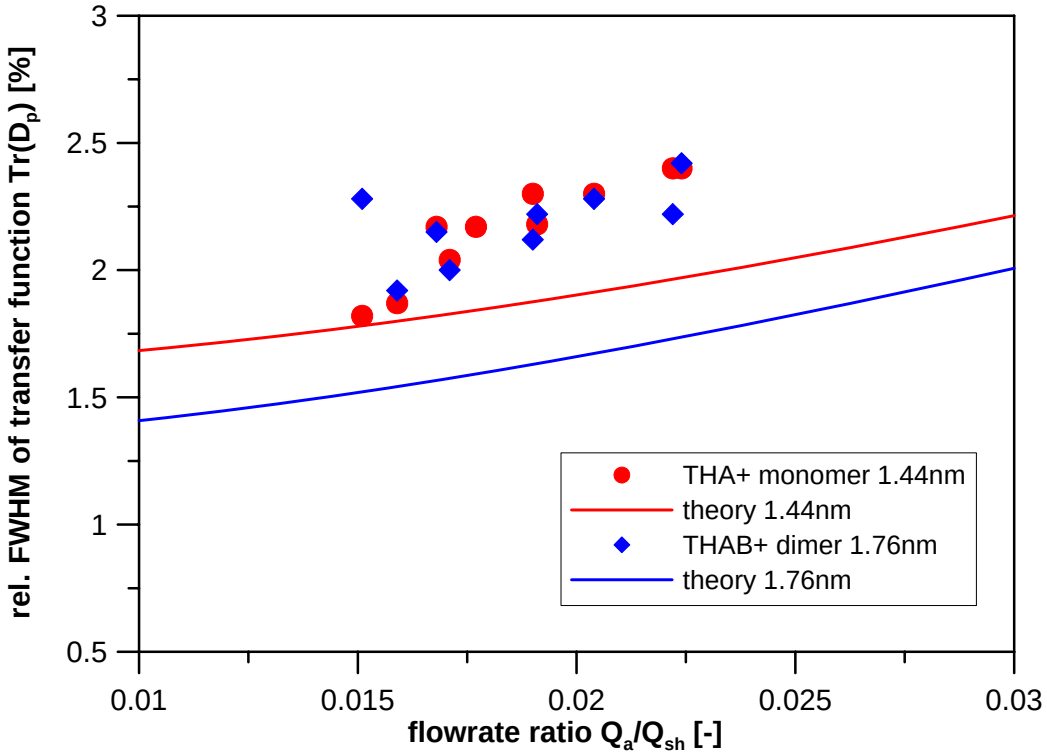

Fig. 3.26 UDMA performance versus cluster diameter

As can be seen, there are significant differences between the experimentally determined data and the theoretical prediction. For the monomer cluster of tetraheptylammonium bromide there is a fairly good agreement between theory and experiment with a worst case difference of 22% and of only 2% in the best case.

However, for the dimer cluster (as it is a larger cluster), where in principle a narrower transfer function would be assumed, the experimental data and the theoretical prediction do not fit at all. The data for the dimer is rather similar to the data that corresponds to the monomer and the experimentally determined width of the transfer function is in worst case more than twice as broad as the calculated diffusion broadening. The only plausible explanation for this observation is that the molecular structure, in other words the molecules'

aspherical shape, is obscuring the mobility classification. Therefore, as already mentioned, one has to be aware that not all molecular ion clusters may considered as monomobile mobility standards.
Still, even the dimer and also n-meres of the commonly used mobility standards are well suited as extremely (but not strictly) monodisperse test aerosols when classified with an appropriated DMA. The UDMA, because of its short classification length, is able to deliver a high resolution power of about 2% relative FWHM at 1.44nm at rather low flow rates (compared to other high resolution instrumentation) to be used as an excellent tool for the analysis and generation of nanometer sized particles.

As the UDMA is able to generate highly monodisperse aerosol, one of its first applications was during a joint study on heterogeneous nucleation where classified molecular ions produced by an ^{241}Am neutralizer and tungsten oxide nano-particles served as seed particles for the experiments. This work was already published by Winkler et al. (2008); the original article and its supplementary online material are attached to this thesis as Appendix B1 and B2. In these experiments, supersaturated *n*-propanol vapour was allowed to condense on the nearly monodisperse aerosol particles and clusters. The vapour supersaturation is achieved by an adiabatic expansion in an expansion condensation particle counter (CPC) type, computer controlled and thermostatted expansion chamber called the Size Analyzing Nuclei Counter (SANC; Wagner et al. 2003). The seed particles induce heterogeneous vapour nucleation which leads to the formation and subsequent growth of liquid droplets. By using the Constant-Angle Mie Scattering (CAMS) detection method (Wagner, 1985) the radius and number concentration of the growing droplets can be determined simultaneously with high time resolution.
This way, the SANC/CAMS method allows the precise determination of heterogeneous nucleation probability curves (ratio of concentrations of activated particles and the total particle number concentration at a corresponding saturation ratio).

Since the initial size distribution of the seed particles strongly influences the slope of the heterogeneous nucleation probability curves, the highly monodisperse particles classified by the UDMA are a crucial prerequisite for the precise determination of the slope of the heterogeneous nucleation probability curves and a correct interpretation of the nucleation process.

As already mentioned, in the work by Winkler et al. (2008) not only charged particles, but also molecular ions, evolving from the ^{241}Am charger were used as seed "particles" for the nucleation experiments. To gain more detail about the size distribution of these ions, the following chapter 4 focuses on the experimental determination of the properties of the ionic molecular clusters produced by the ionizing radiation in an ^{241}Am charger for different operating conditions.

4. Properties of Charger generated Ionic Molecular Clusters

The properties of molecular clusters are of interest for many scientific fields, such as biochemistry and bioengineering, fundamental investigations on heterogeneous as well as homogeneous nucleation, studies related to particle formation in the atmosphere and the manipulation of the properties of condensed matter. For sure, this list can be expanded by many more fields of application.

This chapter will concentrate on the experimental determination of the properties of the ionic molecules that are responsible for the charging of aerosol particles in a neutralizer. High resolution mobility spectrometry allows a precise determination of the ions' electrical mobility. The ions masses can be approximated by an empirical mass-mobility relationship. Both parameters, mobility and mass, are the only necessary input parameters for Fuchs' charging theory which forms the fundamental basis for the applicability of the EMS method for airborne particles ranging from less than 1nm to about 1μm in diameter.

The electrical mobility spectrometry relies on a well defined charging of aerosol particles, or a well defined charging state on the particles respectively. As a stable saturation charging state on the aerosol cannot be assumed a priori, charging devices, to be more precisely neutralizers, have to be used to produce a large number of ions to ensure the condition of a stable saturation charging state on the particles.

No matter what charging mechanism is governing the actual charging on the particles, in all cases, an ion source ensures the ionization of the carrier gas molecules to form primary ions. These primary ions will combine with polar molecules (mostly water) present in the carrier gas to form larger clusters.

There is an intense scientific discussion on the actual nature of the clusters produced in an aerosol charger. In the literature (Cabane and Playe, 1980; Eisele

and Tanner, 1990; Nagato et al., 2006), NO_3^- HNO_3 and HCO_3^- HNO_3 as well as hydrates of the form NO_2^- $(H_2O)_n$, NO_3^- $(H_2O)_n$, NO_3^- HNO_3 $(H_2O)_n$ and HCO_3^- HNO_3 $(H_2O)_n$ are proposed and observed configurations for the ionic clusters of negative polarity.

For positive polarity, $(H_3O)^+$ $(H_2O)_n$, and NH_4^+ $(H_2O)_n$ are suggested to be the most abundant cluster species produced in air (Huertas at al., 1971, Parts and Luts, 2004, Nagato et al., 1999, Eisele and Tanner 1990).
In aerosols science, the most commonly used ionizers rely on radioactive sources, corona discharges, UV radiation and more recently on soft x-ray photo ionizers. Radioactive sources, corona discharge as well as the soft x-ray ionizers bear the advantage of diffusion charging which is almost independent upon aerosol material. In contrast, the charging mechanism based on UV radiation strongly depends upon particle composition and is therefore only suitable for very specific investigations.
To ensure a vast versatility for the charging device, in this work, almost exclusively an aerosol charger purchased from "tapcon & analysesysteme", equipped with an ^{241}Am source was used and investigated. ^{241}Am decays by alpha emission with an energy of 5.5MeV and a small by-product of gamma rays to ^{237}Np with a half live of about 2 million years. The most evident advantage of ^{241}Am chargers, compared to other radioactive chargers equipped with ^{210}Po or ^{85}Kr, is its long half life of 432.2 years (^{210}Po: 138.2 days, ^{85}Kr: 10.8 years). Therefore, a decrease of ion production can be almost completely neglected within our comparably short human lifetime.

A schematic cross section of the "tapcon & analysesysteme" ^{241}Am charger is shown in Fig. 4.1.

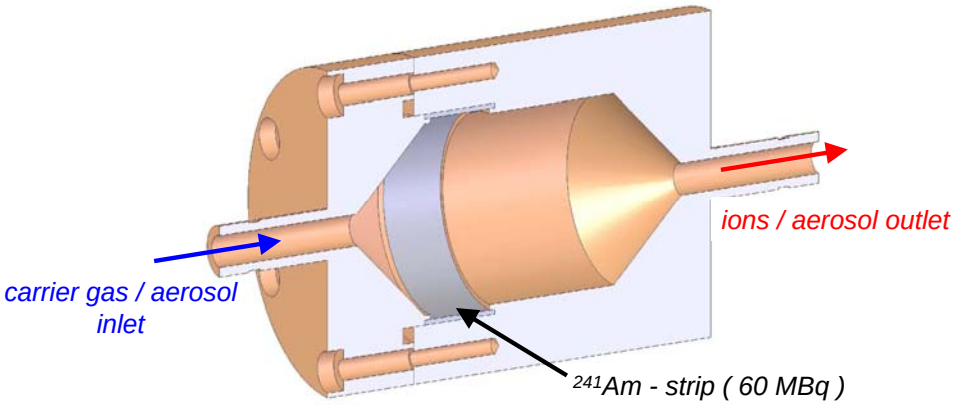

Fig. 4.1 Schematic cross section of the "tapcon & analysesysteme" ^{241}Am charger

The radioactive material is embedded in a gold matrix coated on a strip that is housed in a massive stainless steel body. The ^{241}Am source has an activity of 60 MBq - the only major drawback in the use of ^{241}Am as this activity is far above the permitted limit of 100 kBq and requires special permits for handling and transport.

However, this high activity is necessary to ensure a sufficient ion production to meet the prerequisite of a $N \cdot t$ product (N is the number of ions produced be the ionizing source per unit time and t the residence time of particles in the charging chamber) of approximately 10^7 (Liu and Pui 1974).

4.1. Ion Measurements in Different Gases

For the investigation of ion molecules in the size range around 1nm, high resolution mobility measurements are necessary to separate individual ion species. Additionally, the high flow DMAs, with a sheath air flow rate above 500 L/min, typically used for high resolution measurements, reduce the residence time of the clusters in the DMA's classification channel and therefore minimize diffusion losses – a crucial feature for a proper detection of molecular ions.

Although the important parameter of interest are the ions' electrical mobilities, and although to the DMA classifies the clusters according to their electrical

mobility, in this work all mobility distributions will be converted into size distributions according to Milikan's relationship given in equation [2.73]. Of course, correlating a molecular cluster with a diameter is worthy of discussion, but as we are speaking of the electrical mobility equivalent diameter – a commonly used concept in aerosol science - as defined in section 2.6, this conversion still seems to be reasonable as it allows a direct comparison of the small cluster size to commonly known sizes of aerosol particles.

The high resolution DMA used in this work was already described in detail in chapter 3. The so called "UDMA" achieves a resolution of 2.5% relative FWHM of its transfer function at 1.4nm mobility equivalent diameter at a sheath air flow rate of approximately 700 L/min. With these specifications, the UDMA is a well qualified tool for the precise determination of the electrical mobility of airborne ionic molecular clusters.
For the operation of the UDMA, a closed loop arrangement for sheath air and excess air is used to prevent contaminations of the sheath air that would be possible when using the open loop configuration (sheath air is drawn in from the ambient lab air and not recycled) often used in high flow high resolution mobility spectrometry. For the measurements, a comparably high "aerosol" flow rate of 17 L/min was chosen to catch the ions early after their initial formation (reducing their residence time in the charger) and to reduce diffusion losses on the way to the DMA.

In aerosol science, air will be the most important carrier gas for the investigation of the properties of newly produced ionic molecules. However, to study the influence of the purity and chemical composition of the carrier gas, additionally to carefully purified pressurized air, high grade bottled gases were led through the charger. For the experiments, synthetic air 4.6, argon 4.6 and nitrogen 4.6 were in use, where 4.6 means that the abundance of impurities is less than 0.004%, resulting in an overall purity of 99.996%. Therefore, these gases can be considered as dry too, as the amount of water vapour is specified to less than 0.5ppm.

The experimental setup is shown in Fig. 4.2. Basically, the carrier gas (purified pressurized air or one of the bottled gases) is led through the ^{241}Am charger which is mounted directly in front of the high resolution UDMA. The ion clusters produced by the ionizing radiation immediately enter the UMDA for classification and are detected by a fast Faraday Cup Electrometer (FCE), an updated version of the one described by Winklmayr et al (1991), with a response time of typically 100ms.

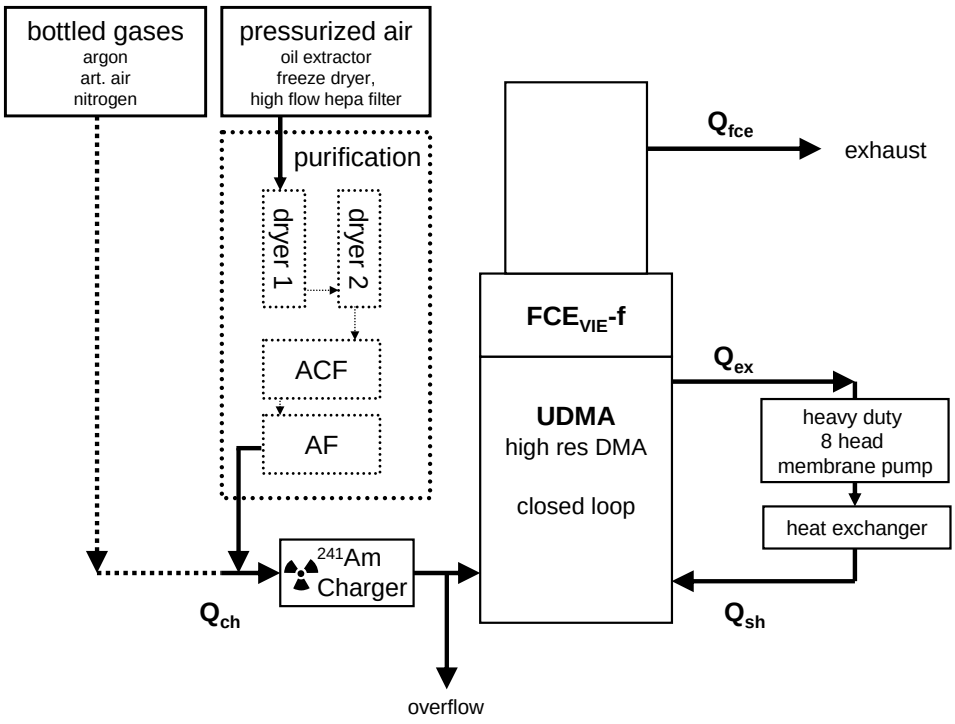

Fig. 4.2 Experimental setup for different carrier gases.

For the purification of the pressurized air, the air supplied by a compressor is first led through an oil extractor, for pre-drying through a freeze dryer and thirdly through a high flow HEPA (high efficiency particulate air) filter. In a second step, at least two silica gel diffusion dryers, one active carbon filter (ACF) and one HEPA filter (AF), ensure a thorough purification of the carrier gas before entering the neutralizer.

As a first result, Fig. 4.3 shows the size distribution of positively charged ions produced in purified pressurized air by the ionizing radiation in the charger.

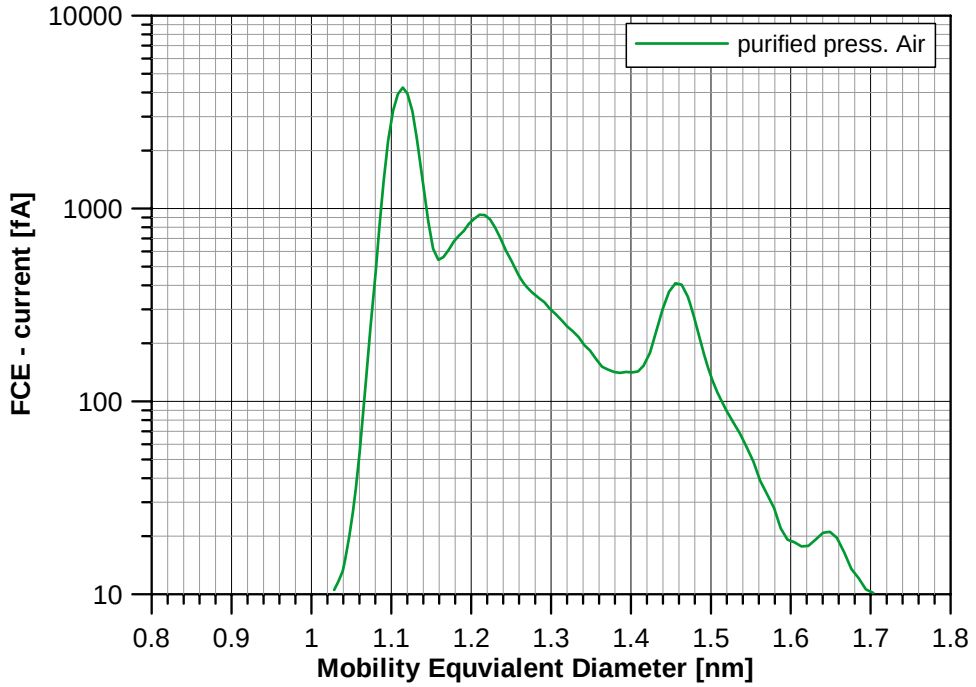

Fig. 4.3 Size distribution of positive ions produced in purified pressurized air.

The size spectrum is dominated by a peak close to 1.12nm, at least two additional individual peaks can be found at 1.22nm and 1.46nm. With the high resolution power of the UDMA, every separated peak can be associated with a specific ion molecule species. Section 4.5 will concentrate on the identification of possible molecular species.

However, when using synthetic air, the size spectrum changes dramatically, as shown in Fig. 4.4.

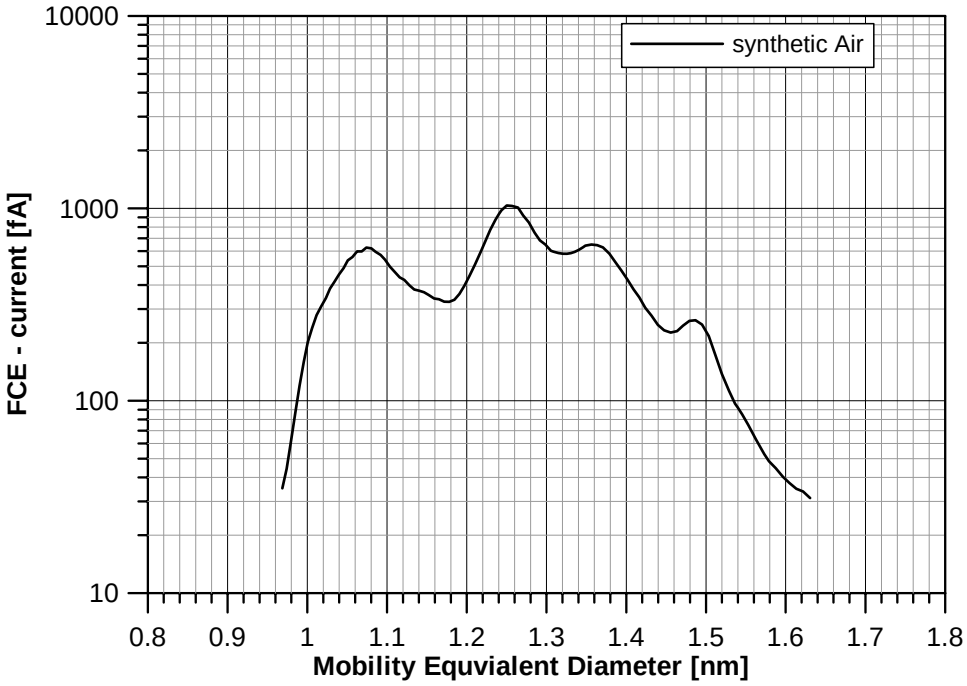

Fig. 4.4 Size distribution of positive ions produced in synthetic air.

Completely different to the measurements in purified pressurized air, the positive ions produced in synthetic air (supplied from a gas cylinder – therefore supposed to be of very high purity) show almost no predominant cluster size. Compared to Fig. 4.3, the peaks are much broader, indicating the presence of many cluster species with similar electrical mobility. Therefore, it seems that this unpronounced size distribution is caused by a higher abundance of impurities in synthetic air than in purified pressurized air.

For high grade nitrogen (Fig. 4.5), almost no difference can be found to synthetic air as carrier gas. Neither a specific ion molecule becomes predominant, nor can a well pronounced pattern be found in the size distribution.

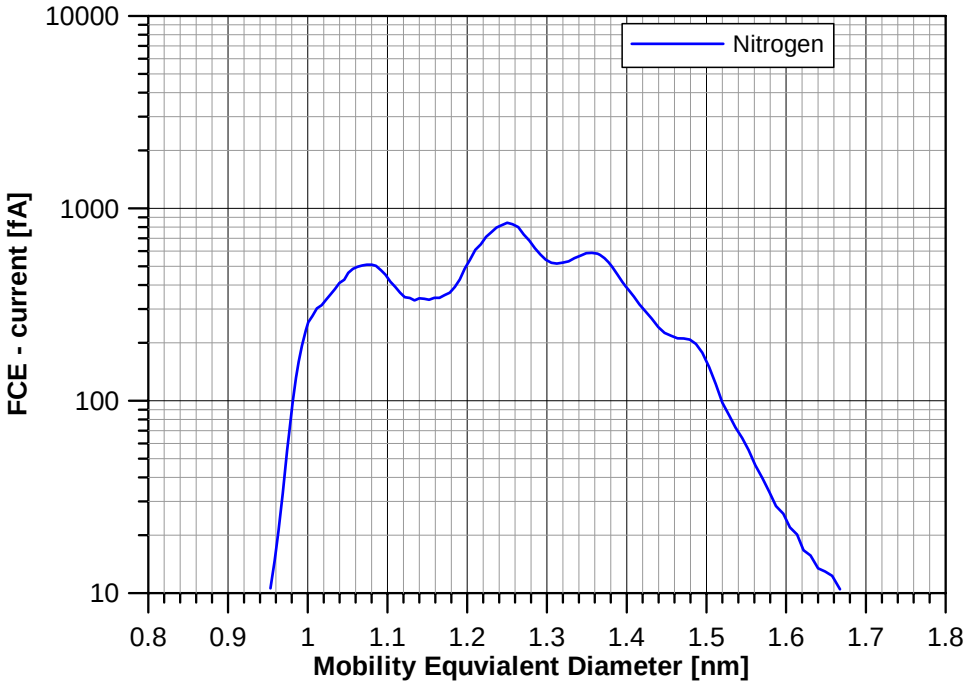

Fig. 4.5 Size distribution of positive ions produced in nitrogen.

Although argon, a noble gas, has completely different properties than air or nitrogen, again, the size distribution of positively charged ions produced in argon (Fig. 4.6) is more or less the same as the one that can be found for synthetic air and nitrogen.

Fig. 4.6 Size distribution of positive ions produced in argon.

To summarize and compare the first results, Fig. 4.7 shows the size distributions of positive molecular ions produced in different gases.

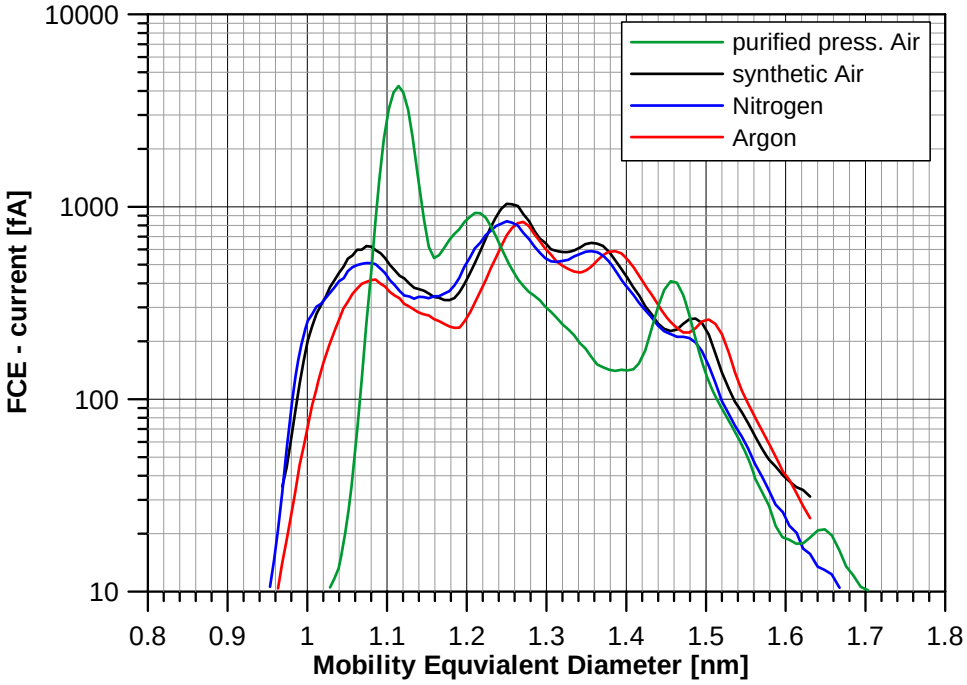

Fig. 4.7 Comparison of the size distribution of positive ions produced in different gases.

Of course, the same experiments where performed with a positive voltage on the UDMA centre rod, yielding the size distribution of negatively charged molecular ions.

Fig. 4.8 starts with the size distribution of negative ions produced in purified pressurized air. Compared to positive ions, the produced negative ions generally appear at smaller cluster sizes. Whereas for positive ions in pressurized air the smallest diameter was found to be around 1.1nm, the minimum cluster size for negative ions is found to be below 1nm at approximately 0.98nm. This peak clearly dominates the whole size spectrum. Additional cluster peaks – lower in their concentration compared to the 0.98nm main peak- are found as a shoulder on the right hand side alongside the main peak and again more pronounced at 1.21nm.

For negative ions, the size spectra of ions produced in purified pressurized air (Fig. 4.8), synthetic air (Fig. 4.9), nitrogen (Fig. 4.10) and argon (Fig. 4.11) again show quite different patterns.

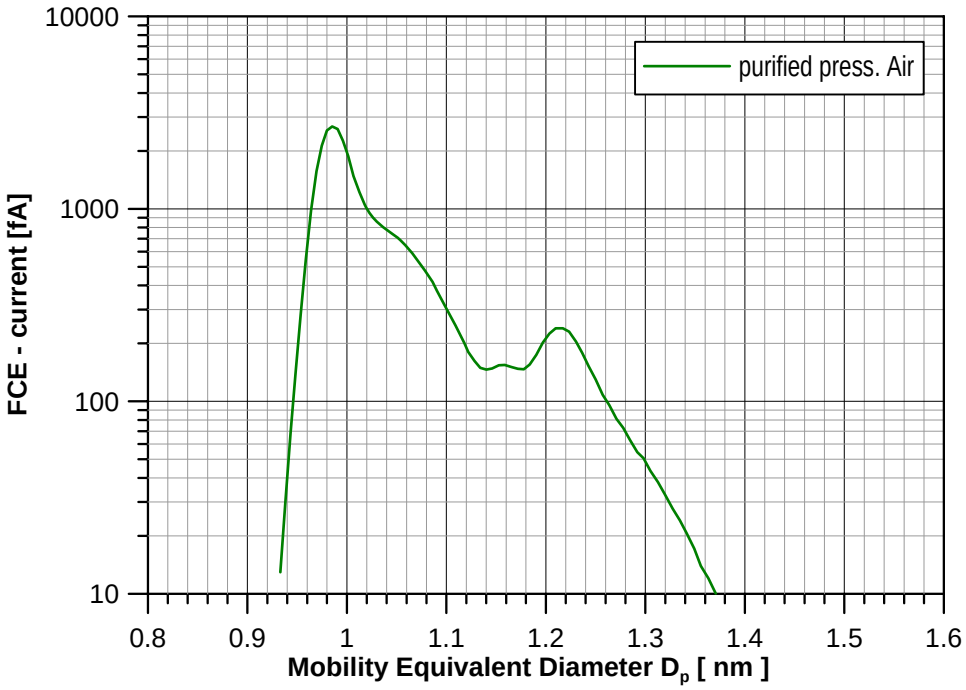

Fig. 4.8 Size distribution of negative ions produced in purified pressurized air.

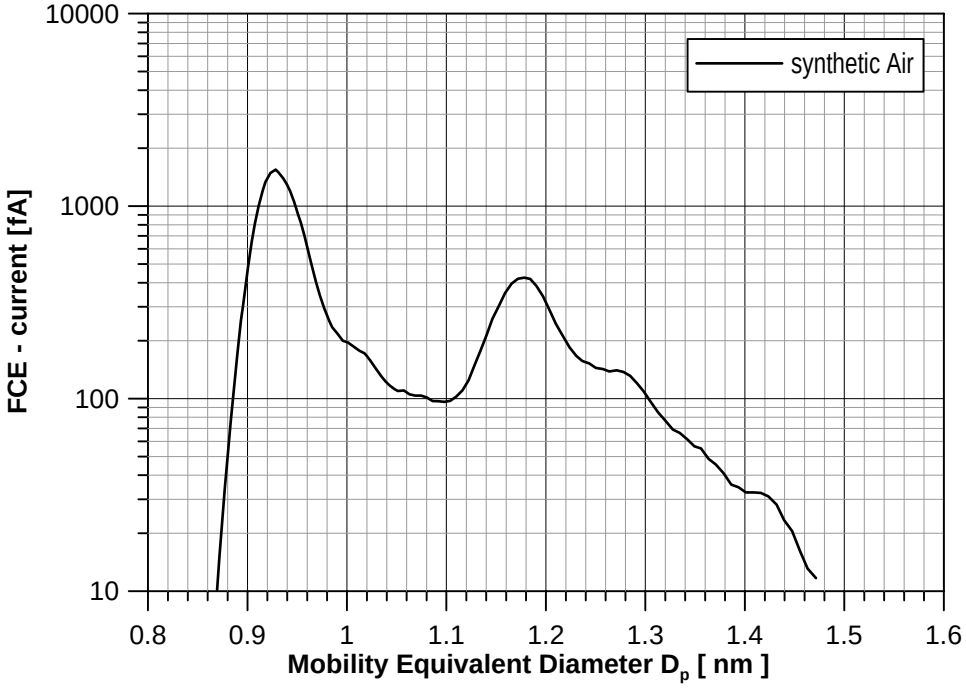

Fig. 4.9 Size distribution of negative ions produced in synthetic air

For synthetic air, obtained directly from the gas cylinder, it seems that the whole spectrum is shifted towards smaller clusters sizes compared to purified pressurized air. Additionally, the abundance of clusters situated between 1 and 1.1nm is about a factor of 4 lower than for pressurized air.

The production of ions in nitrogen seems to behave similar, by showing a profile where the produced ions form a bimodal size distribution with peaks at about 0.94nm and 1.18nm. For argon, the ion production works somehow differently, as the smallest cluster size can be found below 0.9nm.

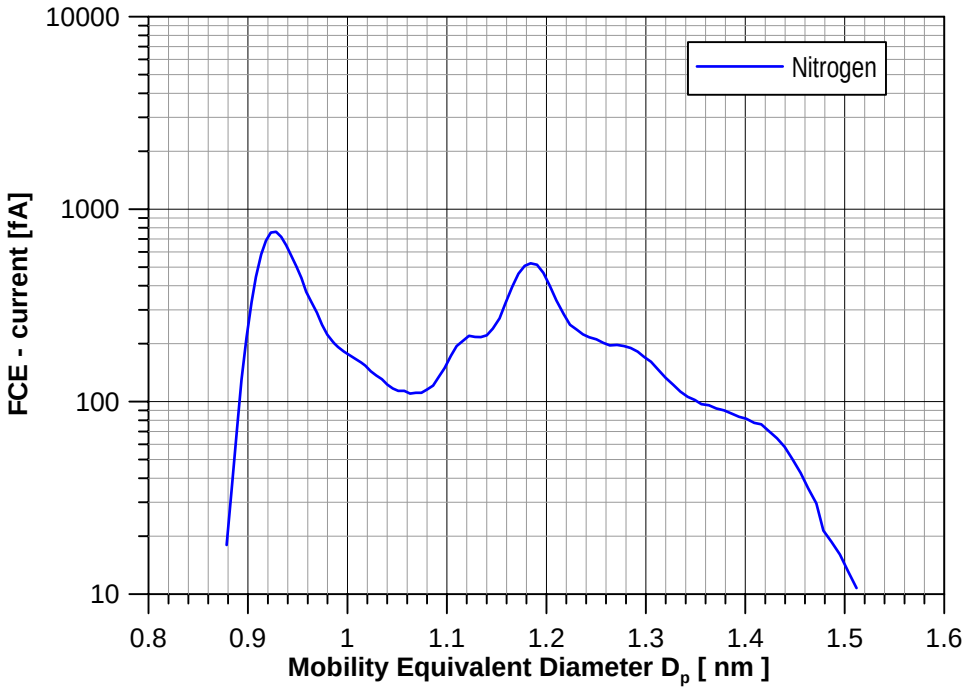

Fig. 4.10 Size distribution of negative ions produced in nitrogen

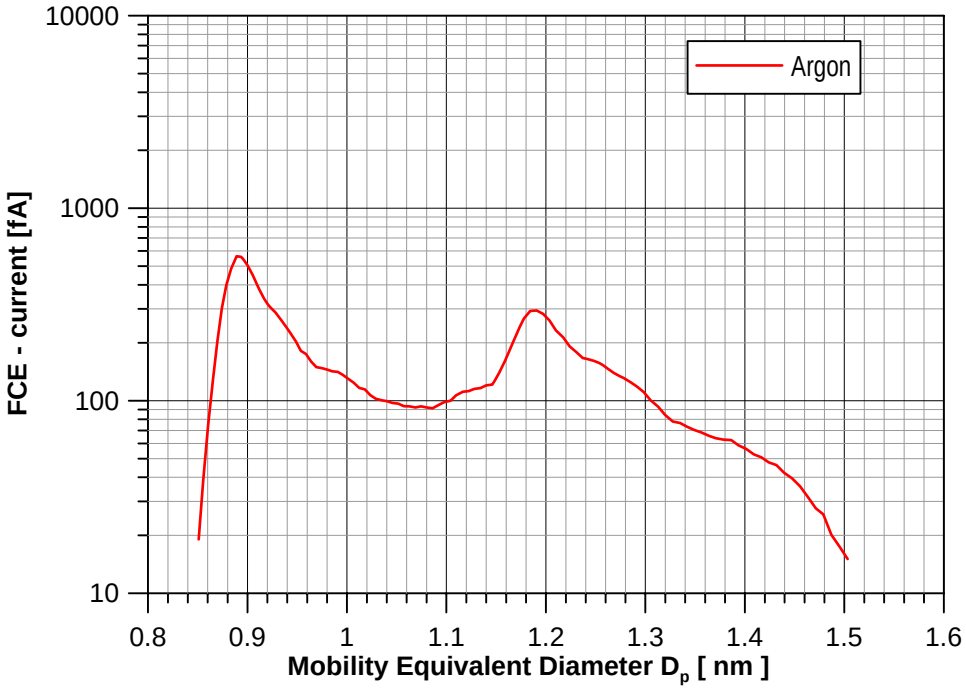

Fig. 4.11 Size distribution of negative ions produced in argon

To study whether this different pattern of the size distribution of ions produced in the different gases is caused by the chemical composition of the carrier gas or by impurities, additional experiments were performed where the bottled gases were purified the same way as the pressurized air supplied by a compressor and led through at least 2 silica gel diffusion driers, an active carbon filter and an absolute filter.

The results of this purification are shown in Fig. 4.12 to Fig. 4.14 for different purification grades. As can be seen clearly, by treating the bottled gases the same way as the pressurized air, the size distributions of ions produced in completely different carrier gases become more or less the same. Generally, the use of HEPA filters (AF) and driers (Dr) shift the size distribution towards larger cluster sizes, but especially the use of active carbon filters (AC) alters the pattern of the size spectra in such a way, that they become almost identical to the spectra measured in purified pressurized air. Only the main peak for ions produced in Argon is slightly shifted towards smaller cluster sizes.

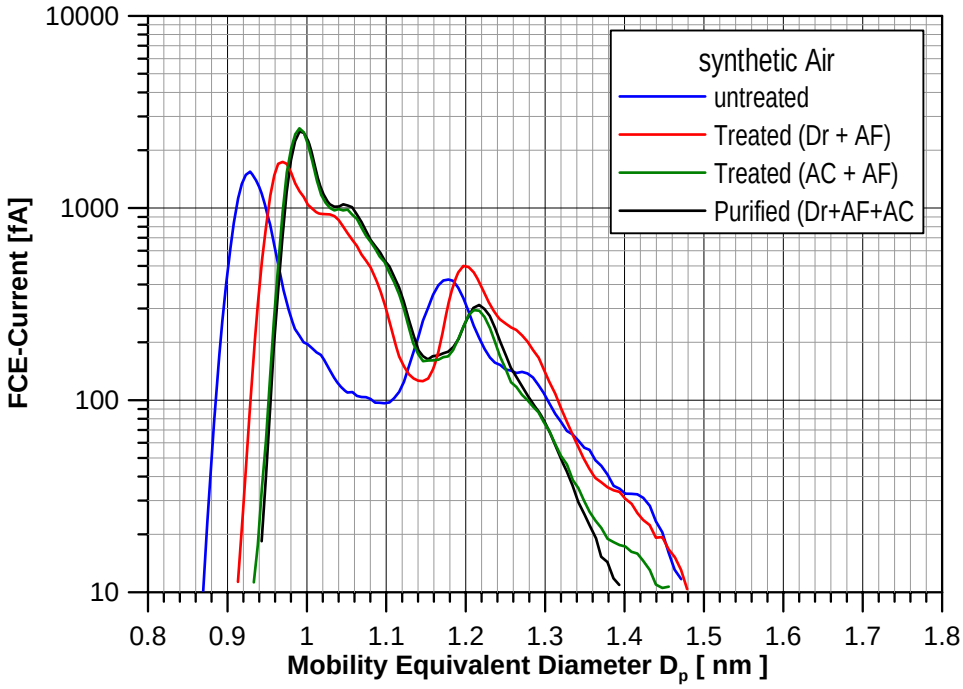

Fig. 4.12 Size distribution of negative ions produced in purified synthetic air

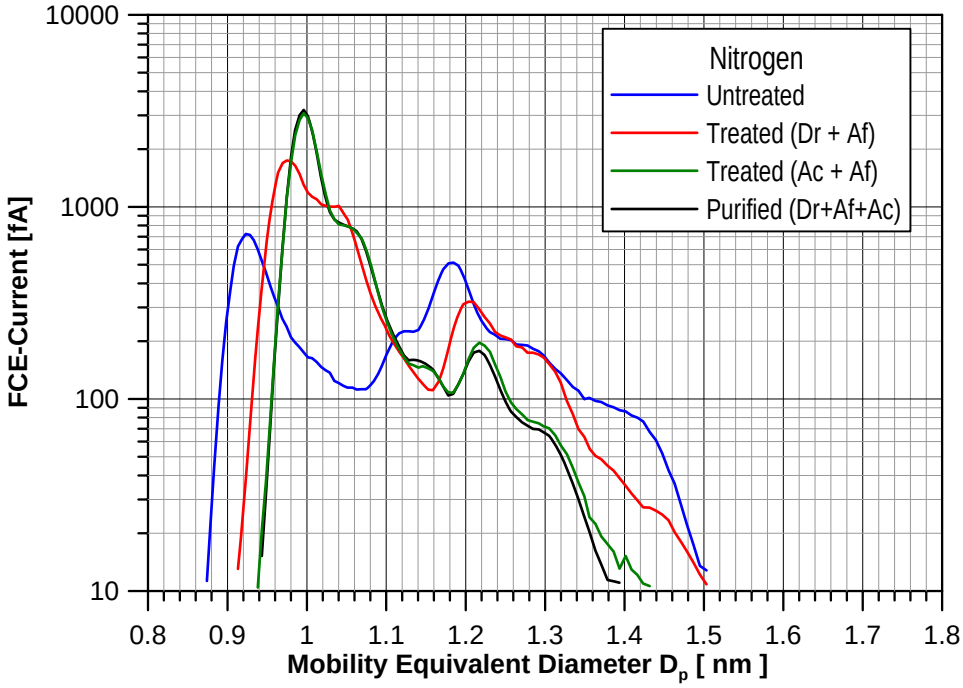

Fig. 4.13 Size distribution of negative ions produced in purified nitrogen

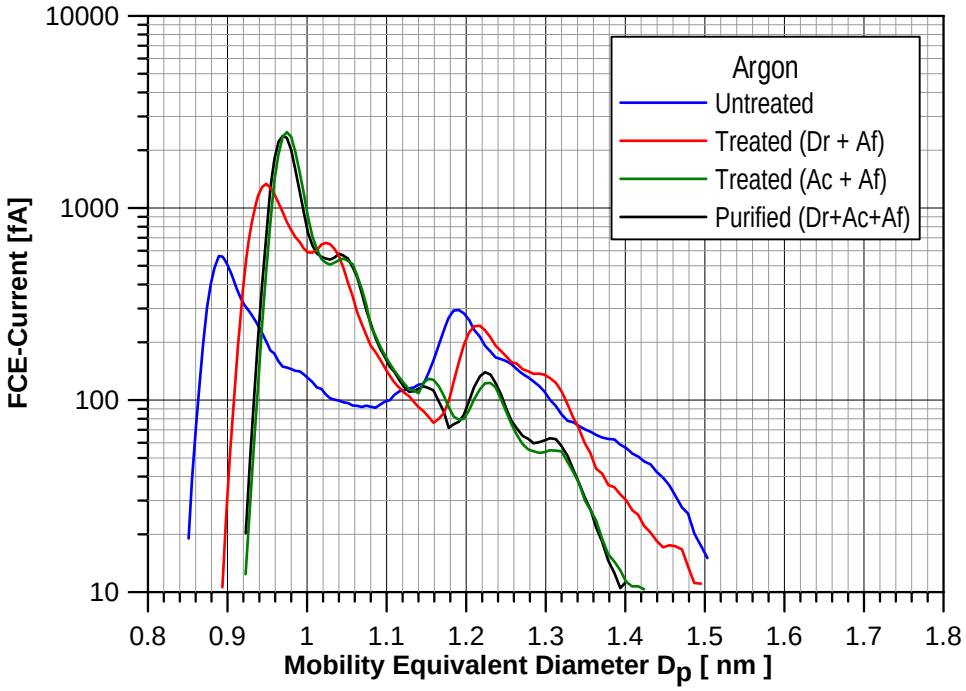

Fig. 4.14 Size distribution of negative ions produced in purified argon

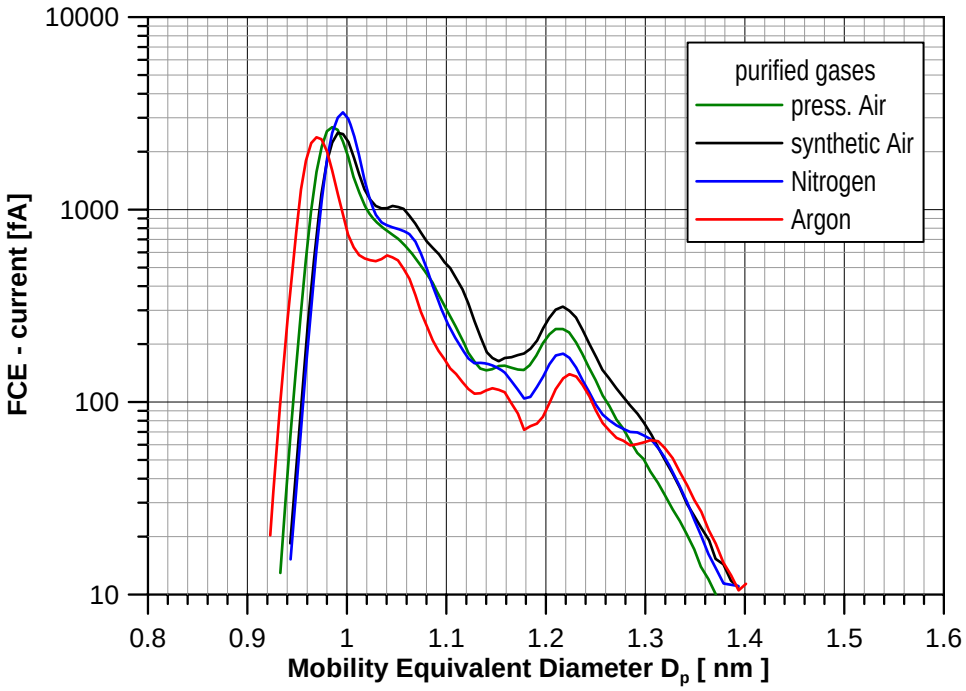

Fig. 4.15 Size distributions of negative ions produced in purified gases.

These experiments showed that even “high grade” labelled bottles gases contain enough impurities to promote the formation of various molecular ions with similar electrical mobility, resulting in an unpronounced and unclear size distribution. Therfore, the experiments of the measurement of the size distribution of molecular ions produced by the ionizing radiation in the charger further allow an estimation of the purity of the specific carrier gas in use.
Although the initially measured size distributions, using various carrier gases, are completely different, the size spectra again become the same or at least very similar when the gases are treated / purified the same way.

4.2. Ion Measurements at Clean and Dry Conditions

The previous experiments have shown that already small amounts of impurities present in the carrier gas have a strong influence on the mobility of the ions produced in the charger. Therefore, section 4.2 will focus on the determination of the ions’ mobilities at the cleanest and driest possible carrier gas and air duct conditions. The experiments in 4.1 have shown that no major differences in the produced cluster species were observed by using different carrier gases. Therefore only pressurized air will be considered in the following.

Similar to the experimental setup used for the investigations concentrating on different gases, pressurized air supplied by a compressor is cleaned in a first step by means of an oil extractor, freeze drier and high flow HEPA filter and in a second step purified by two ultra fine active carbon filters (ACF_{fine}), a standard active carbon filter (ACF), at least three silica gel diffusion driers and a HEPA filter (AF). This way, the pressurized air entering the ^{241}Am charger can be considered as ultra pure and dry, with a relative humidity (r.H.) of approximately 1%, close to the detection limit of the used digital humidity sensors (Sensirion, SHT75) with an accuracy of 1.8 % r.H. and a repeatability of 0.1 % r.H.

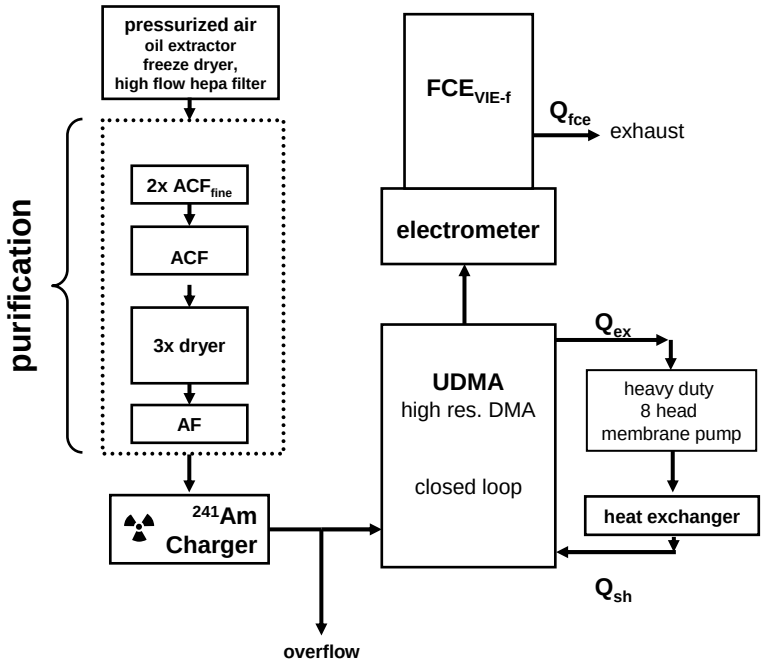

Fig. 4.16 Experimental setup for clean and dry carrier gas conditions, exclusively using stainless steel or PTFE tubing

To avoid any contaminants caused by evaporations of volatile substances from the inner surface of different tubing materials, only air ducts of stainless steel or PTFE are in use. To ensure clean conditions for the whole system, the charger and air ducts were flushed with the purified and dried air as described above for a time period of 3 weeks - 7 days a week and 24 hours a day – before the start of the experiments. Only this way the influence of contaminants and trace gases led through the charger housing in the past can be reduced to a minimum.

The ionic clusters produced in the charger are again analyzed according to their electrical mobility immediately after their generation in the Vienna type high resolution UDMA with a fast Faraday Cup electrometer as sensor.
At these conditions, Fig. 4.17 shows a very typical size distribution of positively charged ionic clusters produced in clean and dry pressurized air.

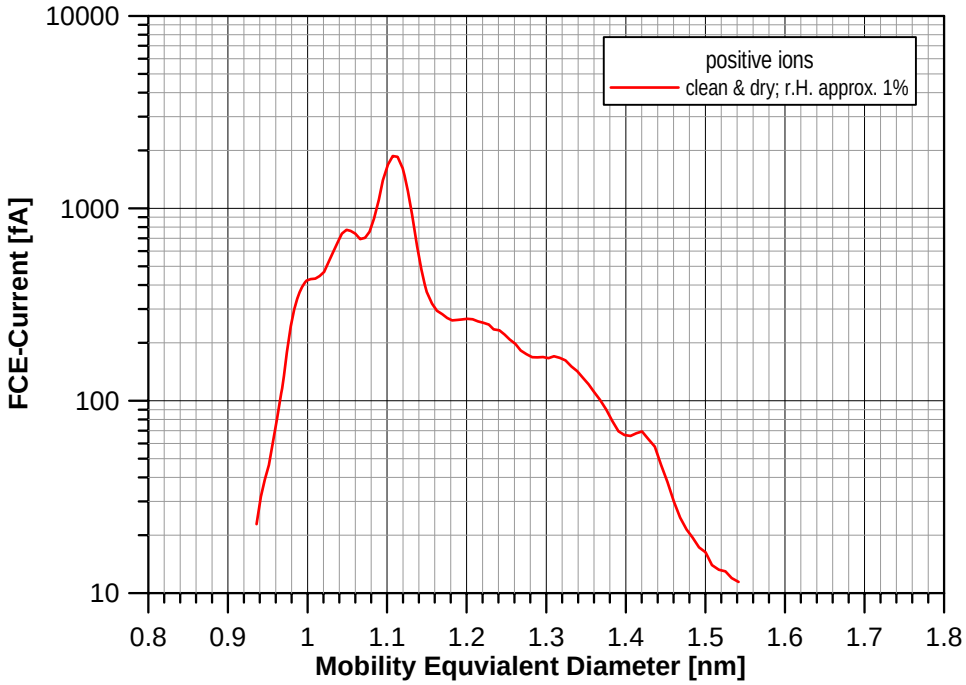

Fig. 4.17 Typical size spectrum of positive ions produced in clean and dry purified air.

Similar to Fig. 4.3 in section 4.1, the size spectrum is dominated by a "main" peak at 1.11nm, but different to the measurement plotted in Fig. 4.3, for very clean conditions, there are at least two additional separate peaks at smaller clusters sizes at 1.00nm and 1.05nm and some larger, not that well pronounced peaks at a.1.21nm, 1.32nm and 1.42nm.

The same measurements were performed for positive DMA inner electrode polarity, yielding the size spectrum of negatively charged air ions – presented in Fig. 4.18. Here, again a sort of "main peak" can be found but at smaller sizes compared to the positive ions. This main peak seems to consist of at least two cluster species with sizes very closely situated to each other at 0.96nm and 0.98nm. At larger sizes, rather broad peaks can be found at 1.05, 1.22 and 1.31nm. But as Fig. 4.18 is plotted with a logarithmic size scale for the FCE current (proportional to the ion cluster concentration), the main peak at 0.96 or 0.98 nm almost exclusively dominates the size spectrum for negatively charged clusters produced in air.

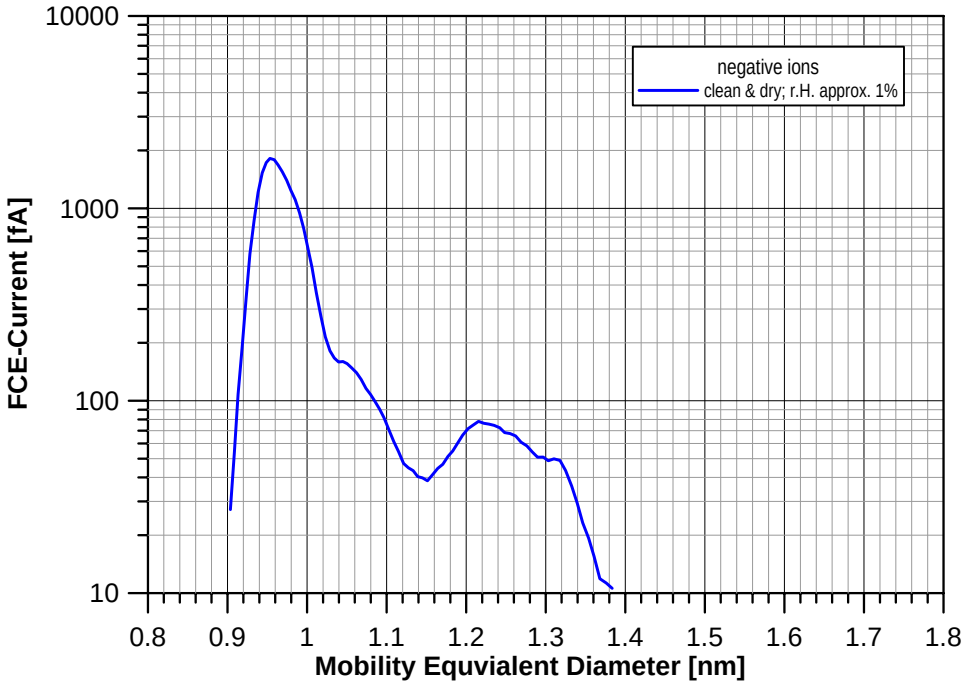

Fig. 4.18 Typical size spectrum of negative ions produced in clean and dry purified air.

4.3. Ion Measurements using Alternative Ionizing Methods

In the last years, the regulations of using radioactive material have become more and more restrictive. As a result, it is not only difficult and time demanding to organize the necessary permissions from the authorities, but almost impossible to move with the radioactive source from its certified application site. Sometimes, moving within buildings is almost considered as crime. Field campaigns and international cooperations are very strongly impaired by these regulations.

The main problem of radioactive sources is that they cannot be switched off and their radiation always bears a potential hazard. Therefore, many recent investigations and developments concentrate on alternative charging mechanisms for aerosol particles based on corona discharges (e.g. Meyer et al., 2008), UV ionization (e.g. Hontanòn and Kruis, 2008) and soft X-ray ionization (e.g. Yun et al. 2009).

A corona discharge is a well known option as ionizing method in aerosol science. Mainly, corona chargers are designed as unipolar ionizers, where a sharply tipped electrode is raised to a high voltage potential. At the tip, the electric field is strong enough to create a plasma which ionizes the surrounding gas molecules. Particles become charged either by field charging or diffusion charging, depending on their size and morphology.

A custom-built corona generator, designed within the framework of this thesis, was used to study the ionic clusters generated by a positive and negative corona discharge. Fig. 4.19 shows a schematic cross section of the used device.

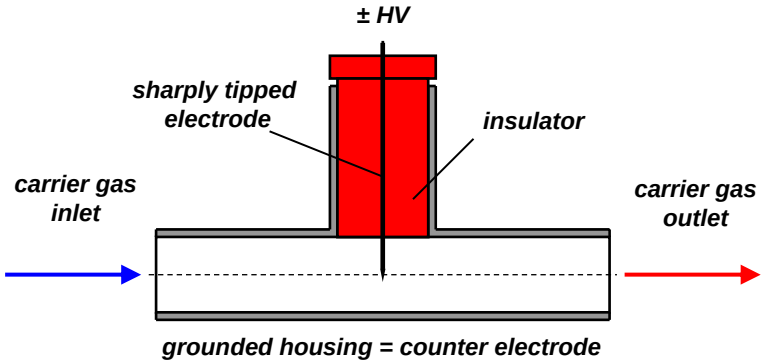

Fig. 4.19 Schematic cross section of the custom built corona generator.

A second alternative charging device as ion generator that was evaluated - in terms of the size distribution of the generated ions - is based on soft x-ray radiation. The soft x-ray charger used for the measurements is a development of one of the Viennese Aerosol Physics group's members who evaluated this prototype during his master thesis (Kallinger, 2010). The device comprises two photoionizers (Hamamatsu, Japan), emitting soft x-rays with an energy between 3keV and 9.5keV, corresponding to a wavelength of 0.41nm to 0.13nm. A sufficient shielding of the radiation is already guaranteed with an aluminium plate of 0.5mm thickness. A schematic cross section of the x-ray charger is shown in Fig. 4.20.

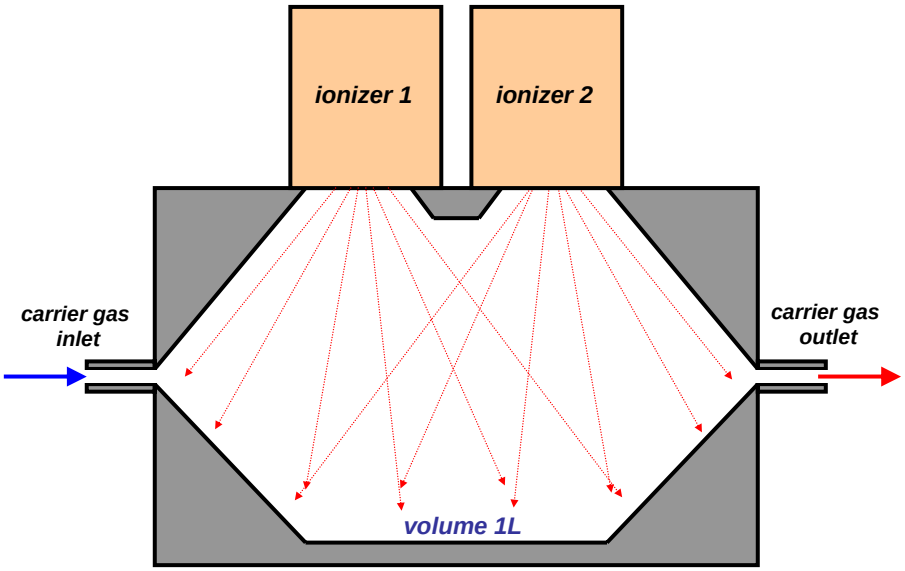

Fig. 4.20 Schematic cut-plot of the soft x-ray charger.

To be able to compare the obtained results with the ones obtained for the measurements using the radioactive ^{241}Am charger, the same setup as described for the very clean and dry ion mobility measurements in purified air (section 4.2) was used – only the ^{241}Am charger was replaced by the corona generator or the soft x-ray charger. (Fig. 4.21)

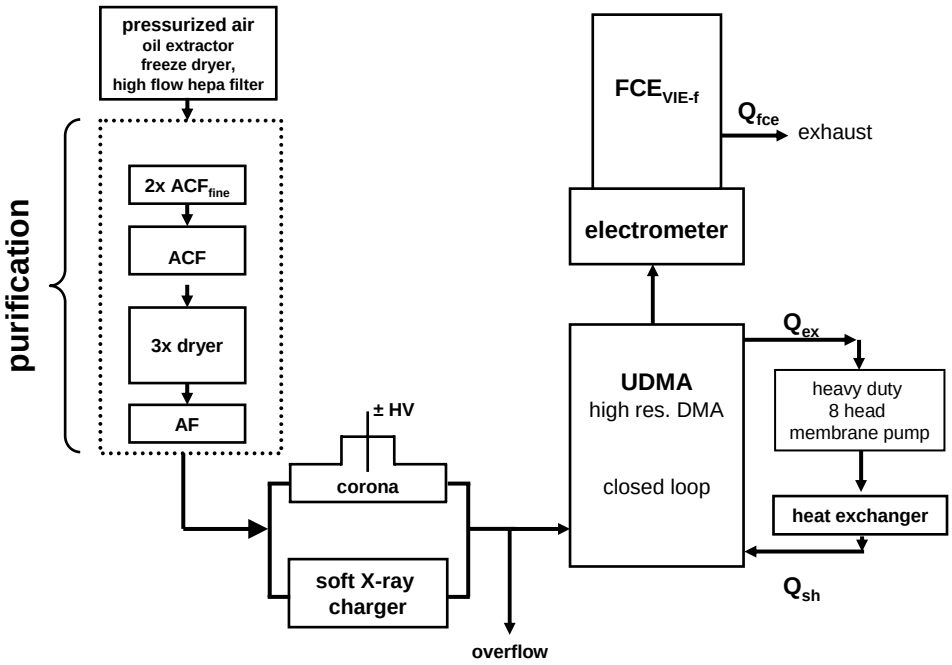

Fig. 4.21 Setup for the alternative charging methods:
corona discharge and soft x-ray

The results for the measurements using the corona charger, supplied with purified pressurized air at very low relative humidity (~1% r.H.) are shown for positive polarity in Fig. 4.22 and for negative polarity in Fig. 4.23.

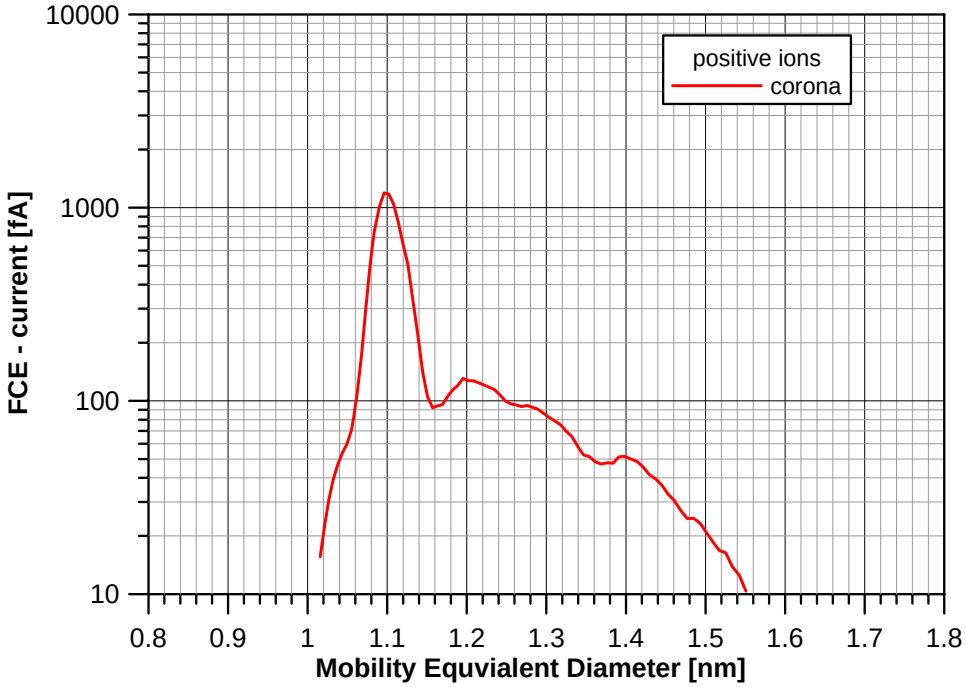

Fig. 4.22 Positive ions produced by a corona discharge in purified air

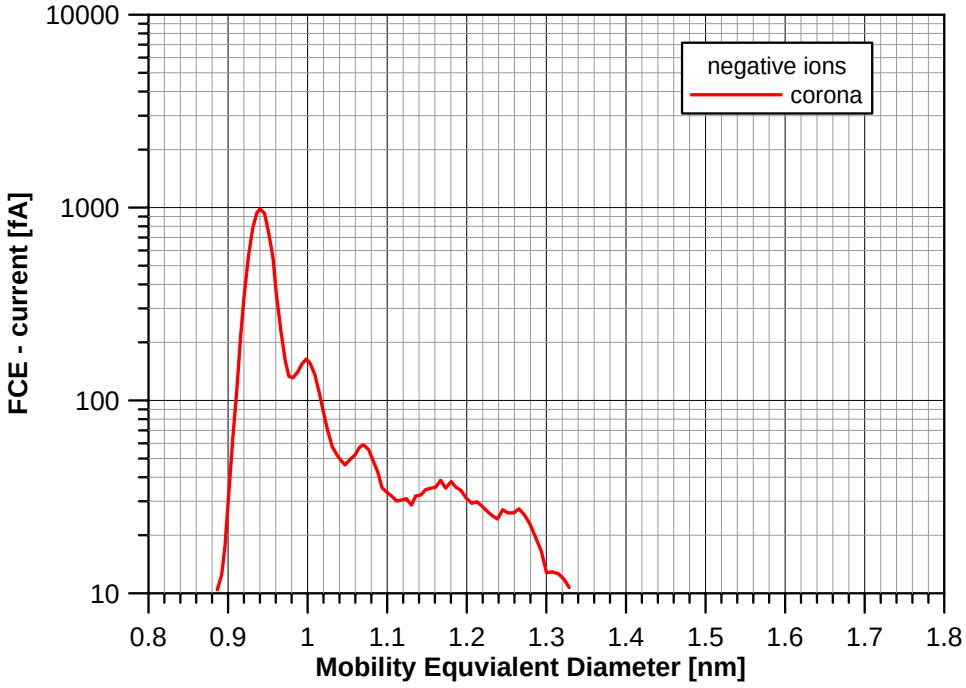

Fig. 4.23 Negative ions produced by a corona discharge in purified air

The resulting graphs for the measurements using the soft x-ray charger, operated at the same carrier gas conditions as the corona generator, are shown in Fig. 4.24 (positive ions) and Fig. 4.25 (negative ions).

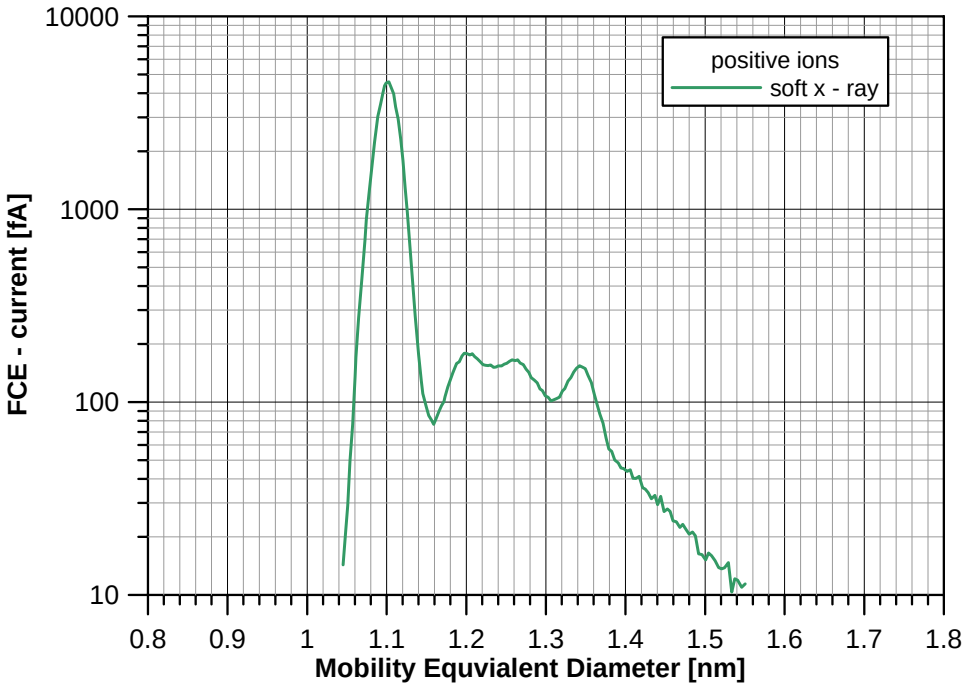

Fig. 4.24 Positive ions produced by soft x-ray radiation in purified air

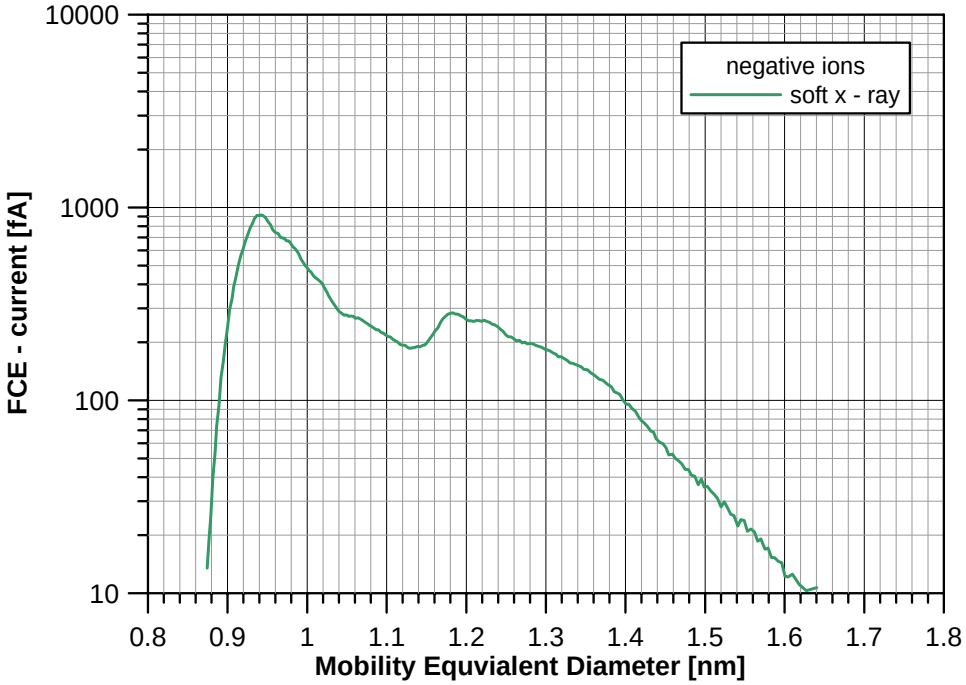

Fig. 4.25 Negative ions produced by soft x-ray radiation in purified air

For a better comparison, Fig. 4.26 compares the size distribution of the ionic molecular clusters generated by the three different ionizing processes – including the measurements with the ^{241}Am charger from section 4.2. for positive ion polarity and Fig. 4.27 for negative polarity.

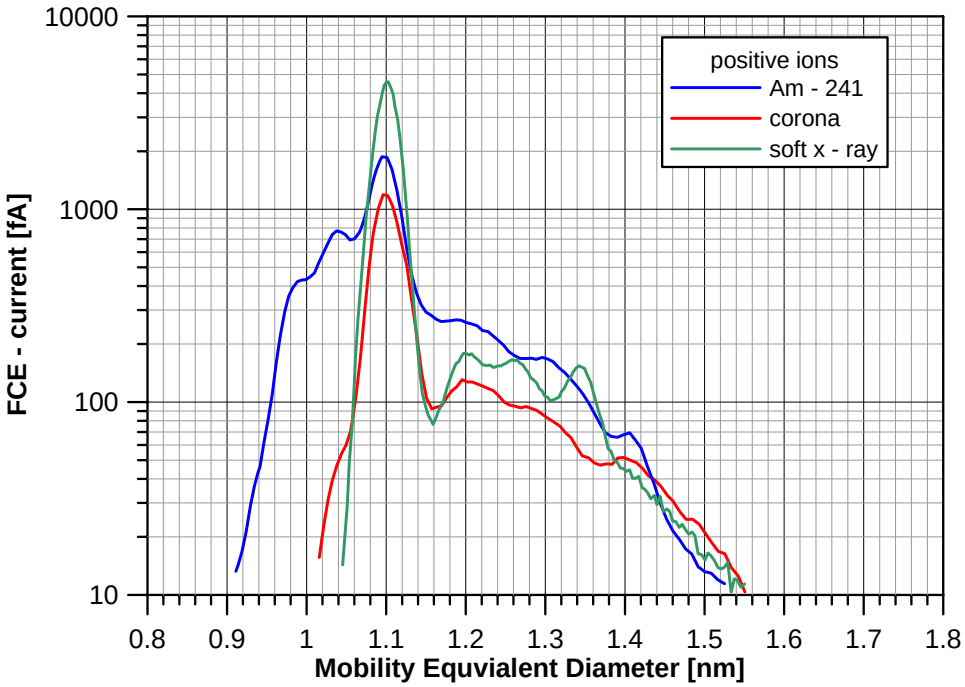

Fig. 4.26 Comparison of positive ions produced by three ionizing methods

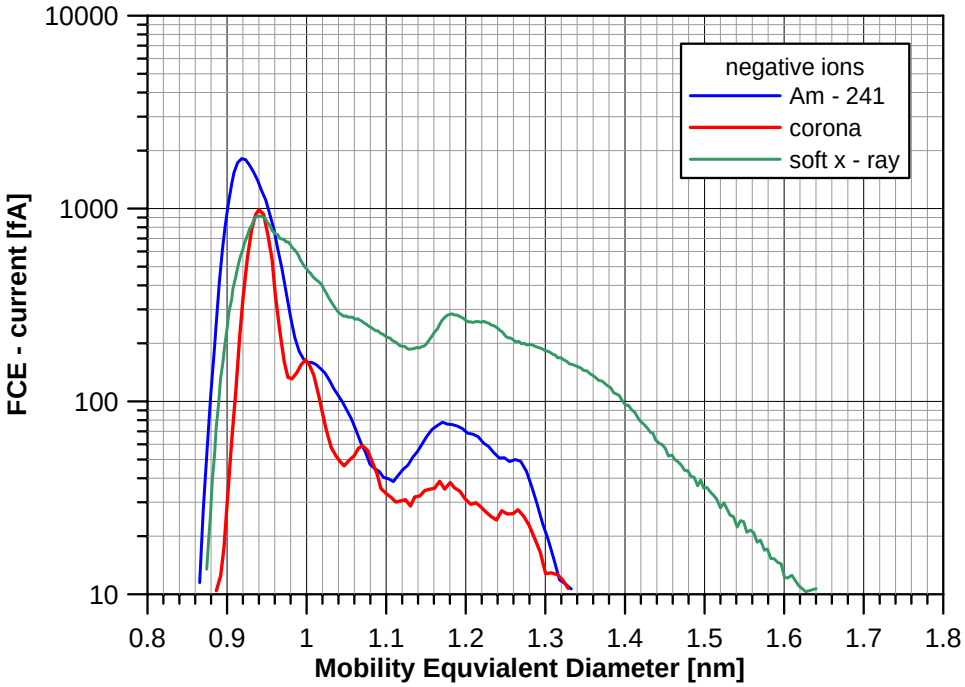

Fig. 4.27 Comparison of negative ions produced by three ionizing methods

As the size distributions of the cluster ions generated by three different ionizing processes strongly resemble each other, it is a strong evidence that the generated ions are of the same or at least very similar cluster configuration.
For positive ions (for all three ionizing processes) a main peak can be found at 1.1nm of only slightly different relative abundance. Also the larger clusters are similarly concentrated. Although also the corona charger as well the soft x-ray charger were treated very carefully and flushed for several hours to avoid potential contamination, no clusters with sizes below the main peak at 1.1nm could be found.
For negative ions, we get a very similar picture. Again, the general pattern of the size distribution of the ions generated by the individual ionizing processes is the same; only the relative abundance of the produced ion clusters is different. However, the situation for the soft x-ray charger seems to be a little bit different, as it induces also the formation of comparably large clusters.

4.4. Ion Measurements at Contaminated Carrier Gas Conditions

Although measurements at clean and dry carrier gas conditions can be easily compared to each other and describe the “genuine” mobility size distribution of ions produced by ionizing radiation, in reality, aerosol measurements always involve contaminations and impurities to some extent. Therefore, a more interesting and realistic scenario is the investigation of the properties of ionic molecular clusters produced during the presence of trace gases or impurities within the carrier gas by the ionizing radiation in the charger.
In this work, different kinds of frequently encountered contaminations were added to the system by placing different tubing material of two meters length in front of the charger – a quite untypical but very practical approach.
The inner surfaces of the tubing materials evaporate trace gases and influence the formation of ionic cluster species in the neutralizer. As the contaminated carrier gas enters the charger, the additional chemical components represent new bonding

partners for the primary ions to form larger clusters. The experimental setup for the measurements involving the contaminated carrier gas is shown in Fig. 4.28

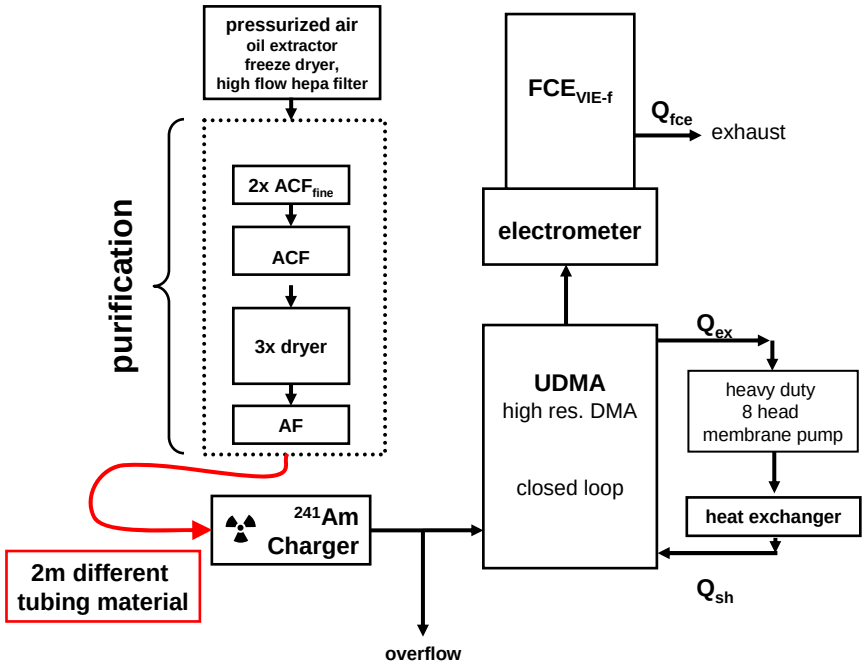

Fig. 4.28 Experimental setup for different tubing material in front of the charger.

In total, five different tubing configurations where investigated: tubing made of polycarbonate, polyurethane (new and aged), PTFE (for "clean" conditions) and a PVC fabric hose. These tubing materials were chosen as they represent the typical air ducts used in experimental setups for aerosol measurements.

The measured size distributions of positive ions produced by an ^{241}Am α-source in purified pressurized air using different tubing materials as air duct in front of the charger are shown in Fig. 4.29 to Fig. 4.32. Fig. 4.33 compares the obtained results.

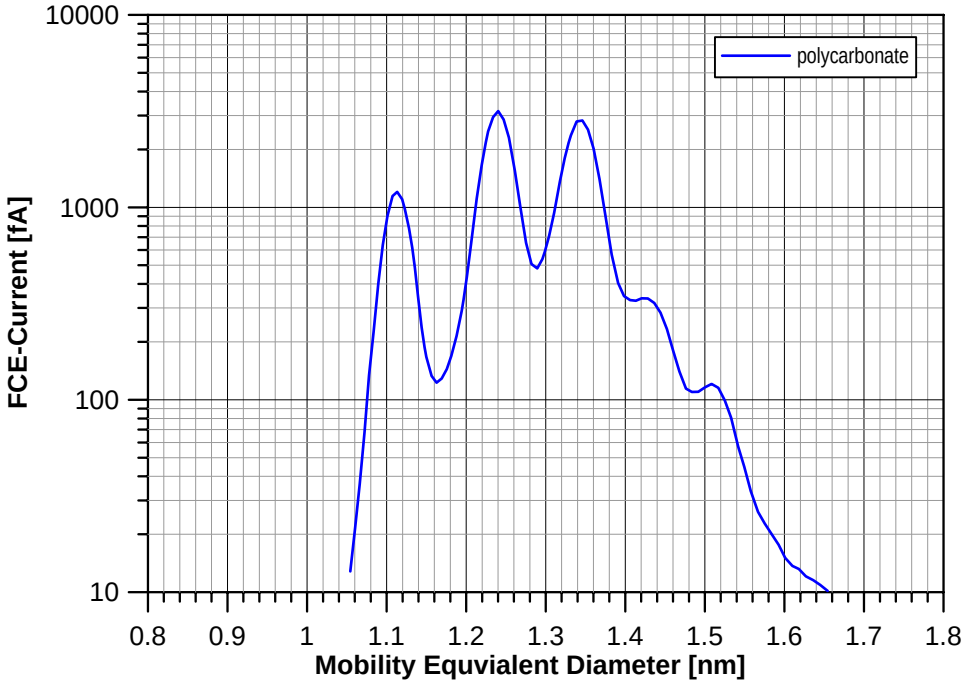

Fig. 4.29 Size distribution of positive ions;
polycarbonate tubing in front of charger

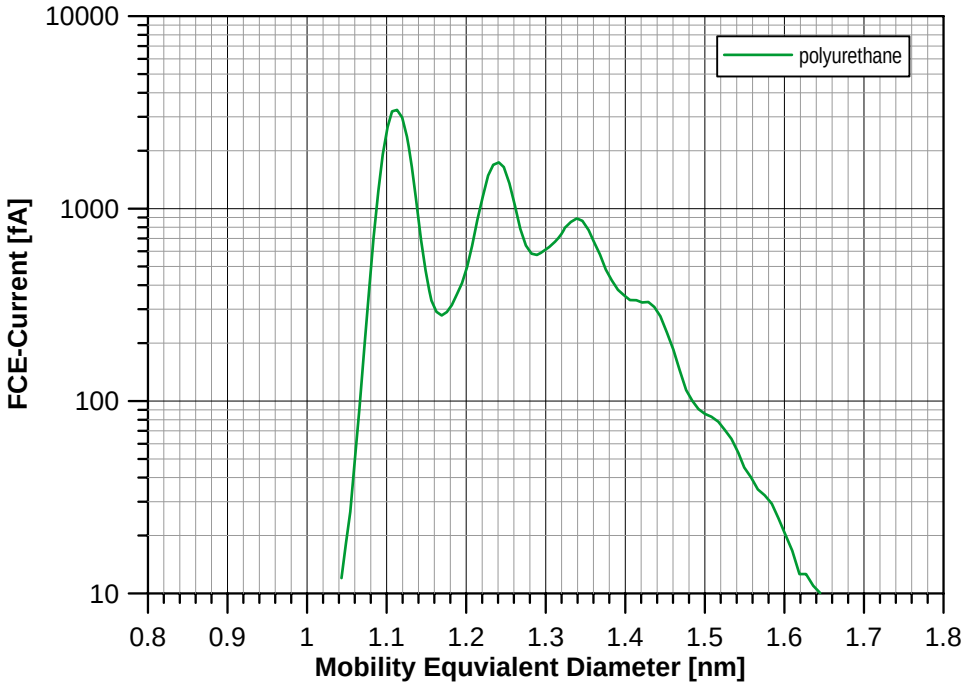

Fig. 4.30 Size distribution of positive ions;
polyurethane tubing in front of charger

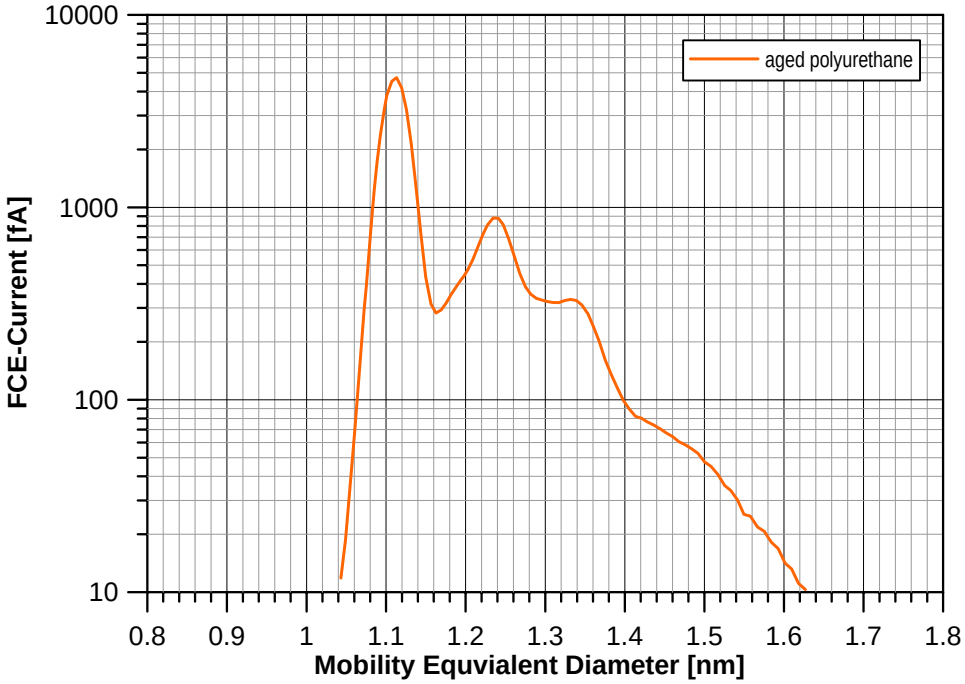

Fig. 4.31 Size distribution of positive ions;
aged polyurethane tubing in front of charger

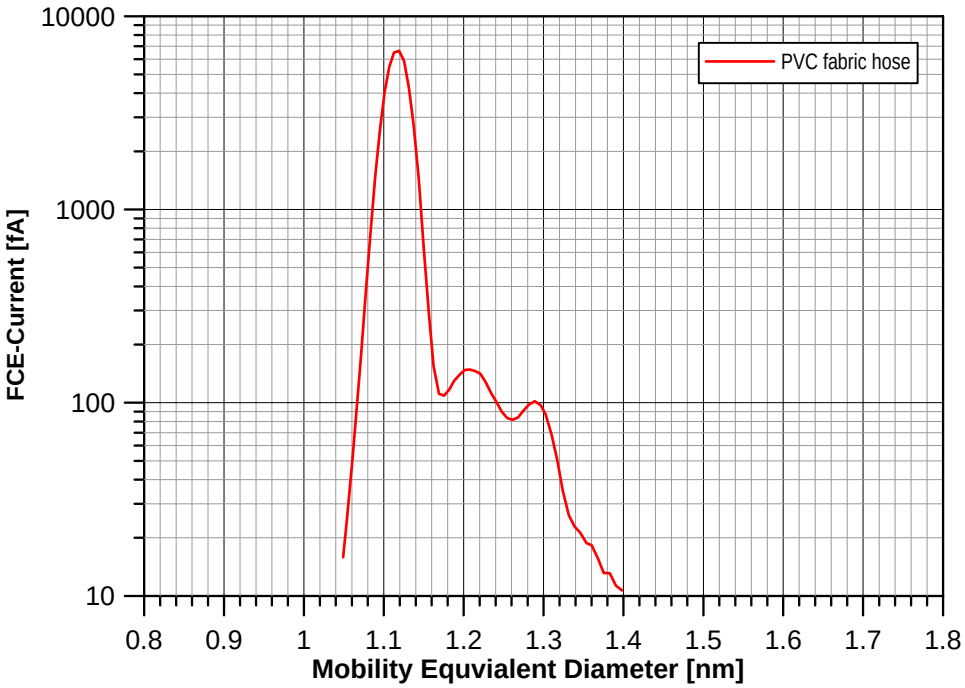

Fig. 4.32 Size distribution of positive ions;
PVC fabric hose in front of charger

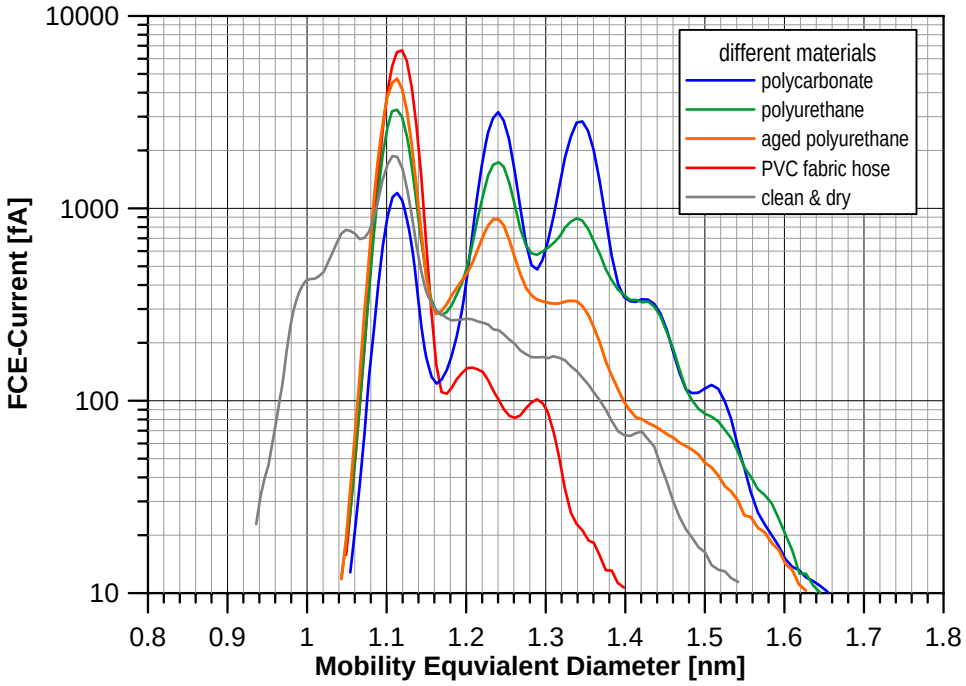

Fig. 4.33 Comparison of the size distribution of positive ion clusters produced during the presence of various tubing materials in front of the charger.

The grey line again represents the measurements performed under very clean and dry conditions, exclusively using PTFE or stainless steel air ducts. There is a "main" peak at 1.11nm, 2 peaks at smaller sizes and some rather unpronounced peaks at larger sizes.

Using polycarbonate or polyurethane (new and aged) tubing in front of the charger, results in the formation of additional ion cluster species at sizes of 1.24nm and 1.34m leading to a trimodal size distribution where the smallest clusters below 1nm disappear.

A completely different pattern can be found using the PVC fabric hose: the "main" peak at 1.11nm becomes almost 2 orders of magnitude higher than any other cluster species. This indicates that either the fabric hose adds contaminants with a higher positron affinity than any other compound present in the carrier gas, yielding this single peak size distribution, or the fabric hose shows a sort of denuder effect that scavenges impurities and contaminations to purify the carrier gas.

Similar results were obtained for negative ions, whereas in general, the mean ion mobility for negative ions is always lower compared to positive ions.

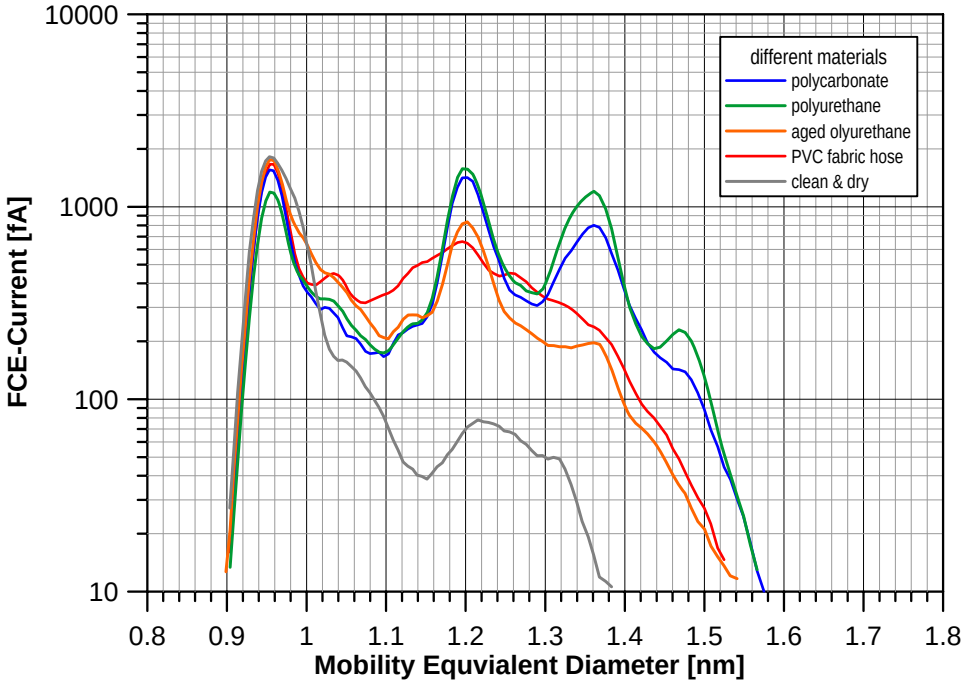

Fig. 4.34 Comparison of the size distribution of negative ion clusters produced during the presence of various tubing materials in front of the charger.

At clean conditions, as described in section 4.2, almost just a single peak at 0.96 or 0.98nm characterizes the size distribution of negatively charged ions. Using different tubing materials, that evaporate various chemical compounds from their inner surface into the previously carefully purified air, again strongly alters the ions' size distribution. For polycarbonate and polyurethane tubing, the initially unimodal size distribution now features three different well pronounced size peaks. The PVC fabric hose again shows a little bit different pattern, but this time with additionally generated clusters at larger sizes with less pronounced corresponding peaks, indicating a larger amount of evenly distributed cluster species.

The most important result from these "contaminated" measurements is the strong dependence of the ions' formation on the chemical composition (trace gases introduced by different tubing material) of the carrier gas.

Depending on the generated cluster species, the mean ion mobility equivalent diameter is shifted towards bigger or smaller diameters. Therefore also the overall mean electrical mobility will alternate between lower or higher values.
It can be assumed, that this variation will affect the calculation of the charging probabilities of ultrafine aerosols, as the overall mean electrical mobility is one of the input parameters for Fuchs' charging theory. In section 4.8., this topic will be discussed in more detail.

4.5. Ion Measurements with Controlled Humidification of the Carrier Gas

So far, the size or mobility of ions evolving form the ionizing radiation in the charger was only studied for very low relative humidity around 1%. Therefore, this chapter will focus on the experimental determination on the mobility spectra of ionic clusters produced by the ionizing process in an ^{241}Am bipolar charger with a controlled humidification of the carrier gas passed through the ionizing chamber. As the clusters produced in the charger are thought to be hydrated clusters, the dependency of generated cluster species/sizes versus the amount of water present in the carrier gas was studied.
The humidifier used in the experiments consists of two concentrical glasstubes where a thermostatted liquid water jacket controls the saturation vapour pressure over a liquid water surface. The saturation vapour pressure further determines the relative humidity of the carrier gas flow passed through the humidifier. For additional experiments, two cooling traps operated with liquid air were used to radically remove any water from the carrier gas flow. Similar to the previous measurements, special attention was paid to the purification of the carrier gas flow with several active carbon filters (ACF), silica gel dryers and HEPA filters (AF).

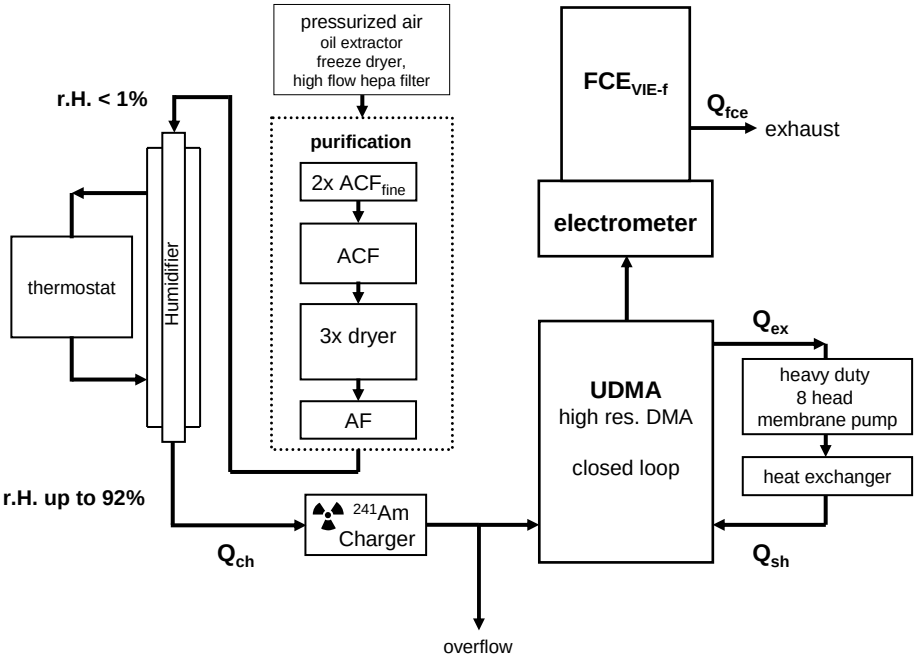

Fig. 4.35 Experimental setup for controlled humidification of the carrier gas

Fig. 4.36 shows a close up of the custom-built air-humidifier with the liquid water jacket and the inlet port of the carrier gas.

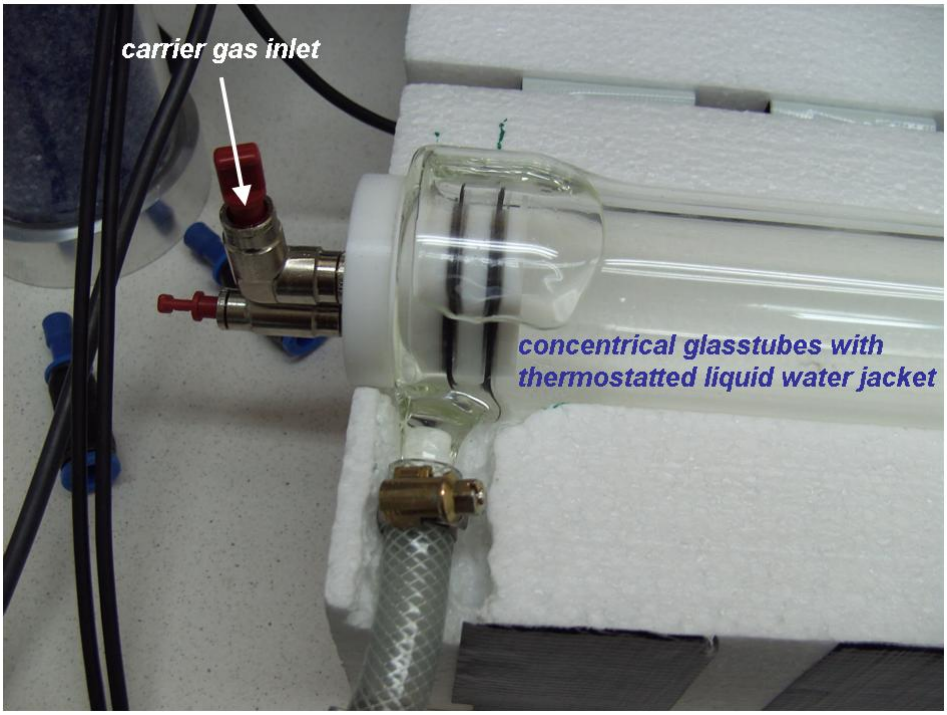

Fig. 4.36 Close up of the custom-built humidifier

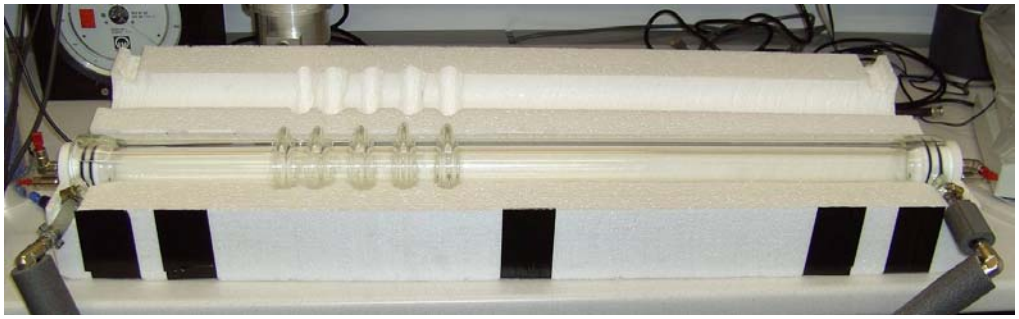

Fig. 4.37 Humidifier in its polystyrene housing

To be able to compare the measurements with controlled humidification with previous measurements performed under clean and dry measurements, Fig. 4.38 shows the mobility size distribution of positively charged ionic molecules at very low relative humidity. Differently to the experiments before, this time the relative humidity of the carrier gas was monitored at several positions in the setup with digital humidity sensors (Sensirion, SHT75) with an accuracy of 1.8 % r.H. and a repeatability of 0.1 % r.H. (right before/after humidifier, before/after charger). The values given in the following figures will always refer to the humidity of the carrier gas entering the bipolar charger.

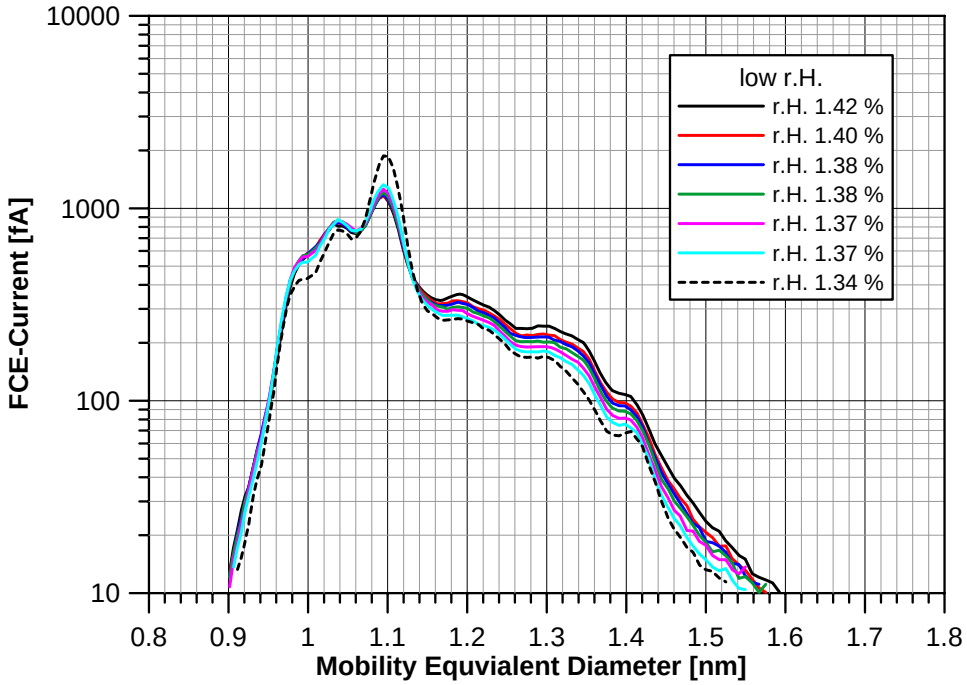

Fig. 4.38 Size distribution of positively charged ionic clusters at low relative humidity

The graph in Fig. 4.38 shows the size distribution of the produced positively charged ions at a relative humidity of approximately 1.3%. For this measurement, the humidifier was already inline to the air duct from the gas purification to the charger, but still out of operation – not filled with water or thermostatted. This way, potential contaminations due to impurities of the interior of the humidifier can be localized. However, as the resulting size distribution strongly resembles that for the clean and dry measurement given in chapter 4.2, impurities seem to be negligible.

Taking the humidifier into operation changes the pattern of the ions size distribution as shown in Fig. 4.39. At a relative humidity of 28.5%, the abundance of the clusters forming the "main" peak at 1.1nm is decreasing, but at the same time the concentrations of the peaks on the left-hand side of the size distribution at smaller sizes is increasing. Furthermore, also the concentration of the larger clusters is increasing. At a relative humidity of almost 60%, the amount of larger clusters is further increasing and the whole size spectrum performs a shift to larger cluster sizes, as the smallest cluster size can be found at approximately 1nm. Raising the relative humidity up to 92% again results in an increase of the larger ion clusters and an overall shift to larger cluster sizes.

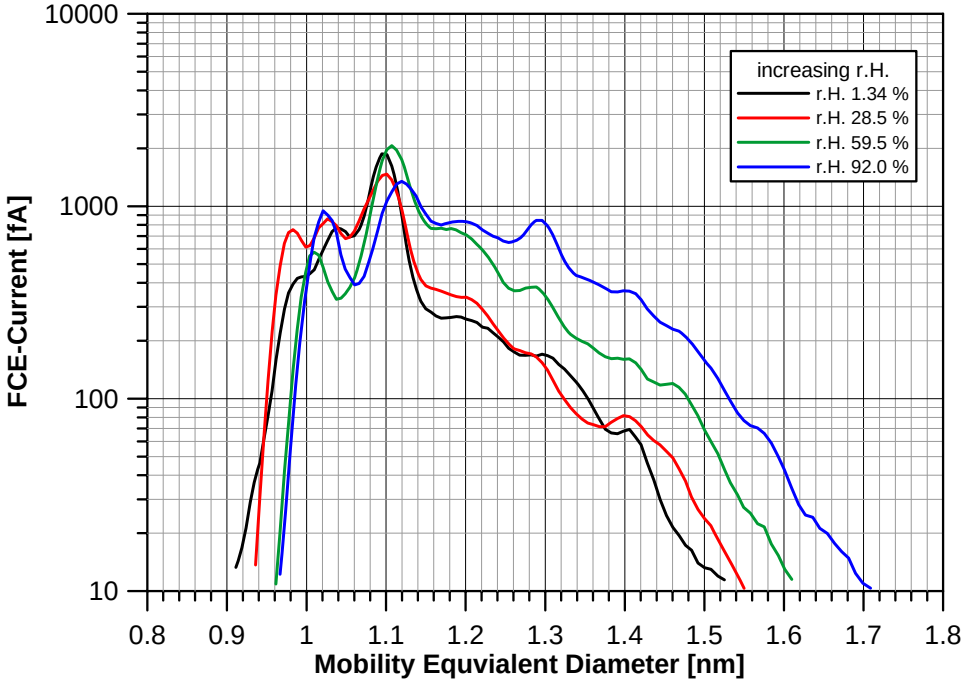

Fig. 4.39 Growth of positive ions during increasing relative humidity

To summarize this experiment, by increasing the relative humidity of the carrier gas and therefore increasing the amount of water vapour in the system, the ion clusters will more likely form larger cluster species but the overall pattern of the size distribution stays the same. This result is a strong evidence that for positive ions, the most likely built cluster species are hydrated ion molecules; most probably of the form $H_3O^+(H_2O)_n$. Unfortunately, the resolution power of the UDMA used for these experiments is too low to be able to separate the inner structure of the size distribution above 1.1nm. However, it is questionable if this inner structure can be resolved at all by means of airborne electrical mobility spectrometry.
Additionally, the experiments have also revealed, that the occurrence of peaks below the "main" peak in terms of size indicate very clean conditions. The introduction of any kind of contamination will force the freshly generated ions to preferably form larger clusters.

Negative ions react a bit differently to the humidification of the carrier gas.
In Fig. 4.40, starting at a relative humidity of 1.1% (solid black line), the "main" peak of the negative ions can be found clearly below 1nm, at 0.92/0.94nm. As typical for the negative clusters, this peak dominates the spectrum and the other peaks at some larger sizes are almost negligible in their concentration. With increasing relative humidity (up to 14% r. H.) this "main" peak shifts towards larger mobility equivalent diameters whereas a less concentrated peak alongside to the main peak at 1.02nm keeps its position in the size distribution and increases its relative abundance. At the same time, the clusters that are forming the low concentrated peaks around 1.2nm vanish completely.

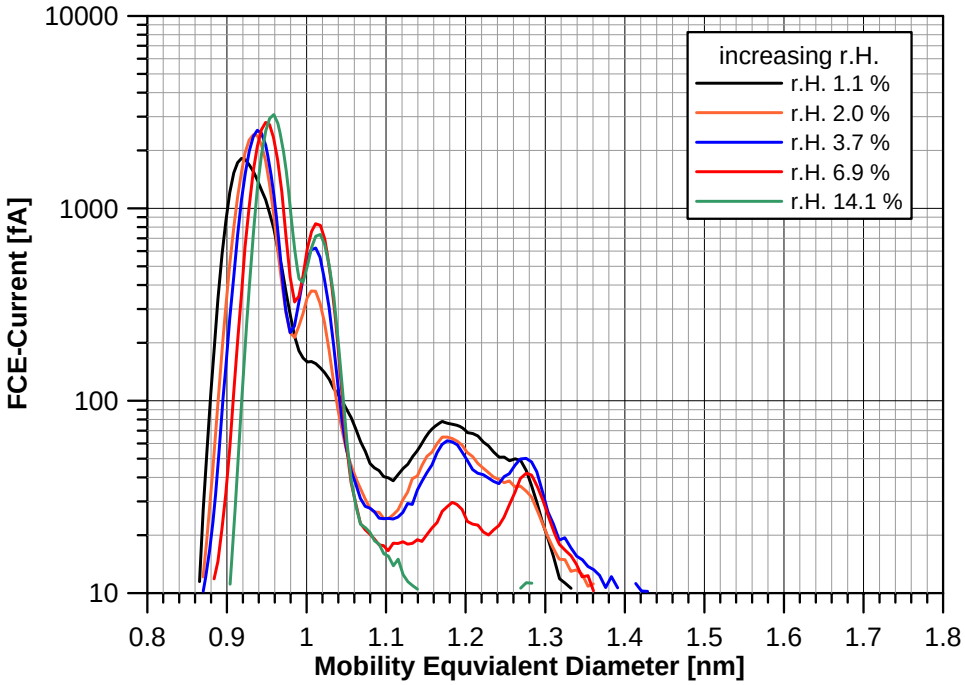

Fig. 4.40 Negative ions during controlled humidification of the carrier gas

Fig. 4.41 continues with the results of the humidified air measurements, showing the data from a relative humidity of 14% up to 88%. Here, the "main" peak continues its shift towards larger sizes and even increases its concentration. Starting from 14% r. H., the amount of larger clusters increases again with a developing well pronounced peak at 1.22nm

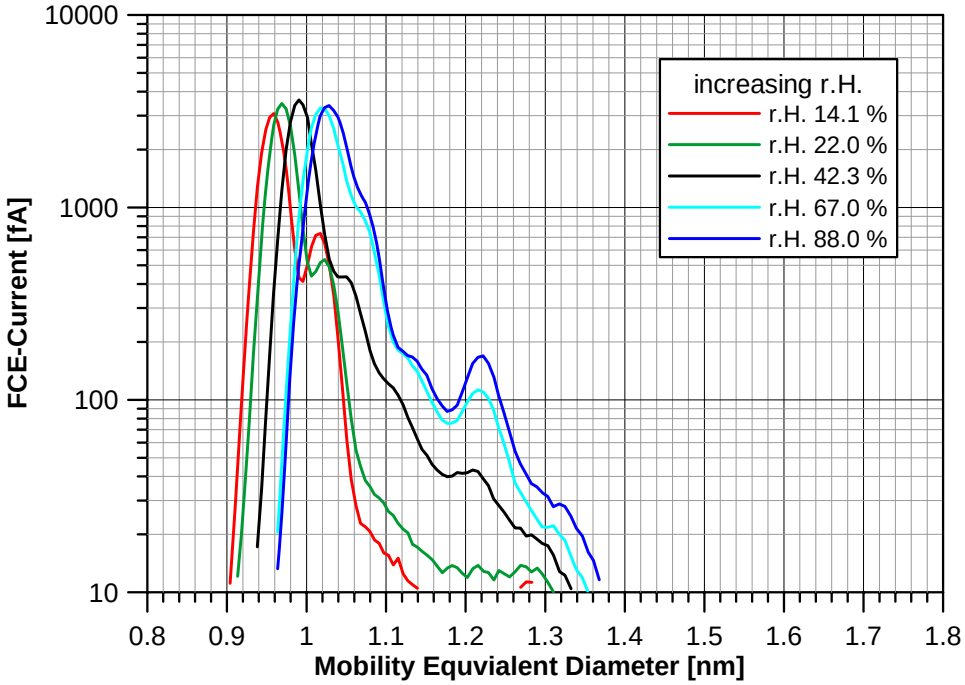

Fig. 4.41 Size distribution of negatively charged ions during r.H. up to 88%

To sum up, during controlled humidification of the carrier gas, the formation of negative ions is affected in a way, that the mean cluster diameter continuously increases to larger sizes with increasing relative humidity. This result again indicates that the amount of water vapour present in the system is a major driving parameter for the generation/formation of ionic molecular clusters studied in this thesis.

To investigate the apparent influence of water vapour on the ion clusters, additional experiments were using cooling traps to radically reduce the amount of water in the gas flow. Schematic drawings of the used cooling trap and of the whole setup are shown in Fig. 4.42 and Fig. 4.43.

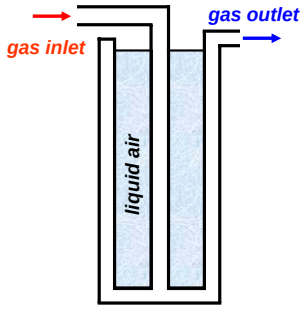

Fig. 4.42 Schematic of the cooling trap

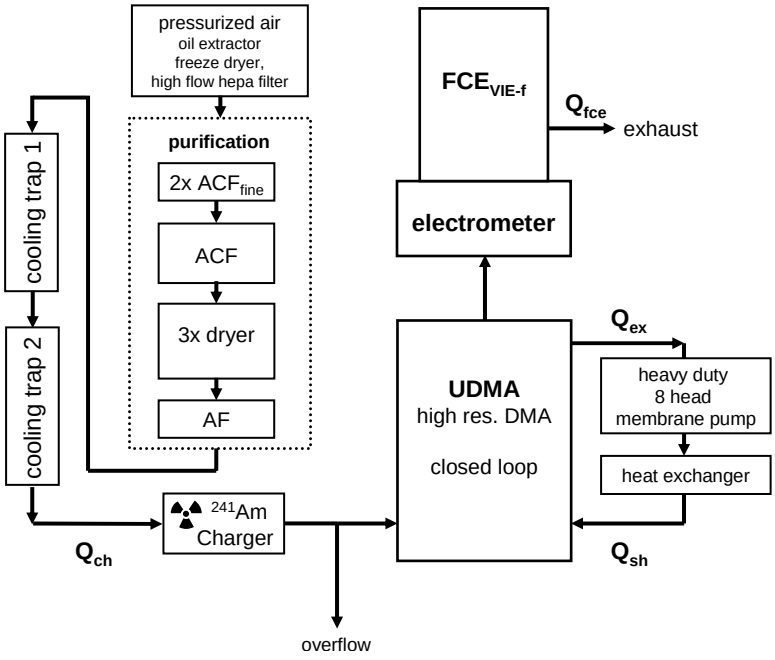

Fig. 4.43 Experimental setup with two cooling traps to radically remove water from the carrier gas flow

The resulting graphs of this experiment are shown in Fig. 4.44 and Fig. 4.45. For positive ions (Fig. 4.44), the black line represents the zero measurement, with the cooling traps out of operation (not filled with liquid air) but inline to the duct of the carrier gas to the charger. As typical for positive ions, the “main” peak at 1.1nm dominates the spectrum. Different to the size distribution that can be found at very clean and dry conditions (Fig. 4.17), no clusters with diameters below the “main” peak at 1.1nm can be found. According to the previous experiments, the absence of the very small ion clusters indicates the presence of contaminations in the system. Here, the contaminants are most likely introduced by the insertion of the cooling traps. Unfortunately, even flushing for several hours with clean air did not change the pattern of the ions size distribution.

However, taking the cooling traps into operation strongly alters the size spectrum Fig. 4.44): The abundance of the clusters forming the “main” peak at 1.1nm slightly increases whereas the amount of clusters forming the bigger molecular species rapidly decreases by more than one order of magnitude.

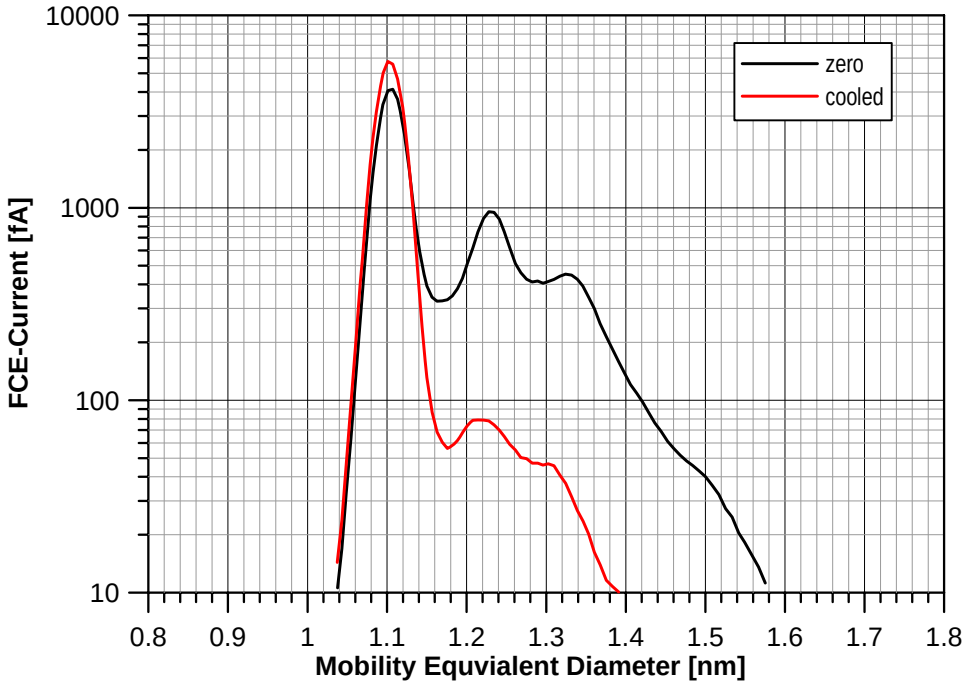

Fig. 4.44 Size distribution of positively charged ions produced in purified compressed air using cooling traps to reduce the amount of water to a minimum.

This result is in agreement with the observations made during the controlled humidification of the carrier gas (Fig. 4.39): The lower the amount of water vapour present in the carrier gas, the smaller the mean ion mobility equivalent diameters and the lower the concentration of clusters larger than 1.1nm.

Also in agreement with the previous experiments concentrating on negative ions during the controlled humidification of the carrier gas, a left shift of the whole ion size distribution can be observed when water vapour is radically removed from the gas flow (Fig. 4.45). The rather unclear and unspecified situation for larger clusters than the negative ion "main" peak below 1nm, again indicates the presence of contamination as already mentioned above. According to these results, the amount of water vapour in the carrier gas has a strong influence on the formation the molecular ions in the 241Am charger. For more information on the produced clusters, section 4.6 will present possible molecular species and the possible hydration state of these.

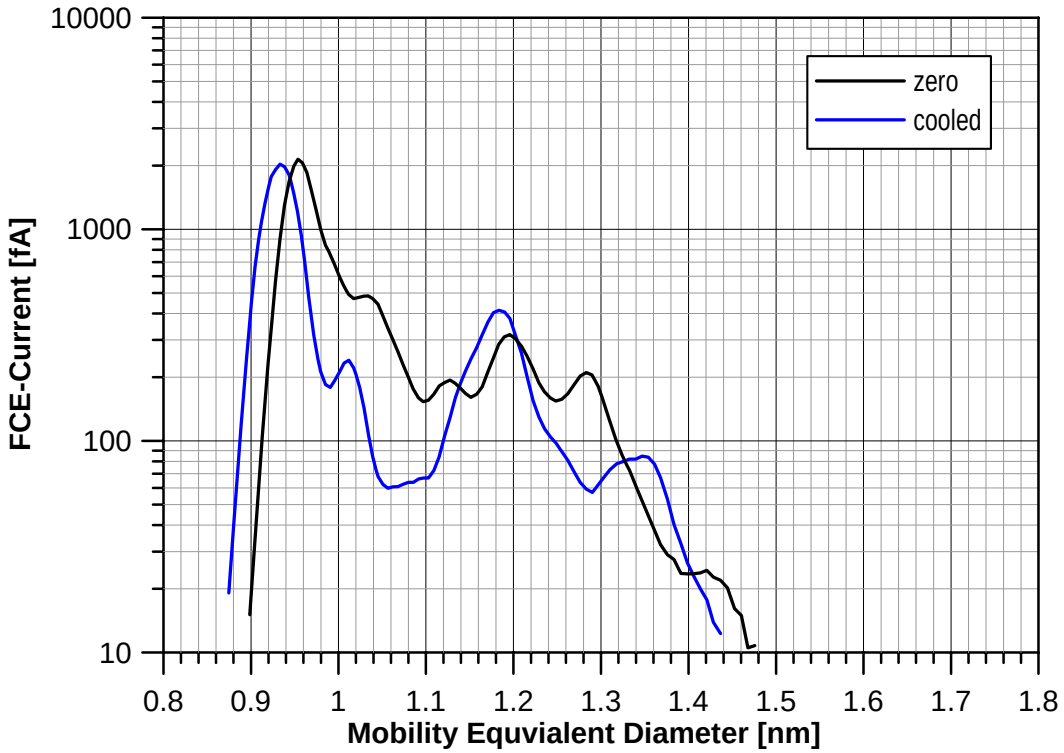

Fig. 4.45 Size distribution of negatively charged ions produced in purified compressed air using cooling traps to reduce the amount of water to a minimum.

4.6. Physical and Chemical Nature of the Ions produced in the Charger

In the last years, the high resolution mobility classification of aerosol particles has improved to a size range, were even the electrical mobility of molecular clusters can be determined with high precision.
Unfortunately, high resolution mobility spectrometry can only derive one important property of aerosol particles or molecular clusters: the electrical mobility. For the proper identification of an unknown aerosol or molecular cluster, a second crucial parameter is the particle/cluster mass.
If genuine mass spectrometric instrumentation is not available, empirical derived mass-mobility relationships are a useful possibility for the mass determination, allowing the calculation of the respective mass out of a measured mobility distribution. Still it has to be mentioned, that there exists no generally excepted conversion from mobility into mass as especially for molecular clusters, also their structure will strongly affect the electrical mobility. Therefore, the conversion is still somewhat uncertain but can be a versatile tool if its limitations are kept in mind.

The most frequently used mass mobility relationship goes back to Kilpatrick (1971) who determined the electrical mobility of twenty five different positive and negative ion molecules with a plasma chromatograph in clean and dry air and/or nitrogen. The masses of the very different molecule species ranged from about 35 amu to 2211 amu. Due to technical reasons, in Kilpatrick's studies, the mobility of the molecular clusters was determined at a temperature of about 200°C. Therefore, all his data is converted into a so called "reduced" mobility Z_0, calculated by the commonly used formula in equation [4.1], referring to a temperature of 273° Kelvin and a pressure of 760 Torr.

$$Z_0 = Z \cdot \frac{p}{760} \cdot \frac{273}{T} \qquad [4.1]$$

Tab. 4.1 and Tab. 4.2 display the molecular mass m and the reduced mobility Z_0 derived by Kilpatrick for the different ion species. In the tables, “BPC” stands for “biphenylchloride”, “tfa”for “trifluoroacetylacetone” and “fod” for “heptafluorodimethyloctanedione”.

positive ion species	m [amu]	Z_0 [cm^2/Vs]
2 · Formaldehyde	60	2.07
Dimethylsulfoxide-d	84	1.84
Isooctane	114	1.73
Octanol	130	1.56
Vanillin	152	1.44
2 · Dimethylsulfoxide-d	168	1.47
BPC-1	188	1.34
Benzoanthracene	215	1.21
2 · Acetophenone	240	1.24
2 · Salicylaldehyde	244	1.27
2 · Benzoic Acid	244	1.28
2 · Naphthalene	256	1.26
BCP-4 (2, 4)	292	1.14
BCP-8	430	0.976
BCP-10	499	0.906
2 · $Mg(tfa)_2$	660	0.842

Tab. 4.1 Kilpatrick’s original data for positively charged molecule species

negative ion species	m [amu]	Z_0 [cm^2/Vs]
Chlorine	35.5	2.49
Nitrogen Dioxide	46	2.36
2 · Formaldehyde	60	2.06
3 · Formaldehyde	90	1.83
Isooctane	114	1.69
Iodine	127	1.52
Vanillin	152	1.46
Diethylphtalate	222	1.27
BPC-4 (2, 4)	292	1.14
BPC-4 (2, 3, 4, 5)	292	1.13
fod (fragment)	295	1.19
BPC-6	361	1.06
Hexachlorophene	407	0.984
BPC-8	430	0.976
BPC-10	499	0.906
$Cr(tfa)_3$	511	0.922
2 · $Mg(tfa)_2$	660	0.820
$Lu(fod)_3$	1061	0.607
Freon (E-9)	1612	0.497
2 · $Lu(fod)_3$	2122	0.411

Tab. 4.2 Kilpatrick's original data for negatively charged molecule species

In Kilpatrick's original publication the data was fitted with a line to guide the eye but without a mathematical background. For a more convenient use of Kilpatrick's empirical data, Mäkelä et al. (1996) fitted a function to Kilpatrick's data given in equation [4.2],

$$Z = \exp[-0.0347 \cdot (\ln(m_i))^2 - 0.0376 \ln(m_i) + 1.46662] \qquad [4.2]$$

where m_i denotes the ion mass in amu and Z the ion mobility in cm^2/Vs. The result of this fit to Kilpatrick's original data is shown in Fig. 4.46.

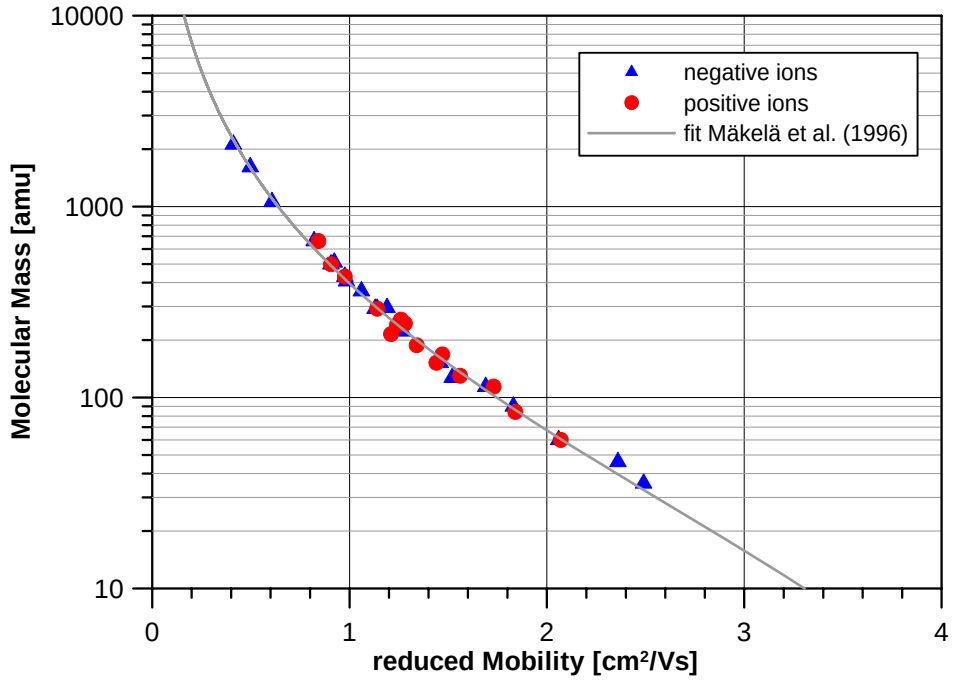

Fig. 4.46 Fit of Mäkelä et al. (1996) to Kilpatrick's original data

An inverted version, for given mobility, related to Mäkelä's fit, can be expressed as following:

$$m = \exp[-0.27 \cdot (\ln(Z))^2 - 2.2\ln(Z) + 6.008] \qquad [4.3]$$

To test Kilpatrick's relation ship, Fig. 4.47 compares the two fits described in equations [4.2] and [4.3] with the properties of Tetraalkylammonium halide clusters as listed in Tab. 3.1 and Tab. 3.2 in chapter 3.2.

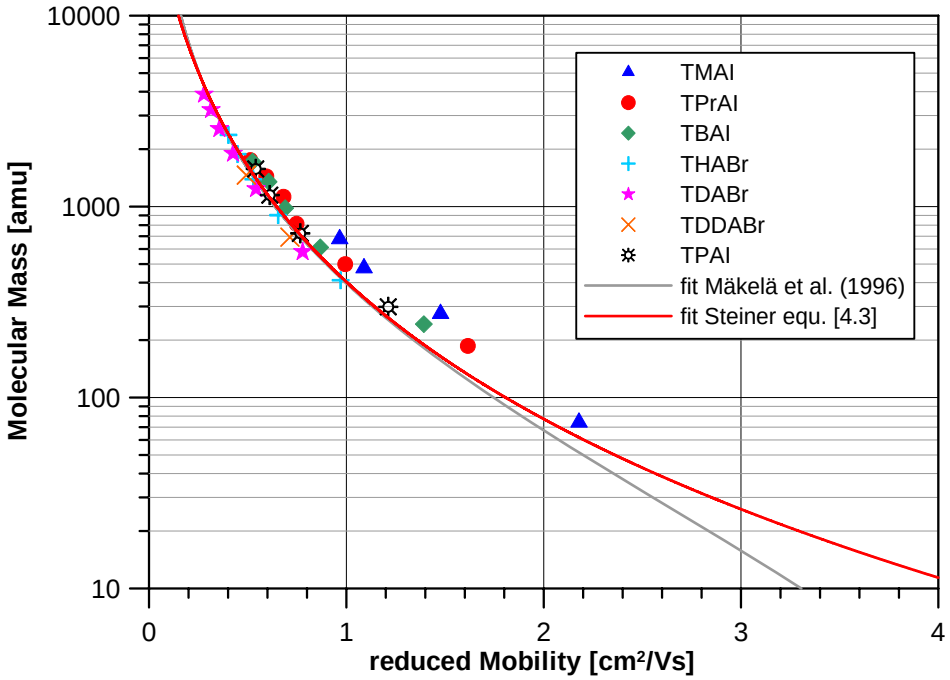

Fig. 4.47 Test of Kilpatrick's relationship with the properties of Tetraalkylammonium halide clusters.

For low mobilities, the data points follow the pattern of Kilpatrick's relation quite well, but deviate quite strongly for higher mobilities. Although the fits depict the general pattern of the data points, still there are differences up to 20% for the mobility according to Kilpatrick for a given mass of a cluster. This underlines the evidence, that the clusters' structure strongly affects the electrical mobility.

Using Kilpatrick's empirical mass-mobility-relationship allows the conversion of an experimentally determined mobility distribution into a mass distribution. Still, it has to be kept in mind that this conversion is only an approximation. By using the definition of the electrical mobility as given in equation [2.73] in chapter 2

$$Z = \frac{i \cdot e_0}{3 \cdot \pi \cdot \eta} \cdot \frac{C(D_p)}{D_p}$$

and the slip correction factor as given in equation [2.70]

$$C(D_p) = 1.0 + A \cdot \left(\frac{\lambda}{D_p}\right) + B \cdot \left(\frac{\lambda}{D_p}\right) \cdot \exp\left(-C \cdot \left(\frac{D_p}{\lambda}\right)\right)$$

with the slip correction constants from [2.71] (Fuchs, 1964)

$$A = 2.492$$
$$B = 0.84$$
$$C = 0.43$$

Kilpatrick's mass mobility relationship can be converted into a mass size relationship (Fig. 4.48).

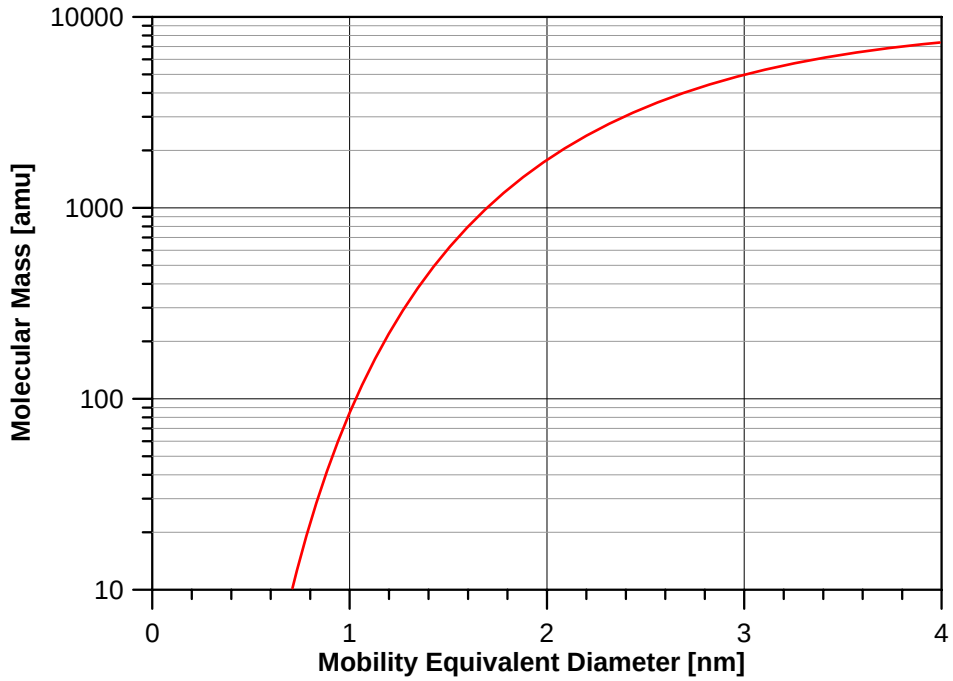

Fig. 4.48 Molecular mass vs. electrical mobility equivalent diameter according to Kilpatrick

This way the size distribution of positively and negatively charged ions from figures Fig. 4.17 and Fig. 4.18, as representative spectra for positive and negative ions, can be converted into a corresponding mass distribution.

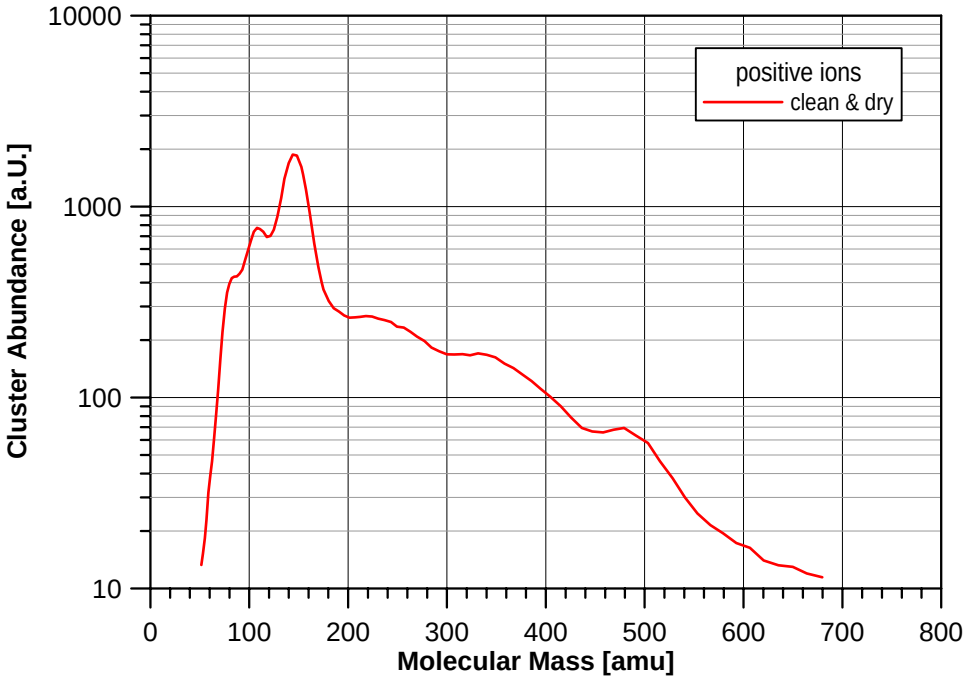

Fig. 4.49 Mass distribution of positively charged ions according to Kilpatrick

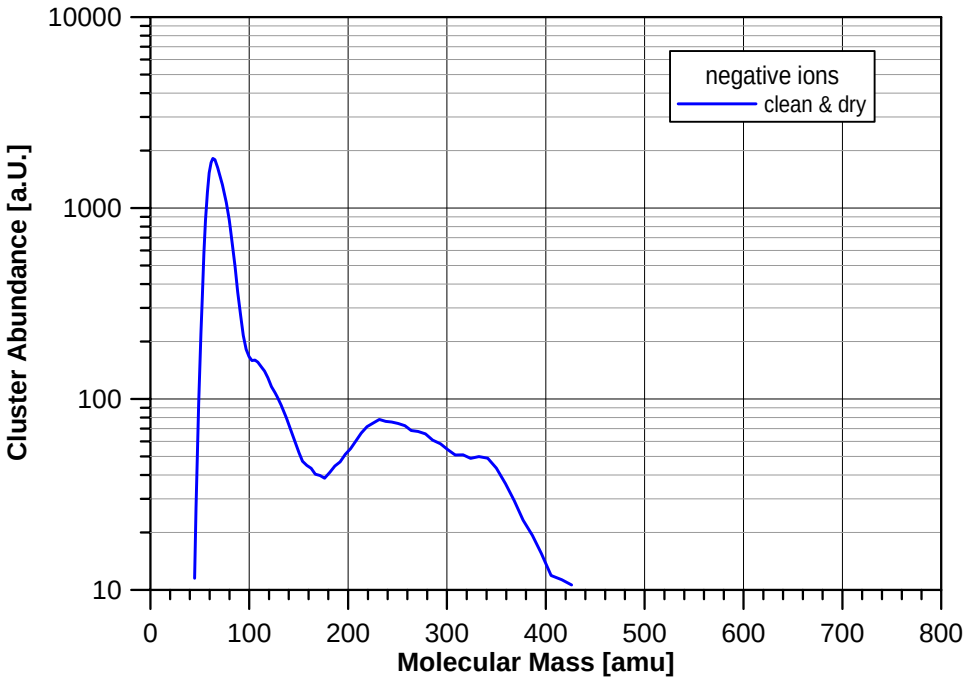

Fig. 4.50 Mass distribution of negatively charged ions according to Kilpatrick

Using Kilpatrick's relationship not only allows the conversion from a mobility distribution into a mass distribution, but of course also the calculation of the corresponding mobility for a given mass. In the previous section, all experiments

indicate a strong evidence for hydrated ion clusters as the predominant cluster species produced during the ionizing processes in the charger. Therefore, the mobility of the most likely n-fold hydrated ion clusters can be easily calculated for positive and negative ions and the hydration state of the most likely clusters can be identified.

As already announced in the beginning of chapter 4, protonated water $H_3O^+$and the ammonia ion NH_4^+ are considered as the most abundant primary ions for positive polarity and, for example, nitric acid NO_3^- and its dimer NO_3^- HNO_3 as most abundant primary ions for negative polarity. Accordingly, Tab. 4.3 and Tab. 4.4 list the positively and negatively charged cluster species with their mass (calculated according to their atomic configuration) and their mobility and mobility equivalent diameter derived according to Kilpatrick (see equation [4.2]). For positive polarity, only H_3O^+ and its hydrates are listed, as the masses of H_3O^+ (m~19amu) and NH_4^+ (m~18amu) are so similar, that there is no relevant difference between their approximated electrical mobilities.

$H_3O^+ (H_2O)_n$							
n	m [amu]	Z [cm²/Vs]	D_p [nm]	n	m [amu]	Z [cm²/Vs]	D_p [nm]
0	19	2.871	0.84	11	217	1.2964	1.25
1	37	2.406	0.92	12	235	1.2543	1.27
2	55	2.1346	0.98	13	253	1.2161	1.29
3	73	1.9467	1.02	14	271	1.1812	1.31
4	91	1.8049	1.06	15	289	1.1491	1.33
5	109	1.6923	1.1	16	307	1.1194	1.35
6	127	1.5996	1.13	17	325	1.0919	1.36
7	145	1.5214	1.16	18	343	1.0663	1.38
8	163	1.454	1.18	19	361	1.0423	1.4
9	181	1.3951	1.21	20	379	1.0198	1.41
10	199	1.343	1.23				

Tab. 4.3 Ion properties of the most likely positive ion clusters

For negative polarity, both hydrates of nitric acid and hydrates of its dimer are included in the list

$NO_3^-(H_2O)_n$				$NO_3^- HNO_3 (H_2O)_n$			
n	m [amu]	Z [cm²/(Vs]	D_p [nm]	n	m [amu]	Z [cm²/(Vs]	D_p [nm]
0	62	2.0544	0.99	0	125	1.6092	1.12
1	80	1.8873	1.04	1	143	1.5295	1.15
2	98	1.7583	1.08	2	161	1.4611	1.18
3	116	1.6543	1.11	3	179	1.4013	1.2
4	134	1.5677	1.14	4	197	1.3485	1.23
5	152	1.4941	1.17	5	215	1.3013	1.25
6	170	1.4302	1.19	6	233	1.2588	1.27
7	188	1.3741	1.22	7	251	1.2202	1.29
8	206	1.3243	1.24	8	269	1.1850	1.31
9	224	1.2795	1.26	9	287	1.1525	1.33
10	242	1.2391	1.28	10	305	1.1226	1.34
11	260	1.2022	1.30	11	323	1.0949	1.36
12	278	1.1684	1.32	12	341	1.0690	1.38
13	296	1.1373	1.34	13	359	1.0449	1.39
14	314	1.1085	1.35	14	377	1.0222	1.41
15	332	1.0817	1.37	15	395	1.0010	1.42
16	350	1.0567	1.39	16	413	0.9809	1.44
17	368	1.0334	1.40	17	431	0.9620	1.45
18	386	1.0114	1.42	18	449	0.9440	1.47
19	404	0.9908	1.43	19	467	0.9270	1.48
20	422	0.9713	1.45	20	485	0.9108	1.49

Tab. 4.4 Ion properties most likely negative ion clusters

Following this procedure, Fig. 4.51 shows the size distribution of positively charged ions derived during dry and clean conditions as explained in detail in

section 4.2 with labels displaying the approximate hydration state of the specific ion clusters. For these conditions, 5 to 6 fold hydrated clusters seem to form the predominant “main” peak that is always present at 1.1nm. The smaller clusters that are only present at extremely clean carrier gas conditions convert to 2 to 3 fold or 3 to 4 fold hydrated H_3O^+ ions. With increasing size, also the hydration state of the clusters increases. Therefore, the larger clusters of relatively low abundance show hydration states from approximately 9 to 19 attached water molecules.

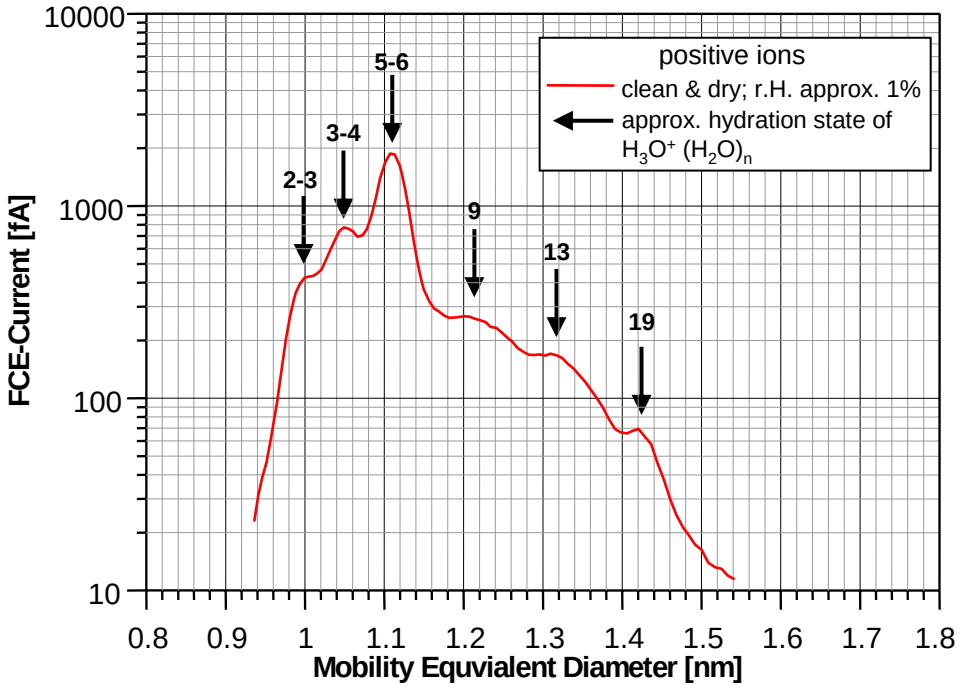

Fig. 4.51 Possible hydration states of the produced positively charged clusters

For negative polarity Fig. 4.52 illustrates the possible ion cluster species and their hydration state. Following the considerations from above, the main peak below 1nm is made up by the nitric acid monomer cluster NO_3^- alone. Because of the big uncertainty of the mobility-mass approximation, the shoulder in the size distribution facing towards larger sizes could be interpreted as a $NO_3^-(H_2O)$ cluster. Accordingly, the larger clusters at 1.94nm convert to $NO_3^-(H_2O)_2$ at 1.22nm to $NO_3^-(H_2O)_7$ or NO_3^- HNO_3 $(H_2O)_4$ and at 1.32 nm to $NO_3^-(H_2O)_{11}$ or NO_3^- HNO_3 $(H_2O)_8$.

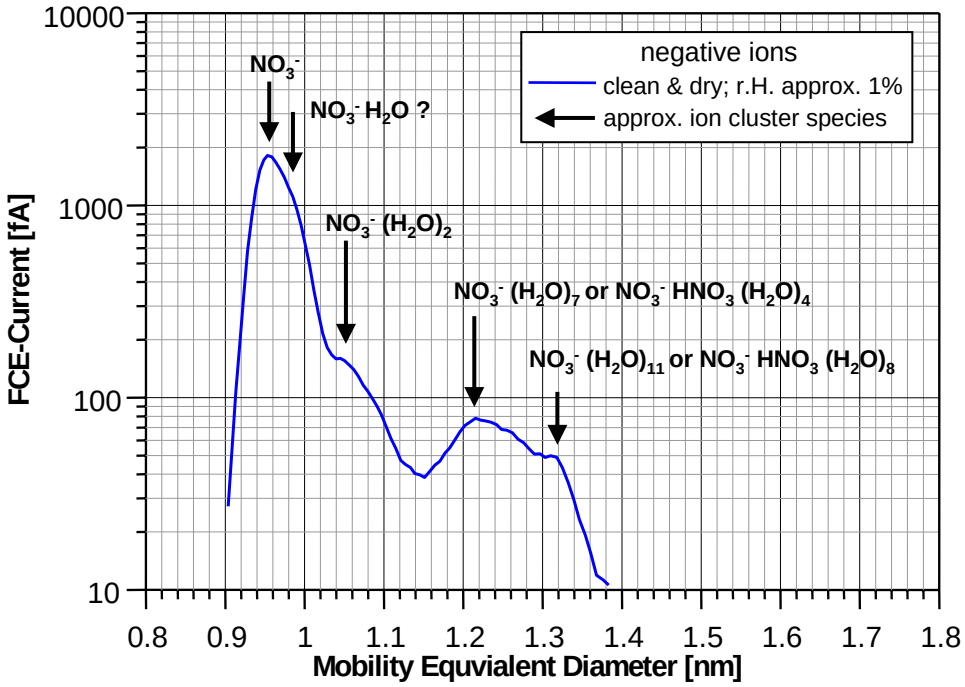

Fig. 4.52 Possible hydration states of the produced negatively charged clusters.

To conclude this section, all measurements performed so far show a strong influence of the amount of water vapour present in the carrier gas on the produced ion cluster species in the charging device. Therefore, it has to be assumed, that the produced clusters are in majority hydrated ions. H_3O^+ for the positive ions and nitric acid n-meres for the negatives are the most likely generated primary ions and the majority of the ionic molecules produced in the charger might be hydrated clusters of these ion species.

Still, as these are only the most likely clusters, numerous other cluster configurations are possible and only thoroughly performed mass spectrometric measurements will be able to moredeliver detailed information on the generated molecular ions.

4.7. Mean Mobility and Mass of Charger generated Ions

As already mentioned several times before, electrical mobility spectrometry relies on charged particles. If there are - a priori - no charged particles present, or in an undefined charging state, the aerosol has to be charged with an appropriate method. As can be seen in section 2.3., not all particles will be charged to the same extent. Therefore the corresponding charging probabilities have to be determined.

For bipolar diffusion charging – as is the case in an ^{241}Am charger – the charging theory by Fuchs (Fuchs 1963) gives the best description of the interaction of ion clusters with aerosol particles during the charging process; with the ions' mean mass and mean mobility as the two crucial input parameters for the calculation of the charging probabilities.

The high resolution measurements performed during this work have determined the mobility/size distributions of the ions that are responsible for the charging of aerosol particles. These experiments were carried out with different carrier gases and carrier gas conditions (contaminated and humidified), resulting in completely different mobility distributions. The different mobility spectra always show a general pattern but with distinctly different relative abundances of the individual cluster species.

Therefore, also the mean mobility of the charging ions is strongly affected by the quality and condition of the carrier gas. The experiments performed in section 4.4., where different tubing material was used as source of contaminations, have shown the widest variety of possible mobility/size distributions. By averaging over the measured mobility distributions, a mean mobility can be determined as representative value for the ion's properties for the specific gas conditions.

The resulting mean mobility values for the ions during the contaminated carrier gas measurements are shown in Fig. 4.53 for positive ions and Fig. 4.54 for negative ions. For comparison, the graphs also show the mean mobility values presented by Reischl et al (1996) as a reference for typically used input parameters for Fuchs' charging theory.

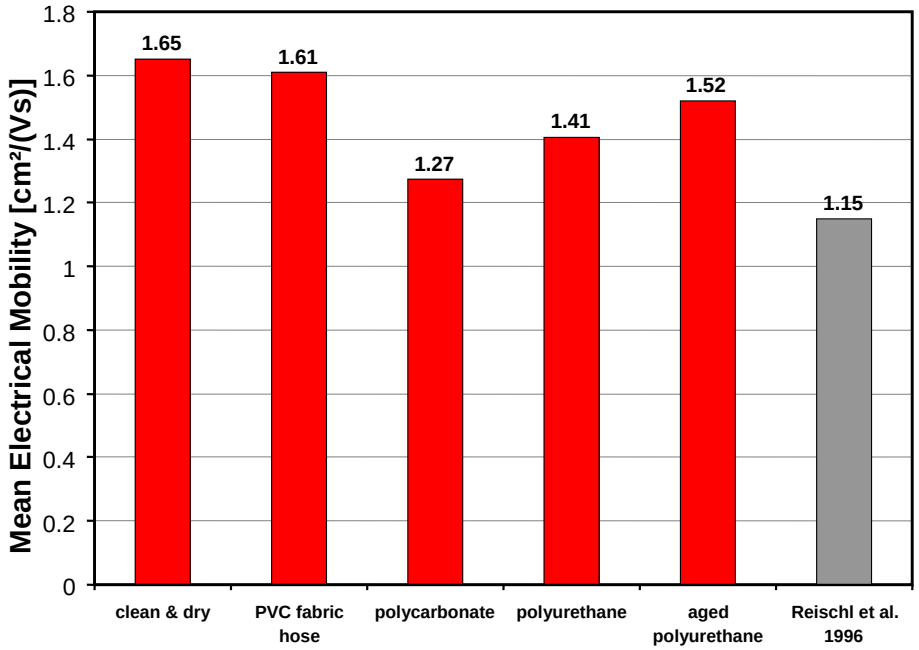

Fig. 4.53 Mean ion mobility $\overline{Z}^{+}$ of positive ions for different tubing materials

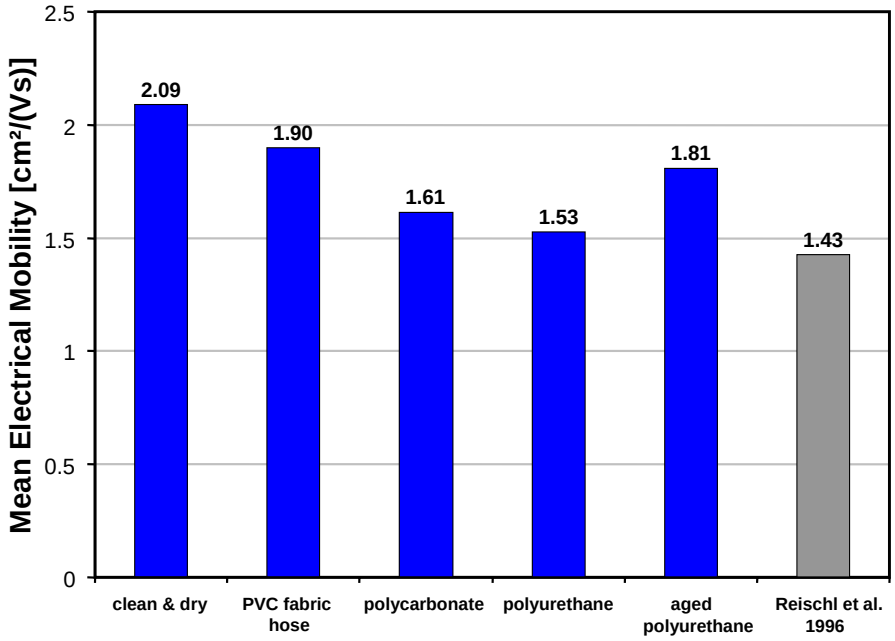

Fig. 4.54 Mean ion mobility $\overline{Z}^{-}$ of negative ions for different tubing materials

For the positive ions, the data by Reischl et al. (1996) gives the lowest mean ion mobility ($\overline{Z}^{+}$ = 1.15 cm^2/Vs) – apparently considering larger ion clusters. For the measurements performed during this thesis, the differences between the mean mobility of positive ions can be up to 30% when comparing the experiments

performed during clean and dry conditions ($\overline{Z}^+$ = 1.65 cm^2/Vs) and the polycarbonate tubing in front of the charger ($\overline{Z}^+$ = 1.27 cm^2/Vs). For negative ions, the mean mobility values are generally higher as the ion molecules form smaller clusters with a maximum mean ion mobility for clean and dry conditions of $\overline{Z}^-$ = 2.09 cm^2/Vs, but also here, differences up to 40% can be found for the mean electrical mobility of the ions.

Kilpatrick's empirical mass-mobility relationship allows (at least a rough) approximation of the corresponding masses to get the second input parameter of Fuchs' charging theory. Doing this, the differences in the resulting mean ion masses become even worse.

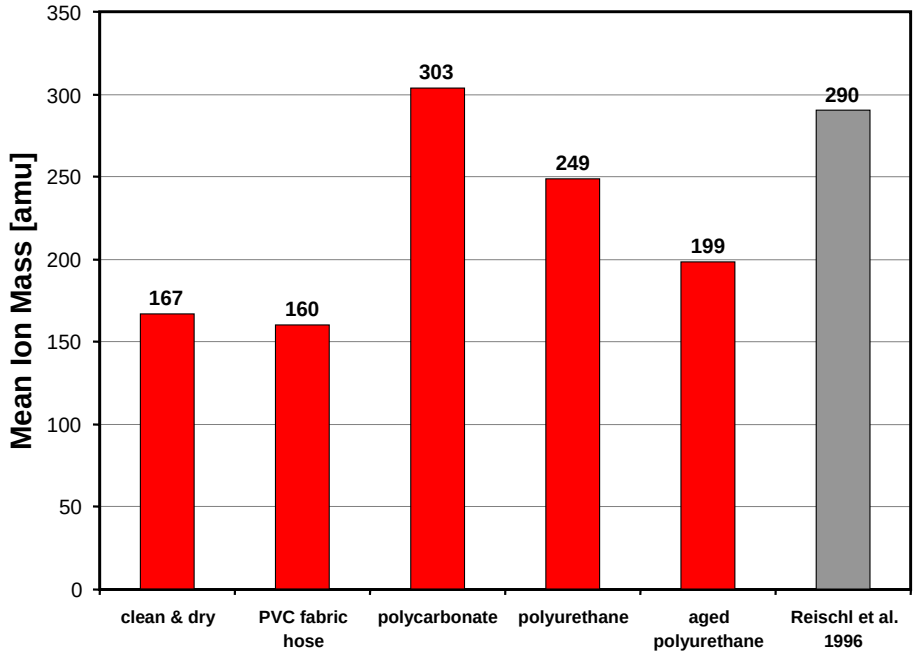

Fig. 4.55 Mean ion mass $\overline{m}^+$ of positive ions for different tubing materials

For positive ions, a maximum difference of 90% can be found by comparing the estimated mean ion masses for the operating conditions with the PVC fabric hose in front of the charger ($\overline{m}^+$ = 160 amu) and the polycarbonate tubing in front of the charger ($\overline{m}^+$ = 303 amu).

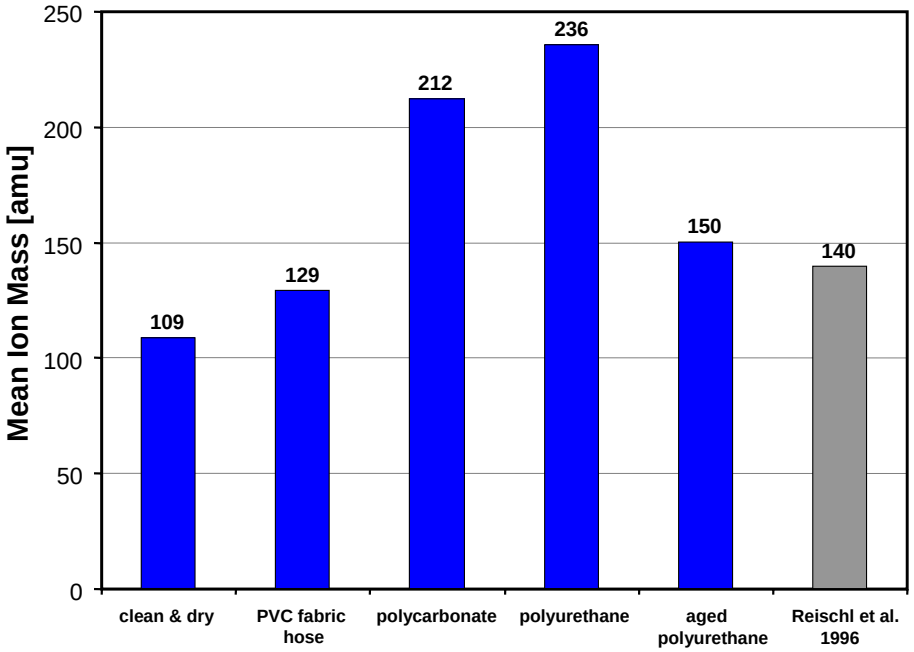

Fig. 4.56 Mean ion mass $\overline{m}^-$ of negative ions for different tubing materials

For negative ions even a maximum difference of more than 200% can be found for the mean ion masses ($\overline{m}^-$ = 109 amu for clean and dry conditions and $\overline{m}^-$ = 236 amu using the polyurethane tubing in front of the charger).Tab. 4.5 finally tabulates the resulting mean ion mobilities $\overline{Z}^{\pm}$ and mean ion masses $\overline{m}^{\pm}$ for positive and negative ions produced by ^{241}Am α-radiation, influenced by the use of different tubing materials in front of the charger. For comparison, also the values given by Reischl et al. (1996) are listed.

tubing material / gas condition	$\overline{Z}^+$ [cm²/Vs]	$\overline{m}^+$ [amu]	$\overline{Z}^-$ [cm²/Vs]	$\overline{m}^-$ [amu]
clean and dry	1.65	167	2.09	109
PVC fabric hose	1.61	160	1.90	129
polycarbonate	1.27	303	1.61	212
polyurethane	1.41	249	1.53	236
aged polyurethane	1.52	199	1.81	150
Reischl et al. 1996	1.15	290	1.43	140

Tab. 4.5 Comparison of mean ion mobilities $\overline{Z}^{\pm}$ and mean ion masses $\overline{m}^{\pm}$

Apparently, there are big differences in the mean ion mobilities and the mean ion masses if contaminations in the carrier gas are present. As these two parameters are the only independent input parameters for the charging ions to calculate the charging probabilities on aerosol particles in Fuchs's charging theory (Fuchs, 1963), it seems reasonable to assume that the calculated charging probabilities will be strongly dependent on the different ion properties. If this is true and how much the charging probabilities will depend on the ions' properties will be evaluated in the upcoming section 4.8.

4.8. Influence of the Ions' Properties on the Charging Probabilities

With the experimentally determined ion mobilities and the approximated ion masses, the remaining ion properties that are necessary for Fuchs's charging theory can be calculated. According to equation [2.34], the mean thermal velocity $\overline{c}^{\pm}$ can be written as:

$$\overline{c}^{\pm} = \sqrt{\frac{8 \cdot k \cdot T}{\pi \cdot \overline{m}^{\pm}}}$$

where k_B is Boltzmann's constant, T the absolute temperature and $\overline{m}^{\pm}$ the mean ion mass. Its determination is important for calculating the mean free path $\lambda^{\pm}$ of the ionic clusters which can be expressed as following: (compare equation [2.32])

$$\lambda^{\pm} = \frac{16\sqrt{2}}{3\pi} \cdot \frac{D^{\pm}}{\overline{c}^{\pm}} \cdot \left(\frac{M}{M + \overline{m}^{\pm}} \right)^{1/2}$$

The diffusion coefficient $D^{\pm}$ of the charging ions can be determined from the Einstein relation

$$D^{\pm} = B^{\pm} \cdot k \cdot T \qquad [4.4]$$

where B is the ions' mechanical mobility that is proportional to the electrical mobility Z (compare equation [2.57])

$$Z^{\pm} = B^{\pm} \cdot e_0 \qquad [4.5]$$

with e_0, the elementary unit of charge.

This way, the ions' properties can be extended by three additional parameters per polarity: the ions' mean thermal velocity $\bar{c}^{\pm}$, their mean free path $\lambda^{\pm}$ and their diffusion coefficient $D^{\pm}$:

tubing material / gas condition	$\bar{c}^{+}$ [m s^{-1}]	λ^{+} [nm]	D^{+} [m^2 s]
clean and dry	192.62	19.98	4.17 E-6
PVC fabric hose	196.86	19.41	4.07 E-6
polycarbonate	142.99	15.94	3.22 E-7
polyurethane	157.95	17.44	3.55 E-7
aged polyurethane	176.72	18.60	3.84 E-6
Reischl et al. 1996	146.26	14.36	2.90 E-7
	$\bar{c}^{-}$ [m s^{-1}]	λ^{-} [nm]	D^{-} [m^2 s]
clean and dry	240.25	24.47	5.34 E-6
PVC fabric hose	220.22	22.59	4.84 E-6
polycarbonate	171.77	19.89	4.11 E-6
polyurethane	163.07	18.98	3.90 E-6
aged polyurethane	204.30	21.82	4.62 E-6
Reischl et al. 1996	211.58	17.08	3.64 E-7

Tab. 4.6 Comparison of ion cluster properties $\bar{c}^{\pm}$, $\lambda^{\pm}$ and $D^{\pm}$, calculated from mean ion mobility $\bar{Z}^{\pm}$ and mean ion mass $\bar{m}^{\pm}$.

As soon as these input parameters are available, the charging probabilities for aerosol particles, being charged by positive or negative ions of very different properties – mainly dependent on the purity of the carrier gas - can be calculated. The resulting graphs for the charging probabilities for positive (Fig. 4.57) and negative (Fig. 4.58) singly charged particles show a quite unexpected behaviour:

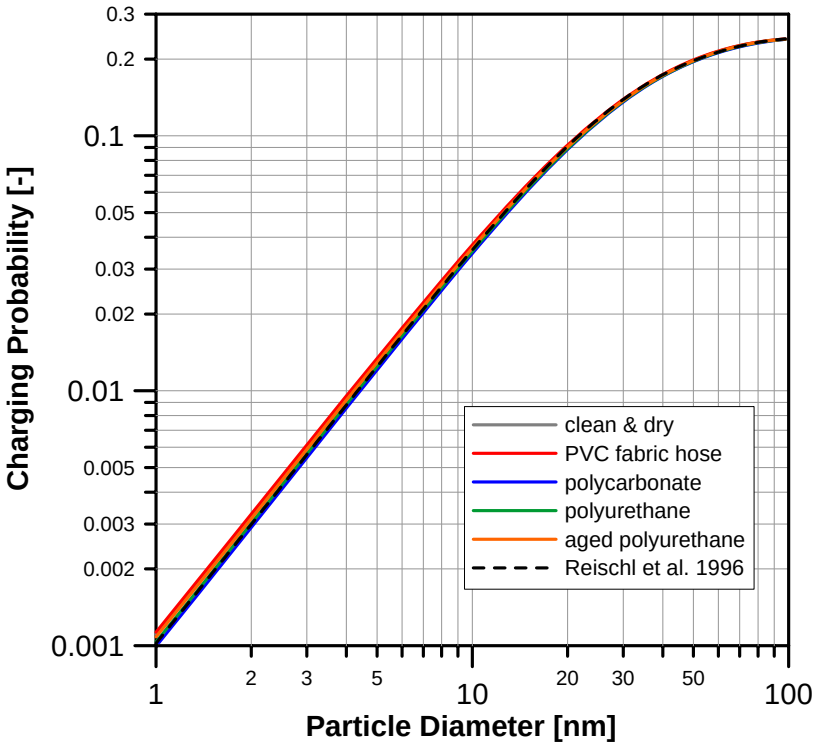

Fig. 4.57 Calculated charging probabilities for singly, positively charged particles using different physical properties of the charging ions.

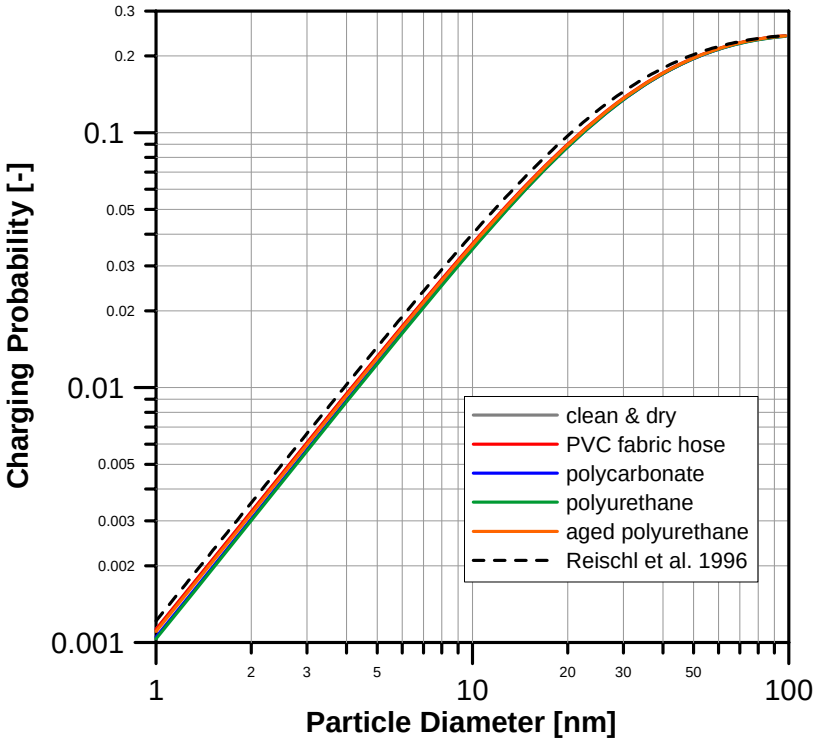

Fig. 4.58 Calculated charging probabilities for singly, negatively charged particles using different physical properties of the charging ions.

The data converges for large particles around 100nm and splits up – for both polarities - only slightly with decreasing particle size, although the input parameters determined from the different positive ions measurements were completely different (compare Tab. 4.5).

By plotting only the most extreme data sets for both polarities, minor differences in the calculated charging probabilities can be found. The red lines in Fig. 4.59 show the highest (solid line) and lowest (dashed line) charging probability curves for positive ions; the blue lines stand for the negative ions.

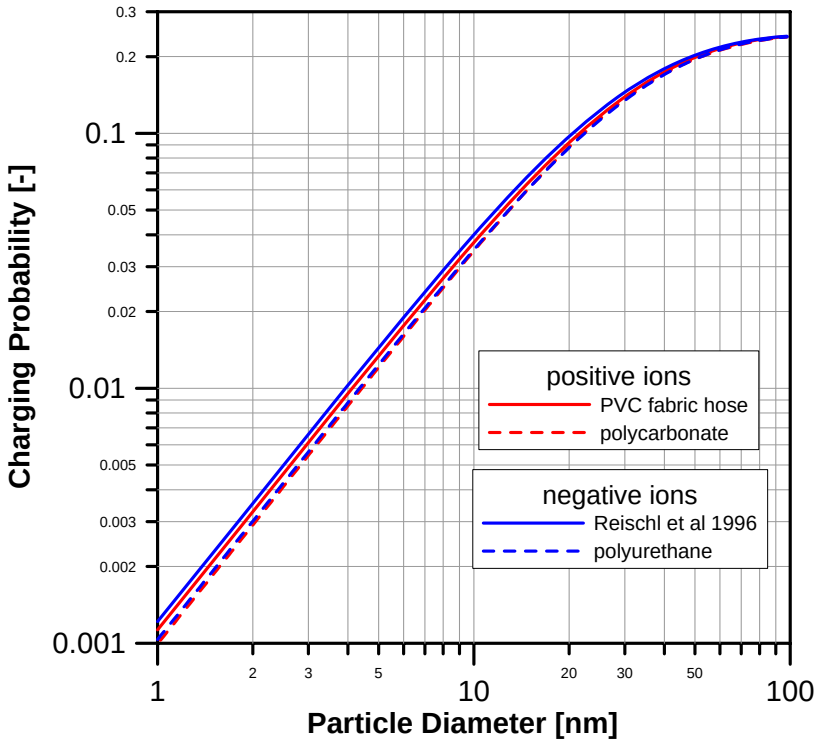

Fig. 4.59 Most extreme data sets for the calculated charging probabilities

Generally, negative ions show a slightly higher charging probability compared to the positive ions. However, the differences between the individual curves are almost negligible, as displayed by a close up for small particles of the most extreme data sets in Fig. 4.60.

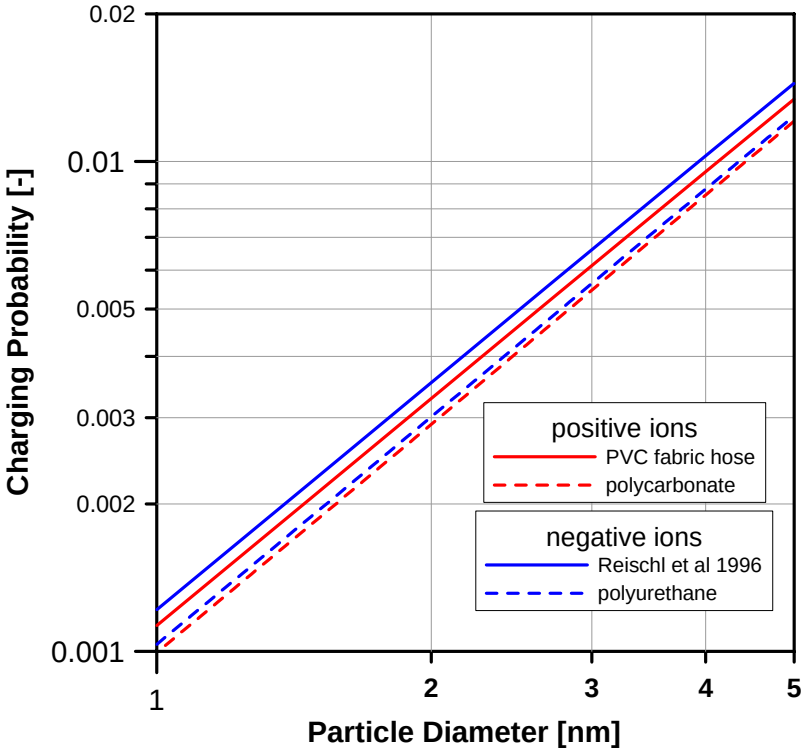

Fig. 4.60 Close up for small particles of the most extreme data sets for the calculated charging probabilities

For the big differences in the experimentally determined mean ion mobilities and masses, for sure a bigger effect on the calculated charging probabilities was expected.

However, the minor effect of the different ion properties on the calculated charging probabilities can be easily explained by looking in more detail into Fuchs' charging theory: There, the ions' mean mobilities and masses are used to calculate the ions mean thermal velocity $\bar{c}^{\pm}$ (see equation [2.34]) and further the ions' diffusion coefficient $D^{\pm}$ (see equations [4.4] and [4.5]). These parameters are needed to calculate the mean free path $\lambda^{\pm}$ of the ions (equation [2.32]) which controls the radius $\delta^{\pm}$ of the limiting sphere (equation [2.31]):

$$\delta^{\pm} = \frac{a^3}{\lambda^{\pm 2}} \left[\frac{1}{5} \left(1 + \frac{\lambda^{\pm}}{a} \right)^5 - \frac{1}{3} \left(1 + \frac{\lambda^{\pm 2}}{a^2} \right) \left(1 + \frac{\lambda^{\pm}}{a} \right)^3 + \frac{2}{15} \left(1 + \frac{\lambda^{\pm 2}}{a^2} \right)^{5/2} \right]$$

Therefore, the larger the mean free path of the ions, the larger the radius of the limiting sphere will become.

These three or four deduced ion properties govern the attachment coefficient η that represents the combination rate of ions and particles from equation [2.43]:

$$\eta_i^{\pm} = \frac{\pi \cdot \delta^{\pm 2} \cdot \bar{c}^{\pm} \cdot \alpha_i^{\pm} \cdot \exp\left[-\frac{\Phi_i\left(\delta^{\pm}\right)}{k \cdot T}\right]}{1 + \exp\left[-\frac{\Phi_i\left(\delta^{\pm}\right)}{k \cdot T}\right] \cdot \frac{\delta^{\pm 2} \cdot \bar{c}^{\pm} \cdot \alpha_i^{\pm}}{4 \cdot D^{\pm} \cdot a} \cdot \int_0^1 \exp\left[\frac{\Phi_i\left(a/x\right)}{k \cdot T}\right] dx}$$

As determined by the conversion from mobility to mass, higher mean ion mobility values implicate a lower mean ion mass and vice versa.

Therefore, according to equation [2.43] with increasing mean ion mobility, the diffusion coefficient D of the ions will become larger and the attachment coefficient η will be increased, resulting in a higher charging probability. At the same time, the attachment coefficient η is reduced by a relative smaller mean thermal velocity $\bar{c}^{\pm}$ of the ions as their mean mass becomes lower with increasing mobility.

This way, the influence of the different ion parameters, triggered by the mean ions' mobilities and masses, that are causing the increase and decrease of the attachment coefficient η almost cancels out.

Although the differences in the calculated charging probabilities seem to be negligible on first sight, Fig. 4.61 shows the maximum uncertainties for the calculated charging probabilities of the ions with different properties.

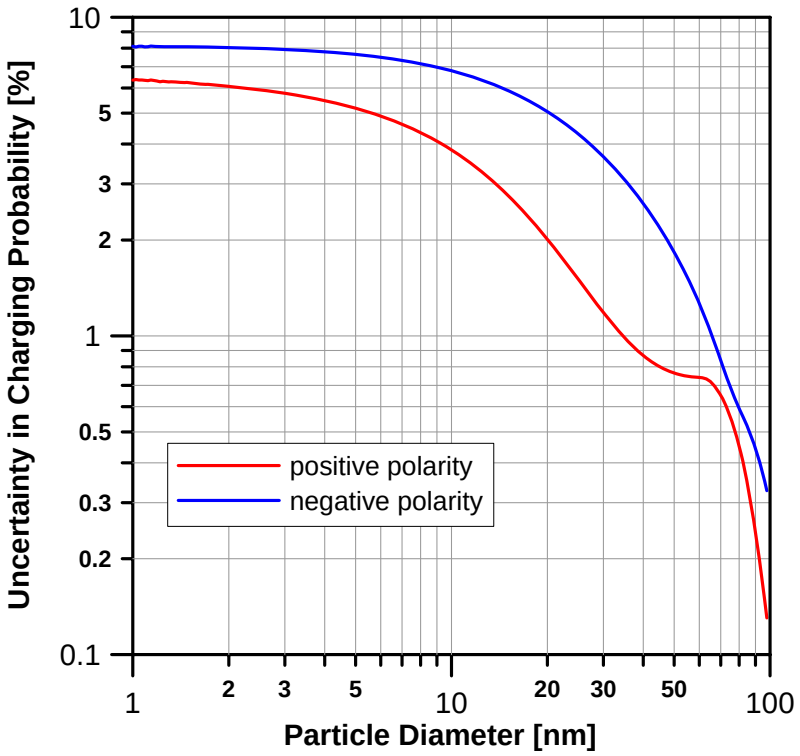

Fig. 4.61 Maximum uncertainties for the calculated charging probabilities for different ion properties

At large particle sizes of 100nm, the differences between the calculated charging probabilities vanish and converge into each other, but for decreasing particle size, the uncertainties increase more and more with a maximum value of ±8.1% for negative ions and ±6.3% for positive ions. That essentially means, that if incorrect ion properties are used for the calculation of the charging probabilities, a measured particle number size distribution that relies on properly calculated charging probabilities will be under- or overestimated by up to ±8.1% or ±6.3% respectively. Of course, these are still rather low deviations, but for atmospheric studies or studies related to particle emissions from internal combustion engines where a very precise determination of the particle concentration is of crucial importance, these uncertainties may be taken into account.

5. Summary and Conclusion

The goal of this doctoral thesis was to gain deeper insights in the properties of molecular ions and their interaction with airborne particles and clusters. For these investigations, the particle and cluster size range below 3nm is of special interest. In the field of aerosol science, Electrical Mobility Spectrometry (EMS) is the most adequate and best known method to access the size range of very small particles. A crucial prerequisite for the EMS method are charged particles as they are classified according to their electrical mobility. Unfortunately, most of the commercially available EMS-systems are limited to the detection of particles > 3nm.

Therefore, in the framework of this thesis, a new high resolution differential mobility analyzer was designed that is able to access particles and molecular clusters below a mobility equivalent diameter of 3nm and has such a high resolution power to be able to separate single molecular clusters in terms of their electrical mobility. The result of this development, the so- called Vienna Type UDMA, is described in detail in chapter 3 and in the paper by Steiner et. al. (2010) given in section 9.1. (Appendix A). The UDMA allows high resolution mobility measurements with a relative FWHM of its transfer function of about 2% at 1.44nm in a recirculating sheath air flow mode, often called “closed loop” arrangement. This operation mode guarantees the well defined condition of the sheath air flow that is necessary for measurements in the lower nanometer size range. Electrospray generated highly monodisperse clusters of various tetraalkylammonium halide salts with a very well defined electrical mobility were used to calibrate the UDMA and to test its resolution power.

The UDMA also proved its abilities for the generation / classification of highly monodisperse molecular clusters as a source for seed particles for experiments focusing on heterogeneous vapour condensation. These investigations are thoroughly described in the paper by Winkler et al. (2008) which is attached to

this thesis in Appendix B1. The Online Supporting Material for the later paper is given in Appendix B2.

With the new UDMA, high resolution mobility measurements of the ions involved in the charging process of aerosol particles, which constitutes the main experimental work of this thesis, were possible. During these experiments the mobility spectra of ions generated in different carrier gases with varying degrees of purity were measured. The results of these experiments revealed that although the ions were generated in different carrier gases, their size distributions show a remarkably similar pattern when the different carrier gases are treated the same way, i.e. if they have the same grade of purification. Especially the use of high efficiency active carbon filters, reducing the amount of organic material in the carrier gas, showed the largest influence on the general profile of the ion size distribution.
With this knowledge, only highly purified laboratory air was used for the determination of the ion mobilities for the cleanest and driest possible conditions. When comparing the size spectra of positive and negative ions, positive ions generally appear at larger sizes in the size spectrum and show a sharp main peak at a mobility equivalent diameter D_p of approximately 1.11nm, corresponding to an electrical mobility Z of 1.63 cm^2/Vs. If the carrier gas conditions are very clean and dry, there are additional cluster species at smaller sizes (higher mobilities) of 1.04nm (1.86cm^2/Vs) and 0.99nm (2.05cm^2/Vs). Negative ions show a dominant peak at about D_p = 0.96-0.98nm (Z=2.18-2.1cm^2/Vs), which appears much broader than its positive counterpart and therefore seems to consist of at least two cluster species with very similar sizes.

Conventional DMAs use radioactive isotopes as ion sources. As these chargers, which provide a theoretically well known bipolar ion distribution, become more and more impractical because of increasing safety restrictions, also alternative ionizing methods (corona discharge and soft X-ray ionization) where tested and investigated in terms of the size distribution of the generated ion clusters. It was seen, that the general pattern of positively and negatively charged ions generated

by the different charging mechanisms strongly resembles each other: an indication that the generated ion clusters are of the same or at least very similar cluster configuration that only depends on the purity and composition of the carrier gas and not on the ionizing method.

To simulate possible sources of contamination that affect the ion formation in the charger, different tubing material of two meters length as duct for the highly purified air was placed in front of the charger. The results of these experiments show completely different patterns of the corresponding ion size distributions. Depending on the generated cluster species, the mean ion mobility equivalent diameter is shifted towards larger or smaller diameters. Therefore also the overall mean electrical mobility is alternating between lower and higher values.
It was found that for positive ions, the use of a PVC fabric hose seems to add the least contamination to the system whereas the most additional ion clusters were produced during the use of polycarbonate tubing. For negative ion polarity, there could not be found any preferable tubing material, as all investigated materials showed the tendency to add contaminations to the system.

Another set of experiments involved a controlled humidification of the carrier gas. These experiments were of special importance, as the primary ions that are directly produced by ionizing radiation will rapidly combine with polar molecules present in the carrier gas to form larger clusters. There is an intense scientific discussion on the actual nature of the clusters produced in an aerosol charger but the current consensus is that at least a large fraction of the newly formed clusters are hydrated molecular ions.

With a specially developed humidifier and liquid air cooling traps, it was possible to change the relative humidity (r.H.) of the carrier gas from less than 1% to over 90% and therefore to study the dependence of the generation of ion clusters on the amount of water vapour present in the system. Here, a slightly different behaviour of the positive and negative ions was observed: with increasing r.H., positive ions more likely form larger clusters but the overall pattern of the size distribution

stays the same. For negative ions, the main peak that can be typically found around 0.96nm shifts towards larger sizes whereas a less abundant peak alongside to the main peak at 1.02nm keeps its position in the size distribution and increases its relative abundance. At the same time, the peaks around 1.2nm, associated to rather less abundant clusters, vanish completely.

This behaviour is a strong evidence that the amount of water vapour present in the system is a major driving parameter for the generation/formation of ionic molecular clusters produced in a bipolar ionic atmosphere and that the different peaks in the ion size distribution most likely correspond to hydration states of preferable and stable primary ion clusters.

By converting the measured mobility distributions into "mass distributions" - derived in this thesis by an empirically derived mass-mobility relationship based on measurements by Kilpatrick (1971), a correlation between the peaks in the mobility spectrum and possible ion cluster configurations can be estimated. According to the literature, the most abundant primary positive ions are proposed to be H_3O^+ or NH_4^+ (e.g. Parts and Luts, 2004). Therefore, following the prevailing idea of the hydration of primary ions, the main peak for positive ions might be interpreted as 5 to 6 fold hydrated H_3O^+ or NH_4^+ clusters. It was seen, that with increasing relative humidity also the fraction of larger clusters is increasing, meaning that the concentration of clusters with higher hydration states is increasing.
For negative ion polarity, the nitric acid monomer ion NO_3^- is thought to be one of the most abundant primary ions (e.g. Nagato et al., 2006). Also in the converted mass distributions from the experimentally determined mobility distributions NO_3^- seems to clearly dominate the spectrum. Again, larger, hydrated clusters are possible but much less abundant compared to the positive ions.

All experiments performed in the course of this thesis have shown that depending on the operating conditions, carrier gas, carrier gas purity and amount of water vapour present in the system, very different ion clusters are produced and the

mean ion mobility (mean ion mobility equivalent diameter) and consequently also the overall mean ion mass is alternating between higher or lower values.

As mean ion mobility and mean ion mass are the only necessary input parameters of the charging ions for the calculation of the charging probabilities for aerosol particles according to Fuchs' charging theory (Fuchs, 1963), it seems reasonable to assume, that the high variability of the physical properties of the ions will strongly affect the calculated charging probabilities especially for very small nanoparticles.

In principle, this is true, but as can be seen in the resulting charging probabilities in section 4.8., the influence of the ions' properties has an almost negligible effect on the calculated charging probabilities. As determined by the conversion from mobility to mass, higher mean ion mobility values implicate a lower mean ion mass and vice versa. In Fuchs' charging theory, on the one hand, inertial interaction will dominate the charging process for low ion mobilities and large ion masses because of the higher kinetic energy of the ions. On the other hand, low ion masses and high ion mobilities promote a diffusive interaction between ions and aerosol particles and transferring this way the charge to the particles. For the molecular ions experimentally investigated during this work, the effect of these two competing processes almost cancels out, resulting in a very weak dependence of the calculated particle charging probabilities on the ions' physical properties.

6. References

Adachi, M., Kousaka, Y. and Okuyama, K. (1985) Unipolar and bipolar diffusion charging of ultrafine aerosol particles. *J. Aerosol Sci., 16, 2, 109.*

Arendt, P. and Kallmann, H. (1926). Über den Mechanismus der Aufladung von Nebelteilchen. *Z. Phys. 35, 421*

Berner, A. (1976) Zur Theorie der Messung von Aerosolgrößenverteilungen mittels einfacher und vielfacher Kaskadenimpaktoren. *Staub, Reinhaltung der Luft 36, 9, 385-390.*

Bricard, J. (1949). L'equilibre ionique de la basse atmosphere. *Journal of Geophysical Research, 54, 1, 39-52*

Brunelli, N.A., Flagan, R.C., Giapis, K.P., (2009). Radial Differential Mobility Analyzer for One Nanometer Particle Classification. *Aerosol Science and Technology, 43, 1, 53-59*

Cabane M. and Playe P. (1980). Mass spectra of negative ions in air-like gas mixtures at atmospheric pressure. *Journal of Aerosol Science, 11, 5-6, 475-482*

Chen, D.-R., Pui, D.Y.H., Kaufman, S.L. (1995). Electrospraying Of Conducting Liquids For Monodisperse Aerosol Generation In The 4nm To 1.8 μm Diameter Range. *Journal of Aerosol Science, 26, 6, 963-977*

De Juan, L. and Fernández de la Mora, J., (1998). High resolution size analysis of nanoparticles and ions: Running a Vienna DMA of near optimal length at Reynolds numbers up to 5000. *Journal of Aerosol Science, 29, 617–626*

Eisele F.L. and Tanner D.J. (1990) Identification of ions in continental air. *Journal of Geophysical Research 95 (1990), pp. 20539–20550.*

Einstein, A. (1905). Über die von der molekularkinetischen Theorie der Wärme geforderte Bewegung von in ruhenden Flüssigkeiten suspendierten Teilchen. *Ann. d. Phys. 17, 549*

Fenn, J. B., Mann, M., Meng, C. K., Wong, S. K., and Whitehouse, C. (1989) Electrospray ionization for mass spectrometry of large biomolecules. *Science 246, 64–71.*

Fernández de la Mora, J. (1999). Method and apparatus for separation of ions in a gas for mass spectrometry. *United States Patent 5,869,831.*

Fernández de la Mora, J. and Attoui, M. (2007). A DMA covering the 1-100 nm particle size range with high resolution down to 1nm. *European Aerosol Conference 2007, Salzburg, Austria, Abstract T02A029.*

Fernández de la Mora, J. (2002). Diffusion broadening in converging differential mobility analyzers. *Journal of Aerosol Science, 33, 411-437*

Fernández de la Mora, J., Thomson, B.A., Gamero-Castaño, M. (2005). Tandem Mobility Mass Spectrometry Study of Electrosprayed Tetraheptyl ammonium bromide Clusters. *Journal of the American Society for Mass Spectrometry 16, 5, 717-732*

Flagan, R.C. (1998). History of Electrical Aerosol Measurements. *Aerosol Science and Technology, 28:4, 301-380.*

Friedlander, S. K. (2000). Smoke, dust and haze. (2nd ed.), Oxford: Oxford University Press.

Fuchs, N.A. (1963). On the stationary charge distribution on aerosol particles in a bipolar ionic atmosphere. *Geofis. Pura Appl. 56, p. 185*

Fuchs, N.A. (1964). The Mechanics of Aerosols. *Pergamon Press, Oxford*

Gamero-Castaño, M. and Fernández de la Mora, J. (2000a). Modulations in the Abundance of Salt Clusters in Electrosprays. *Analytical Chemistry, 72, 7, 1426-1429*.

Gamero-Castaño, M. and Fernández de la Mora, J. (2000b). A Condensation Nucleus Counter (CNC) Sensitive to Singly Charged Sub-Nanometer Particles. *Journal of Aerosol Science, 31 7, 757-772*

Gunn, R. (1954). Diffusion charging of atmospheric droplets by ions, and the resulting combination coefficients. *Journal of Meteorology, 11,5, 339-347*

Heim, M., Attoui, M. and Kasper, G. (2010) The efficiency of diffusional particle collection onto wire grids in the mobility equivalent size range of 1.2 to 8 nm. *Journal of Aerosol Science ,41: 2, 207-222*

Hermann, W., Eichler, T., Bernardo, N. and Fernandez de la Mora, J. (2000). Turbulent Transition Arises at Reynolds number 35,000 in a Short Vienna type DMA with a Large Laminarization Inlet. *Annual Conference of the AAAR, St. Louis, Misouri*

Hewitt, G.W. (1957). The charging of Small Particles for Electrostatic Precipation. *Trans. Am. Inst. Elect. Engrs. 76, 294*

Hinds, W. (1999). Aerosol Technology: Properties, behavior, and measurement of airborne particles 2nd edition, Wileyand Sons, New York.

Hogan, C.J. and Fernández de la Mora, J. (2009). Tandem Ion Mobility-Mass Spectrometry (IMS-MS) Study of Ion Evaporation from Ionic Liquid-

Acetonitrile Nanodrops. *Physical Chemistry Chemical Physics, 11, 36, 8079-8090*

Hontanón E. and Kruis F.E. (2008). Single Charging of Nanoparticles by UV Photoionization at High Flow Rates. *Aerosol Science and Technology, 42:310-323*

Hoppel, W.A. and Frick, G.M. (1986) Ion-aerosol attachment coefficients and the steady-state charge distribution on aerosols in a bipolar ion environment. *Aerosol Sci. Technol. 5, 1.*

Huang, D.D. and Seinfeld, J. H. (1988) On the relation between binary diffusivity and mean free path. *J. Colloid Interface Sci. 125, 2, 733.*

Huertas, M.L., Marty, A.M., Fontan J., Alet, I. and Duffa G. (1971) Measurement of Mobility and Mass of Atmospheric Ions. *Journal of Aerosol Science, 2, 145-150.*

Hussin A., Scheibel H.G., Becker K.H. and Porstendörfer J. (1983) Bipolar diffusion charging of aerosol particles - I: experimental results within the diameter range 4–30 nm. *Journal of Aerosol Science, 14, 5, 671.*

Imanaka, M, Okada, Y., Ehara, K., Takeuchi, K. (2006). Size measurements of gasborne poly(amidoamine) (PAMAM) dendrimers using a differential mobility analyzer (DMA). *Journal of Aerosol Science, 37, 1643 – 1648*

IPCC (2007) Climate Change 2007: The Scientific Basis. Contribution of Working Group I to the Fourth Assessment Report of the Intergovernmental Panel on Climate Change. *Cambridge Univ. Press, New York edited by S. Solomon et al.*

Jokinen, V. and Mäkelä, J.M. (1997) Closed-Loop Arrangement with Critical Orifice for DMA Sheath/Excess Flow System. *Journal of Aerosol Science, 28, 4, 643-648*

Kallinger, P. (2010) Experimentelle Untersuchung der bipolaren Diffusionsbeladung von Aerosolen mit Weichröntgenstrahlung sowie der Nanopartikelbildung unter Weichröntgenstrahlung. *Master's Thesis, Faculty of Phyiscs, University of Vienna.*

Kilpatrick, W.D. (1971), An Experimental Mass-Mobility Relation for Ions in Air at Atmospheric Pressure. In *Proc. Ann. Conf. Mass Spectrosc. 19th, p. 320-326*

Knutson, E.O. and Whitby, K.T. (1975a). Aerosol Classification by Electric Mobility: Apparatus, Theory and Applications. *Journal of Aerosol Science, 6, 443*

Knutson, E.O. and Whitby, K.T. (1975b). Accurate Measurement of Aerosol Electric Mobility Moments. *Journal of Aerosol Science 6, 453*

Ku, B.K. and Fernández de la Mora, J. (2009). Relation between Electrical Mobility, Mass, and Size for Nanodrops 1-6.5 nm in Diameter in Air. *Aerosol Science and Technology, 43, 3, 241-249*

Kulmala, M., Riipinen, I., Sipilä, M., Manninen, H.E., Petäjä, T., Junninen, H., Dal Maso, M., Mordas, G., Mirme, A., Vana, M., Hirsikko, A., Laakso, L., Harrison, R., Hanson, I., Leung, C., Lehtinen, K.E.J., Kerminen, V.-M. (2007). Toward Direct Measurement of Atmospheric Nucleation. *Science, 318, 5847, 89-92*

Liu, B.Y.H. and Pui, D.Y.H. (1974). Equilibrium Bipolar Charge Distribution of Aerosols. *Journal of Colloid and Interface Science, Vol. 49, No. 2, 305-312*

Mäkelä, J.M., Riihelä, M., Ukkonen, A., Jokinen, V, Keskinen, J. (1996) Comparison of mobility equivalent diameter with Kelvin-Thomson diameter using ion mobility data. *J. Chem. Phys. 105 (4), 1562-1571*

Martínez-Lozano, P. and Fernández de la Mora, J. (2005). Effect of Acoustic Radiation on DMA Resolution. *Aerosol Science and Technology, 39:9 866-870*

Martínez-Lozano, P. and Fernández de la Mora, J. (2006). Resolution improvements of a nano-DMA operating transonically. *Journal of Aerosol Science, 37, 500-512*

Mesbah, B., Boulaud, D., Pourprix, M. and Renoux, A. (1993). Circular Electric Mobility Spectrometer. *Journal of Aerosol Science, 24, 219*

Meyer N.K, Fierz, M., Houle, C., Steigmeier, P. and Burtscher, H. (2008). A new electrical bi-polar aerosol neutralizer. *Abstract T04A047P European Aerosol Conference 2008, Thessaloniki, Greece*

Nagato, K., Tanner, D.J., Friedli, H.R. and Eisele, F.L. (1999) Field measurement of positive ion mobility and mass spectra at a Colorado site in winter, *Journal of Geophysical Research 104 (1999), pp. 3471–3482.*

Nagato, K., Matsui, Y., Miyata, T., Yamauchi, T. (2006). An analysis of the evolution of negative ions produced by a corona ionizer in air. *International Journal of Mass Spectrometry 248, 142-147*

Ooghe, M., Mesbha, B., Pourprix, M. and Boulaud, B. (1994). Radial Flow Differential Mobility Analyzer (RF-DMA). *Proc. of the 4th Int. Aerosol Conference, Los Angeles 1994, pp. 463 – 464*

Parts T.-E. and Luts A. (2004). Observed and simulated effects of certain pollutants on small air ion spectra: I, Positive Ions. *Atmospheric Environment 38, pp. 1283–1289*

Rader, D.J. and McMurry P.H. (1986). Application of The Tandem Differential Mobility Analyzer To Studies of Droplet Growth or Evaporation. *Journal of Aerosol Science, 17, 5, 771-787*

Reischl G.P., Scheibel, H.G., Porstendörfer, J. (1983). The Bipolar Charging of Aerosols: Experimental Results in the Size Range below 20-nm Particle Diameter. *Journal of Colloid and Interface Science, 91, 1, 272-275*

Reischl, G.P. (1991). Measurement of Ambient Aerosols by the Differential Mobility Analyzer Method: Concepts and Realization criteria for the Size Range between 2 and 500 nm. *Aerosol Science and Technology*, *14, 5*

Reischl, G.P., Mäkelä, J.M. and Necid, J. (1996). Bipolar Charging of ultrafine Particles in the Size Range below 10 nm. *Journal of Aerosol Science. 27, 931*

Reischl, G.P., Mäkelä, J.M. and Necid, J. (1997). Performance of Vienna Type Differential Mobility Analyzer at 1.2-20 Nanometer. *Aerosol Science and Technology*, *27, 651-672*

Romero-Sanz, I., Aguirre-de-Carcer, I. and Fernández de la Mora, J. (2005) Ionic propulsion based on heated Taylor cones of ionic liquids, *J. Prop. and Power, 21, No. 2, 239-242*

Rosell-Llompart, J. and Fernández de la Mora, J (1994). Generation of monodisperse droplets 0.3 to 4μm in diameter from electrified cone-jets of highly conducting and viscous liquids. *Journal of Aerosol Science, 25, 6, 1093-1119*

Rosell-Llompart, J., Loscertales, I.G., Bingham, D. and Fernández de la Mora, J. (1996). Sizing nanoparticles and ions with a short differential mobility analyzer. *Journal of Aerosol Science, 27, 695–719*

Rosser, S., and Fernández de la Mora, J. (2005). Vienna type DMA of high Resolution and high flow rate. *Aerosol Science and Technology*, *39,12, 1191-1200*

Steiner, G. (2006). Generierung von Nanopartikeln – Über die Konstruktion eines Heizdraht- Wolframoxid Generators. *Diploma Thesis, Faculty of Physics, University of Vienna*

Steiner, G., Attoui, M., Wimmer, D. and Reischl, G.P. (2010). A Medium Flow, High Resolution Vienna DMA running in Recirculating Mode. *Aerosol Science and Technology, 44: 4, 308 – 315*

Stolzenburg, M. R. (1988). An Ultrafine Aerosol Size Distribution Measuring System, *PhD. Thesis, Mechanical Engineering Department, Univ. of Minnesota, Minneapolis*

Stolzenburg, M.R. and McMurry, P.H. (2008) Equations Governing Single and Tandem DMA Configurations and a New Lognormal Approximation to the Transfer Function. *Aerosol Science and Technology, 42, 421-432*

Tammet, H. (1970). The aspiration method for the Determination of Atmospheric-Ion Spectra. *IPST for NSF, Jerusalem*

Taylor, G (1964). Disintegration of Water Drops in an Electric Field *Proc. R. Soc. Lond. A July 28, 1964 280:383-397; doi:10.1098/rspa.1964.0151*

Ude, S. and Ferández de la Mora, J. (2005). Molecular monodisperse mobility and mass standards from electrosprays of tetre-alkyl ammonium halides. *Journal of Aerosol Science, 36, 1224-1237*

Wagner, P.E., (1985) A Constant-Angle Mie Scattering Method (CAMS) for Investigation of Particle Formation Processes. *J. Colloid Interface Sci. 105, 456*

Wagner, P.E., Kaller,D., Vrtala, A., Lauri, A., Kulmala, M. Laaksonen, A.(2003) Nucleation probability in binary heterogeneous nucleation of water-n-propanol vapor mixtures on insoluble and soluble nanoparticles. *Phys. Rev. E 67, 02160*

Wiedensohler, A. (1988). An approximation of the bipolar charger distribution for particles in the submicron size range. *J. Aerosol. Sci., 19, 3, 387-389*

Wiedensohler, A. and Fissan, H. J. (1991) Bipolar Charge Distributions of Aerosol Particles in High-Purity Argon and Nitrogen. *Aerosol Science and Technology, 14, 3, 358.*

Wimmer, D. (2009). Generation and Classification of Airborne Molecular Clusters. *Master Thesis, Faculty of Physics, University of Vienna*

Winkler, P.M., Steiner, G., Vrtala, A., Vehkamäki, H., Noppel, M., Lehtinen, K.E.J., Reischl, G.P., Wagner, P.E. and Kulmala, M. (2008). Heterogeneous nucleation experiments bridging the scale from molecular ion clusters to nanoparticles. *Science, 319, 5868, 1374-1377*

Winklmayr, W., Reischl, G.P., Lindner, A.O. and Berner A. (1991). A New Electromobility Spectrometer for the Measurement of Aeorosol Size Distribution in the Size Range from 1 to 1000 nm. *Journal of Aerosol Science, 22, 289*

Yun, K.M., Lee, S.Y., Iskandar, F., Okuyama, K., Tajima, N. (2009). Effect of X-ray energy and ionization time on the charging performance and nanoparticle formation of a soft X-ray photoionization charger. *Advanced Powder Technology, 20, 529-536*

Zeleny, J. (1929). The Distribution of Mobilities of Ions in Moist Air. *Phys. Rev. 34, 310-334*

Zhang, S. H., Akutsu, Y., Russell, L.M., Flagan, R.C. and Seinfeld, J.H. (1995). Radial Differential Mobility Analyzer. *Aerosol Science and Technology*, *23, 357*

Zhang, S.H., Flagan, R.C. and Seinfeld, J.H. (1996). Resolution of the Radial Differential Mobility Analyzer for Ultrafine Particles. *Journal of Aerosol Science, 27, 1179*

7. Index of Tables and Figures

8. Curriculum Vitae

Name	Gerhard Steiner
Citizenship	Austrian
Degree	„Magister der Naturwissenschaften“ (Mag. rer. nat.)
Date of birth	16th of May, 1980
Place of birth	Eisenstadt, Burgenland, Austria
Marital status	married
Child	Maximilian, born in 2010
E-mail	g.steiner@univie.ac.at

Education (including military service)

starting 03 / 2006	Doctoral studies of natural sciences at the University of Vienna, supervisor: Prof. Georg P. Reischl
03 / 2006	Graduation with merits with the academic degree Mag. rer. nat. title of diploma thesis: „Generation of Nanoparticles – About the construction of a heating wire tungsten oxide particle generator“
03 / 1999 – 03 / 2006	Studies of Physics at the University of Vienna
07 / 1998 – 03 / 1999	Military service in Austria’s Federal Armed Forces
09 / 1990 – 06 / 1998	Bundesgymnasium und Bundesrealgymnasium (Grammar school) Neusiedl am See, Burgenland
09 / 1986 – 06 / 1990	Volksschule (Elementary school) Wallern im Burgenland

Scientific Career & Teaching

since 2011	Referee for the Journal “Atmospheric Measurement Techniques”
since 2010	Referee for the Journal “Aerosol Science and Technology”
since 10 / 2009	Lecturer for „Introduction to Physics I & II“ together with Prof. Paul Wagner
since 06 / 2008	Project co-worker FWF grant P20837-N20 “Simultaneous mobility-mass determination of charged molecular clusters”
since 2008	Member of the “Gesellschaft für Aerosolforschung”
03 / 2007-06 / 2007	Lecturer in laboratory courses “Practical in Physics for Biologists”
since 10 / 2006	Lecturer for introductory courses “Methods of Experimental Physics I & II”

Vienna, April 2011 Gerhard Steiner

9. Appendix

9.1. Appendix A

Steiner et al. (2010)

A Medium Flow, High Resolution Vienna DMA running in Recirculating Mode. *Aerosol Science and Technology, 44: 4, 308 – 315*

Aerosol Science and Technology, 44:308–315, 2010

ISSN: 0278-6826 print / 1521-7388 online
DOI: 10.1080/02786821003636763

A Medium Flow, High-Resolution Vienna DMA Running in Recirculating Mode

G. Steiner,[1] M. Attoui,[2] D. Wimmer,[1,3] and G. P. Reischl[1]

[1]*Aerosol-, Bio- and Environmental Physics, Faculty of Physics, University of Vienna, Vienna, Austria*
[2]*Département de Physique, Université Paris XII, Val de Marne, France*
[3]*Institute for Atmospheric and Environmental Sciences, Goethe—University Frankfurt am Main, Frankfurt am Main, Germany*

In this work we present the latest design of the Vienna type Differential Mobility Analyzer (DMA). The so-called UDMA is specially designed for high-resolution mobility measurements for the particle size range between 1 and 5 nm and has been optimized to be combined with a mass spectrometer to provide a well-defined mobility fraction of molecular clusters. As the UDMA is designed for this narrow size range it features high-resolution mobility measurements already at flow rates of approximately 700 L/min, marked as medium flow conditions. This readily allows operating the UDMA in a recirculating sheath air flow system with gas cleaning filters, as the control over the purity of the sheath air is crucial for operating the UDMA inline with a mass spectrometer or other carrier gas sensible devices.

The performance of the newly developed UDMA was tested by the analysis of well-defined molecular clusters produced by an electrospray source and compared with one of the state-of-the-art high resolution DMAs also known as "Attoui DMA." For the UDMA, a relative FWHH of the transfer function of 2.5% in mobility-size was found for the monomer clusters of Tetraheptylammoniumbromide (THAB) at 1.44 nm mobility equivalent diameter.

1. INTRODUCTION

The idea of the classification of particles according to their electrical mobility goes back to Rohman (1923) and further to Zeleny (1929). Knutson and Whitby (1975a,b) improved the theory as well as the classifying device. Over the past decades, several designs for the instrumentation have been developed. Differential mobility spectrometry has become a reliable method and a standard technique for the determination of particle number size distributions over several orders of magnitude of particle size and the generation of monodisperse particles. Good overviews on the development of Differential Mobility Analyzer (DMA) designs can be found in the reviews by Rosell-Llompart et al. (1996), Reischl et al. (1997), Winklmayr et al. (1991), and Knutson and Whitby (1975a,b).

The DMA development in Vienna was initiated by Benjamin Liu in the late 1970s. He suggested applying the technologies developed in Vienna for building high precision aerosol centrifuges and cascade impactors to DMAs. The first Vienna type DMAs were designed and used for ambient aerosol particle measurements and were optimized for a large size range from 3 nm to 1000 nm. The major difference to the Minneapolis design (Hewitt's design) was a bullet shaped center electrode providing a steadily accelerating sheath air flow in the region where the aerosol is overlaid to the sheath air flow and an improved aerosol inlet system. As Hewitt's design used a radial inlet of the aerosol flow, the Vienna type introduced a tangential inlet of the aerosol flow into the DMA. Also the excess air outlet was redesigned to avoid distortions of the flow pattern in the classifying channel. Although the Vienna DMA was designed for a large size scale, shortened versions of the initial design were found to be able to extend the lower particle size limit to 1 nm. That way it was possible to determine the mobility distribution of ionic molecular clusters originating from bipolar diffusion chargers (Winklmayr et al. 1991). Juan Fernández de la Mora improved the Vienna design by remodeling the sheath air inlet section and obtained laminar flow conditions at Reynolds numbers up to 5000 (De Juan & Fernández de la Mora 1998). The first high flow DMA designs by Juan Fernández de la Mora had the high voltage applied to the outer electrode in an unsafe operation mode. Michel B. Attoui changed the high voltage back to the inner electrode to avoid this unsafe operation.

Nowadays, at least four types of DMAs are mentioned in the literature; the "TSI type" (Knutson and Whitby 1975a), based on Hewitt's design (Hewitt 1957), "Vienna type" (Reischl 1991; Winklmayr et al. 1991), the "French radial type" called "SMEC" (Mesbah et al. 1993; Ooghe et al. 1994), and the "American radial type" also known as the "Caltech RDMA" (Zhang et al.

Received 24 August 2009; accepted 17 January 2010.

We gratefully thank Prof. M. Kulmala for fruitful discussions and the support by the University of Helsinki. Further, this work was supported by the Austrian Science Fund (FWF, Project No. P20837-N20).

Address correspondence Gerhard Steiner, University of Vienna, Faculty of Physics, Aerosol-, Bio- and Environmental Physics, Boltzmanngasse 5, 1090 Wien, Austria. E-mail: g.steiner@univie.ac.at

1995–1996). The TSI and Vienna types have a cylindrical design and the French and American instruments are radial designs.

Most of the commercially available DMAs based on these designs are limited to the detection of particle sizes in the range from approximately 1000 nm to 3 nm. As the behavior of nanometer-sized particles down to molecular clusters has become of special interest in the last years (Kulmala et al. 2007; Winkler et al. 2008), several authors have reported improved DMA designs capable of accessing the size range below 3 nm and optimized to measure the mobility distribution of molecular clusters (Rossell-Llompart et al. 1996; Eichler 1997; De Juan & Fernández de la Mora 1998; Hermann 2000; Rosser & Fernández de la Mora 2005; Martínez-Lozano & Fernández de la Mora 2006; Brunelli et al. 2009).

These developments also include design modifications, carried out to obtain a better resolution regarding ion mobility and ion mobility equivalent diameter, respectively. In all cases, the most important point is to improve the DMA's performance by minimizing diffusion losses and the diffusion broadening of the transfer function. The crucial parameters for high resolution measurements of molecular clusters are the channel length L, the aspect ratio $L/(R_2 - R_1)$ of the classifying region, where R_1 is the outer diameter of the inner electrode and R_2 the inner diameter of the outer electrode, and the sheath air flow Q_{sh}.

Following the basic ideas of improving the DMA resolution from 1996, a redesign of the Vienna type DMA with a short channel length L of 15.5 mm and an aspect ratio $L/(R_2 - R_1)$ of about 2 (Vienna type NDMA) was investigated for flow rates up to 43 L/min (Steiner 2006). This DMA was designed for an improved performance in the size range below 10 nm compared to the performance of the original Vienna DMA ($L = 110$ mm, aspect ratio: 13.75). The NDMA was mainly used for the generation of monodisperse aerosol particles between 2 nm and 10 nm with a resolution power ranging from a relative FWHH of the transfer function of 9% to 15% in mobility size.

However, the NDMA could not reach the theoretically obtainable resolution, mainly because of an inadequate sheath air laminarization in the inlet system.

The high-flow, high-resolution DMAs developed in the last few years mainly obtain the necessary resolution power by an increased sheath air flow rate up to several cubic meters per minute.

Due to the lack of suitable leak free high flow pumps, the high flow, high resolution DMAs are mostly operated as open systems. The enormous sheath air flow is typically maintained by modified vacuum cleaner pumps (Fernández de la Mora and Attoui 2007), where the sheath air is drawn from the ambient laboratory air into the DMA. Unfortunately, in this operation mode, the option of a well defined and controlled composition of the gas flow through the DMA, which is a crucial feature for operating a DMA inline with carrier gas sensible devices, is lost.

However, in recent studies, where high flow DMAs have been used as mobility classifier in front of a highly sensitive condensation nucleus counter (Gamero-Castaño and Fernández de la Mora 2000a,b) and a mass spectrometer (Fernández de la Mora et al. 2005; Hogan and Fernández de la Mora 2009), low leakage vacuum cleaner pumps have been successfully used for operating the high flow DMAs in a closed loop arrangement, where the excess air flow Q_{ex} is established by an aspirated gas flow and recirculated to the DMA as sheath air flow Q_{sh} (Jokinen and Mäkelä 1997).

Nevertheless, most standard DMAs operating in a closed loop arrangement do not provide the required resolution power in this size range. Typically, they are operated at relatively low sheath air flow rates compared to their channel length and therefore show a large diffusion broadening of their transfer function.

For the purpose of satisfying the above mentioned experimental needs, we modified the design of the above mentioned Vienna type NDMA to obtain the desired resolution without abandoning the option to operate the DMA in a closed loop arrangement. In principle, two major changes were carried out: the aspect ratio of the classifying region was reduced from about 2 to 1 and the inlet section of the sheath air flow was completely redesigned to guarantee a laminar flow through the classification channel. The result of these and other improvements is the so called Vienna type UDMA which already has been used during a joint study on heterogeneous nucleation (Winkler et al. 2008), where classified molecular ions produced by an ^{241}Am neutralizer and tungsten oxide nano-particles served as seed particles for the experiments.

2. DESIGN CONSIDERATIONS/MEASUREMENT TECHNIQUE

For the description of the method of Differential Mobility Spectrometry we would like to refer to Knutson (1976), Liu et al. (1979), and Reischl (1991) as we will assume in the following, that the reader is familiar with the basic theory of the electrical classification of particles in a DMA.

The UDMA is a refinement of the well-known Vienna type DMA design, and has the form of a vertical cylindrical capacitor. To reduce weight, most parts of the UDMA are manufactured of aluminum. Special attention was paid to the quality of the polishing of the interior surfaces, as only well polished optically reflective surfaces provide a well-defined homogeneous electric field between the electrodes. The tube joints for the inlet and outlet flow ports are made of stainless steel; bottom and top insulators are made of PEEK (polyetheretherketone).

In general, two groups of parameters determine the performance of the DMA: the geometry parameters (R_1-outer radius of the inner electrode, R_2-inner radius of the outer electrode, L-effective axial distance between aerosol inlet and aerosol outlet), and the operating conditions (Q_{sh}- sheath air flow rate, Q_a- aerosol flow rate, Q_s- sample air flow rate, Q_{ex}– excess air flow rate). A cross-section of the UDMA is shown in Figure 1.

The purified sheath air Q_{sh} is introduced by four tangential stainless steel connection tubes at the top of the UDMA. The

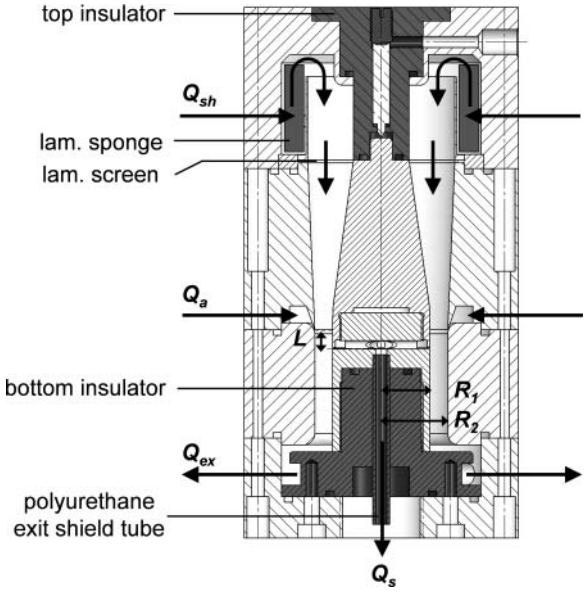

FIG. 1. Cross-section of the UDMA. $L = 6.5$ mm; $R_1 = 17.5$ mm; $R_2 = 24$ mm. The purified sheath air Q_{sh} enters the UDMA by four tangential inlet ports. To provide a uniform laminar flow through the UDMA, a stainless steel laminarization sponge and a 0.2 mm nylon laminarization screen with a mesh size of 50 μm eliminate the tangential component of Q_{sh}. The main parts of the UDMA are made of aluminum; insulating parts, made of PEEK, are shaded in dark gray.

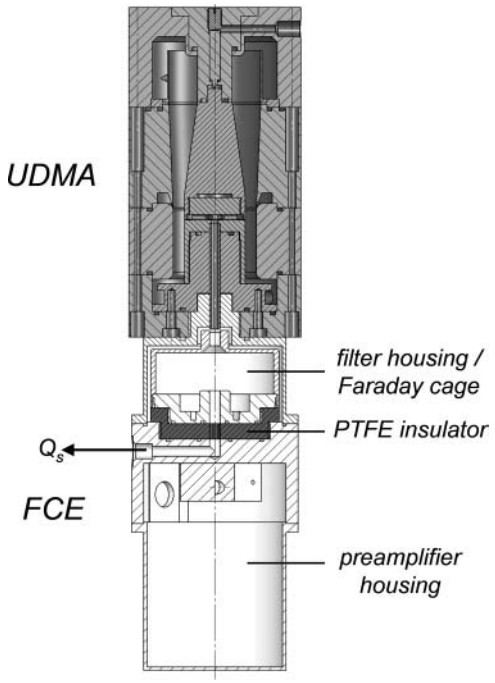

FIG. 2. UDMA with directly flanged custom-built Faraday Cup Electrometer (FCE).

interior upper part mainly consists of a cup-shaped bracket for a woven nylon laminarization screen of 0.2 mm thickness and a mesh size of 50 μm. The cavity between the sheath air inlet ports and the outer wall of the cup-shaped bracket is filled with a stainless steel laminarization sponge to eliminate the tangential component of Q_{sh} in order to provide a uniform laminar flow through the UDMA. For the laminarization sponge, an ordinary stainless steel scrub pad, mainly utilized for dish washing, was used. The upper part of the channel between the electrodes is converging to further accelerate the sheath air flow.

The aerosol inlet volume flow Q_a is fed tangentially through an inlet port in the outer electrode into an annular cavity. A blade like shape of the inner walls and a curvature at the inner side of the outer electrode provide a smooth transition of the aerosol flow into the sheath air flow. Therefore, both airflows can be merged very smoothly which is a main criterion for the classification characteristics.

The classified clusters exit the classification channel as sample air flow Q_s by a narrow annular exit slit in the inner electrode and subsequently enter a directly flanged custom-built Faraday Cup Electrometer (FCE) for detection (see Figure 2). The used FCE is a slightly modified and updated version of the one described by Winklmayr et al. (1991). At the bottom of the UDMA, the residual air flow Q_{ex} exits the UDMA by four tangential connection tubes mounted antipodal to the sheath air inlet ports.

To provide the electrical field between the UDMA's electrodes, a high voltage potential (max. 10 kV; positive and negative polarity are possible) is applied to the inner electrode. Here, one major redesign was applied to the terminal port of the high voltage power supply. In the usual Vienna-type DMA design the high voltage connection for the inner electrode is installed in the bottom insulator. To reduce diffusion losses in the exit section, one design goal was to keep the axial distance between the annular exit slit in the inner electrode and the inlet port of the FCE as short as possible. Therefore, in the new UDMA, the high voltage joint is mounted at the top of the UDMA. The high voltage power cord is fixed to a cylindrical brass pin, localized in the center axis of the top insulator. The high voltage pin is shaped on one end to a sharply tipped cone to safely connect the high voltage power supply to the inner electrode.

Another improvement in the exit section is a polyurethane exit shield tube which minimizes surface charge effects acting on the particles on their way through the bottom insulator to the outlet port.

As Brownian motion is one of the limiting factors for mobility measurements in the size range below 3 nm, one of the main goals was to minimize the residence time of the particles and clusters within the UDMA. For fixed electrode radii R_1 and R_2, the controlling parameters for the residence time are the sheath air flow rate Q_{sh} and the channel length L. In this design, we decided on an equal channel length and width of 6.5 mm (aspect ratio of 1) as Rossell-Llompart et al. (1996) suggested a channel length to width ratio near unity (based on a detailed analysis of the Peclet number) to minimize diffusive broadening.

One of the major tasks of this work was to set up clean and purified sheath air flows (Q_{sh}) in a closed loop arrangement. The design of the flow control system was carried out in two steps. In a first instance, we designed a flow control unit consisting of four high performance membrane pumps (HYCO, type ABF71/4C-7R). Four silica gel diffusion dryers (each with a volume of approximately 1 liter), four active carbon filters and four HEPA filters provide an efficient purification of the sheath air flow. A plenum chamber with a volume of 31 liters was installed to absorb and reduce pressure shocks on the vacuum side of the membrane pumps. By merging the four membrane pumps, a flow rate up to 300 L/min of clean and purified air is achieved.

As the UDMA is designed to operate at much higher flow rates, in a second step, a heavy duty 8-head membrane pump (HYCO type ML-130.85-ZV-D14/1.3 kW) capable of providing the UDMA with 540 L/min sheath air flow was used. Due to the gas compression at the outlet of the pump, a high flow heat exchanger unit had to be installed to cool the air flow and to stabilize its temperature to prevent temperature effects on the mobility measurements. Another approach to cool the high air flow is to use stainless steel tubing for the duct of the sheath air flow and to immerse it into a tank of chilled water (Fernández de la Mora & Attoui 2007). Without the cooling, the temperature of the sheath air flow increases by 30°C in a few minutes.

By combining both available flow systems, a stable sheath air flow of approximately 700 L/min was achieved for operating the UDMA in closed loop.

The sample air flow Q_s is maintained by drawing an air flow of typically 6.5 L/min, fixed by a critical orifice, through the FCE. As the UDMA is operated under symmetric flow conditions ($Q_{sh} = Q_{ex}$ and therefore $Q_s = Q_a$), this way an equally sized inlet aerosol volume flow Q_a is provided.

3. CALIBRATION AND PERFORMANCE

Well-defined and well-known operating conditions are a crucial prerequisite for high-resolution mobility measurements. Unfortunately, the precise determination of volumetric flow rates up to several m^3/min is a very difficult and time consuming task and small deviations of the effective channel length from the nominal value have a large impact on the DMA's classification characteristics. As it is difficult to determine actual/effective channel length and actual sheath air flow rate, high flow and high resolution DMAs have to be calibrated with an adequate mobility standard. Assuming a constant but unknown sheath air flow rate Q_{sh} and channel length L, the DMA equation (e.g., Knutson and Whitby 1975a)

$$Z = \frac{1}{V} \cdot \frac{\ln(R_2/R_1)}{2 \cdot \pi \cdot L} \cdot Q_{sh}, \qquad [1]$$

where Z is the aerosol particle's electrical mobility, V the voltage applied to the inner electrode, R_1 the outer diameter of the inner electrode, and R_2 the inner diameter of the outer electrode, can be transformed to

$$Z = K \cdot \frac{1}{V} \qquad [2]$$

where

$$K = \frac{\ln(R_2/R_1)}{2 \cdot \pi \cdot L} \cdot Q_{sh} \qquad [3]$$

is the DMA's operational characterization factor. The latter can be determined experimentally by feeding aerosol particles with a well known electrical mobility to the DMA and recording the voltage where most of the particles are transferred from Q_a to Q_s (the voltage at the peak signal of the mobility spectrum). Applying this method, the calibrated DMA can be operated without knowing exactly the geometric parameters and the sheath air flow rate (Rosell-Llompart et al. 1996; De Juan and Fernández de la Mora 1998). The generation of monodisperse particles for DMA calibration in the size range above 4 nm is discussed by Chen et al. (1995) and for sizes down to about 2.6 nm by Imanaka et al. (2006) using an electrospray generator.

Primary electrical mobility standards, also generated with an electrospray source, were reviewed by Ude and Fernández de la Mora (2005) using Tetraalkylammonium halide clusters and by Ku and Fernández de la Mora (2009) using clusters of a larger diversity of substances. Throughout this study, we used Tetraheptylammoniumbromide (THAB) dissolved in high grade methanol, yielding a unique mobility distribution of three cluster species of the form $A^+(AB)_n$, where "A" denotes the Tetraheptylammonium ion and "AB" the Tetraheptylammoniumbromide molecule, at 0.9708 cm^2/Vs (1.44 nm; $A^+(AB)_0$, monomer), 0.65402 cm^2/Vs (1.76 nm, $A^+(AB)_1$, dimer) and 0.52826 cm^2/Vs (1.96 nm, $A^+(AB)_2$,trimer) as test aerosol. The corresponding mobility equivalent diameters are calculated using Equation (4).

$$Z = \frac{i \cdot e_0 \cdot C(D_p)}{3 \cdot \pi \cdot \eta \cdot D_p} \quad \left[m^2/\,V \cdot s\right] \qquad [4]$$

In Equation (4), Z denotes the electrical mobility, i the charging state of the aerosol, e_0 the elementary charge, η the gas viscosity, D_p the mobility equivalent diameter and

$$C(D_p) = 1.0 + 2.492 \cdot \frac{\lambda}{D_p} + 0.84 \cdot \frac{\lambda}{D_p} \cdot \exp\left(-0.43 \cdot \frac{D_p}{\lambda}\right) \qquad [5]$$

the slip correction factor where λ corresponds to the mean free path of the carrier gas molecules. Slight deviations from the values given by Ude and Fernández de la Mora (2005) are caused by the use of different slip correction coefficients. Here we are using the values given by Fuchs (1964).

Since these clusters are formed by molecules of single species (monomer) or double species (dimer) and so on they are considered as standards in terms of size and mass and are well

qualified for the calibration of DMAs and mass spectrometers. For the generation of the clusters, a slightly modified version (Wimmer 2008) of an electrospray source, initially presented by Rosser and Fernández de la Mora (2005), was used. The main idea for a redesign was to improve the observation technique of the interior of the electrospray chamber, especially of the Taylor cone to control its stability.

These monomobile clusters are not only highly suitable for the calibration of DMAs but also for the investigation of its performance and the evaluation of their transfer functions.

The performance of a DMA is specified by the full width at half height (FWHH) of its transfer function $Tr(Z)$ and the extent of diffusion losses within the DMA. In general, a transfer function describes the relation between inlet and outlet signals, depending on one or more parameters. For a DMA, the transfer function describes the relation between the concentrations of the inlet aerosol and the classified particles, depending on particle mobility and the voltage applied to the inner electrode. Therefore, it describes the proportion of the aerosol entering the DMA at Q_a that reaches the sample outlet Q_s at a given voltage (having a defined mobility). Only at symmetric flow conditions ($Q_{sh} = Q_{ex}$, $Q_a = Q_s$) the transfer function for non diffusing particles has the form of an isosceles triangle (Figure 3), resulting in a minimum of the half width. In this case, the ratio between the half width (ΔZ) to Z is equal to the ratio between Q_a and Q_{sh} (Equation (6)).

$$\frac{\Delta Z}{Z} = \frac{Q_a}{Q_{sh}} \qquad [6]$$

A broadening of the transfer function, especially caused by diffusion processes of very small particles, can be calculated with numerical methods (Stolzenburg 1988; Reischl et al. 1997; Fernández de la Mora 2002; Tammet 1970). In principle, this broadening depends on the geometry of the DMA as well as on the operating conditions such as volume flow rates, carrier gas composition, air pressure, and the carrier gas temperature.

The first performance test was carried out in a so-called "tandem DMA" setup (Rader & McMurry 1986) (Figure 4) together with one of the state of the art high resolution DMAs

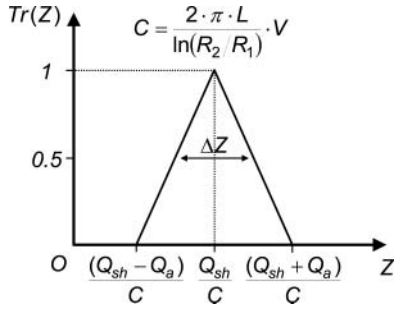

FIG. 3. At symmetric flow conditions ($Q_{sh} = Q_{ex}$, $Q_a = Q_s$), the transfer function $Tr(Z)$ of the DMA has the form of an isosceles triangle with a minimum of the half width and therefore maximum resolution power.

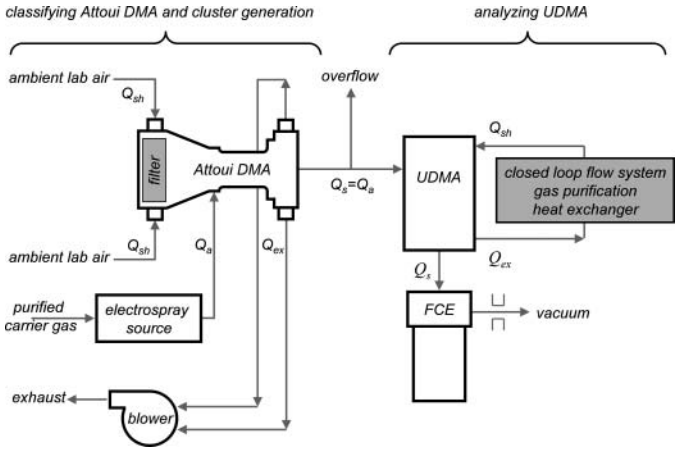

FIG. 4. "Tandem setup" of the "Attoui DMA" and the UDMA to determine the UDMA's resolution power.

developed by Juan Fernández de la Mora and Michel B. Attoui ($R_2 = 33.95$ mm; $R_1 = 24.95$ mm at the aerosol outlet slit, $L = 110$ mm), which is typically referred as "Attoui DMA."

For the evaluation of DMA transfer functions, a "tandem setup" usually consists of two identical DMAs lined up in series as classifier DMA and analyzer DMA. The classifying DMA extracts one mobility band out of the broad size distribution of a test aerosol. By analyzing the monodisperse mobility fraction with the second DMA, the FWHH of the mean mobility can be determined. As the DMAs are supposed to be identical in their geometry and are operated at the same flow conditions, the measured FWHH corresponds to the FWHH of the transfer function twice as large as for one of the DMAs. The general equations governing a configuration of two DMAs in series are recently summarized by Stolzenburg and McMurry (2008) including different geometric dimensions and operating conditions of the two DMAs as well as the broadening of the transfer function due to particle diffusion.

In the case of using molecular clusters with a well-known electrical mobility and a negligible standard deviation as test aerosol (mobility standards), the classifier and analyzer DMA do not need to be identical in their geometric dimensions, nor be operated at the same gas flow conditions, as the aerosols selected by the classifier DMA still can be considered as monomobile. In this setup, the classifier DMA ("Attoui DMA") was run at a sheath air flow rate of approximately 1400 L/min provided by a modified vacuum cleaner blower. At that time, the analyzing UDMA was not yet equipped with the stainless steel laminarization sponge in the inlet region of the sheath air flow and was operated at a comparably low sheath air flow of approximately 280 L/min, only using the flow control unit consisting of four high performance membrane pumps. The result of this first performance test is given in Figure 5, showing the THAB scan of the "Attoui DMA" as a gray line with a FWHH of the THAB monomer peak at 1.44 nm of 5.7% in mobility size. For the calibration, the "Attoui DMA" was set to a fixed voltage

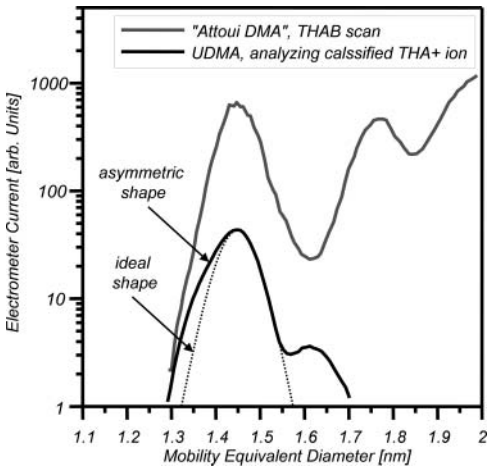

FIG. 5. Results of the performance test in a "tandem setup" showing a relative FWHH of the THAB monomer peak at 1.44 nm of 5.7% (in mobility-size) for the "Attoui DMA" at a sheath air flow rate of 1400 L/min and 6.6% (in mobility-size) for the UDMA at a sheath air flow rate of 280 L/min without installed laminarization sponge, resulting in poor flow conditions.

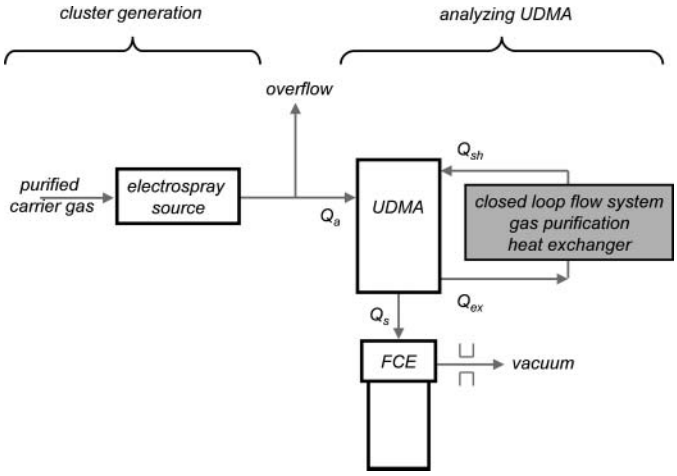

FIG. 6. Setup for the second performance test by feeding electrosprayed Tetraheptylammoniumbromide (THAB) directly to the UDMA and analyzing its mobility spectrum.

corresponding to the $A^+(AB)_0$ monomer peak, only allowing these clusters to pass the classifier DMA. Surprisingly, at these inappropriate flow conditions the monodisperse monomer peak analyzed by the UDMA (black line) shows only a slightly broader FWHH of the $A^+(AB)_0$ peak (6.6%), but also a notably asymmetric shape of the analyzed peak.

This asymmetry indicates poor flow conditions within the UDMA caused by turbulence in the sheath air flow, distorting the UDMA's transfer function. Most likely, this swirl is caused by the tangential inlet system of the sheath air flow. As a result, we installed the stainless steel laminarization sponge to minimize the tangential component of the air flow to provide a uniform laminar flow of the sheath air, which is in general the most crucial condition for high resolution mobility measurements.

For a second performance test with the installed laminarization sponge, we also increased the sheath air flow rate of the UDMA up to approximately 700 L/min by combining both available flow units. Other than before, for this measurement we used the approach of Rosell-Llompart et al. (1996) by feeding electrosprayed Tetraheptylammoniumbromide (THAB) directly to the UDMA and analyzing its mobility spectrum (Figure 6).

As the identified cluster species can be considered as strictly monodisperse with a negligible width of their size distribution, the measured mobility distribution directly yields the transfer function of the UDMA, broadened by diffusion processes of the small clusters within the UDMA. To check the stability of the mean mobility of the analyzed clusters with respect to time, Figure 7 shows the peak concentration (peak current) of the Tetraheptylammonium monomer ions ($A^+(AB)_0$) versus a UDMA runtime of 5,000 s. Small variations of less than 1% in the concentration (current) are mainly caused by short fluctuations in the stability of the Taylor cone of the electrospray generator. The small variability in the peak concentration of the THAB monomer also indicates very stable sheath air flow conditions as an unstable airflow would result in big variations of the concentration of the classified aerosol

The black line in Figure 8 shows a single scan of the number size distribution of singly charged Tetraheptylamoniumbromide (THAB) clusters ($A^+(AB)_0$ monomer, $A^+(AB)_1$ dimer and $A^+(AB)_2$ trimer) obtained from an electrosprayed 1 mMolar solution of THAB in high grade methanol measured with the UDMA.

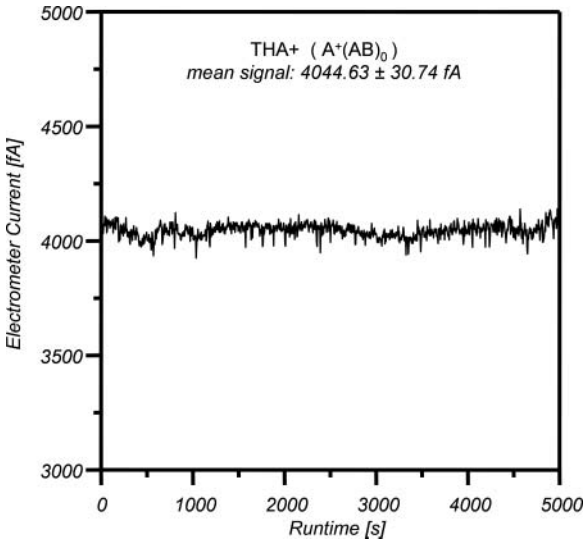

FIG. 7. Results of the stability check of the peak concentration of the Tetraheptylammonium monomer ions ($A^+(AB)_0$) versus a UDMA runtime of 5,000 seconds. Small variations of less than 1% in the concentration are mainly caused by short fluctuations in the stability of the Taylor cone of the electrospray generator. The small variability in the peak concentration also indicates very stable sheath air flow conditions as an unstable airflow would result in big variations of the concentration of the classified aerosol.

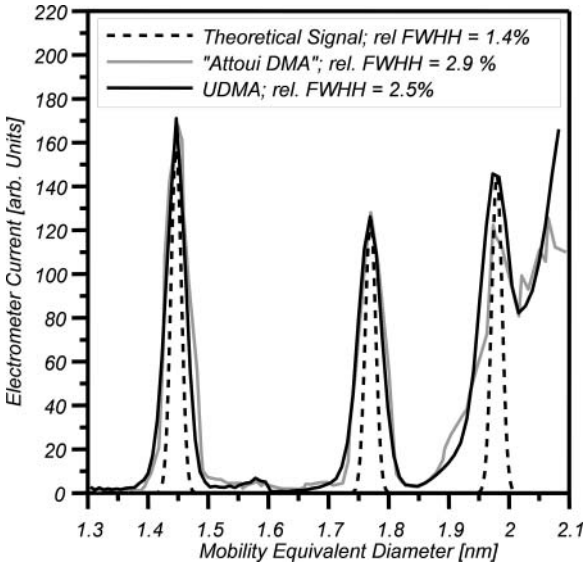

FIG. 8. Comparison of measured and simulated size distributions of THAB normalized to the experimental data. At optimal conditions, the UDMA shows a relative FWHH of its transfer function of 2.5% in mobility-size (black line) at a sheath air flow rate of approx. 700 L/min in a closed loop arrangement. The theoretical signal (black dashed line) is calculated according to Stolzenburg (1988) assuming spherical molecules. At $Q_{sh} = 2400$ L/min (light gray line), the THAB scan of the "Attoui DMA," normalized to the UDMA Data, shows comparable resolution power of 2.9% in mobility size.

A relative FWHH of the transfer function of 2.5% in mobility size was found for the $A^+(AB)_0$ monomer clusters at 1.44 nm mobility equivalent diameter, only slightly larger than the theoretically obtained relative FWHH of 1.4% calculated according to Stolzenburg (1988) for the flow rates used for the UDMA and assuming spherical particles. For comparison, Figure 8 also shows the measured number size distribution of THAB using the "Attoui DMA" to illustrate a typical performance of a state of the art high resolution DMA.

As the "Attoui DMA's" improved exhaust system shows essentially no pressure drop, it permits sheath gas flow rates well above 8,000 L/min. However, due to technical reasons, during the instrument intercomparison, the "Attoui DMA" was operated at a sheath air flow rate of approximately 2400 L/min (light gray line) maintained by drawing filtered ambient laboratory air into the "Attoui DMA." At this sheath air flow rate, the "Attoui DMA" shows a resolution power of 2.9% in mobility size for the $A^+(AB)_0$ monomer clusters.

It has to be noted that the "Attoui DMA" with a channel length $L = 110$ mm and a large aspect ratio slightly above 12 was designed to cover a much wider particle size range than the UDMA. Therefore, the sheath air flow rates have to be much higher to achieve a comparable resolution power.

At the flow conditions used during this work, the UDMA operated with well controlled and purified sheath air flows in a closed-loop arrangement, features a slightly better resolution power to that of the "Attoui DMA."

We would like to point out that this result does not imply that the performance of the UDMA is generally superior to the "Attoui DMA," but that the UDMA operated at rather low flow rates is able to deliver comparable results.

4. SUMMARY

The newly developed Vienna Type UDMA, operated in a closed loop arrangement, was shown to have the necessary resolution power to separate charged molecular clusters for a future use in combination with a mass spectrometer. The possibility to apply a closed loop system with a well controlled composition of the gas flow through the UDMA, ensures high-quality mobility measurements of charged molecular clusters. The comparable low sheath air flow rate reduces the technical problems (e.g., pressure drop through gas cleaning devices, leakage) that might arise by the use of high volume blowers to provide the large gas flow rates needed for most other high resolution DMAs to obtain the desired resolution power. On the other hand, the range of possible mobilities is reduced and the versatility is limited when using smaller aspect ratio DMAs with low sheath air flows. However, the UDMA still suits the purpose of generating monodisperse clusters in a reasonable mobility range in a controlled clean carrier gas and has been found suitable to be combined with other instrumentation (Winkler et al. 2008).

REFERENCES

Brunelli, N. A., Flagan, R. C., and Giapis, K. P. (2009). Radial Differential Mobility Analyzer for One Nanometer Particle Classification. *Aerosol Sci. Technol.* 43(1): 53–59.

Chen, D.–R., Pui, D. Y. H., and Kaufman, S. L. (1995). Electrospraying Of Conducting Liquids for Monodisperse Aerosol Generation in the 4 nm to 1.8 μm Diameter Range. *J. Aerosol Sci.* 26(6): 963–977.

De Juan, L., and Fernández de la Mora, J. (1998). High Resolution Size Analysis of Nanoparticles and Ions: Running a Vienna DMA of Near Optimal Length at Reynolds Numbers up to 5000. *J. Aerosol Sci.* 29: 617–626.

Eichler, T. (1997). A Differential Mobility Analyzer for Ions and Nanoparticles: Laminar Flow at High Reynolds Numbers. *Senior Graduation Thesis Presented to Fachhochschule Offenburg, Germany.*

Fernández de la Mora, J. (2002). Diffusion Broadening in Converging Differential Mobility Analyzers. *J. Aerosol Sci.* 33: 411–437.

Fernández de la Mora, J., Thomson, B. A., and Gamero-Castaño, M. (2005). Tandem Mobility Mass Spectrometry Study of Electrosprayed Tetraheptyl Ammonium Bromide Clusters. *J. Amer. Soc. Mass Spectrom.* 16(5) 717–732.

Fernández de la Mora, J., and Attoui, M. (2007). A DMA Covering the 1–100 nm Particle Size Range with High Resolution Down to 1 nm. *European Aerosol Conference 2007, Salzburg, Austria, Abstract T02A029.*

Fuchs, N. A. (1964). *The Mechanics of Aerosols*. Pergamon Press, Oxford.

Gamero-Castaño, M., and Fernández de la Mora, J. (2000a). Modulations in the Abundance of Salt Clusters in Electrosprays. *Anal. Chem.* 72(7) 1426–1429.

Gamero-Castaño, M., and Fernández de la Mora, J. (2000b). A Condensation Nucleus Counter (CNC) Sensitive to Singly Charged Sub-Nanometer Particles. *J. Aerosol Sci.* 31(7): 757–772.

Hermann, W., Eichler, T., Bernardo, N., and Fernandez de la Mora, J. (2000). Turbulent Transition Arises at Reynolds Number 35,000 in a Short Vienna Type DMA with a Large Laminarization Inlet. *Annual Conference of the AAAR, St. Louis, Missouri.*

Hewitt, G. W. (1957). The Charging of Small Particles for Electrostatic Precipation. *Trans. Am. Inst. Elect. Engrs.* 76: 294.

Hogan, C. J., and Fernández de la Mora, J. (2009). Tandem Ion Mobility-Mass Spectrometry (IMS-MS) Study of Ion Evaporation from Ionic Liquid-Acetonitrile Nanodrops. *Physical Chemistry Chemical Physics,* 11(36): 8079–8090.

Jokinen, V., and Mäkelä, J. M. (1997). Closed-Loop Arrangement with Critical Orifice for DMA Sheath/Excess Flow System. *J. Aerosol Sci.* 28(4): 643–648.

Knutson, E. O., and Whitby, K. T. (1975a). Aerosol Classification by Electric Mobility: Apparatus, Theory and Applications. *J. Aerosol Sci.* 6: 443.

Knutson, E. O., and Whitby, K. T. (1975b). Accurate Measurement of Aerosol Electric Mobility Moments. *J. Aerosol Sci.* 6: 453.

Knutson, E. O. (1976). In *Fine Particles: Aerosol Generation, Measurement, Sampling, and Analysis,* B. Y. H. Liu, ed., Academic Press, New York, 739–762.

Ku, B. K., and Fernández de la Mora, J. (2009). Relation between Electrical Mobility, Mass, and Size for Nanodrops 1-6.5 nm in Diameter in Air. *Aerosol Sci. Technol.* 43(3): 241–249.

Kulmala, M., Riipinen, I., Sipilä, M., Manninen, H. E., Petäjä, T., Junninen, H., Dal Maso, M., Mordas, G., Mirme, A., Vana, M., Hirsikko, A., Laakso, L., Harrison, R., Hanson, I., Leung, C., Lehtinen, K. E. J., & Kerminen, V.-M. (2007). Toward Direct Measurement of Atmospheric Nucleation. *Science,* 318(5847): 89–92.

Liu, B. Y. H., Pui, D. Y. H., and Kapadia, A. (1979). Electrical Aerosol Analyzer. History, Principle and Data Reduction. In *Aerosol Measurement*, D.A. Lundgren et al., eds., University of Florida Press, Gainesville, Florida, 341–383.

Martínez-Lozano, P., & Fernández de la Mora, J. (2006). Resolution Improvements of a Nano-DMA Operating Transonically. *J. Aerosol Sci.* 37: 500–512.

Mesbah, B., Boulaud, D., Pourprix, M., and Renoux, A. (1993). Circular Electric Mobility Spectrometer. *J. Aerosol Sci.* 24: 219.

Ooghe, M., Mesbha, B., Pourprix, M., and Boulaud, B. (1994). Radial Flow Differential Mobility Analyzer (RF-DMA). *Proc. of the 4th Int. Aerosol Conference,* Los Angeles 1994, pp. 463–464.

Rader, D. J., and McMurry, P. H. (1986). Application of the Tandem Differential Mobility Analyzer to Studies of Droplet Growth or Evaporation. *J. Aerosol Sci.* 17(5): 771–787.

Reischl, G. P. (1991). Measurement of Ambient Aerosols by the Differential Mobility Analyzer Method: Concepts and Realization criteria for the Size Range between 2 and 500 nm. *Aerosol Sci. Technol.* 14: 5.

Reischl, G. P., Mäkelä, J. M., and Necid, J. (1997). Performance of Vienna Type Differential Mobility Analyzer at 1.2–20 Nanometer. *Aerosol Sci. Technol.* 27: 651–672.

Rohman, H. (1923). Methode zur Messung der Größe von Schwebeteilchen. *Z. Physik* 17: 253.

Rosell-Llompart, J., Loscertales, I. G., Bingham, D., and Fernández de la Mora, J. (1996). Sizing Nanoparticles and Ions with a Short Differential Mobility Analyzer. *J. Aerosol Sci.* 27: 695–719.

Rosser, S., and Fernández de la Mora, J. (2005). Vienna Type DMA of High Resolution and High Flow Rate. *Aerosol Sci. Technol.* 39(12): 1191–1200.

Steiner, G. (2006). Generierung von Nanopartikeln—Über die Konstruktion eines Heizdraht—Wolframoxid Generators. Diploma Thesis, Faculty of Physics, University of Vienna.

Stolzenburg, M. R. (1988). An Ultrafine Aerosol Size Distribution Measuring System, PhD. Thesis, Mechanical Engineering Department, Univ. of Minnesota, Minneapolis.

Stolzenburg, M. R., and McMurry, P. H. (2008). Equations Governing Single and Tandem DMA Configurations and a New Lognormal Approximation to the Transfer Function. *Aerosol Sci. Technol.* 42: 421–432.

Tammet, H. (1970). The Aspiration Method for the Determination of Atmospheric-Ion Spectra. *IPST for NSF,* Jerusalem.

Ude, S., and Ferández de la Mora, J. (2005). Molecular Monodisperse Mobility and Mass Standards from Electrosprays of Tetre-Alkyl Ammonium Halides. *J. Aerosol Sci.* 36: 1224–1237.

Wimmer, D. (2008). Generation and Classification of Airborne Molecular Clusters. Diploma Thesis, Faculty of Physics, University of Vienna.

Winkler, P. M., Steiner, G., Vrtala, A., Vehkamäki, H., Noppel, M., Lehtinen, K. E. J., Reischl, G. P., Wagner, P. E., and Kulmala, M. (2008). Heterogeneous Nucleation Experiments Bridging the Scale from Molecular Ion Clusters to Nanoparticles. *Science,* 319(5868): 1374–1377.

Winklmayr, W., Reischl, G. P., Lindner, A. O., and Berner A. (1991). A New Electromobility Spectrometer for the Measurement of Aeorosol Size Distribution in the Size Range from 1 to 1000 nm. *J. Aerosol Sci.* 22: 289.

Zeleny, J. (1929). The Distribution of Mobilities of Ions in Moist Air. *Phys. Rev.* 34: 310–334.

Zhang, S. H., Akutsu, Y., Russell, L. M., Flagan, R. C., and Seinfeld, J. H. (1995). Radial Differential Mobility Analyzer. *Aerosol Sci. Technol.* 23: 357.

Zhang, S. H., Flagan, R. C., and Seinfeld, J. H. (1996). Resolution of the Radial Differential Mobility Analyzer for Ultrafine Particles. *J. Aerosol Sci.* 27: 1179.

9.2. Appendix B1

Winkler et al. (2008)

Heterogeneous nucleation experiments bridging the scale from molecular ion clusters to nanoparticles. *Science, 319, 5868, 1374-1377*

a physiological temperature of 37°C at ~2°C/min (*30*) (Movie S1), leads to a pronounced reduction of E'. Whereas the neat PVAc (dry E'_s = 1.8 GPa at 25°C) instantly softens under these conditions (Fig. 4B), the E' of the whisker-reinforced nanocomposites (see Fig. 4B for a 12.2% v/v nanocomposite) is reduced slowly over a period of 15 min. The whisker-reinforced nanocomposite displays a much higher dry E' (4.2 GPa at 25°C) than the neat PVAc, but both materials reach nearly identical moduli upon immersion in ACSF at 37°C (1.6 MPa).

Our data support a simple and versatile strategy for the creation of polymer nanocomposites, whose architecture and mechanical adaptability closely mimic the proposed architecture and observed response of the sea cucumber dermis. The mechanical properties of these chemoresponsive materials can selectively and reversibly be controlled through the formation and decoupling of a three-dimensional network of well-individualized nanofibers in response to specific chemical triggers. It will be interesting to explore whether the framework can be adapted to nonchemical triggers, for example, optical or electrical stimuli.

References and Notes

1. T. Heinzeller, J. Nebelsick, Eds., *Echinoderms* (Taylor & Francis, London, **2004**).
2. T. Motokawa, *Comp. Biochem. Physiol. B* **109**, 613 (1994).
3. F. A. Thurmond, J. A. Trotter, *J. Exp. Biol.* **199**, 1817 (1996).
4. I. C. Wilkie, *J. Exp. Biol.* **205**, 159 (2002).
5. J. A. Trotter, T. J. Koob, *Matrix Biol.* **18**, 569 (1999).
6. G. K. Szulgit, R. E. Shadwick, *J. Exp. Biol.* **203**, 1539 (2000).
7. J. A. Trotter *et al.*, *Biochem. Soc. Trans.* **28**, 357 (2000).
8. J. C. Grunlan, L. Liu, Y. S. Kim, *Nano Lett.* **6**, 911 (2006).
9. M. M. de Souza Lima, R. Borsali, *Macromol. Rapid Commun.* **25**, 771 (2004).
10. J. A. Jaber, J. B. Schlenoff, *J. Am. Chem. Soc.* **128**, 2940 (2006).
11. D. M. Loveless, S. L. Jeon, S. L. Craïg, *J. Mater. Chem.* **17**, 56 (2007).
12. P. S. Belton, S. F. Tanner, N. Cartier, H. Chanzy, *Macromolecules* **22**, 1615 (1989).
13. A. Sturcova, J. R. Davies, S. J. Eichhorn, *Biomacromolecules* **6**, 1055 (2005).
14. O. van den Berg, J. R. Capadona, C. Weder, *Biomacromolecules* **8**, 1353 (2007).
15. M. A. S. Azizi Samir, F. Alloin, A. Dufresne, *Biomacromolecules* **6**, 612 (2005).
16. J. R. Capadona *et al.*, *Nat. Nanotech.* **2**, 765 (2007).
17. M. Takayanagi, S. Uemura, S. Minami, *J. Polym. Sci. C* **5**, 113 (1964).
18. N. Ouali, J. Y. Cavaillé, J. Pérez, *J. Plast. Rubber Comp. Process. Appl.* **16**, 55 (1991).
19. Swelling increased the volume of the nanocomposites and reduced the volume fraction of whiskers, X_r. For example, when a nanocomposite with X_r = 19% v/v was swollen with water, X_r decreased to 14%. The representation of data in Fig. 2A considers this effect to allow for analysis by the Halpin-Kardos model. A direct comparison of dry versus wet composites for the same fiber loading is shown in fig. S6.
20. J. Kunzelman, B. R. Crenshaw, C. Weder, *J. Mater. Chem.* **17**, 2989 (2007).
21. J. C. Halpin, J. L. Kardos, *J. Appl. Phys.* **43**, 2235 (1972).
22. P. Hajji, J. Y. Cavaillé, V. Favier, C. Gauthier, G. Vigier, *Polym. Compos.* **17**, 612 (1996).
23. $\eta_L = [(E_{lr} / E'_s) - 1]/[(E_{lr} / E'_s) + 2A]$, and $\eta_T = [(E_{tr} / E'_s) - 1]/[(E_{tr} / E'_s) + 2]$. A is the aspect ratio of the whiskers, ϕ is equal to the volume fraction of the phase, and the subscripts s and r represent the soft phase and the rigid phase, respectively. E_{lr} is the longitudinal Young's Modulus (130 GPa), and E_{tr} is the transverse Young's Modulus (5 GPa) of an individual cellulose whisker (*22*). To determine the tensile storage modulus of the isotropic nanocomposite (E'), E'_L and E'_T must be inserted into one equation using the Halpin-Kardos model: $E' = 4U_5(U_1 - U_5)/U_1$ where $U_1 = 1/8(3Q_{11} + 3Q_{22} + 4Q_{66})$; $U_5 = 1/8(Q_{11} + Q_{22} - 2Q_{12} + 4Q_{66})$; $Q_{11} = E'_L/(1 - \nu_{12}\nu_{21})$; $Q_{22} = E'_T(1 - \nu_{12}\nu_{21})$; $Q_{12} = \nu_{12}Q_{22} = \nu_{21}Q_{11}$; $Q_{66} = G_{12}$; $\nu_{12} = \phi_r\nu_r + \phi_s\nu_s = 0.3$; $G_{12} = G_s(1 + \eta\phi_r)/(1 - \eta\phi_r)$; $\eta = (G_r/G_s - 1)/(G_r/G_s + 1)$, ν is the Poisson's ratio, G is the shear modulus, and G_r = 1.77 GPa.
24. D. M. Taylor, S. I. H. Tillery, A. B. Schwartz, *Science* **296**, 1829 (2002).
25. A. B. Schwartz, *Annu. Rev. Neurosci.* **27**, 487 (2004).
26. R. Biran, D. C. Martin, P. A. Tresco, *J. Biomed. Mater. Res.* **82A**, 169 (2007).
27. W. L. C. Rutten, *Annu. Rev. Biomed. Eng.* **4**, 407 (2002).
28. D. H. Szarowski *et al.*, *Brain Res.* **983**, 23 (2003).
29. K. Najafi, J. F. Hetke, *IEEE Trans. Biomed. Eng.* **37**, 474 (1990).
30. Materials and methods are available as supporting material on *Science* Online.

31. We thank F. Carpenter for the photography of the sea cucumber and L. McCorkle, J. Johnson, and M. Hitomi for assistance with the SEM, AFM, and TEM experiments, respectively. Financial support from DuPont (Young Professor Award to C.W.), the L. Stokes Cleveland VAMC Advanced Platform Technology Center, an Ohio Innovation Incentive Fellowship (to K.S.), the Department of Veterans Affairs Associate Investigator Career Development Program (to J.C.), and the National Institutes of Health are gratefully acknowledged. The authors declare that they have no competing financial interest.

Supporting Online Material

www.sciencemag.org/cgi/content/full/319/5868/1370/DC1
Materials and Methods
Figs. S1 to 10
Table S1
References
Movie S1

6 November 2007; accepted 1 February 2008
10.1126/science.1153307

Heterogeneous Nucleation Experiments Bridging the Scale from Molecular Ion Clusters to Nanoparticles

Paul M. Winkler,[1] Gerhard Steiner,[1] Aron Vrtala,[1] Hanna Vehkamäki,[2] Madis Noppel,[3] Kari E. J. Lehtinen,[4] Georg P. Reischl,[1] Paul E. Wagner,[1] Markku Kulmala[2]*

Generation, investigation, and manipulation of nanostructured materials are of fundamental and practical importance for several disciplines, including materials science and medicine. Recently, atmospheric new particle formation in the nanometer-size range has been found to be a global phenomenon. Still, its detailed mechanisms are mostly unknown, largely depending on the incapability to generate and measure nanoparticles in a controlled way. In our experiments, an organic vapor (*n*-propanol) condenses on molecular ions, as well as on charged and uncharged inorganic nanoparticles, via initial activation by heterogeneous nucleation. We found a smooth transition in activation behavior as a function of size and activation to occur well before the onset of homogeneous nucleation. Furthermore, nucleation enhancement for charged particles and a substantial negative sign preference were quantitatively detected.

Condensational growth, evaporation, and heterogeneous chemistry are important phenomena in materials science, fluid dynamics, aerosol physics and technology, and atmospheric chemistry, including cloud microphysics and cloud chemistry. A prerequisite for the start of condensation is homogeneous nucleation of new particles or the activation of preexisting particles by heterogeneous nucleation. The latter can occur either on ions, soluble particles, or insoluble particles, and is energetically easier than homogeneous nucleation (*1*). Both particle formation processes are of fundamental as well as practical importance and have been the subject of investigations for more than a century (*2*). Important examples representing the different processes are given by the use of the Wilson cloud chamber (*3*) in high-energy physics for the case of ions, the formation of cloud droplets in the troposphere for the case of soluble particles, and the occurrence of ice nucleation for the case of insoluble seed particles (*4*). Atmospheric observations suggest that the initial formation and growth are two uncoupled processes (*5*–*7*), and therefore the activation mechanism of small clusters is of vital importance. Understanding the formation and initial growth processes in detail is also crucial to control the production of nanomaterials (*8*).

In this paper, we present experimental results for the activation of molecular cluster ions, charged and neutral clusters, and nanometer-size particles having almost monodisperse size distributions,

[1]Fakultät für Physik, Universität Wien, Boltzmanngasse 5, A-1090 Wien, Austria. [2]University of Helsinki, Department of Physical Sciences, Post Office Box 64, 00014 University of Helsinki, Finland. [3]Institute of Physics, University of Tartu, 18 Ülikooli Street, 50090 Tartu, Estonia. [4]Department of Physics, University of Kuopio and Finnish Meteorological Institute, Post Office Box 1627, 70211 Kuopio, Finland.

*To whom correspondence should be addressed. E-mail: markku.kulmala@helsinki.fi

with mean diameters ranging from 1 to 24 nm and geometric SDs between 1.021 and 1.058. Particle number concentrations were between 2000 and 10,000 cm^{-3}. We used insoluble inorganic seed aerosol (WO_x) and condensable organic vapor (*n*-propanol) to determine the dependence of activation diameter on charging state and vapor saturation ratio. For comparison, other insoluble inorganic seed aerosols [Ag and $(NH_4)_2SO_4$] were also used (*9*). The range of particle sizes studied—together with the fact that the particles are, in practice, monodispersed—is the main novelty of our work: To our knowledge, this is the first time that activation of neutral particles has been studied for particles smaller than 3 nm in diameter.

The experimental system (*9*) includes a source of monodispersed particles and a vapor generation unit. Vapor supersaturation is achieved by adiabatic expansion in a computer-controlled thermostated expansion chamber [the size-analyzing nuclei counter (SANC)]. Droplet growth is observed by means of the constant-angle Mie scattering (CAMS) detection method (*10*). Details of the experimental system are presented elsewhere (*11*).

We generated well-defined nearly monodispersed nanoparticles using different types of particle generators in combination with an electrostatic classification system capable of selecting particles with specified charging state and mobility diameters down to and even below 1 nm. Ions were obtained from a radioactive source in a ^{241}Am charger. Charged particles leaving the classifier were either passed through a ^{241}Am neutralizer to obtain neutral particles or passed by the neutralizer to preserve charging properties. In order to remove ions, which were produced in the neutralizer, from the aerosol flow, we applied an ion trap. *n*-Propanol vapor was added to the system by controlled injection of a liquid beam and subsequent quantitative evaporation in a heated unit. Those particles inducing heterogeneous nucleation in the SANC expansion chamber at the vapor supersaturations considered lead to the formation and growth of liquid droplets, which were optically detected.

We measured heterogeneous nucleation (activation) probabilities using the above described SANC-CAMS method. For all experiments reported in this paper, the nucleation temperature was kept constant at about 275 K. For each *n*-propanol vapor saturation ratio, the fraction of activated particles relative to total particle number concentration was determined, resulting in a nucleation-activation probability curve. Experimental nucleation probabilities, determined for molecular ions and nanometer-size particles, are shown in Fig. 1. The diameters of the seed objects range from 4 nm down to 0.9 nm. The smaller the size, the higher the saturation ratio that is needed for activation, reflecting the well-known curvature effect first observed by Thomson (*12*). As can be seen, at 4 nm, the nucleation probability curves are mainly overlapping, whereas with decreasing particle size, the curves split up, indicating that charge effects increasingly promote the nucleation process. Negatively charged particles are found to require smaller saturation ratios to activate for nucleation than positively charged particles and neutral ones.

Each probability curve can be represented by the corresponding onset saturation ratio (i.e., the saturation ratio where 50% of the particles of a certain size are activated). Experimental onset saturation ratios as functions of mobility diameter, together with the Kelvin diameter and the homogeneous nucleation limit, are shown in Fig. 2. The Kelvin diameter corresponds to the size at which the vapor and aerosol particles, whose surfaces are coated with *n*-propanol, are in equilibrium (*9*). In principle, if the particle size is larger than the Kelvin diameter, the aerosol particles will grow; if the particle size is smaller, they will evaporate. However, in our experiments, all particles considered are activated and start to grow at sizes clearly smaller than those indicated by the Kelvin equation and at saturation ratios well below the onset of homogeneous nucleation.

For particles with diameters around 4 nm and above, nucleation behavior was found to be independent of charging state. However, as seen already in Fig. 1, charge effects become increasingly important with decreasing particle size. Differences between heterogeneous nucleation on charged and neutral particles were experimentally observed, starting at diameters below 3 nm. Clearly, a "sign effect" can be seen, meaning that negatively charged particles appear to be more easily activated for growth than positively charged particles. Smaller saturation ratios are generally required to activate charged particles for nucleation. For example, at a saturation ratio of 2.75, the activation size is 1.4 nm for negative clusters and 1.8 nm for neutral ones. A smooth transition from molecular ions to particles is observed, thereby bridging the scale from molecular ion clusters to nanoparticles. Consistently, for ions, a similar sign effect has been found as for charged particles. Recently, Nadykto *et al.* (*13*) have proposed that the sign can be reproduced by quantum chemical methods and may be positive or negative, depending on the nature of the ions considered.

In Fig. 2, we also compare our experimental findings with an onset activation curve predicted by heterogeneous nucleation theory (*9*, *14*). In heterogeneous nucleation, the critical cluster is formed on a preexisting surface, and only part of the vapor-liquid surface needs to be built from scratch, because part of it can be borrowed from the preexisting interface; this fact decreases the energy barrier of cluster formation as compared with homogeneous nucleation (*1*, *11*). The angle between the preexisting surface and the surface of the nucleating cluster is called the contact angle θ. The value that we used for the contact angle was 0°, corresponding to the recent observations for *n*-propanol droplets nucleating on an Ag surface (*11*). Substantially larger contact angles would lead to a predicted activation diameter being larger than the Kelvin diameter (*1*), which is in contrast to our experimental findings; thus, we conclude that the particles are, in practice, totally wettable to the *n*-propanol vapor. In atmospheric and materials science, heterogeneous nucleation is typically ignored. This is mainly because no proper experimental data have so far existed at particle sizes small enough to be relevant to formation and initial growth. Our results, however, show that the theory developed by Fletcher 50 years ago predicts the observed onset activations for neutral particles and clusters exceedingly well, even at the size range of small molecular clusters.

The effect of charge on the onset activation curves can be estimated by ion-induced nucleation theory—with Gibbs free energies calculated based on the Thomson theory (*15*)—together with the Fletcher theory (*9*), hereafter referred to as the "combined" theory. The onset activation satura-

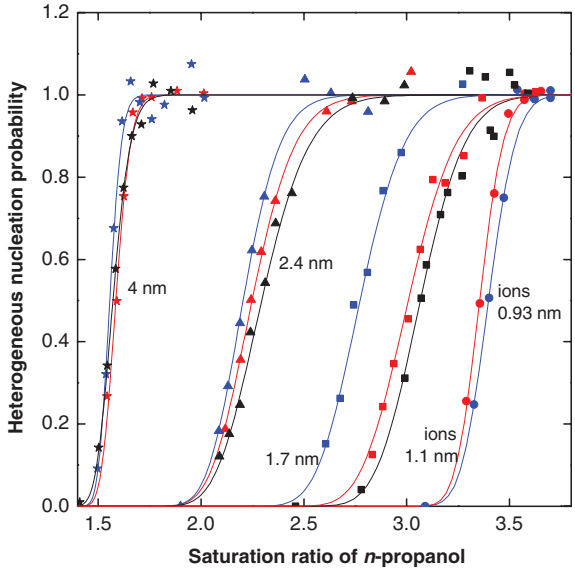

Fig. 1. Heterogeneous nucleation probabilities versus vapor saturation ratio for nucleation of *n*-propanol on ions as well as charged and uncharged WO_x clusters of different diameters: WO_x, 4 nm (stars); WO_x, 2.4 nm (triangles); WO_x, 1.7 nm (squares); positive ions, 1.1 nm (red circles); and negative ions, 0.93 nm (blue circles). Colors refer to different charging states: blue (negatively charged), red (positively charged), and black (neutral). Solid lines are shown to guide the eye.

tion ratio as a function of diameter, estimated by the combined theory, is also superimposed in Fig. 2, showing an even lower supersaturation required for activation. The combined theory provides no explanation why negative particles activate before positive ones of the same size. However, the difference between the Fletcher theory (heterogeneous nucleation) and the combined theory (heterogeneous and ion-induced nucleation) seems to provide a useful estimate for the difference in onset activation supersaturations between charged and neutral particles.

The use of the recently developed heterogeneous nucleation theorem (*16*) will provide an estimation of the number of molecules in the nucleating cluster. In the experiments presented here, the number is around 20 to 25 molecules. The ratio of the experimental activation diameter to the Kelvin diameter is almost size-independent and is around 0.65. Our experimental technique can thus be used to produce particles, with a well-defined surface layer consisting of a small number of molecules, for future technical and industrial purposes.

So far, it has been generally accepted (*1*, *17*) that activation of (neutral) particles is predicted by the Kelvin equation. The fact that particles are activated at much smaller sizes than indicated by the Kelvin equation is thus unexpected; apparently, heterogeneous nucleation has been typically forgotten or at least ignored, and the Fletcher theory has not been applied to small clusters or nanoparticles. The latest findings will give insight to some aspects of materials science, atmospheric particle formation, and especially to measurement techniques of small aerosol particles. Based on laboratory experiments, atmospheric observations, and modeling (*18*–*20*), it is often predicted that homogeneous nucleation will produce particles with diameters around 1 to 2 nm. Indeed, Strey *et al*. (*21*) have shown that, for the case of homogeneous nucleation (i.e., in the absence of seed particles), the critical cluster size agrees well with the Kelvin equation; this indicates that the Kelvin equation remains generally valid for critical clusters down to the size range of 1 to 2 nm. Our results show that, for example, if the Kelvin diameter is 2 nm, then the activation diameter is around 1.2 nm; this finding indicates that all seed particles with diameters larger than 1.2 nm are capable of acting as nuclei for condensation, which is also consistent with the recent observation of size-dependent aerosol growth (*6*). As described by the Fletcher theory (*9*, *14*), small embryos have a thermodynamic barrier to cross, but critical size clusters are nevertheless formed on seed particles as a result of statistical fluctuations. They reach the critical size and become stable for growth when their radius coincides with the Kelvin curvature. The work of formation of an embryo on a seed particle is always smaller than the work of formation of a Kelvin-size embryo in homogeneous nucleation, even if the seed particle diameter is below the Kelvin size. This is manifested by our finding that organic vapor will condense much easier on even the smallest preexisting seed particles than form new particles.

In nanomaterial production, there are several examples of experiments where the detailed particle formation, activation, and/or initial growth mechanisms are unknown, and modeling attempts have been unsuccessful (*22*, *23*). These modeling efforts are typically based on the application of classical homogeneous nucleation theory with some adjustable factor, together with coagulation and condensation models for the growth. The heterogeneous nucleation-activation stage is typically neglected, and condensation is assumed to start at the Kelvin limit. The present study proposes one severe deficiency in these approaches, because we clearly observe that activation and condensational growth can start at sizes significantly smaller than previously expected from the Kelvin equation.

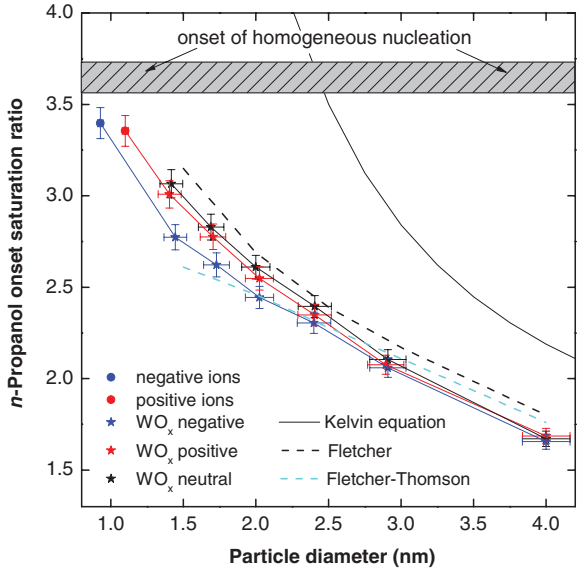

Fig. 2. Experimental onset saturation ratio as a function of seed particle mobility diameter for ions as well as for charged and uncharged WO_x particles. The Kelvin diameter (solid black line) and the homogeneous nucleation onset [cross-hatched shaded area (*29*)] are shown for comparison. We also show the predictions by the Fletcher theory for heterogeneous nucleation on uncharged particles (dashed black line) and the combined theory accounting for the charge of the seed particles (dashed cyan line) (*9*). Error bars indicate the measurement uncertainty when measuring saturation ratio and particle diameter.

One of the main implications of this study is that the detection limit of condensation particle counters (CPCs) can be extended to considerably smaller sizes (*24*, *25*). The operating principle of these devices is based on activation of particles in supersaturated vapors and consequent growth to sizes detectable by optical methods. A major concern has been possible homogeneous nucleation of new particles when the application of high supersaturations is required to activate nanoparticles. However, this study shows that, rather than nucleating homogeneously to form new particles, the vapors tend to nucleate heterogeneously and further condense onto the preexisting particles at sizes much smaller than believed in the past. This fact has already been used in atmospheric studies (*1*).

In the literature, there are some laboratory studies concerning the effect of ions on the nucleation rate. However, they are not typically related to activation of existing particles or clusters. For example, Kim *et al*. (*26*) investigated homogeneous and ion-induced nucleation in the ternary $NH_3/SO_2/H_2O$/air mixture. As a result of their study, they proposed that the main particle production mechanism is homogeneous nucleation of $(NH_4)_2SO_4$ molecules produced by the H_2SO_4-NH_3 reaction. Several years ago, Gamero-Castaño and de la Mora (*17*) proposed clusters as "impurities in the gas phase" using their CPC. Their study focused on the activation of ions and charged nanoclusters with the use of a CPC, but did not include any comparison between charged and neutral particles.

The presence of ions, and electric charge on particles, will enhance not only the activation probabilities but also the growth rates of very small (nanometer-size) aerosol particles and air ions (*27*, *28*). The condensing vapors may exhibit dipole nature and can thus be electrostatically attracted to charged particles. This effect decreases rapidly with increasing particle size, which means that if this mechanism dominates the growth of freshly nucleated particles, the particle growth rate should decrease as a function of the particle size. However, no sign of such a growth dependence has been reported. Although the condensation enhancement factor caused by the presence of electric charges varies between the different theories, all of the theories predict a fairly similar size dependence for this effect (*6*). However, according to our present study, the possible difference in growth has a much smaller effect on atmospheric aerosol formation than the activation probability. Therefore, we can conclude that the key process in atmospheric investigations is the activation of preexisting clusters and nanoparticles.

From the point of view of atmospheric aerosols and their climate interaction, our observation allows a more accurate description of cluster activation leading to aerosol formation. In atmospheric processes, several different organic compounds are undoubtedly participating in the activation process.

References and Notes

1. M. Kulmala *et al.*, *J. Aerosol Sci.* **38**, 289 (2007).
2. C. T. R. Wilson, *Philos. Trans. R. Soc. London Ser. A* **189**, 265 (1897).
3. N. N. Das Gupta, S. K. Ghosh, *Rev. Mod. Phys.* **18**, 225 (1946).
4. H. R. Pruppacher, J. D. Klett, *Microphysics of Clouds and Precipitation* (Kluwer Academic, Dordrecht, Netherlands, 1997).
5. M. Kulmala, L. Pirjola, J. M. Mäkelä, *Nature* **404**, 66 (2000).
6. M. Kulmala *et al.*, *Atmos. Chem. Phys.* **4**, 2553 (2004).
7. M. Kulmala, K. E. J. Lehtinen, A. Laaksonen, *Atmos. Chem. Phys.* **6**, 787 (2006).
8. T. T. Kodas, M. J. Hampden-Smith, *Aerosol Processing of Materials* (Wiley-VCH, New York, 1999).
9. Detailed information on experimental methods, further results, and theory is available as supporting material on *Science* Online.
10. P. E. Wagner, *J. Colloid Interface Sci.* **105**, 456 (1985).
11. P. E. Wagner, D. Kaller, A. Vrtala, A. Lauri, M. Kulmala, *Phys. Rev. E Stat. Nonlin. Soft Matter Phys.* **67**, 021605 (2003).
12. W. Thomson, *Proc. R. Soc. Edinburgh* **7**, 63 (1870).
13. A. B. Nadykto, A. A. Natsheh, F. Yu, K. V. Mikkelsen, J. Ruuskanen, *Phys. Rev. Lett.* **96**, 125701 (2006).
14. N. Fletcher, *J. Chem. Phys.* **29**, 572 (1958).
15. M. Noppel, H. Vehkamäki, M. Kulmala, *J. Chem. Phys.* **119**, 10733 (2003).
16. H. Vehkamäki *et al.*, *J. Chem. Phys.* **126**, 174707 (2007).
17. M. Gamero-Castaño, J. F. de la Mora, *J. Aerosol Sci.* **31**, 757 (2000).
18. M. Kulmala, *Science* **302**, 1000 (2003).
19. M. Kulmala *et al.*, *J. Aerosol Sci.* **35**, 143 (2004).
20. D. Kashchiev, *Nucleation: Basic Theory with Applications* (Butterworth-Heinemann, Oxford, 2000).
21. R. Strey, P. E. Wagner, Y. Viisanen, *J. Phys. Chem.* **98**, 7748 (1994).
22. M. Wilck, F. Stratmann, *J. Aerosol Sci.* **28**, 959 (1997).
23. U. Backman, J. K. Jokiniemi, A. Auvinen, K. E. J. Lehtinen, *J. Nanoparticle Res.* **4**, 325 (2002).
24. P. H. McMurry, *Atmos. Environ.* **34**, 1959 (2000).
25. M. Kulmala, K. E. J. Lehtinen, L. Laakso, G. Mordas, K. Hämeri, *Boreal Environ. Res.* **10**, 79 (2005).
26. T. O. Kim, T. Ishida, M. Adachi, K. Okuyama, J. H. Seinfeld, *Aerosol Sci. Technol.* **29**, 111 (1998).
27. F. Yu, R. P. Turco, *Geophys. Res. Lett.* **27**, 883 (2000).
28. A. A. Lushnikov, M. Kulmala, *Eur. Phys. J. D* **29**, 345 (2004).
29. J. Wedekind, K. Iland, P. E. Wagner, R. Strey, in *Nucleation and Atmospheric Aerosols 2004*, M. Kasahara, M. Kulmala, Eds. (Kyoto Univ. Press, Kyoto, 2004), pp. 49–52.

30. This work was supported by the Austrian Science Foundation (Project No. P16958-N02 and P19546-N20), the Estonian Science Foundation (Grants 6223 and 6988), and the Academy of Finland. The authors declare no competing interests. Authors' contributions statement: experiments (P.M.W. and P.E.W.), nanoparticle generation (G.S., G.P.R., and P.M.W.), data analysis (P.M.W. and A.V.), theory and model calculations (M.K., M.N., H.V., and K.E.J.L.), writing (M.K., P.E.W., P.M.W., G.S., K.E.J.L., M.N., and H.V.).

Supporting Online Material

www.sciencemag.org/cgi/content/full/319/5868/1374/DC1
SOM Text
Figs. S1 to S5
Table S1
References

9 August 2007; accepted 24 January 2008
10.1126/science.1149034

Age and Evolution of the Grand Canyon Revealed by U-Pb Dating of Water Table–Type Speleothems

Victor Polyak,* Carol Hill, Yemane Asmerom

The age and evolution of the Grand Canyon have been subjects of great interest and debate since its discovery. We found that cave mammillaries (water table indicator speleothems) from nine sites in the Grand Canyon showed uranium-lead dating evidence for an old western Grand Canyon on the assumption that groundwater table decline rates are equivalent to incision rates. Samples in the western Grand Canyon yielded apparent water table decline rates of 55 to 123 meters per million years over the past 17 million years, in contrast to eastern Grand Canyon samples that yielded much faster rates (166 to 411 meters per million years). Chronology and inferred incision data indicate that the Grand Canyon evolved via headward erosion from west to east, together with late-stage (~3.7 million years ago) accelerated incision in the eastern block.

Ever since the first geologist known to set eyes on the Grand Canyon, John Strong Newberry in 1858, and the famous John Wesley Powell expedition of 1869 (*1*), the age and origin of the Grand Canyon have remained a subject of great scientific and popular interest. Accurate incision rate data have, until now, come from dating basalt flows and travertine deposits, but these results have not been able to record both the downward and headward incision of the Grand Canyon over its entire history beyond 1 million years ago (Ma) and higher than 100 m above the river (*2*). More than 50 years ago, Arthur Lange, a speleologist, proposed that the study of cave sediments and speleothems (cave formations) could produce an accurate minimum age for the Grand Canyon (*3*). U-series dating of speleothems, and consequently landscape evolution determinations using caves, began in the 1970s by alpha spectrometry (*4*) and were greatly improved by the application of mass spectrometry in the mid-1980s (*5*).

The realization that certain speleothems such as mammillary coatings (Fig. 1) form near groundwater tables [herein referred to as water tables (*6*)], and the fact that many Grand Canyon caves contain mammillary speleothems (*7*), has allowed us to take advantage of advances in U-Pb and U-series analytical techniques in an effort to make the long-sought chronology possible. For the Grand Canyon area (Fig. 2), there is no better niche than caves to find both clastic and chemical sediments that were deposited before, during, and after the incision of the canyon. Equally important, these cave deposits are located throughout the canyon. Caves are not only well suited to contain these deposits, they also provide an ideal environment that preserves and protects them from weathering. These mammillary coatings in the Grand Canyon caves contain sufficient uranium-lead ratios and yield U-Pb dates that place the water table within the canyon at a particular place and at an absolute time. This allows for the incision history of the Grand Canyon to be reconstructed

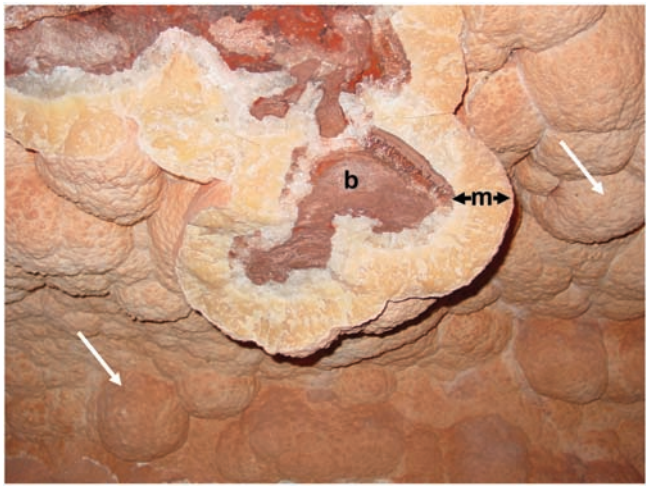

Fig. 1. Cave mammillaries coat cave walls below but near the water table. A cross section of broken mammillaries (m) and exposure of underlying bedrock (b) from site 6 (Tsean Bida) are shown. The unbroken form of this speleothem type (white arrows) indicates a subaqueous origin.

Department of Earth and Planetary Sciences, University of New Mexico, Albuquerque, NM 87131, USA.

*To whom correspondence should be addressed. E-mail: polyak@unm.edu

9.3. Appendix B2

Supporting Online Material for Winkler et al. (2008)

Supporting Online Material for

Heterogeneous Nucleation Experiments Bridging the Scale from Molecular Ion Clusters to Nanoparticles

Paul M. Winkler, Gerhard Steiner, Aron Vrtala, Hanna Vehkamäki, Madis Noppel, Kari E. J. Lehtinen, Georg P. Reischl, Paul E. Wagner, Markku Kulmala*

*To whom correspondence should be addressed. E-mail: markku.kulmala@helsinki.fi

Published 7 March 2008, *Science* **319**, 1374 (2008)

DOI: 10.1126/science.1149034

This PDF file includes:

Supporting Online Material

for the manuscript entitled 'Heterogeneous nucleation experiments bridging the scale from molecular ion clusters to nanoparticles' by Winkler et al.

Experiments and experimental results for nucleation mode aerosol particles

In this supplementary information we present the experimental and theoretical details of the studies on activation of molecular ions, charged and neutral clusters and nm-size particles for mobility diameters from below 1 nm to 24 nm using insoluble inorganic seed aerosols of different composition – WO_x, Ag, $(NH_4)_2SO_4$ – and a condensable organic vapour – *n*-propanol – in order to determine the dependence of vapour saturation ratio on seed particle size and charging state. A schematic diagram of the experimental system is shown in Fig. S1.

The nanoparticles considered in this study were generated using different experimental methods. Ag particles were formed by nucleation and subsequent condensation in vapours obtained by evaporation in a high-temperature tube furnace. Ammonium sulphate particles were obtained by spray-drying of dilute aqueous solutions of ammonium sulphate. WO_x particles were generated by means of a newly developed tungsten oxide particle generator which is described in detail below.

Vapour was added to the system by controlled injection of a liquid beam and subsequent quantitative evaporation in a heated unit. In order to achieve the desired vapour supersaturations, a well-defined and nearly saturated binary vapour-air mixture together with the seed particles were passed into the thermostated expansion chamber of a Size Analyzing Nuclei Counter (SANC). During a computer controlled measurement cycle the chamber was subsequently connected to a low pressure buffer tank resulting in an adiabatic expansion with expansion time around 8 ms and a well-defined vapour supersaturation was obtained. Temperature and vapour phase activity after expansion were determined using Poisson's law. For all experiments in this study the initial temperature after expansion was kept constant at about 275 K.

The seed particles, which are inducing heterogeneous vapour nucleation, lead to formation and subsequent growth of liquid droplets. Using the Constant-Angle Mie Scattering (CAMS) detection method (*S1*) the radius and number concentration of the growing droplets can be determined simultaneously at various times during the growth process without any external calibration.

We have measured activation (heterogeneous nucleation) probabilities using the SANC/CAMS method. The nucleation/activation probability is expressed as

$$P = \frac{N_{activated}}{N_{total}} = 1 - \exp(-kt) \qquad \text{(S1)}$$

Here k is related to heterogeneous nucleation rate and t is the time for activation.
We define the onset conditions as the conditions where the nucleation probability reaches the value P = 0.5.

Experimental onset saturation ratios determined for *n*-propanol for particles of different diameters and compositions are shown in Fig. S2. The diameters of the seed particles in Fig. S1 are ranging from 24 down to 1 nm and even below. The smaller the particle, the higher the saturation ratio needed for activation. It can be seen that for all seed particle compositions considered nucleation behaviour is practically identical. A similar observation was made by Dusek et al. (*S2*) showing that size dominates chemical effects for cloud droplet activation. Below 3 nm charge effects become increasingly important clearly showing a negative sign preference.

Nano-Particle Generation using NDMA2005 and UDMA2006

A newly developed Tungsten-Oxide heating wire particle generator (WO_x-Generator) (*S3*) allows the generation of aerosols with particle diameters in the range of 1 to 10 nm. Its first prototype was built at the Institute of Chemical Kinetics and Combustion in Novosibirsk and characterized by Necid (*S4*). Steiner (*S3*) improved some features such as the particle size range and the stability. In cooperation with Grimm-Aerosoltechnik GmbH. & Co. KG, a second prototype of the WO_x-Generator was built and a somewhat modified version (type 7.860 tungsten generator) was made commercially available. The latter was used in the experiments on heterogeneous nucleation of supersaturated vapour on nanometer size seed particles.

The principle of operation of the WO_x-Generator is based on the sublimation of tungsten oxide. Heated tungsten reacts in dry clean air to several oxides and nitrates of different valences (0, +2, +3, +4, +5 and +6). The oxidation of pure tungsten in ambient air leads to WO_3, a bright yellowish brittle substance. A heating wire around the WO_x coils provides a temperature of approximately 900°C; the sublimation temperature of WO_3. Tungsten oxide sublimates into the surrounding gas and is transported out of the generator by a flow of purified air (Q_{wox}) through the generator core (schematic diagram Fig. S3).

For temperatures close to the sublimation temperature of WO_3 and high dilution air flow rates, WO_3 monomers and dimers at mobility equivalent diameters of 1.25 nm and 1.58 nm, respectively, can be detected (*S3*). At higher temperatures and/or lower dilution rates, coagulation leads to a wide size distribution with mean particle diameters around 2.5 to 4.5 nm. With appropriate classification by a suitable Differential electrical Mobility Analyzer (DMA) a stable monodispersed aerosol can be obtained in a size range of 1.25 to 10 nm with concentrations up to 10^5 cm^{-3}. Detailed information on operation principle of DMAs can be found e.g. in (*S5*).

The Vienna type NDMA and UDMA are of cylindrical design. Two groups of parameters determine the performance of the DMA, the geometry parameters (R_1-outer radius of the inner electrode, R_2-inner radius of the outer electrode, L-effective axial distance between aerosol inlet and aerosol outlet) and the operating conditions (Q_{sh}-sheath air flow rate, Q_a-aerosol flow rate, Q_s-sample air flow rate, Q_{ex}-excess air flow rate).
The UDMA is designed for extremely high sheath air flow rates. Both DMAs are operated in a closed loop arrangement (*S6*). The excess air is carefully purified and used as sheath air. To reduce diffusion losses in the aerosol exit of the DMA, when used as an analyzer, the aerosol sensor (faraday-cup electrometer) is integrated in the base of the DMA.

The standard deviation of the classified aerosol is, for particles larger than 10nm, only determined by the choice of DMA flow rates:

$$\frac{dD_p}{D_p} = \psi(D_p) \cdot \frac{dZ}{Z} = \psi(D_p) \cdot \frac{Q_a}{Q_{sh}}, \tag{S2}$$

where $\Psi(D_p) = \frac{1}{D_p} \cdot \frac{C(D_p)}{D_p} \cdot \left(\frac{\partial}{\partial D_p} \left(\frac{C(D_p)}{D_p} \right) \right)^{-1} \equiv \frac{d \ln(D_p)}{d \ln(Z_p)}$

Here Z is the electrical mobility, D_p the electrical mobility equivalent particle diameter and $C(D_p)$ the slip correction factor.

For particles smaller than 10nm the corresponding equation is

$$\frac{dD_p}{D_p} \cong 0.5 \cdot \frac{dZ}{Z} \cong 0.5 \cdot \frac{Q_a}{Q_{sh}}, \tag{S3}$$

Due to the diffusion broadening the width of the transfer function becomes broader, depending on Sheath air flow rate and DMA geometry (*S7,S8*). Fig. S4 shows the dependence of the geometric standard deviation of the classified aerosol on mean particle size for the Vienna type NDMA2005 (L = 15 mm, R_1 = 17.5 mm, R_2 = 24.1 mm). Fig. S5 shows the same relationship for the Vienna type UDMA2006 (L = 6.5 mm, R_1 = 17.5 mm, R_2 = 24.1 mm).

Theory

We restrict this theoretical description to the simplest case where the nucleating vapour consists of one component only. We use equimolar surfaces as the dividing surfaces between the phases throughout the paper, thus setting the surface excess numbers to zero and assume the surface of tension to coincide with equimolar surface. In the classical homogenous nucleation theory (*S9,S10*) Kelvin equation gives the radius of the critical cluster as

$$r^* = \frac{2v\sigma_{g,l}}{kT \ln S}, \tag{S4}$$

where $\sigma_{g,l}$ is the gas-liquid surface tension, v is the partial molecular volume in the liquid, k is the Boltzmann constant, T is the temperature and S saturation ratio in the nucleating vapour. The number of molecules in the critical cluster, assumed spherical, is

$$\Delta n^*_{\text{hom}} = \frac{4\pi r^{*3}}{3kTv}, \tag{S5}$$

and the formation free energy of a general cluster is

$$\Delta G_{\text{hom}}(n) = -nkT \ln S + A_{g,l}\sigma_{g,l} \tag{S6}$$

where $A_{g,l}=4\pi r^2$ is the surface area of a spherical cluster. For a critical cluster the formation free energy reduces to

$$\Delta G^*_{\text{hom}} = \frac{4\pi r^{*2}\,\sigma_{g,l}}{3kT}. \tag{S7}$$

In the classical heterogeneous nucleation theory the critical cluster is assumed to be cap-shaped part of a sphere, the radius of which is equal to that of a homogenous critical cluster (see eq. (S4)).
The seed particle is also assumed spherical. The ratio of seed particle radius R_{seed} and the radius of the critical cluster is denoted by X

$$X \equiv \frac{R_{seed}}{r^*} = \frac{R_{seed} kT \ln S}{2v\sigma_{g,l}}. \tag{S8}$$

The classical formation free energy of a heterogeneous cluster is

$$\Delta G_{het}(n) = -nkT \ln S + A_{g,l}\sigma_{g,l} + A_{l,seed}(\sigma_{l,seed} - \sigma_{g,seed}) \tag{S9}$$

where $\sigma_{g,seed}$ and $\sigma_{l,seed}$, are the surface tension between the gas-phase and the seed particle, and the liquid phase and the seed particle, respectively. $A_{l,seed}$ is the area of the contact interface between the cluster and the seed particle. For a critical heterogeneous cluster the formation free energy is proportional to the formation free energy of a homogeneous cluster (*S11*)

$$\Delta G^*_{het} = f_g(m, X)\Delta G^*_{\text{hom}} \tag{S10}$$

where the geometric factor f_g is

$$f_g = \frac{1}{2}\left[1 + \left(\frac{1 - Xm}{g}\right)^3 + X^3\left(2 - 3\left(\frac{X - m}{g}\right) + \left(\frac{X - m}{g}\right)^3\right) + 3mX^2\left(\frac{X - m}{g} - 1\right)\right], \tag{S11}$$

with

$$g = \sqrt{1 + X^2 - 2Xm}\ , \tag{S12}$$

and Young's equation (*S12*) relates the contact parameter m=cosθ and thus the contact angle θ , to the surface tensions

$$m \equiv \cos\theta = \frac{(\sigma_{g,seed} - \sigma_{l,seed})}{\sigma_{g,l}}. \tag{S13}$$

Also the number of molecules in the critical heterogeneous cluster Δn_{het} is proportional to that in a homogeneous cluster

$$\Delta n^*_{het} = f_n(m, X)\Delta n^*_{\text{hom}}, \tag{S14}$$

where f_n is another geometric factor (*S13*)

$$f_n = \frac{1}{4}\left[2 + 3\left(\frac{1 - Xm}{g}\right) - \left(\frac{1 - Xm}{g}\right)^3 - X^3\left(2 - 3\left(\frac{X - m}{g}\right) + \left(\frac{X - m}{g}\right)^3\right)\right] \tag{S15}$$

The heterogeneous nucleation rate J_{het} is given by

$$J_{het} = K \exp\left(\frac{-\Delta G^*_{het}}{kT} \right), \tag{S16}$$

where K is a kinetic pre-factor which depends only weakly on the seed particle radius, saturation ratio, temperature and number density of vapour molecules adsorbed at the seed particle surface. The probability that heterogeneous nucleation occurs in a chosen time period t is related to the nucleation rate through (*S14*)

$$P = 1 - \exp(-J_{het} 4\pi R_{seed}^2 t), \tag{S17}$$

assuming that the nucleation rate is expressed per unit seed particle surface area and unit time (units $m^{-2}s^{-1}$). From the heterogeneous nucleation probability P according to Eq. (S17) the heterogeneous onset saturation ratio can be obtained as the saturation ratio, at which $P = 0.5$. The corresponding R_{seed} is called Fletcher radius.

The onset saturation ratio is very insensitive to the specific formula used for the kinetic pre-factor K. We have used $K=\beta Z N_{ads}$ with the impingement rate β, the Zeldovich factor Z and the surface concentration of adsorbed molecules $N_{ads}(1/m^2)$ are given by

$$\beta = \frac{S p_s A_{g,l}}{\sqrt{2\pi m k T}} \qquad Z = \frac{v}{2\pi r^2} \sqrt{\frac{\sigma}{kT}}, \qquad N_{ads} = \frac{S p_s}{\sqrt{2\pi m k T}} \frac{1}{\upsilon} \exp\left(\frac{L}{kT} \right), \tag{S18}$$

where p_s is the saturation vapour pressure, v and m, are the molecular volume and mass, respectively, υ is the vibration frequency of a molecule of the seed particle surface and L is the latent heat of vaporization per molecule. Our model thus uses the direct vapour deposition approach and approximates the Zeldovich factor by the formula for homogenous nucleation *(S15)*.

The classical Thompson's theory states that in a system containing ions with charge q (radius R_{dry}), the formation free energy of a spherical cluster centered around an ion is (*S16*):

$$\Delta G(n) = -nkT \ln S + A_{g,l}\sigma_{g,l} + \frac{q^2}{8\pi\varepsilon_0} \left(1 - \frac{1}{\varepsilon_r} \right) \left(\frac{1}{r} - \frac{1}{R_{seed}} \right), \tag{S19}$$

where ε_0 is the vacuum permittivity, and ε_r is the relative dielectric constant of the liquid which forms the cluster. More general expression for the formation free energy of an ion is given in (*S17*), but for the case of coincidence of surface tension and equimolar dividing surfaces that is assumed here and ignorance of possible spontaneous polarization of interface molecules the more general expression reduces to Eq. (S19).

The equivalent of the Kelvin equation (or actually Thomson equation) in the ion induced case, obtained by setting the derivative of the formation free energy (Eq. (S19)) to zero and using $A_{g,l}=4\pi r^2$ is

$$r = \frac{2\sigma v}{kT \ln S}\left[1 - \frac{q^2\left(1-\frac{1}{\varepsilon_r}\right)}{64\pi^2\sigma\varepsilon_0 r^3}\right], \tag{S20}$$

which, for not too high supersaturations, has two solutions, r_1 corresponding to a minimum of the free energy (stable clusters around the ions) and r_2 corresponding to a free energy maximum (unstable critical clusters on verge of continuous growth). The numbers of molecules in the cluster is in this case

$$\Delta n = \frac{4}{3v}\pi\left(r^3 - R_{seed}^3\right). \tag{S21}$$

The energy barrier for ion induced nucleation is

$$\begin{aligned}\delta\Delta G &= \Delta G(r_2) - \Delta G(r_1) \\ &= -\frac{4\pi\left(r_2^3 - r_1^3\right)}{3v_i}kT\ln S + 4\pi\sigma\left(r_2^2 - r_1^2\right) + \frac{q^2}{8\pi\varepsilon_0}\left(1-\frac{1}{\varepsilon_r}\right)\left(\frac{1}{r_2}-\frac{1}{r_1}\right).\end{aligned} \tag{S22}$$

If the cluster forming on the charged particle is a cap-shaped part of a sphere, instead of a full sphere, the formation free energy has contributions from both the geometry as in the heterogeneous nucleation, and the electrostatic interactions as in the ion induced nucleation (Eq. S19,S22) (*S18*). However, here we consider the case, when contact angle is very small and we can use the approximation of full sphere i.e.

$$\Delta G(n) = -nkT\ln S + A_{g,l}\sigma_{g,l} + A_{l,seed}(\sigma_{l,seed} - \sigma_{g,seed}) + \frac{q^2}{8\pi\varepsilon_0}\left(1-\frac{1}{\varepsilon_r}\right)\left(\frac{1}{r_2}-\frac{1}{r_1}\right), \tag{S23}$$

and the actual nucleation barrier is calculated taking into account that $r_1 = r_{seed}$.

The number of molecules in a critical cluster is related to the critical cluster radius through Eq. (S14) and (S15). The energy barrier for critical cluster formation is inserted to Eq. (S16) and (S17) to calculate the nucleation rate and nucleation probability.

The first heterogeneous nucleation theorem (*S19*) can be used to extract the number of molecules in the critical cluster $n^* \approx \Delta n^* = n^* - n_g$ from measurements of nucleation probability P as a function of the saturation ratio S at constant temperature

$$\Delta n^* = \frac{\partial \ln\left(\ln\frac{1}{1-P}\right)}{\partial \ln S} + \frac{\partial \ln K}{\partial \ln S}, \tag{S24}$$

where the contribution of the kinetic pre-factor K, is of the order of 1 and usually neglected. and n_g is the number of molecules in vapor phase per volume of critical cluster.

Table S1 summarizes all the thermodynamic data used in the theoretical calculations. We have used $m = \cos\theta = 0.99999$ ($\theta \approx 0.3°$), and our results are qualitatively unchanged if we use $m = \cos\theta = 0.999$ ($\theta \approx 2.6°$) instead. Unfortunately there is no direct data for the contact angle, or for the seed-liquid and seed- gas surface tensions linking the contact angle and the gas-

liquid surface tension through Young's equation (S13). Our experimental results suggest that when the microscopic process of cluster formation is mapped into the idealized framework of classical heterogenous nucleation, a representative value for the contact angle is close, but not necessarily strictly equal, to zero.

On the size-mobility relationship

Differential mobility analyzers (DMA) measure directly the mobilities of charged aerosol particles. The particle sizes are then calculated from the measured mobilities. However, there is no unique way to determine the size or even mass of the nanoparticles from the mobilities (*S25,S26*). In principle, the data conversion is based on a size-mobility relationship (Stokes-Cunningham-Millikan). Since it is obtained for larger particles, it does not take into account the long range interaction between particles and gas molecules nor the size of the colliding molecules. These effects are, however, negligible for larger particles. Comparisons of experimental and theoretical results have shown that particles, which are smaller than the mean free path of molecules but still large compared with gas molecules, scatter molecules predominantly diffusely in collisions. Due to this diffuse scattering the environment exerts a larger drag force on moving particles compared to the elastic-specular scattering case (*S27, S28)*. i.e. mobilities are lower. On the other hand experimental mobilities of molecular size clusters are well described with elastic scattering when realistic interaction potentials between clusters and environment molecules are applied (*S29*). At a certain size there is a transition from predominately diffuse scattering to elastic scattering. All considered effects control the size that can be inferred from measured mobilities of nanometer range particles. While the transition to elastic scattering diminishes the drag force, the account of attractive interaction between particles and molecules and their finite sizes increases the drag force. In recent years several investigations (*S30, S31, S32, S33, S34*) have focused on these issues but the problem is still unresolved. The hindering factors are the scarcity of reliable experimental results for sizes less than 10 nm and difficulties in the theoretical treatment to describe the diffuse-specular transition of scattering.

As a summary we can state that the exact relationship between mobility and mass and size of particles is still an open issue. The mobility diameter (measured using DMA) and Kelvin and Fletcher diameter are not generally the same. In principle, Kelvin and Fletcher diameters are mass diameters (or geometric diameters), since they have been obtained using classical theories (see above). The mass diameter is typically said to be somewhat smaller than the mobility diameter (*S25, S34)*. However, the exact difference between those diameters is still an open question but is expected to be in the range 0 – 0.5 nm.

References:

S1. P. E. Wagner, *J. Colloid Interface Sci.* **105**, 456 (1985).

S2. U. Dusek *et al.*, *Science* **312**, 1375 (2006).

S3. G. Steiner, *Generierung von Nanopartikeln – Über die Konstruktion eines Heizdraht-Wolframoxidgenerators* (Masters Thesis, Univ. Wien, Fakultät für Physik, Wien, 2006).

S4. J. Necid, *Ladungswahrscheinlichkeiten von Nanopartikeln in einer bipolaren Ionenatmosphäre* (Masters Thesis, Univ. Wien, Fakultät für Formal- und Naturwissenschaften, Wien, 1998).

S5. E. O. Knutson, K. T. Whitby, *J. Aerosol Sci.* **6**, 443 (1975).

S6. V. Jokinen, J. M. Mäkelä, *J. Aersosol Sci.* **28**, 4, 643 (1997).

S7. M. R. Stoltzenburg, *An Ultrafine Aerosol Size Distribution Measuring System* **(**PhD. Thesis, Mechanical Engineering Department, Univ. of Minnesota, Minneapolis, 1988).

S8 G. P. Reischl, J. M. Mäkelä, J. Necid, *Aerosol Sci. Tech.* **27**, 651 (1997).

S9. R. Becker, W. Döring, *Ann. Phys. (Leipzig)* **24**, 719 (1935).

S10 M. Volmer, *Kinetik der Phasenbildung* (Verlag Von Theodor Steinkopff, Dresden und Leipzig, 1939).

S11. N. H. Fletcher, *J. Chem. Phys* **29**, 572 (1958).

S12. T. Young, Philos. Trans. R. Soc. **95**, 65 (1805).

S13. A. Määttänen *et al.*, *Journal of Geophysical Research* **110**, E02002 (2005).

S14. M. Lazaridis, M. Kulmala, B. Z. Gorbunov, *Journal of Aerosol Science* **23**, 457 (1992).

S15 A. Määttänen, H. Vehkamäki, A. Lauri, I. Napari, M Kulmala, J. Chem. Phys. **127,** 134710 (2007.)

S16. G. K. Yue, L. Y. Chan, *J. Colloid Interface Sci.* **68**, 501 (1979).

S17. M. Noppel, H., Vehkamäki, M. Kulmala, *J. Chem. Phys*. **119**, 10733 (2003).

S18. M. Noppel *et al.,* in *Nucleation and Atmospheric Aerosols* , C. O'Dowd, P. E. Wagner, Eds. (Springer, Galway, 2007), pp. 327-331.

S19. H. Vehkamäki *et al.*, *J. Chem. Phys.* **126**, 174707 (2007).

S20. J. Timmermans, *Physico-chemical constants of pure organic compounds*, Vol 2 (Elsevier, New York, 1965)

S21. C. Yaws, Ed., *Chemical Properties Handbook*, (McGraw-Hill, New York, 1999)

S22. J. Dean, Ed, *Lange's Handbook of Chemistry* 15th Ed (McGraw-Hill, NewYork, 1999)

S23. T. Schmeling, R. Strey, Ber. Bunsenges. Phys. Chem. **87,** 871 (1983).

S24. M. Kulmala, A. Lauri, H. Vehkamäki; A. Laaksonen, D. Petersen, P. E. Wagner, *J. Phys. Chem.* B 105, 11800 (2001).

S25. J. Mäkelä *et al*., *J. Chem. Phys*. **105**, 1562 (1996)

S26. S. Ude and J. Fernández de la Mora, *J. Aerosol Sci.* **36**, 124 (2005)

S27. R.A: Millikan, *Phys. Rev.* **22**, 1 (1923).

S28. P.S: Epstein, *Phys. Rev.* **23**, 710 (1924).

S29. A.A: Shvartsburg, G.C. Schatz, and M. F. Jarrold, *J. Chem. Phys*, **108**, 2416 (1998).

S30. H. Tammet, *Journal of Aerosol Science*, **26**, 459 (1995).

S31. J. Fernández de la Mora, L. de Juan, T. Eichler, and J. Rosell, *Trends in Analytical Chemistry,* **17**, 328 (1998).

S32. Z. Li, and H. Wang. *Phys. Rev. E,* **68**, 061206, (2003).

S33. Z. Li, and H. Wang. H., *Phys. Rev. E*, **68**, 061207 (2003).

S34. S.D. Shandakov., A.G. Nasibulin., and E. I. Kauppinen., *J. Aerosol Sci.* **36**, 1125, (2005).

Table

Quantity	symbol	Value	ref	units
Liquid density	*m/v*	1047.94 - 0.835978×T	*(20)*[a]	Kg/m^3 ,T in Kelvin
Saturation vapour pressure	p_s	133.322×10^(31.52-3.46×10^3 /T-7.52×log10(T)-4.29×10^{-11}×T+ 1.3×10^{-7} ×T^2)	*(21)*	Pa, T in Kelvin
Surface tension	$\sigma_{g,l}$	[25.26-0.0777×(T-273.15)]/1000	*(22)*	N/m, T in Kelvin
Molecular mass	*M*	60.11		amu
Latent heat	*L*	60.11 ×10^{-3}(1.1840 ×10^6-1.285 ×10^3 ×T)	*(23)*	J/mol, T in Kelvin
Vibration frequency	υ	1/1.13×10^{-12}	*(24)*	1/s

Table S1: Thermodynamic parameters for *n*-propanol used in the model calculations.

[a] Linear fit to the data of Timmermans *(20)*

Figures

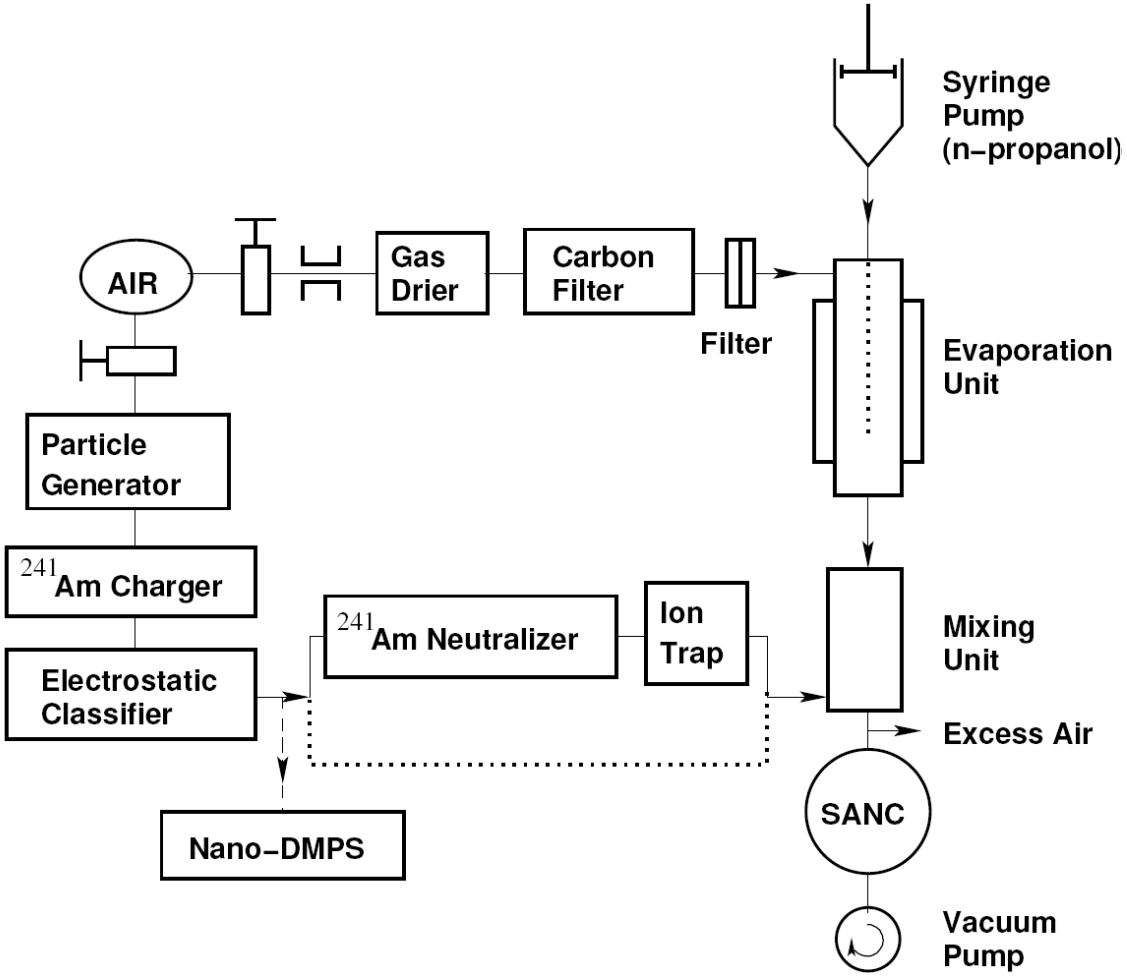

Figure S1: Experimental laboratory set-up.

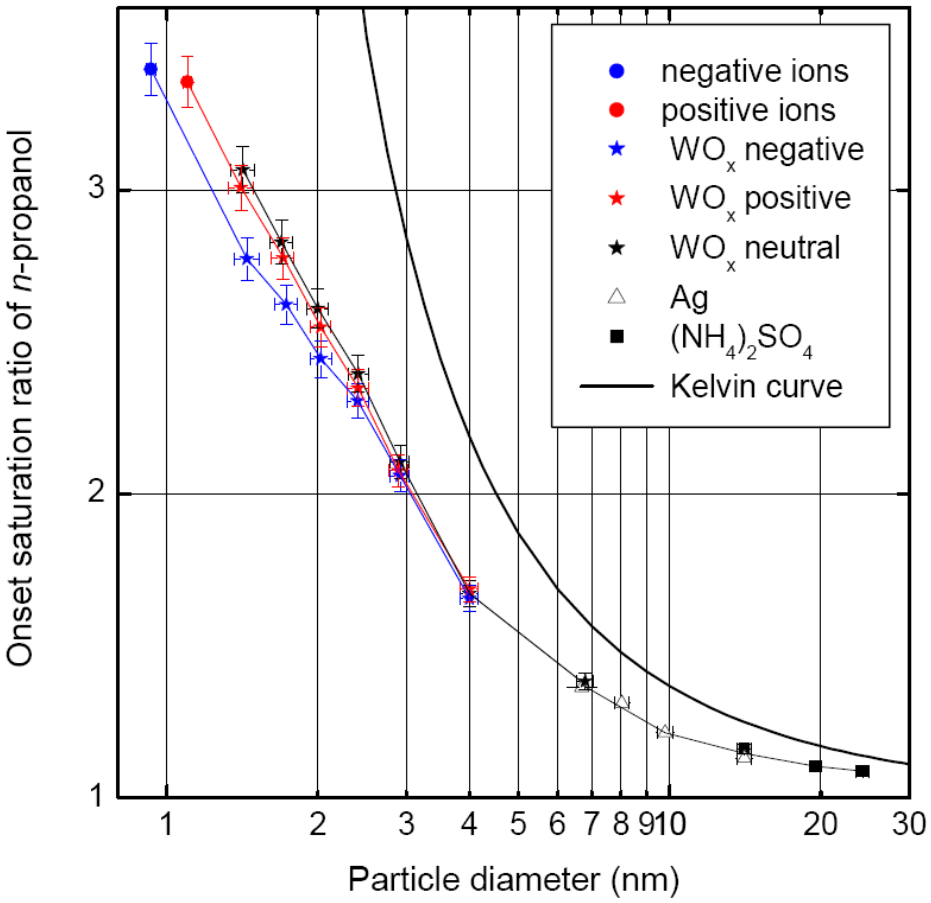

Figure S2. Experimental onset saturation ratios compared to Kelvin equation for heterogeneous nucleation of supersaturated *n*-propanol vapour on seed particles of various different compositions.

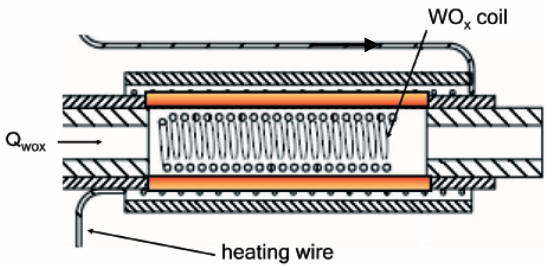

Figure S3: WO_x-Generator core.

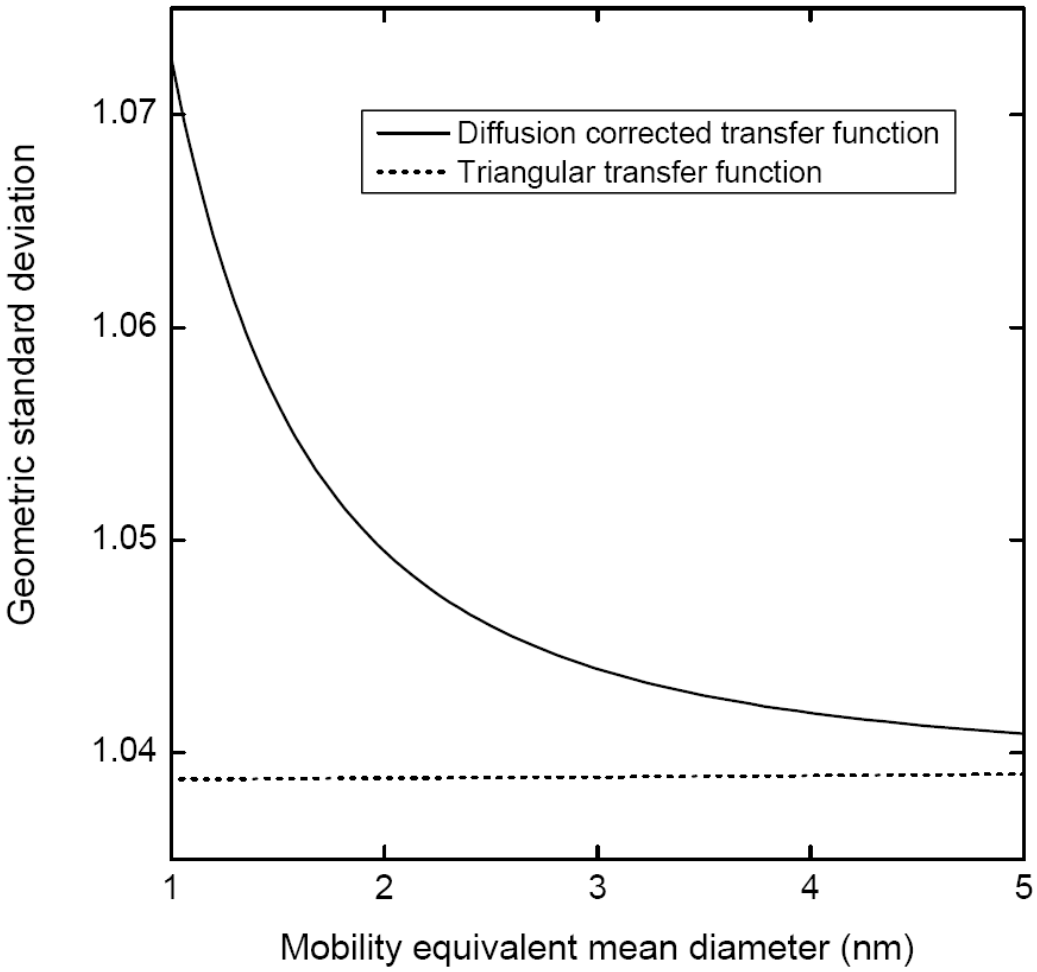

Figure S4: Calculated geometric standard deviation of classifier output aerosol NDMA (R_2 = 0.0241 m, R_1 = 0.0175 m, L = 0.015 m), Qsh = 25.0 l/min, Qs = 4.6 l/min.

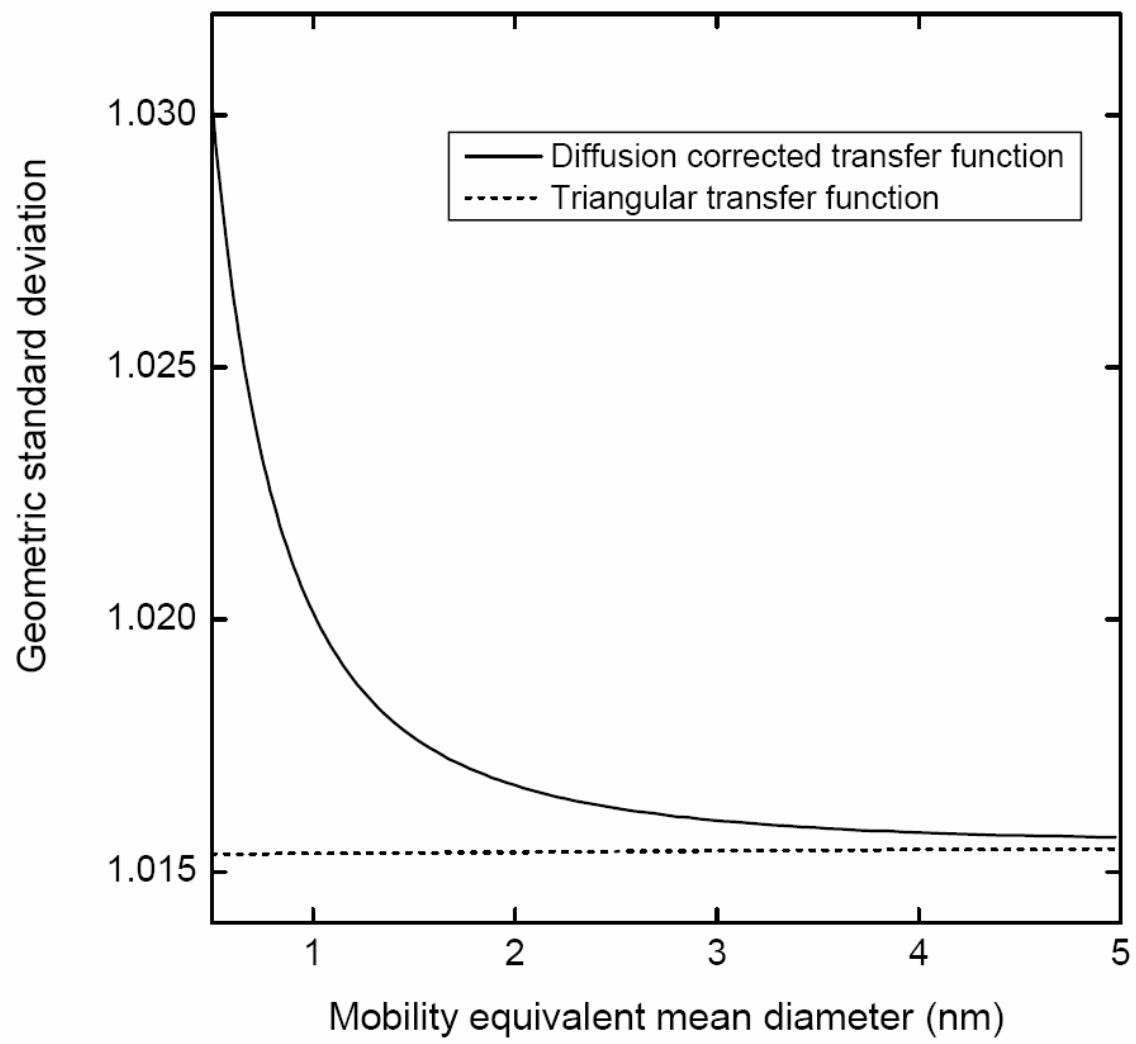

Figure S5: Calculated geometric standard deviation of classifier output aerosol UDMA (R_2 = 0.0241 m, R_1 = 0.0175 m, L = 0.0065 m), Qsh = 300.0 l/min, Qs = 21.6 l/min.